GRANULAR FLOW, SEGREGATION AND AGGLOMERATION IN BLADED MIXERS

by

BRENDA REMY

A Dissertation submitted to the

Graduate School-New Brunswick

Rutgers, The State University of New Jersey

in partial fulfillment of the requirements

for the degree of

Doctor of Philosophy

Graduate Program in Chemical and Biochemical Engineering

written under the direction of

Professor Benjamin J. Glasser

and approved by

____

____

____

____

New Brunswick, New Jersey

October 2010

Abstract of the Dissertation

Granular Flow, Segregation and Agglomeration in Bladed Mixers

By BRENDA REMY

Dissertation Director:
Professor Benjamin J. Glasser

A large number of industrial processes involve the transport, mixing and storage of particulate systems. While prevalent in industry, particulate processes are commonly plagued by problems due to the complex rheology of these systems. In this work, the behavior of granular materials in a bladed mixer, an industrially relevant geometry, was investigated using computational and experimental techniques. Experimental flows were characterized via Particle Image Velocimetry and image analysis. Discrete element simulations were carried out to examine the effect of a wide range of system parameters.

Particulate flows in bladed mixers were found to be periodic with complex flow patterns developing throughout the particle bed. Cohesionless flows were initially studied. For monodisperse flows, two distinct flow regimes were observed: a quasi-static regime where blade speed provides the time scale for momentum transfer and an intermediate regime where stresses scale linearly with blade speed. Particle and wall roughness were found to significantly affect bladed mixer flows. Systems with higher roughness are characterized by enhanced particle motion and mixing. Simple scaling relationships were observed for monodisperse flows in the quasi-static regime. Particle velocities and diffusivities were found to scale linearly with mixer size and blade speed, while stresses scaled linearly with particle bed weight. In polydisperse flows, size

segregation was found to occur due to sieving. However, it was found that the extent of segregation can be reduced by introducing intermediate particle sizes in between the smallest and largest particles.

Finally, wet particle flows were examined. At low moisture contents, enhanced particle velocities and mixing kinetics were observed in comparison to dry flows. However, at higher moisture contents, particle velocities and mixing rates were observed to decrease. Wet particle flows were characterized by the formation of particle agglomerates. Agglomerate formation led to an increase in particle bed roughness which significantly influenced macroscopic and microscopic flow properties.

These findings contribute to the understanding of granular behavior in complex systems. Improved understanding of granular flows will enable the development of first-principles based models which can assist in the design and scale-up of bladed mixer operations and the identification of critical processes parameters.

Acknowledgements

During the course of this project I benefited greatly from the guidance, advice and encouragement of a number of individuals. I begin by thanking my thesis advisor, Prof. Benjamin J. Glasser, for his guidance, support and mentoring. Special thanks for all his technical insight, for his careful review of my manuscripts and for all the helpful suggestions regarding the direction and execution of this research work. I thank our collaborators from Graz University of Technology, Stefan Radl and Prof. Johannes G. Khinast, for the many helpful discussions. I thank my committee members, Prof. Henrik Pedersen, Prof. Nina Shapley and Prof. James F. Gilchrist for their feedback and suggestions. I would like to express my gratitude to Prof. Fernando Muzzio, Prof. Carl Wassgren and Prof. Christine Hrenya for their insight and technical advice regarding modeling and experimentation. Many thanks to the undergraduate researchers Thomas M. Canty, Brian Pizza, Nike Isijola, Martina Gsöll and Sarah Wilson for all their assistance.

I would also like to thank Bristol-Myers Squibb Co. for a doctoral fellowship award which enabled the completion of this research. Special thanks for the support of all my colleagues in the Process Research & Development organization, in particular Dr. Jean Tom, Dr. San Kiang, Dr. David Kronental and Dr. Mauricio Futran. I thank my fellow graduate students for their friendship and for making graduate school a very enjoyable experience. I particularly want to thank Matthew Metzger, Carolyn Waite, Kiernan LaMarche, Athanas Koynov and Xue Liu for their friendship, their encouragement and for all the fun times. Finally, I thank my husband Jean for his patience, love and support and for his technical assistance with computer problems. I would not have been able to accomplish this without you by my side.

Table of Contents

List of Tables

List of Figures

Chapter 1. Introduction

1.1. Motivation

Particulate processing operations are commonly encountered in a wide variety of industries. It has been estimated that roughly 60% of all manufactured products required some sort of particle processing [1]. Examples of unit operations involving granular materials include fluidized catalytic reactions (bulk chemical industry) [2], compression of drugs into tablets (pharmaceutical industry) [3], freeze drying (food industry) [4], mixing and blending (cosmetic industry) [5] and concrete production (construction industry) [6]. Despite granular systems being so pervasive in industry, processes involving these types of materials are often poorly understood compared to their fluid processing counterparts [7]. This reality stems in part from the fact that we lack a set of constitutive equations derived from first-principles that describe granular flows under a specified initial state and boundary conditions. The lack of fundamental understanding of granular systems leads to broad assumptions during process design, poor identification of critical process parameters and scale-up complications which are not easily explained [8]. It has been reported that close to 94% of solids processing plants experience some kind of major processing problem [9]. Traditionally, heuristic rules-of-thumb have been used to limit these problems, but these have not reliably prevented complications such as non-uniform flow, jamming and segregation from occurring during scale-up or commissioning. A more desirable approach is the ability to quantitatively predict flow behavior from fundamental principles, material properties and small-scale laboratory tests, and then to engineer processes accordingly.

Attempts to describe granular systems via continuum-like approaches have had limited success since, unlike molecular fluids, granular systems are discrete in nature and inhomogeneities at the microscopic/particle level have a profound impact at the macroscopic scale [10]. These characteristics make the continuum assumption in classical mechanical models questionable for granular systems. Additionally, granular flows exhibit a tremendous range of behavior ranging from solid-like quasi-static flows to rapid fluid-like ones [11]. The ability to capture the breath and depth of granular behavior with a single set of fundamental equations is therefore challenging.

The relevance of granular materials, coupled with the need for the development of a rigorous theoretical framework, has motivated the study of particulate systems by many researchers. Following the approach from the early days of fluid flow research, several scientists have strived to understand the behavior of model granular systems (monodisperse, cohesionless smooth spheres) [12-17] in simple geometries such as shear flows [18-21], Couette cells [22-26], chute flows [27-30] and rotating drums [31-33]. These studies have provided rich information on the transient and dynamical behavior of granular materials since they contain one or more of the key elements of industrial flows such as shear, physical boundaries and a body force or gravity. While these efforts have elucidated some of the underlying physics involved in the transport and mixing of granular materials, the connection between the behavior observed in these simple systems and the behavior expected in the more complex, industrial systems remains elusive. The rigorous study of granular flows in industrially relevant geometries has received far less attention in the literature.

The need for understanding the behavior of complex particulate systems is of critical importance to the pharmaceutical industry, where close to 80% of pharmaceutical products are formulated as tablets, pills or capsules [34]. Pharmaceutical processes require a high level of process control, quality monitoring and reproducibility to ensure the efficacy of the drug and the safety of the patients. However, pharmaceutical processes often involve complex equipment configurations and multi-component particulate systems making the design, commissioning and control of these processes difficult. Problems are frequently encountered, some even during the latter stages of development, culminating in the manufacturing of an out-of-specification product. These issues could lead to the recall of product from the market and could potentially delay the administration of life-saving drugs to patients.

Many industrial processes involving granular materials employ the use of mixers with mechanical agitators that provide shear, induce flow and encourage mixing. The appeal of these mixers comes from their ability to handle a wide variety of solids ranging from free flowing to cohesive powders and even pastes [5]. Mixer characteristics such as shape, size and agitator configuration determine the flow patterns, degree of mixing and the shear profile achieved in such devices [35, 36]. Currently it is difficult - if not impossible - to predict granular behavior in mechanically agitated beds.

The cylindrical mixer geometry mechanically agitated by an impeller is one of the most commonly used mixer configurations in industry. While in many cases agitated mixers are used to homogenize a blend of solid particles, they also serve to enhance heat and mass transfer (e.g., agitated dryers). Similar equipment is also used in high-shear granulation processes and in tablet press operations to encourage flow in the feed-frame assemblies. While simple in form, the mechanisms by which particle motion is generated in cylindrical mixers are still poorly understood. Problems, such as segregation, particle attrition and agglomeration [37-39], are known to occur in this geometry but the role of operating parameters and particle properties on flow behavior remains unclear. The work presented here was performed in an effort to develop a fundamental understanding of how granular flow, segregation and agglomeration occur in bladed mixers through the use of numerical simulations and experimental techniques. We seek to answer some of the questions that still remain regarding the operation and design of these devices such as "how do microscopic/particle properties affect bulk behavior?" and "what are the most important parameters for scale-up?"

1.2. Granular Flow Regimes

The rheological behavior of granular materials is significantly different from that of molecular fluids. While the dynamics of fluid systems are often adequately described by continuum treatments such as the Navier-Stokes equations, an equivalent set of equations for granular systems is not readily available. The relationship between stress and strain rates is not well established due to the diverse behavior exhibited by granular materials. A granular material may behave as an elastic solid or as a liquid depending on the localized concentration and stress. When a granular material behaves as an elastic solid, it is able to support large loads such as building foundations by distributing the load across frictional contacts within the particle bed [40]. In contrast, natural disasters such as avalanches and landslides occur when particles within a granular assembly move freely and independently from each other leading to a liquid like-behavior.

In general, the amount of stress generated in granular assemblies is mostly associated with the particle interactions and the influence of the interstitial fluid on stress generation is often negligible [41]. Stress in granular assemblies is generated by three different mechanisms [41]:

i) momentum transport due to the collisions of particles in a flowing layer.

ii) momentum transport due to the apparent random velocities of particles flowing across moving layers.

iii) momentum transport due to the forces generated by sustained contacts.

The first mode of stress generation is analogous to the molecular momentum transport in liquids [41] while the second mode is similar to the molecular momentum transport in turbulent gases (i.e. analogous to the Reynolds stress [42]). The third mode does not resemble any of the modes found in molecular fluids and it's responsible for some of the elastic solid behavior observed in granular materials. The relative importance of each mechanism on the total stress generated during flow will depend on the behavioral regime.

Three distinct behavioral regimes are known to exits in granular flows: the slowly deforming or quasi-static regime, the rapid flow regime and the intermediate regime. The regime in which granular flows occur will depend on the system's concentration, compression state and applied shear [19]. The boundaries at which flow regime transition occurs are still not well defined. Traditionally, shear rate has been used to define the limits where regime transition occurs. Tardos et al. [43] proposed a flow regime map based on the dimensionless shear rate, $\gamma^{O*} = \gamma^{O}[d_p / g]^{1/2}$, where γ^{O} is the shear rate, d_p is the particle's diameter and g is the acceleration due to gravity. The proposed flow regime map is presented in Figure 1.1. Granular systems at high concentrations and low shear rates tend to behave in the quasi-static regime where particles experience sustained contacts with their neighbors and momentum transfer is governed by the forces generated from the particle-particle contacts [19]. In this regime, the frictional particle contacts give rise to a yield stress which must be overcome in order to induce flow [41]. As the granular material begins to flow, the sustained contacts generate stresses which are independent of the rate of deformation. Additionally, when particles flow past a solid surface in the quasi-static regime, the drag force experienced by the particles is not steady but fluctuates in time due to the frictional nature of the particle-solid surface interactions. This behavior is known as stick-slip and it can lead to velocity fluctuations on the same order of magnitude as the bulk velocity [44].

Some gravity-driven flows, such as flow from a hopper [42], as well as some industrial mixing processes at low shear rates [45] and most geological flows [44] occur in the quasi-static regime. Continuum-like models for quasi-static flows have been developed in the past by considering stress at equilibrium conditions and incorporating a yield condition and a flow rule [41, 46]. The yield condition describes the normal and shear stresses at the failure point and the flow rule correlates the rate of deformation during flow to the failure point stresses. Use of these models requires a large number of experiments to determine the region of yield stresses in the principal stress space for a desired material [47]. In addition, solving these models for industrially relevant geometries can prove to be difficult and they can only provide average values for the stress distribution within the particle bed. This limits the usefulness of these constitutive relations as practical tools for quantitative prediction of granular behavior.

Systems at low concentrations and high shear rates tend to fall in the rapid flow regime. This regime is characterized by short lived binary collisions of particles which can be approximated as instantaneous. These instantaneous collisions give rise to local fluctuations in the stress, strain rate and solids fraction [48]. Momentum transfer in this regime is therefore controlled by inter-particle collisions and the apparent random velocities of particles moving across flowing layers. The shear stress in the rapid flow regime scales with the square of the shear rate. The first dependency comes from the fact that shear rate controls the amount of momentum exchange during each particle-particle collision. The second dependency comes from the rate of inter-particle collisions which is also controlled by the shear rate [11].

Fluidized beds generally operate in the rapid flow regime [49] as well as pneumatic conveying processes in industry and some geological flows such as avalanches [50]. Continuum models derived from classical hydrodynamics such as the kinetic theory of dense gases provide a suitable description of granular flows in this regime [14, 17, 51]. These models use equations for the conservation of kinetic energy, momentum and mass. From this viewpoint, the concept of a "granular temperature" arises. The granular temperature is analogous to the definition of the thermodynamic temperature for fluids and represents the amount of kinetic energy due to the difference in velocity for individual particles relative to an ensemble average. Since the particle-particle contacts in granular systems are inelastic, the granular temperature of an ensemble of particles is not maintained and without an external source of energy the particles can reach an 'absolute zero' state [52]. The rapid flow description of granular systems is only suitable for a limited range of conditions and concentrations.

In between the quasi-static and the rapid flow regimes lies an intermediate regime where momentum transfer is controlled by both inter-particle collisions and sustained particle-particle contacts. The transition between the quasi-static regime and the intermediate regime is not well defined. Research efforts in granular flows have traditionally concentrated on the quasi-static and rapid flow regimes with the intermediate regime receiving far less attention. In the intermediate regime, shear stress tends to scale linearly with shear rate, a behavior similar to that of fluids. More specifically, the behavior of granular materials in this regime resembles that of visco-plastic fluids such as Bingham fluids [53]. A yield stress needs to be overcome in order to induce flow (due to the frictional inter-particle contacts) and, once flow has been achieved, the shear rate is linearly proportional to the strain rate times a proportionality constant (i.e., an apparent viscosity). The Bingham model has been employed by various researchers to describe the rheology in the intermediate regime [53, 54] where the yield stress and apparent viscosity values are obtained from experimental measurements or from soil mechanics theories. The limitation of these visco-plastic models comes from the fact that the yield stress and apparent viscosity are functions of system size and particle properties.

In recent years, other continuum models have been developed for the intermediate flow regime which relate stress and strain rates to fluctuating values [43, 55]. These fluctuations are considered to be spatial and temporal in nature. At low values of theses fluctuations, the system behaves similarly to a quasi-static system while at large fluctuations the behavior approximates that of the rapid flow regime. These continuum models fail to capture some of the inhomogeneties that are known to exist in high concentration systems such as shear bands and force chains.

1.3. Segregation

Particulate de-mixing or segregation is a phenomenon known to occur in several granular flow processes which does not posses a molecular fluid analog. Under the presence of shear, granular materials will self-organize into segregated regions where particles with similar size, shape, density or surface characteristics assemble [56]. This makes the mixing of particulate systems with different components challenging. Everyday examples of granular materials experiencing segregation are found in the rising of larger grains to the top of a muesli mixture, and in finding the larger rocks at the bottom of the mountain and the smaller ones near the top after a landslide or avalanche.

Segregation is a complex process which is still not well understood. Some of the complexity surrounding segregation can be observed in Figure 1.2. Depending on operating conditions and scale of operation, a previously homogeneous mixture in a rotating drum can segregate into bands of large or small particles in the axial [57, 58] or in the radial [59] directions with complex patterns being formed. Currently, no general way exists to prevent the occurrence of segregation or to predict the final segregation state in cases where it does occur. Industrial processes are significantly affected by segregation, contributing greatly to the meager 60% operating efficiency of most solids processes [60]. Complications due to segregation arise in several industrial scenarios such as bin blending, tumbler mixers, pneumatic conveying and hopper discharge [9]. In the pharmaceutical industry, segregation often threatens the drug content uniformity of tablets and could lead to the production of an out-of-specification product.

Early efforts in segregation research focused on the identification of mechanisms leading to segregation and thus far approximately 13 different mechanisms have been proposed [61]. However, many of these mechanisms rarely occur in industrial scenarios and many are special cases of other mechanism [62]. Tang and Puri [62] classified the different segregation patterns reported in the literature into 4 main mechanisms (Figure 1.3):

i) Trajectory segregation - occurs when large and small particles have different velocity profiles due to inertial effects during flow. This type of segregation occurs in gravity driven flows such as flows in vertical pipes [63].

ii) Sieving segregation - occurs when smaller particles fall through the gaps that form between larger particles during flow as a result of localized shearing. Known to occur in vertically vibrated systems [64-66], rotating drums [67] and agitated devices [68].

iii) Fluidization segregation - caused by differences in drag/weight ratios between smaller/lighter particles and larger/heavier particles. This mechanism causes the smaller/lighter particles to remain near the top surface during filling of silos or during the operation of fluidized beds [49, 69].

iv) Agglomeration segregation - arises when smaller particles form agglomerates under the presence of cohesion forces triggering segregation due to differences in agglomerate mobility (i.e. larger agglomerates with greater mobility). This type of segregation could occur in drying processes and in handling of fine, cohesive powders.

Identification of the dominant segregation mechanisms has enabled the development of processing strategies that minimize the tendency for segregation to occur. Reducing the emptying time of units lowers the probability of segregation. Avoiding unit operations where particles roll pass each other (i.e. inclined chutes) reduces the potential for trajectory segregation to occur [9]. Reducing the drop height in between unit operations or avoiding long transfer lines is recommended. Narrowing the width of the particle size distribution has been proven effective in mitigating sieving segregation [62]. Modification of equipment configurations could also limit the occurrence of segregation. In rotating drums, changing the shape of the rotating drum from circular to non-circular induces chaotic advection leading to higher mixing rates and a lower degree of segregation [70]. Adding baffles in low shear mixers along the axis of rotation reduces segregation [71]. The baffles induce periodic mixing in the flowing layer by inverting the orientation of the granular material. These strategies address only a small number of the potential causes for segregation and, in some cases, are impractical or difficult to implement.

Most researchers agree that the main factor leading to segregation is particle size differences [72, 73]. Binary mixtures represent the simplest case of a granular material in which segregation due to particle size differences occurs. This realization has motivated the investigation of segregation for binary mixtures in fundamental geometries which could be viewed as simplified versions of complex equipment configurations. Binary mixture segregation has been studied in Couette flows *via* the kinetic theory approach [23] and with the use of particle dynamic simulations [74]. These studies found that granular energy is not equally distributed between the small and large particles and that species segregation is a result of three competing forces: thermal diffusion, ordinary diffusion and pressure diffusion. Additionally, the formation of particle clusters in Couette flows was found to induce segregation. The segregation of binary mixtures in vertically vibrated systems has been extensively studied in the literature [64, 65, 75, 76]. These studies demonstrated that the frequency and amplitude of the vibrations determine whether the small or the large particles are present in the top segregated layer. Wall friction has been shown to give rise to convection cells in vibrated systems which, at lower large particle concentrations lead to segregation, but promote mixing at higher large particle concentrations.

The effect of particle size ratio in binary system has also been studied. In general, higher particle size ratios increase the amount of segregation observed. In systems where segregation by sieving occurs, the rise velocity of the large particles increases with an increase in size ratio as the probability of the smaller particles filling the voids in between the large particles increases [73]. For situations where trajectory segregation is the main mechanism, an increase in size ratio increases the differences in velocity profiles between the large and small particles due to inertial effects. This has been observed experimentally in flows through vertical pipes [63]. In fluidized systems, an increase in size ratio increases the difference in the drag/weight ratio between the large and small particles [69].

Segregation in polydisperse mixtures has not been as extensively studied as the binary mixture cases due to the added complexity that arises from the presence of multiple particles species. Rosato et al. [66] studied the segregation behavior of a three component system in a vertically vibrated cylinder. The authors noticed that during the initial shaking cycles, 3 different regions developed in the vibrated bed: a top region composed of mostly large particles, a well mixed center region and a lower region composed of mostly small particles. As the system continued to be vibrated, a completely segregated bed was obtained. The authors also showed that the sorting order between the particle species is affected by changes in the size ratio. Dahl and Hrenya [49, 77] studied size segregation of granular materials with continuous size distributions in a simple shear system and a fluidized bed using the discrete element method. Gaussian and lognormal particle size distributions were studied in both systems. In the simple shear system, they found that species segregation occurs due to the presence of a granular temperature gradient, with larger particles accumulating in the low temperature areas for all the size distributions studied. In the fluidized bed case, large particles accumulated towards the bottom plate and the walls of the system for both the Gaussian and lognormal distributions. However, axial segregation was higher for the lognormal case than for the Gaussian distribution. The localized particle size distribution was found to be of the same form as the overall size distribution for both the simple shear and the fluidized bed case.

1.4. Cohesive Granular Flows

The presence of inter-particle adhesion forces is often encountered in many real granular systems. These forces give rise to different phenomenological behaviors in cohesive granular materials from what is observed in non-cohesive systems. For example, the tensile strength of static piles increases in the presence of cohesion [78]. This characteristic enables the creation of sand castles from wet sand since a stable shape cannot be created with dry sand [79]. The angle of repose of a granular pile is usually increased by cohesion [80]. Cohesive forces can increase dilation of granular materials during flow and can induce hysteresis [81, 82]. The apparent friction between particles increases even with a small amount of cohesion in the system [83]. This complex behavior makes the prediction and control of cohesive granular flows difficult. The presence of cohesion in industrial scenarios leads to operational problems which are not easily solved or prevented. Cohesion can often lead to problems such as bridging, channeling, discontinuous mass flows, material accumulation on equipment walls and broadening of particle size distributions [9, 84]. The majority of research in granular flows has focused on non-cohesive systems. Studies involving the flow of cohesive granular materials are not as commonly encountered in the literature. The need for fundamental studies dealing with the transport and storage of cohesive granular materials is therefore substantial.

The bulk cohesion of a granular material is controlled by intrinsic material properties (surface energies, elastic moduli, etc.), particle properties (size, size distribution, morphology, etc.) and moisture content in the system [85]. In general, three types of forces contribute to the amount of cohesion present in a system: van der Waals forces, electrostatic forces and capillary forces. The van der Waals forces occur at the molecular level and are proportional to the separation distance between particles times a proportionality constant called the Hamaker constant. The value of the Hamaker constant depends on material properties such as chemical composition and surface roughness [86]. The van der Waals binding energy is usually small compare to the kinetic energy during flow for particles with a radius above 20 μm [80]. Therefore, in most granular flow scenarios, van der Waal forces tend to weakly influence the behavior of the system. For fine powders, the effect of van der Waal forces becomes important during flow.

Electrification of particles could occur during flow due to repeated collisions between particles with different material surface properties [87]. This process is called triboelectrification and it often leads to the development of electrostatic adhesive forces between particles. The development of these forces during flow could cause complications such as electric discharges which increase the risk of dust explosions [88]. While electrostatic effects are of particular importance due to the associated hazards, the magnitude of electrostatic forces between particles has been shown to be one order of magnitude smaller than van der Waals forces for particles above the micro size range [86].

The presence of moisture in a granular system gives rise to cohesion due to capillary forces. When particles are in contact in wet systems, a meniscus is formed between the contacting surfaces as capillary action attracts the liquid on the nearby surfaces [85]. This leads to the formation of a liquid bridge which creates an attractive force due to surface tension and the hydrostatic pressure inside the bridge [89]. Capillary forces can have a significant effect on the behavior of granular materials. For example, the magnitude of capillary forces doubles that of gravity for particles with a diameter above 100 μm [80]. Particles in a wet system can exist in a number of different states depending on the moisture content of the system. These states are the pendular state (low moisture content), the funicular state (intermediate moisture content), and the capillary state (high moisture contents) (see Figure 1.4) [90]. The resulting behavior in wet systems is dictated by the amount of liquid present in the system and the distribution of the liquid via capillary bridge networks [80]. The presence of moisture also leads to the development of viscous forces between particles. However, at low moisture contents, the effect of these forces is secondary to the effect of the capillary forces [91].

The importance of the cohesion forces relative to gravitational and shearing forces can be determined by a set of dimensionless numbers. The granular Bond number is the ratio of the cohesive force to the gravitational force. For slowly shearing systems, the effect of cohesion becomes important when the granular Bond number is above one. For systems experiencing high shear, the collision number determines the relative importance of cohesive forces. The collision number is given by the ratio of the maximum cohesive force to the collisional force due to Bagnold [92]. Cohesion forces dominate the flow of granular material for collision numbers above one.

For systems containing particles of different sizes or surface characteristics, cohesion forces can act to enhance mixing or to promote segregation [93]. Recently, researchers have developed phase diagrams to assist in the determination of the final state of a multi-component granular mixture under the presence of shear and cohesion [92, 93]. These diagrams are developed by taking into account the values of the granular Bond number and collisional number for each combination of particle type interactions. When the magnitude of the adhesion forces between dissimilar particle types is greater than the magnitude of the forces due to gravity and shearing, segregation is mitigated. However, if the cohesion forces between similar particle types are higher, segregation is enhanced by the presence of cohesion in the system [94].

1.5. High Shear Mixers

Granular flow research in high shear mixers has received increased attention in recent years due to the industrial relevance of such devices. Most high shear mixers can be classified into two categorizes based on the axis of rotation: horizontal mixers and vertical mixers. Horizontal cylindrical mixer studies have been performed by Malhotra et al. [95-97], Laurent et al. [98, 99], Jones et al. [100] and Bridgwater et al. [101]. The studies by Malhotra et al. [95-97] focused on 2-dimensional geometries and provide information on mixing kinetics and heat transfer coefficients for agitated dryers. The ratio of the blade height to bed height was found to have a significant impact on particle mixing while heat transfer mechanisms were affected by the shape and cohesiveness of the particles. A 3-dimensional picture of flows in horizontal mixers emerged with the use of positron emission particle tracking (PEPT). Radioactive tracers are inserted within the particle bed and gamma ray detectors record the position of these particles as they follow the movement of the bulk flow in the system. Laurent et al. [98, 99] found that particulate flows in this geometry are periodic in nature and that axial dispersion coefficients linearly increase with blade speed. Jones et al. [100] observed slower mixing as the fill level was increased and blade speed was decreased. These researchers also found that axial transport was lower for cohesive materials compared to that of the dry materials. Bridgwater et al. [101] observed the development of three-dimensional recirculation zones in a ploughshare (horizontal) mixer above a critical impeller speed.

Early experimental studies in vertical mixers by Bagster and Bridgwater [102, 103] focused on the power and torque requirement on 2-dimensional flows to determine strain rates at the failure point. The side wall was found to have a considerable effect on the resulting strain field. These studies also found the existence of particle recirculation patterns that move with the blade. Knight et al. [104] studied the effect of impeller speed and configuration on the impeller torque in a 3-dimensional vertical mixer. They found that the dimensionless torque on a disc impeller was independent of impeller speed while torque for a flat blade impeller varied linearly with speed. Impeller angle and height also had a significant effect on the measured torque. The PEPT technique was used by Stewart et al. [105] to study flow over two flat blades in a vertical mixer. This study found that particles move radially forming recirculation zones and the size of some of these zones varied significantly with fill level. Additionally the velocity profiles inside the mixer were found to vary linearly with the rotational speed of the blade. A more complex blade configuration consisting of four blades pitched at a 45° angle was studied by Conway et al. [106] and Lekhal et al. [107] utilizing Particle Image Velocimetry (PIV). This technique records particle positions at the free surface and near transparent walls which allows for the characterization of the flow fields and the determination of particle trajectories. The study by Conway et al. [106] found that particle movement within the mixer was periodic and that its frequency depended on the speed of the blade rotation, a behavior similar to what was found in horizontal mixers. Striation patterns that developed through stretching and folding were observed for low-shear operations which were consistent with chaotic granular mixing. This behavior was not present during high-shear operations. Lekhal et al. [107] examined the effect of moisture on granular flows in a bladed mixer. Two flow regimes were identified at different levels of bed moisture. At low moisture contents, granular flow was dominated by the motion of individual grains, while at high moisture contents the flow is controlled by the motion of small agglomerates that formed due to cohesive forces.

Granular flow, mixing and segregation in vertical bladed mixers has also been studied *via* numerical simulations. Numerical simulation techniques have the potential of bridging the knowledge gap, since they allow for the study of parameters that are difficult to measure or vary experimentally. The discrete element method (DEM) has been widely used in recent years to examine granular flow in a variety of systems ranging from simple shear flows to more complex, industrially relevant geometries. Stewart et al. [108] and Zhou et al. [109, 110] performed numerical studies using DEM for bladed mixers with two flat blades. Stewart et al. [108] demonstrated the ability of the DEM technique to accurately capture glass bead flows in a bladed mixer. The studies by Zhou et al. [109, 110] focused on the effect of particle friction, size distribution and particle density on the flow and segregation patterns that developed inside bladed mixers. The particles' frictional characteristics were found to affect velocity profiles and mixing kinetics, while particle size and particle density affected segregation patterns. Sinnott et al. [36] performed 3-dimensional DEM simulations and investigated the effect of different blade configurations on granular mixing. Two configurations were studied: a flat rectangular blade and a horizontal bottom disc. The authors found that the degree of mixing was affected by the blade configuration. More recently Sato et al. [111] showed that agitator torque increases with rotational speed in a vertical bladed mixer and that particle kinetic energy can be related to the measured torque.

While previous work has provided insight into the granular behavior in bladed mixers, these studies have been limited to the effect of a small set of process parameters and particle properties on the measured variables. These studies have not clearly correlated operating parameters and particle properties to macroscopic properties. Additionally, little is currently known about the stress evolution in bladed mixers and the parameters that affect it. High-shear granulation processes depend on stresses developed *via* agitation to achieve controlled agglomeration and attrition of granules. In contrast, agitated drying processes in the pharmaceutical industry are generally designed to minimize the effect of attrition and agglomerate formation due to shearing. Uncontrolled shearing could lead to broad particle size distributions, formation of fines or large agglomerates and even loss of crystallinity. The numerical studies performed for bladed mixer thus far have focused on relatively simple blade configurations. More industrially relevant blade configurations remain to be examined and it is uncertain, whether the results obtained with the simplified geometries can be extended to the more complex industrial cases.

For bladed mixers, the majority of past studies have focused on dry granular materials. The case of granular flow in bladed mixers in the presence of cohesion has received less attention despite the fact that cohesion is present in many industrial scenarios where bladed mixers are used (i.e. wet granulation, agitated drying). Most of the research on wet granular flows has been perform for prototypical geometries such as chute flows, Couette cells, or rotating drum. These studies mostly focused on developing mathematical models to predict the inter-particle forces that arise due to the presences of moisture. The modeling of wet particle interactions has not been extended to the more complex case of granular flow in bladed mixers.

1.6. Wet Granulation

Wet granulation is a process by which a blend of fine powders is mixed with a liquid binder to form larger agglomerates or granules. This technique is widely used in industry as it allows for better control of product bulk density, particulate flowability, blend compactibility and drug content uniformity [112], the latter being a crucial quality attribute of pharmaceutical tablets. Wet granulation processes are usually performed in one of two equipment configurations: a fluidized bed or a high shear mixer [112]. Litster [113] has identified three key classes of rate processes which control the density and size distribution of the granules formed: wetting and nucleation, growth and consolidation, and attrition and breakage (see Figure 1.5). These rate processes occur in both the fluidized bed and the high shear mixer configurations and are influenced by the mixing and shearing profiles achieved in the granulator. Wetting and nucleation is controlled by the distribution of liquid binder throughout the powder bed, where the best conditions for nucleation arise when each drop of liquid forms a nucleus of a granule. Growth and consolidation are controlled by the deformation and compaction of granules under shear [114]. Attrition and breakage is controlled by the amount of shear stress transferred to the particle bed due to interactions with the equipment walls and with other particles.

Most wet granulation research in high shear mixers has focused on the prediction and control of granule properties from equipment variables or operating conditions. Traditionally, scale-up rules based on impeller speed kinematics have been used to control granulation processes at different scales. Rahmanian et al. [115] studied the effect of impeller speed on granule properties at different scales. The authors used 3 different scaling rules to compare results across granulator scales: the constant tip speed rule, the constant Froude number rule and the constant shear stress rule. They found that the constant tip speed and the constant shear stress rules produce granules with similar properties across scales ranging from 1 to 250 liter. This was not observed with the constant Froude number rule.

One of the most commonly used techniques for wet granulation control is to monitor agitator torque or power consumption. In previous years several researchers have related torque or power consumption measurements to granule properties such as granule strength, size distribution and compressibility achieved in laboratory scale high shear granulators [116-118]. More recently Sirois and Gordon [119] found that by using a normalized impeller work parameter to determine granulation end-point, one could control bulk density, average particle size and the cohesion index across scales ranging from 5 to 125 liters. The normalized impeller work end-point was found to be independent of impeller speed, geometry or granulator size. Sato et al. [120] showed that granule strength increases linearly with agitator power per unit volume regardless of vessel scale, and that granule mass and mean diameter can be correlated to agitator power.

Less attention has been given to the characterization of velocity profiles, flow patterns and stress distribution in high shear granulators. Litster et al. [121] measured powder velocity at the free surface at different impeller speeds. The authors identified two different flow regimes in this study: a bumping flow regime where the material rotates slowly and the surface of the particle bed deforms by forming a “bump” as the blades pass, and a roping flow regime where the material rotates faster and mixes in the vertical direction. In the bumping regime, surface velocities increase linearly with impeller speed while in the roping regime surface velocities appear independent of impeller speed. Watano et al. [122] measured stress above the blades of a high shear granulator with the use of a strain gauge. Their measurements showed that shear stress increases linearly with impeller speed and that shear stress is highest by the granulator’s wall. Tardos et al. [123] used calibrated particles with a well-defined yield strength to indirectly measure stresses within mixer granulators at 3 different scales. The researches found that shear stress is most sensitive to the amount of liquid binder present in the system with higher shear stresses achieved as the amount of cohesion in the system increased. From the measured stress data, the authors suggested a scaling rule for achieving "equal shear stress" across granulator scales in which the tip speed of the impeller is scaled by the impeller diameter to the 0.8 power.

Efforts to model wet granulation processes have mostly focused on the used of population balance methods to predict granule particle size distributions [124-126]. In this methodology, the particle size distribution is divided into discrete size range intervals. The rate of change of the amount of particles in each size range is determined from probability functions representing the nucleation, coalescence and breakage processes. The population balance models tend to be complex and several assumptions are needed to facilitate the numerical solution of the equations [112]. The challenge in the population balance is the determination of the kernels associated with each rate process from the fundamental mechanisms of granule formation, growth and breakage. Currently, the dynamics of these mechanisms are not well understood [124] making the verification of the simplifying assumptions difficult. This limits the usefulness of population balance methods in the design and scale-up of wet granulation processes. Recently, researchers have resorted to the use of the discrete element method (DEM) for the determination of population balance kernels [127, 128]. However, in these studies only a small portion of the particulate flow within the granulator was simulated and the effect of cohesion on particle velocities was ignored. A complete 3-dimensional analysis of particle agglomeration and attrition under the presence of shear and cohesion, which is needed to construct reliable population balance models, is still lacking.

1.7. Agitated Drying

The bladed mixer configuration is also found in agitated drying processes used in industry. Agitated drying is a contact drying process in which a wet particle bed is dried under heat and vacuum in the presence of shear. Heat is usually introduced into the system by jacketed cylinder walls, and in some cases by a heated impeller. Currently, little is known about the parameters affecting heat and mass transfer in agitated dryers. This makes the design, scale-up and control of drying operations difficult. Agitated drying processes are plagued by complications such as agglomerate formation, particle attrition and over-drying. Most of the work done on agitated contact drying has focused on the use of empirical models to predict drying [129, 130]. Heat transfer is modeled as a penetration process where a drying front of particles moves into the wet particle bed and heat conduction occurs. Mixing is accounted for in these models by empirical correlations which relate the system's Froude number to the contact time between dry and wet particles. The mixing parameters in these models are assumed to be constants. These correlations fail to account for the complex motion of particles in agitated devices.

Recent work in agitated dryers has explored the effect of drying conditions on particle attrition and agglomeration. Lekhal et al. [37, 39] studied the effect of drying at different conditions on the morphology of KCl (cubic particles) and L-threonine (needle-like particles). The authors found that attrition and agglomeration occur to a significant extent only after a critical moisture level was achieved. Attrition of particles was the prevalent mechanism affecting particle size changes at low drying temperatures and high shear rates for both the KCl and L-threonine systems. In contrast, at high drying temperatures and low shear rates, agglomeration dominated over particle attrition. Particle shape and aspect ratio was shown to be affected by the amount of shearing during drying, with a higher degree of particle attrition occurring for the needle-like particles vs. the cubic particles. Lee and Lee [38, 131] performed a force balance for the material in front of a pan dryer blade to develop an expression for the force experienced by the particles. Utilizing the developed expression, they were able to show that the force on the particles in front of the blade decreases with an increase in the pitch angle of the blades.

1.8. Outstanding Issues and Path Forward

Many questions still remain regarding the behavior of granular materials in mechanically agitated devices. Most of the previous work done on bladed mixers has focused on specific unit operations (i.e. blending, wet granulation or agitated drying) and on the parameters affecting the performance of these processes. The majority of these studies have not thoroughly investigated the underlying physics of particulate flows in bladed mixers limiting the usefulness of the findings.

Few studies are found in the literature which attempt to explain the observed behavior via mechanistic arguments. Previous studies have been limited to a small set of process variables and have not clearly correlated operating parameters and particle properties to macroscopic properties. Little is currently known about the evolution of stress in bladed mixers and the parameters that affect the stress. Relatively simple blade configurations have mostly been studied. More industrially relevant blade configurations remain to be examined.

Industrial bladed mixer operations often involve the use of components with particle size distributions and with a certain amount of moisture. Most of the fundamental segregation studies in bladed mixers have been performed using binary mixtures of small and large particles. The effect of increasing polydispersity on segregation has not been explored. It is unclear whether the binary mixture results can be extended to the more complicated case of pseudo-continuous particle size distributions. The effect of moisture content on granular flow in bladed mixers has not been extensively studied. The most prominent effect of moisture is an increase in interparticle cohesiveness, which directly impacts the bulk flowability of the granular material.

The work presented here addresses some of the questions that still remain regarding the behavior of particulate systems in bladed mixers. Chapter 2 introduces the experimental and numerical methods used to examine flows in the bladed mixer geometry. Characterization of monodisperse flows via numerical simulations is presented in Chapter 3. Chapter 4 highlights the effect of mixer properties and mixer scale on granular behavior. Accompanying experiments are described in Chapter 5 which validate the applicability of the numerical simulations and reveal the effect of shear rate on flow regime transitions. Polydisperse systems are examined numerically and experimentally in Chapter 6. Experimental and numerical examination of wet particulate flows is included in Chapter 7. Conclusions are presented in Chapter 8 along with recommendations for future work.

1.9. Figures for Chapter 1

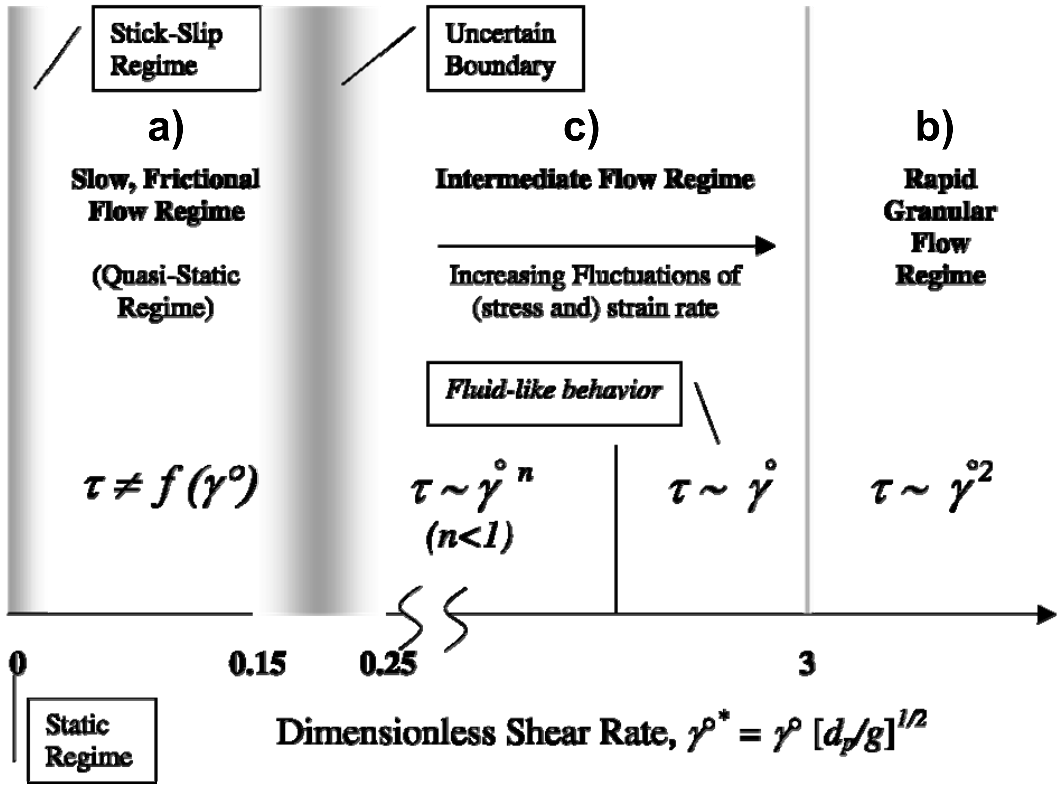

Figure 1.1 Tentative schematic of particulate flow regimes a) Slow, frictional flows, b) Rapid flows, and c) Intermediate flows. From Tardos et al. [43].

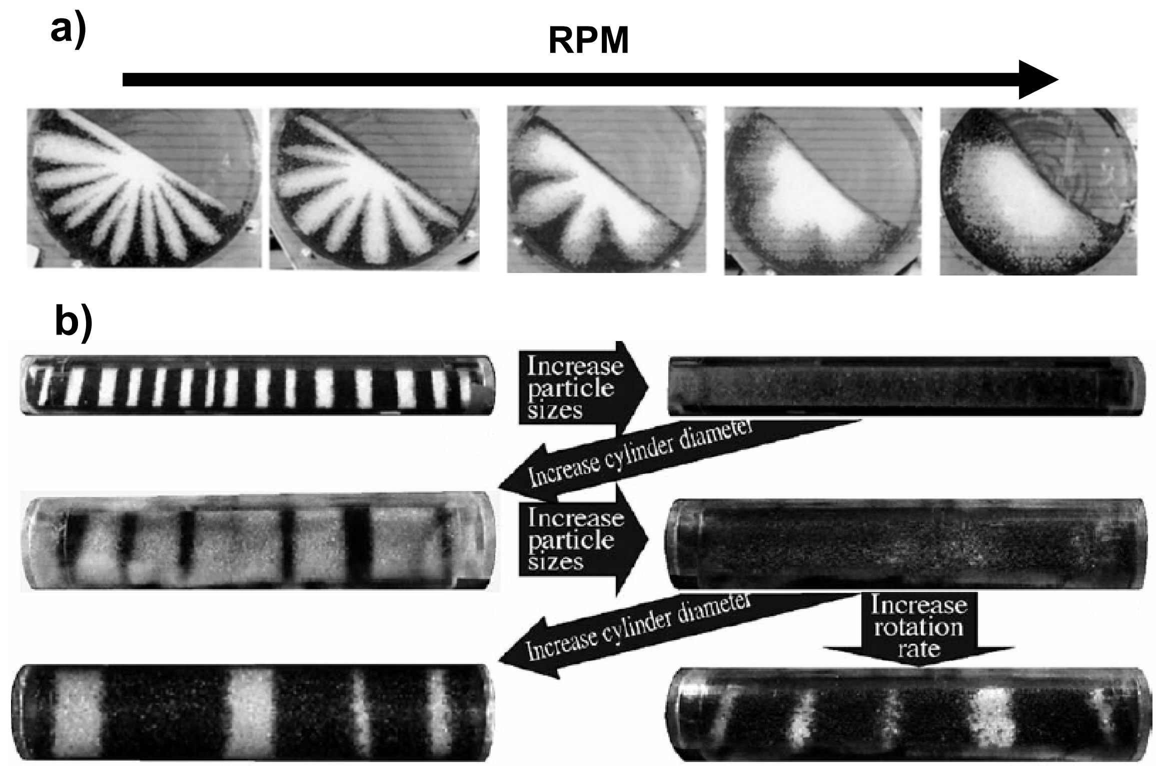

Figure 1.2 Segregation patterns in a rotating drum. a) Effect of rotation rate on radial banding. From Hill et al. [59]. b) Effect of particle size, cylinder diameter and rotation rate on axial banding. From Alexander et al. [57].

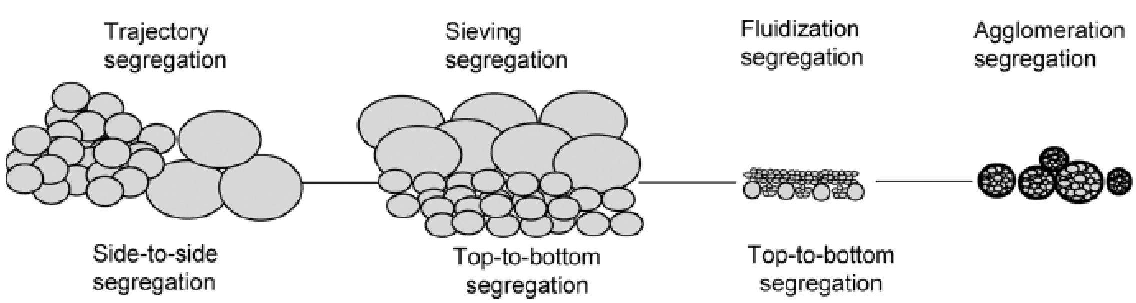

Figure 1.3 The four main proposed mechanism for segregation. From Tang et al. [62].

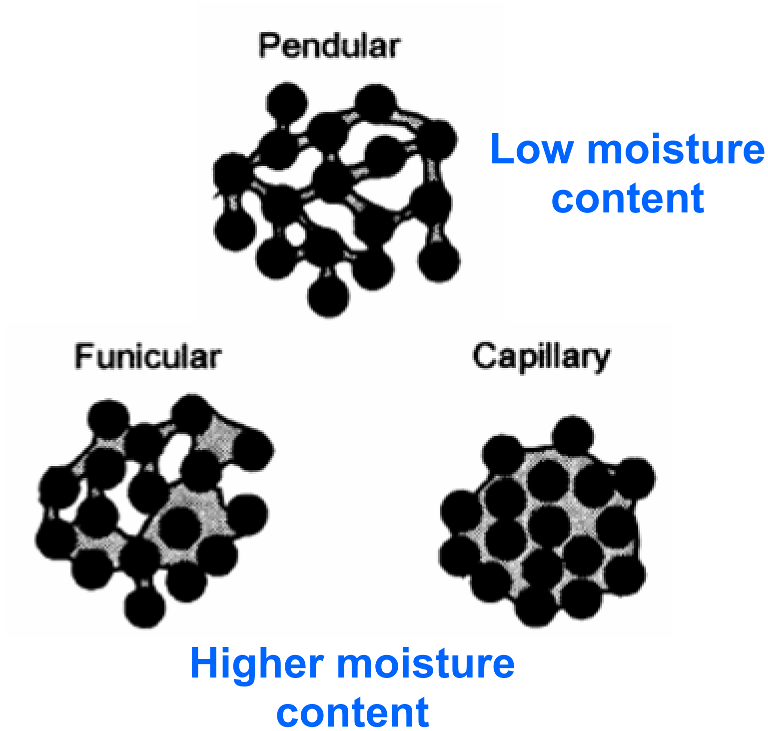

Figure 1.4 The different states of wet granular flows. From Papadakis et al. [90].

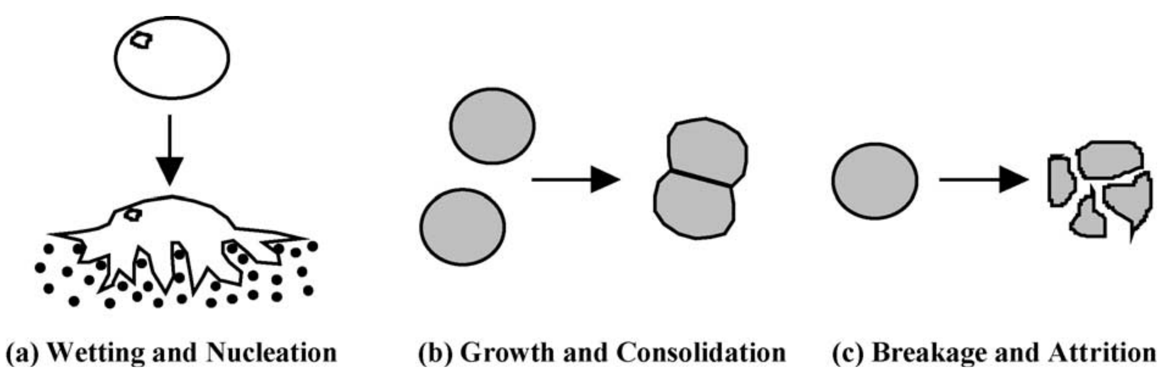

Figure 1.5 Rate processes in wet granulation. From Litster [113].

Chapter 2. Numerical and Experimental Methods

2.1. Numerical Simulations

While experimental studies can provide insight into the behavior of granular materials during flow, these studies are often limited by the capabilities of current analytical techniques. Experimental measurements are usually restricted to off-line analysis of samples removed from the particle bed or to on-line measurements of a small number of variables at specific locations. In contrast, the use of numerical simulation techniques can reveal a greater level of detail of how granular flows develop in complex equipment configurations. The discrete element method (DEM) is one of the most widely used numerical tools in the study of granular flows [86]. This technique provides insight into the system's dynamics and transient behavior and allows for the study of parameters that are difficult to measure or vary experimentally. For example, DEM simulations can generate information on localized flow, contact networks and stress profiles; information that with current experimental techniques is difficult if not impossible to obtain. In the following sections, we discuss the DEM models used in this work along with the theoretical considerations associated with these models. Methods for determining important macroscopic quantities from the discrete simulation data are also described.

2.1.1. Theoretical Basis

The macroscopic flow of particulate systems is governed by the particle interactions that occur at the microscopic level. As such, DEM describes the behavior of a particulate system by considering the inter-particle contacts. In general, DEM models are classified into two categories: hard-sphere models and soft-sphere models [132]. In hard-sphere particle simulations (also referred to as event-driven simulations), particle collisions are assume to be binary and instantaneous. These assumptions are generally valid for low concentration systems in which the collision time is orders of magnitude lower than the mean free flight time between collisions (i.e. granular gases) [133]. In this type of simulation, the time to the next binary collision is calculated and used to update the positions and velocities for all the particles in the system. Post-collision velocities are calculated from the coefficient of restitution, a material quantity which relates the amount of kinetic energy dissipation that occurs during a collision to the particle velocities. The effect of surface roughness is usually accounted for by imposing a coefficient of tangential restitution which limits the angular velocity of the particles after contact [134]. The limitation of the hard-sphere models comes from the assumption of instantaneous particle collisions, which makes this type of approach inappropriate for simulating systems experiencing enduring contacts (i.e. quasi-static flows and intermediate regime flows).

Soft-sphere models, on the other hand, are appropriate when particle contacts are sustained. In these types of simulations (also referred to as time-stepping simulations), Newton's equations of motion are numerically integrated with time for each particle starting from an initial system configuration. If the time-step for integration is sufficiently small, it can be assumed that the state of a particle is only affected by contact with its neighbors and boundaries, as well as body forces [86]. Thus, at any given time-step, the soft-sphere models consider only pair-wise interactions of neighboring particles. Figure 2.1 depicts the microscopic particle-particle (Figure 2.1a) and particle-boundary (Figure 2.2b) contacts.

The motion of each particle is described by

$$m_i \frac{dv_i}{dt} = \sum_j (F_{ij}^N + F_{ij}^T) + m_i g \qquad \textbf{(2-1)}$$

$$I_i \frac{d\omega_i}{dt} = \sum_j (R_i \times F_{ij}^T) + \tau_{rij} \qquad \textbf{(2-2)}$$

where m_i, R_i, I_i, v_i and ω_i are the mass, radius, moment of inertia, linear velocity and angular velocity of particle i, and g is the acceleration due to gravity. Solution of equations 2-1 and 2-2 requires explicit expressions of the forces experienced by particles during contact as a result of the particles undergoing deformation. These forces are generally decomposed into normal (F_{ij}^N) and tangential (F_{ij}^T) components. Continuum approaches such as contact mechanics or the Finite Element Method could be used to estimate the value of the contact forces. However, these approaches would be very computationally expensive [133]. To achieve computational efficiency, several simplified models have been developed for spherical particles which relate the magnitude of these forces to the amount of deformation that occurs during contact. The extent of deformation in the normal direction is characterized by the overlap or normal displacement (δ_n) of two spherical particles [135]:

$$\delta_n = \max(0, (R_i + R_j) - |r_i - r_j|) \qquad \textbf{(2-3)}$$

where r_i and r_j represent the position vectors for particles i and j respectively.

In general, 3 types of mechanisms can govern the deformation of particles during contact: elasticity, viscoelasticity, and plastic deformation [132]. Elastic collisions occur when the contact displacement is reversible and no kinetic energy is lost as a result of particles colliding. However, loss of kinetic energy usually occurs in realistic materials [52]. In viscoelastic contacts, the deformation incurred during a collision is reversible but the amount of displacement is dependent on the displacement rate. For plastic collisions, the deformation of particles is permanent and the amount of displacement is independent of the displacement rate. The latter two mechanisms lead to the dissipation of energy during contact. Therefore, most soft-sphere DEM models consider either a viscoelastic or a plastic mechanism in the formulation of contact force expressions.

For viscoelastic DEM models, the force expressions include two terms: a repulsion (or elastic) term and a dissipation (or viscous) term. The simplest viscoelastic force model is the linear spring-dashpot model which assumes a linear relationship between the elastic force and the displacement and a linear dependence of the viscous dissipation on the displacement rate [136]. The repulsion term is calculated assuming a Hooke-type relation between the stiffness of the particles and the displacement. The dissipation term is calculated by multiplying the displacement rate by a damping constant [137]. The linear spring-dashpot model yields an analytical solution for the collision time [135] making it computationally efficient. However, this model is not based on contact mechanics and it leads to a constant coefficient of restitution and a constant collision time. Experimental data has shown that both the coefficient of restitution and the collision duration are functions of the pre-collision velocity [132, 135].

The limitations of the linear viscoelastic models can be overcome by using non-linear models based on Hertz contact theory. In these models, the elastic force is obtained from the stiffness of the particles multiplied by the displacement to the $3/2$ power. The stiffness coefficient is obtained from the physical properties of the material such as the

Young's modulus and the Poisson ratio [138]. This facilitates the implementation of these force models as stiffness values can be obtained from material properties which are readily available in the literature for a variety of materials. In general, these models lead to coefficient of restitutions and collision durations which are collision velocity dependent. However, most of these models do not allow for the analytical solutions of their differential equations and must be solved numerically making them more computationally expensive than the linear models.

DEM models which allow for the plastic deformation of particles during contact are often referred to as hysteretic models. In these models, the contact forces are set to zero when the final amount of particle deformation is reached. At this point, the particles are no longer in contact. An ideal plastic behavior can be easily implemented in a DEM algorithm by using different stiffness values for the loading and unloading phases of particle contact (i.e. approach and retraction). Linear and non-linear hysteretic models are found in the literature, but the linear models provide an analytic solution for determining the final amount of particle deformation during contact [133] making them more computationally efficient. When the loading and unloading stiffness coefficients are assumed to be constant, these models yield a constant coefficient of restitution but a velocity-dependent collision time. The challenge in using the plastic models is the determination of the loading and unloading stiffness from physical material properties. Often, the value of the stiffness coefficients is set so that a particular value of the coefficient of restitution is achieved during contact.

2.1.2. Contact Force Model

The contact model used in this work is based on the work of Tsuji et al. [131], which provides a non-linear force based on Hertzian contact theory. The normal contact force is given by

$$F^N = -\tilde{k}_n \delta_n^{3/2} - \tilde{\gamma}_n \dot{\delta}_n \delta_n^{1/4} \qquad \textbf{(2-4)}$$

where $\tilde{k}_n$ is the normal stiffness coefficient, and $\tilde{\gamma}_n$ is the normal damping coefficient. The normal stiffness coefficient is obtained from

$$\tilde{k}_n = \frac{E\sqrt{2R^*}}{3(1-\sigma^2)} \qquad \textbf{(2-5)}$$

with E being the particle's Young's modulus and σ the particle's Poisson ratio. R^* is defined as the effective radius of the contacting particles and is obtained by

$$R^* = \frac{R_i R_j}{R_i + R_j} \;. \qquad \textbf{(2-6)}$$

The normal damping coefficient is given by

$$\tilde{\gamma}_n = \ln e \frac{\sqrt{m\tilde{k}_n}}{\sqrt{\ln^2 e + \pi^2}} \qquad \textbf{(2-7)}$$

where e is the coefficient of restitution. This model assumes a constant coefficient of restitution and results in a velocity-dependent collision time. While experimental data suggest an impact-velocity dependent coefficient of restitution, this model has been shown to produce DEM results in good agreement with experimental data [131, 139-141] and comparable with other commonly used contact models [133, 142].

The tangential force is calculated from

$$F^T = -\tilde{k}_t \delta_t - \tilde{\gamma}_t \dot{\delta}_t \delta_n^{1/4} \quad \textbf{(2-8)}$$

where $\tilde{k}_t$ is the tangential stiffness coefficient, δ_t is the tangential displacement and $\tilde{\gamma}_t$ is the tangential damping coefficient. The tangential stiffness coefficient is based on the work from Mindlin [143] and is given by

$$\tilde{k}_t = \frac{2\sqrt{2R^* G}}{2-\sigma} \delta_n^{1/2} \quad \textbf{(2-9)}$$

where G is the particle's Shear modulus. The tangential displacement is calculated by

$$\delta_t = \int v_{rel}^t dt \quad \textbf{(2-10)}$$

where v_{rel}^t is the relative tangential velocity of the colliding particles and is defined as

$$v_{rel}^t = (v_i - v_j) \cdot s + \omega_i R_i + \omega_j R_j \quad \textbf{(2-11)}$$

In equation 2-11, s is the tangential decomposition of the unit vector connecting the centers of the particles. The tangential force is limited by the Coulomb condition, $F^T < \mu_s \left| F^N \right|$. When the tangential force obtained from equation 2-8 exceeds the Coulomb limit, the tangential displacement is set to $\delta_t = F^T / \tilde{k}_t$ in order to account for slip during a contact. It is interesting to note that as a consequence of setting δ_t equal to $F^T / \tilde{k}_t$, δ_t is always less than $F^N / \tilde{k}_t$. The effect of rolling friction is included in the term $\tau_r = -\mu_r \left| F^N \right| R\omega$. In this work, the tangential damping coefficient is assumed to be the same as the normal damping coefficient.

2.1.3. Cohesive Force Model

The effect of moisture content in granular flows can be investigated via DEM simulations by including an extra term in the equation of linear motion [144]:

$$m_i \frac{dv_i}{dt} = \sum_j (F_{ij}^N + F_{ij}^T) + F_{ij}^C + m_i g \qquad \textbf{(2-12)}$$

where F_{ij}^C is the cohesive force experienced by particle i due to the formation of a liquid bridge between it and particle j. For the case of low moisture contents (also known as the pendular regime), it can be assumed that discrete liquid bridges form only when particles come into contact. This assumption makes the inclusion of a capillary force into a DEM algorithm straight forward. The existence of liquid bridges in the pendular regime depends on the amount of liquid in the system, the surface characteristics of the particles and on the pore size distribution [145, 146]. The transition between the pendular regime and the funicular regime is not well defined. Several authors have reported a transition from the pendular to the funicular regime for liquid-to-solid volume ratios ranging from 4% to 17% [145-149].

A schematic representation of a liquid bridge in the pendular regime is shown in Figure 2.2. The capillary force resulting from the surface tension and the pressure difference inside the liquid bridge can be expressed as [144]

$$F_c = 2\pi\gamma \sin\beta \sin(\beta + \theta) + \pi R^2 \Delta P \sin^2 \beta \qquad \textbf{(2-13)}$$

where β is the half filling angle, θ is the contact angle, γ is the surface tension and ΔP is the pressure difference across the air-fluid interface. In order to solve equation 2-13, an expression relating the hydrostatic pressure within the liquid bridge to its geometry is needed. The Laplace-Young equation provides this relationship by assuming that the mean curvature of the meniscus is constant and proportional to ΔP. Several analytical and numerical solutions of the Laplace-Young equation are available in the literature [86, 150] but many of these solutions tend to be complex and not easily implemented in discrete simulations. However, explicit force expressions derived from approximate solutions of equation 2-13 and the Laplace-Young equation [89, 144] can be included in DEM algorithms without compromising computational efficiency. The cohesion force model proposed by Mikami et al. [144] was used in this work. This model is based on regression expressions obtained from numerical solutions of these two equations. From this model, the cohesion force is given by

$$\widehat{F}_c = \exp(A\widehat{h} + B) + C \qquad \textbf{(2-14)}$$

$$A = -1.1\widehat{V}^{-0.53} \qquad \textbf{(2-15)}$$

$$B = (-0.34\ln\widehat{V} - 0.96)\theta^2 - 0.019\ln\widehat{V} + 0.48 \qquad \textbf{(2-16)}$$

$$C = 0.0042\ln\widehat{V} + 0.0078 \qquad \textbf{(2-17)}$$

where $\widehat{F}_c$ is the normalized capillary force ($\widehat{F}_c = F_c / 2\pi R\gamma$), $\widehat{V}$ is the dimensionless liquid bridge volume ($\widehat{V} = V / R^3$), $\widehat{h}$ is the dimensionless separation distance between the surface of the particles ($\widehat{h} = h / R$); and A, B and C are constants. The Mikami model has been shown to yield capillary forces in good agreement with experimental data and with other numerical solutions of the Laplace-Young equation [89, 151].

When pendular bridges are stretched, the thickness of the liquid layer decreases leading to the formation of Rayleigh instabilities within the liquid bridge [152]. These instabilities eventually cause the rupture of the liquid bridge at large separation distances.

The distance at which a pendular bridge breaks is determined by using the expression proposed by Lian et al. [150]

$$\widehat{h}_c = (0.62\theta + 0.99)\widehat{V}^{0.34} \qquad \textbf{(2-18)}$$

The presence of moisture also leads to the development of viscous forces between particles. The capillary number relates the magnitude of the viscous force to the capillary forces in a liquid bridge, and is calculated by

$$Ca = {}^{\eta U}\!/_{\gamma} \qquad \textbf{(2-19)}$$

where η is the dynamic viscosity of the liquid and U is the characteristic velocity. For a water wet granular material flowing at a velocity of 0.2 m/sec (a typical velocity in a bladed mixer), the value of the capillary number is $Ca < 0.01$. This indicates that the effect of the viscous forces is negligible compared to the effect of the capillary forces. The effect of dynamic viscous forces will not be considered in this work.

The following assumptions were made in the implementation of the liquid bridge model into the DEM algorithm:

1. The total amount of liquid in the system is perfectly mixed throughout the entire particle bed such that each liquid bridge has the same volume of liquid.
2. No condensation or evaporation of the liquid occurs.
3. A pendular liquid bridge is formed at the point of contact when two particles come in contact.
4. A pendular liquid bridge is formed at the point of contact when a particle comes in contact with the walls.
5. Liquid bridges move tangentially slipping over the surface of the particles and the walls (i.e. the capillary force acts only in the normal direction).

2.1.4. Mixer Geometry and Input Parameters

A schematic of the mixer geometry used in this work is presented in Figure 2.3. In our coordinate system, the origin is located at the center of the cylinder's bottom plate. Table 2.1 shows the mixer dimensions that were used for the base case simulations. The effect of increasing mixer size is discussed in Chapter 4. The amount of particles in the base case simulations was set such that the top of the particle bed covered the top of the blades. The effect of increasing particle bed height beyond the top of the blades is discussed in Chapter 4. In the base case simulations, the particles were assumed to be monodisperse and cohesionless. The effect of polydispersity is discussed in Chapter 6 while the effect of cohesion is discussed in Chapter 7. Particles are created in the computational space and allowed to settle under gravity while the blades remain stationary. Blade movement is started once particle deposition has been completed. Measurements are taken after the system has reached steady state. The system is considered to be at steady state when the total kinetic energy of the system reaches a constant value, indicating that the amount of energy lost due to inelastic collisions is the same as the amount of energy gained from the movement of the blade. Under the conditions of our simulations, steady state is reached within 2 sec of blade movement.

The input parameters for the base case simulations are listed in Table 2.2 and are, in general, those of glass. The value of Young's modulus was decreased to reduce computational time. Parametric sensitivity studies showed that reducing the value of Young's modulus had a negligible effect on flow patterns, velocity profiles and inter-particle shear stresses. These observations are consistent with the literature [108-110, 153, 154]. The parametric studies also showed that the amount of viscous dissipation in the normal and tangential directions had a negligible effect on the results obtained in our bladed mixer. The maximum normal overlap observed in the simulations was 4%, and the average overlap was < 1%. The physical properties listed in Table 2.2 were used for the particles, the blades and cylinder walls in the base case simulations. The effect of varying the cylinder wall parameters is discussed in Chapter 4.

2.1.5. Macroscopic Flow Properties

Important macroscopic quantities can be calculated from the discrete particle data by implementation of temporal and spatial averaging procedures. In this section we describe the various averaging procedures used in the determination of macroscopic variables.

The granular temperature is one of the macroscopic quantities of interest as it provides a measurement for the degree of random movement of the particles in the system. The granular temperature is defined as [107]

$$T = \frac{1}{2}\left\langle u'u' \right\rangle \qquad \textbf{(2-20)}$$

were *u'* is the fluctuation velocity. The mean velocity for a group of particles within a control area at a specific time is subtracted from the velocity of each particle yielding the fluctuation velocity. $\langle \ \rangle$ denotes the temporal averaging of the quantity *u'u'* (the square of the fluctuation velocity of each particle). Temporal averaging is done once the particle system is at steady state.

The local void fraction within the particle bed is calculated using the method of overlapping spheres. Spherical control volumes are created throughout the computational domain and the number of particles which overlap with each spherical control volume is determined. The local void fraction is calculated by subtracting the overlapping volume of each particle from the control volume size

$$\varepsilon = 1 - \frac{\sum_k (\pi (R_c + R_k - a)^2 [a^2 + 2a(R_k + R_c) - 3(R_k^2 + R_C^2) + 6R_k R_C])}{12 a V_C} \qquad \textbf{(2-21)}$$

where R_C is the radius of the spherical control volume, R_k is the radius of particle *k*, *a* is the distance between the center of the particle and the center of the control volume and V_C is the size of the control volume.

We gauge particle motion at the microscopic level by calculating particle diffusivities which describe the mass flux rate due to the particles' "random walk". The diffusive tensor calculation was taken from Campbell [155] and is given by

$$\boldsymbol{D}_{ij} = \left\langle (\Delta \boldsymbol{x}_i - \overline{\Delta \boldsymbol{x}_i})(\Delta \boldsymbol{x}_j - \overline{\Delta \boldsymbol{x}_j}) \right\rangle \Big/ 2\Delta \boldsymbol{t} \qquad \textbf{(2-22)}$$

where Δx_i represents the particle displacement in the *i* direction relative to the particle's initial position, $\overline{\Delta x_i}$ is the mean particle displacement and D_{ij} is the corresponding diffusion coefficient in the *i* direction due to a gradient in the *j* direction. Particle diffusivities were computed with a Δt of ¼ of a revolution and were averaged over all the particles within the computational domain. The convective and diffusive contributions to particle motion are compared by calculating the Peclet number

$$Pe_{ij} = \frac{U_i R}{D_{ij}} \qquad \textbf{(2-23)}$$

where U_i is the average particle speed in the *i* direction, R is the mixer radius and D_{ij} is the corresponding diffusion coefficient.

The degree of mixing obtained within the particle system is determined by dividing the computational domain in half across the horizontal plane and coloring particles on the left side differently from the particles on the right. We then perform statistical analysis on particle concentration for a specific color particle. At a particular time step, we compute the relative standard deviation (RSD) of particle concentration for the entire system. The RSD is obtained from the following formula:

$$RSD = \frac{\sigma_{conc}}{M_{conc}} \qquad \textbf{(2-24)}$$

where σ_{conc} is the standard deviation of the particle concentration over all the samples taken, and M_{conc} is the overall mean particle concentration. The RSD value obtained can be highly sensitive to sample size and sample number. The sample grid size for the RSD calculation was determined by varying the sample number and size until the RSD value obtained was independent of sampling grid (~ 5 particle diameters). A perfectly mixed system would yield an RSD value of zero while a fully segregated system would yield an RSD value of 1.

For polydisperse systems, a metric capable of characterizing mixing in systems composed of multiple particle sizes is required for a fair comparison across systems. The mixing metric, M [156], is used to calculate degree of mixing for polydisperse systems and is given by

$$M = \frac{S}{S_{mix}} \qquad \textbf{(2-25)}$$

where S represents the degree of mixing of all particle species at a specific time step and S_{mix} is the degree of mixing for a well mixed system. The computational domain is divided into k cells and the value of S is obtained from

$$S = \sum_k (n_k \sum_i x_i^k \ln x_i^k) \qquad \textbf{(2-26)}$$

where n_k is the total particle number fraction in cell k and x_i^k is the number fraction of species i in cell k . S_{mix} is calculated by assuming that the number concentration of a species in each cell is equal to the system concentration for that species. The size of the sampling cell was determined by varying this parameter until the value of M obtained was independent of cell size (~ 5 particle diameters). This metric considers the variation in concentration of each particle size in the system. A perfectly mixed system would yield $M = 1$ while a fully segregated system would yield $M = 0$.

Stresses within the particle bed were calculated following the procedure outlined by Campbell [19]. Collisional stresses are obtained from

$$\tau_{ij} = \frac{d}{V_c} \langle F_i k_j \rangle \qquad \textbf{(2-27)}$$

where d is the diameter of the particle, V_c is the size of the control volume, F_i is the total contact force and k_j is the unit vector pointing along the line connecting the centers of the colliding particles. As before, $\langle\ \rangle$ represents the temporal averaging within the control volume. Stresses in granular systems are known to be scale-dependent [157]. As such, the calculated stress values are affected by the size of the control volume. The size of the control volume used here was determined by varying this parameter until the stress values obtained were independent of control volume size (~ 5 particle diameters). In this work, only the contribution of collisional stresses is considered as kinetic stresses were found to be 3 orders of magnitude smaller.

The collisional stress tensor was calculated in a 3-dimensional cylindrical coordinate system. Our analysis showed that a symmetric stress tensor is obtained following this procedure (i.e. $\tau_{\theta r} = \tau_{r\theta}$). We focused our attention on the average normal stress and the shear stress component in the plane of the blade rotation, $\tau_{\theta r}$. From the normal stresses, the pressure inside the particle bed is given by

$$P = \frac{1}{3}\left(\tau_{\theta\theta} + \tau_{rr} + \tau_{yy}\right) \qquad \textbf{(2-28)}$$

where $\tau_{\theta\theta}$, τ_{rr} and τ_{yy} are the normal stresses in the tangential, radial and vertical direction, respectively.

2.2. Experimental Method

The lack of information on flow kinematics in bladed mixers can lead to problems during process design, operation and scale-up. Particle velocities affect the rates of mixing, heat and mass transfer and, in the case of wet granulation, the rates of agglomerate formation. In addition, the role of particle surface characteristics on process performance is still not well understood. While numerical simulations can yield vast amounts of information on granular flows, few bladed mixer numerical studies are found in the literature where the results obtained from these simulations are compared and validated against those obtained experimentally. Stewart et al. [108] compared the particle velocities from DEM simulations in a two-flat-blade mixer to those obtained via PEPT for glass beads. A detailed comparison between DEM simulations and experimentally measured particle velocities in more complex blade configurations is still lacking. In the following sections, the experimental techniques used to examine particle flows in bladed mixers are described. Experimental procedures for roughening of glass bead surfaces via coating are also detailed. These procedures enable the investigation of surface roughness effects on resulting granular flows in bladed mixers.

2.2.1. Experimental Set-up

The experimental bladed mixer geometry is similar to the geomtery used in the simulations and is also illustrated by Figure 2.3. The dimensions for the laboratory mixer are shown in Table 2.3. The laboratory unit consisted of a glass cylindrical vessel agitated by an impeller with a glass shaft and 4 Teflon® blades pitched at a 45° angle. The granular material used in this work was Dragonite® glass beads (Jaygo Incorporated, Union, NJ) with diameters of 2, 3 and 4 mm (± 0.3 mm). Three types of 2 mm beads were used: clear beads, surface-colored red beads and surface-colored blue beads. The red and blue beads were used for the PIV experiments while the red and clear beads were used for mixing experiments and wet particle experiments. The 3 mm beads used were surface-colored black while the 4 mm beads were white colored. Shear cell analysis and SEM inspection of the glass bead surfaces showed that the surface coloring of the beads did not significantly affect the surface roughness of the particles or the flow behavior of the particles under the conditions of our work.

For the PIV experiments, the granular material was loaded into the laboratory mixer to an initial bed height of ~27 mm. This bed height was sufficient to cover the top tip of the blades. The impeller was driven by a motor with a speed controller with an accuracy of ± 0.1 RPM under load. Once the material was loaded into the mixer, the impeller was rotated counterclockwise which leads to a blade pitch that has an obtuse angle relative to the movement of the particles [106]. This blade orientation is most common in particle processing operations. The flow was allowed to stabilize before measurements were taken and flow stabilization was usually achieved within 2 sec of impeller rotation.

2.2.2. Particle Image Velocimetry

The PIV technique allows for the tracking of particles in a granular bed from high-speed CCD images. PIV has been successfully applied to the study of granular flows in some prototypical geometries, such as chute flows [27] and rotating drums [32]. In PIV consecutive images of the flow field are taken over a known time interval. The displacement of particles between the two images is calculated using a cross-correlation algorithm. The images are divided into rectangular regions called interrogation cells. A cross-correlation function relates the light intensity within an interrogation cell at a specific coordinates with the light intensity for other interrogation cells in the subsequent image. From this analysis, the displacement of a group of particles present in each interrogation cell is calculated to give an average particle displacement vector.

The discrete cross-correlation function is given by

$$f_g(m,n) = \sum_{k=-\infty}^{k=\infty} \sum_{l=-\infty}^{l=\infty} f(k,l) \cdot g(k+m, l+n) \quad \textbf{(11)}$$

where $f(k,l)$ is the function that describes the light intensity within the interrogation cell with pixel coordinates (k,l) recorded at time t, and $g(k+m,l+n)$ is the light intensity function for a pixel at coordinates $(k+m,l+n)$ taken at time $t+\Delta t$ [158]. The position of the highest correlation peak in the correlation plane corresponds to the average particle displacement in the interrogation cell. The time required for the cross-correlation calculation to be performed can be reduced by use of the Fast Fourier Transform (FFT). This is done by performing a complex conjugate multiplication of each corresponding pair of Fourier coefficients instead of performing a sum over all the elements present in the sampled region. The set of coefficients are then transformed from the frequency domain to the image domain to obtain the cross-correlation function [107, 158]. In this work the movement of each particle is tracked to avoid particle identification errors which could occur when a small number of "seeding" particles are used [159]. Particle tracking is done by shining a halogen light onto the bed and creating a glare spot on each particle. The glare spot acts as the tracer for each particle and facilitates the correct identification of particles in between frames. This allows for the tracking of each particle in the surface and minimizes identification errors.

The PIV technique yields both instantaneous and mean velocity vector fields for 2-D flows structures at the bed top free surface and through the transparent sidewalls. The PIV experimental set-up is illustrated in Figure 2.4. A high speed camera (Redlake MotionScope Model PCI 1000S) is placed directly above one quadrant of the flow in the bladed mixer and is used to record images of the free-surface at 250 frames per second. The top surface image spans the entire radius of the container. After the measurements on the top surface are taken, the camera is then placed on the side of the mixer to obtain velocity fields near the cylinder walls. Sequential images are analyzed using cross-correlation and a 3x3 interrogation cell smoothing. The cross-correlation analysis is performed using the commercially available software FlowManager v4.71® from Dantec Measurement Technology. Mean velocity fields are obtained by averaging over a minimum of 512 frames.

2.2.3. Particle Surface Roughening via Surface Coating

In order to study the effect of particle surface roughness on flow kinematics, procedures for the surface modification of the 2 mm glass beads were developed. In these procedures a rotating drum is used to coat the surface of beads with silica sand or with magnesium stearate (MgSt). Silica sand and MgSt were chosen as coating materials due to the increased asperity and irregular shape of their primary particles. The silica sand particles used were angular in shape with a mean particle diameter of 300 µm, while the MgSt was composed of irregular plates with a 15 µm mean diameter. The rotating drum used as the coater was made out of glass with an outer diameter of 20.5 cm and a height of 8 cm. The rotating drum contained 4 Teflon® baffles equally spaced along the side wall of the drum. The baffles were 3 cm deep and 7 cm in height.

For the coating with silica sand, 200 to 400 grams of 2 mm glass beads were placed inside the rotating drum. The top surface of the beads was then sprayed with 5 to 10 grams of spray glue dissolved in organic solvents (Super 77 Multipurpose Adhesive glue from 3M). Silica sand was then added to the rotating drum (100 to 200 grams) and the pressure was reduced to below 200 mbar via vacuum. The drum was then rotated at 30 RPM while still under vacuum for 15 min to dry the beads. Some bead and sand agglomerates were formed during this coating procedure. In order to separate the evenly coated beads from the agglomerates, the mixture was sieved through No. 8 and No. 12 sieves. The large agglomerates were captured in the No. 8 sieve and disposed of. The evenly coated beads were captured in the No. 12 sieve. This afforded silica sand coated beads with a diameter ranging from 2.4 mm to 1.7 mm. To coat the glass beads with MgSt, we relied on the adhesive interaction between MgSt and the surface of the glass beads. The MgSt used in particle coating was obtained from Mallinckrodt Chemicals (CAS No. 557-04-0). 200 to 400 grams of glass beads were added to the rotating drum followed by 50 to 100 grams of MgSt. The drum was rotated at 30 RPM under atmospheric pressure for 15 min. Some small MgSt agglomerates were created during the coating procedure. The resulting mixture was sieved through a No. 8 and No. 12 sieves in order to separate the coated beads from the MgSt agglomerates. The resulting MgSt coated beads had a particle diameter ranging from 2.4 mm to 1.7 mm.

2.3. Figures for Chapter 2

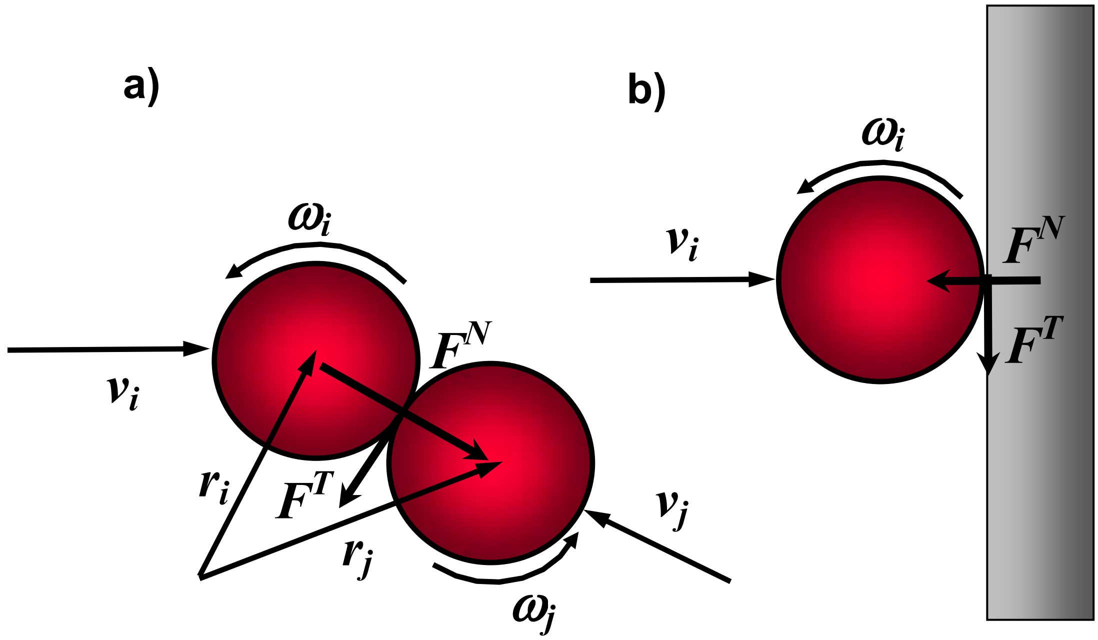

Figure 2.1 Schematic representations of microscopic contacts and the quantities considered by soft-sphere particle simulations. a) particle-particle contacts b) particle-boundary contacts.

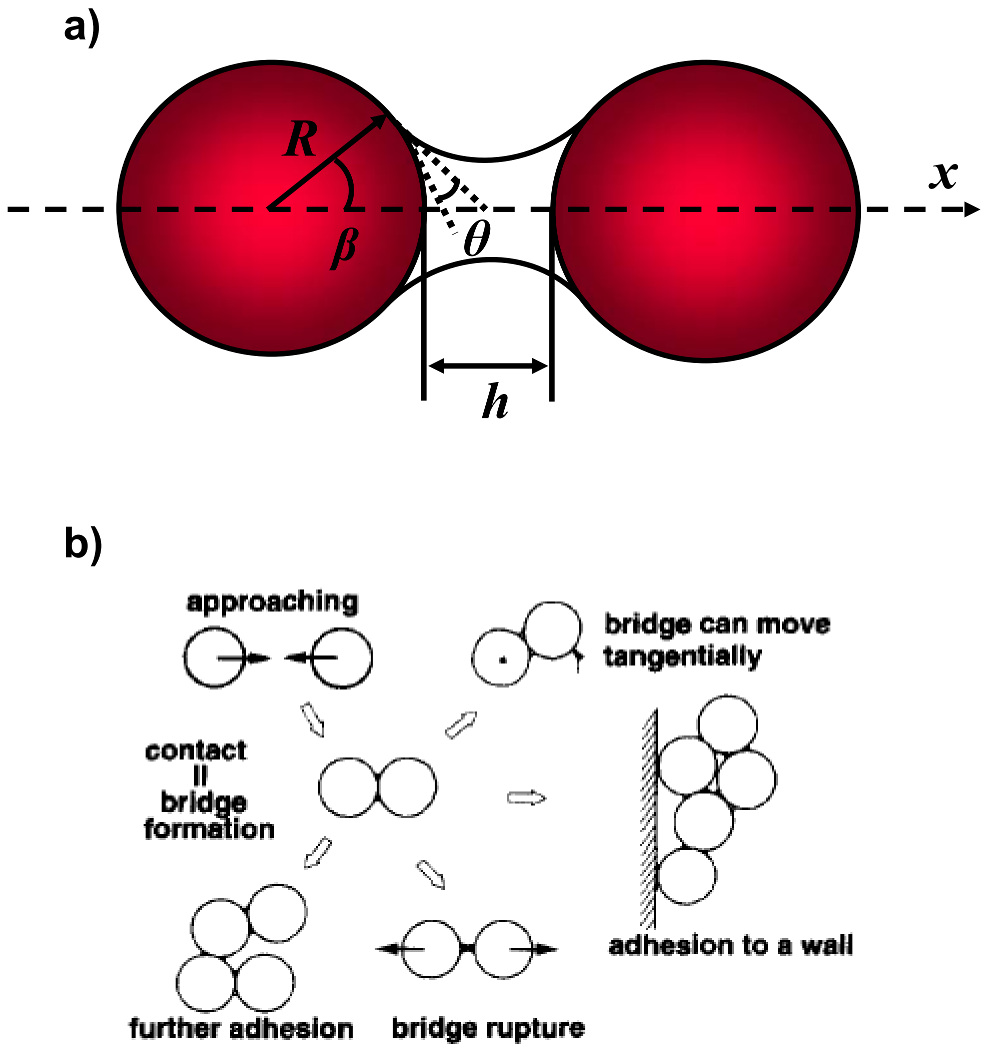

Figure 2.2 Capillary force model. a) schematic representations of a liquid bridge between two particles and b) dynamics of liquid bridge formation. From Mikami et al. [144].

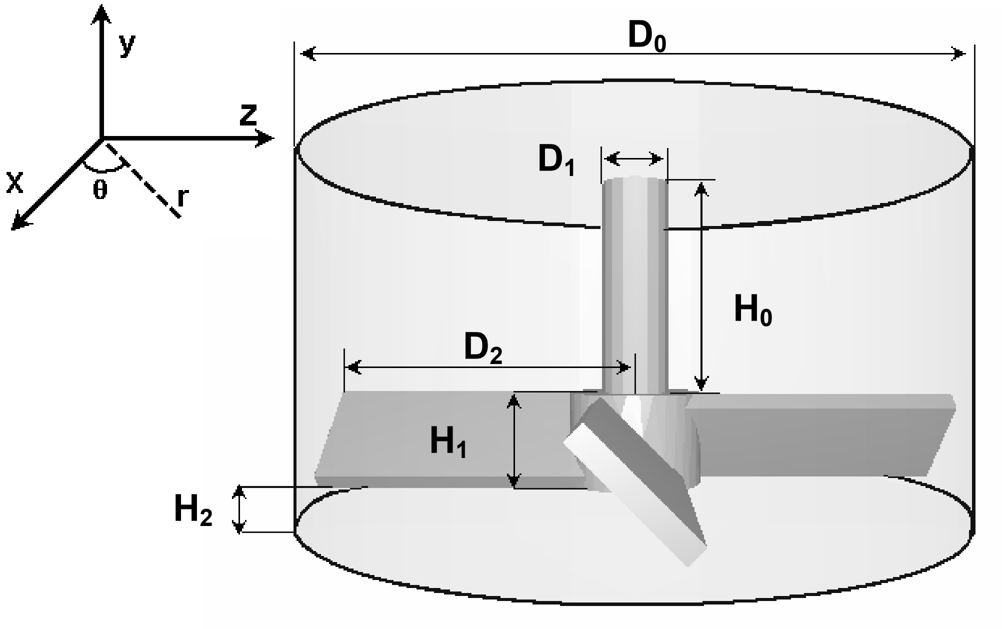

Figure 2.3 Mixer Schematic and coordinate system.

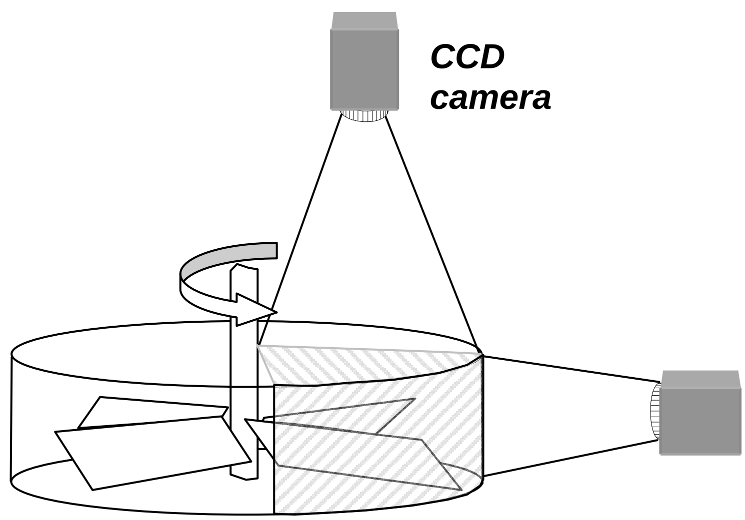

Figure 2.4 Laboratory PIV set-up.

2.4. Tables for Chapter 2

Dimension	Value (mm)
D_0	315
D_1	32.5
D_2	152.5
H_0	115
H_1	45
H_2	10

Table 2.1. Mixer dimensions for base case simulations.

Variable	Symbol	Value
Rolling Friction Coefficient	μ_r	0.005
Sliding Friction Coefficient	μ_s	0.1-0.5
Particle density	ρ	2.2 g/ml
Young's modulus	E	2.6×10^6 Pa
Coefficient of restitution	*e*	0.6
Particle Diameter (d)	d	2-10 mm
Number of Particles	N	5000-200000
Poisson's ratio	σ	0.25
Time step		$< 1 \times 10^{-5}$ sec

Table 2.2. Input parameters for base case simulations.

Dimension	Value (mm)
D_0	100
D_1	12.5
D_2	45
H_0	70
H_1	25
H_2	2

Table 2.3. Laboratory mixer dimensions.

Chapter 3. Numerical Characterization of Monodisperse, Cohesionless Flows

In order to understand the behavior of complex granular flows in bladed mixers, such as polydisperse flows and wet flows, the behavior of monodisperse, cohesionless systems must first be explored. Understanding the effect of operating parameters and particle properties on macroscopic properties like density, pressure, stress and granular temperature is necessary for the effective operation, scale-up and design of bladed mixers. This knowledge is also necessary for the development of continuum models that would accurately describe the flow of granular materials in bladed mixers. In this chapter, we use DEM to provide a 3-dimensional picture of granular behavior in bladed mixers including flow patterns, mixing kinetics, bulk density, granular temperature and pressure and shear-stress profiles. We examine the effect of blade orientation, sliding friction and shear rates on the temporal and spatial averages of these parameters as well as fluctuating values. We compare our results to previously reported experimental and computational results. The findings presented are relevant to the operation and optimization of industrial processes as they provide insight on parameters that may affect mixing, segregation, heat transfer, particle attrition and particle agglomeration. The simulation results present in this chapter were obtained with a fill level just covering the top of the blades and blade speed of 10 and 20 RPM.

3.1. Effect of Blade Orientation

We begin by characterizing the flow of granular material for different blade orientations. For the blade configuration shown in Figure 2.3, the granular material can be sheared at two different blade pitches. By rotating the blades counter-clockwise, the blade pitch relative to the movement of particles has an obtuse angle. This blade orientation is most common in particulate processing equipment. Rotating the blade clockwise produces an acute blade pitch. While less common, this blade orientation is used in industrial processing during unloading operations or smoothing of beds in filter dryers. In the results presented, a counter-clockwise rotation is denoted by a positive tangential velocity; a clockwise rotation is denoted by a negative tangential velocity. We compare the flow structures and highlight the differences obtained for each configuration. The blade speed for both blade orientations was set to 20 RPM. The results listed in the following sections were obtained using 5 mm particles with sliding friction coefficients (μ_s) of 0.3, a typical value for glass beads.

3.1.1. Velocity Profiles

Instantaneous velocity profiles at radial position r = 0.09 m and height h = 0.06 m are shown in Figure 3.1 for the obtuse and acute blade pitches. A cubic control volume with a size of 6 particle diameters was created at these coordinates. This position was chosen as the control volume would be located halfway between the impeller shaft and the cylinder wall and would include particles above and within the span of the blades. The velocity components were calculated by averaging over the control volume at a particular time-step. The velocity profiles in Figure 3.1 show a periodic behavior for both the obtuse and acute blade pitches. A Fast Fourier Transform (FFT) analysis of the tangential velocity component (V_t) revealed that the main frequency of this fluctuation is 1.3 Hz which corresponds to the rotation frequency of the blades. This analysis was carried out using the Fast Fourier Transform algorithm in *MATLAB*. The same main frequency was obtained when this analysis was extended to the radial (V_r) and vertical velocities (V_y). This periodic behavior was observed experimentally by Lekhal et al. [37]

for velocity surface measurements. Here we are able to track velocity fluctuations throughout the particle bed. The power spectrum obtained from this analysis is shown in Figure 3.1d for the obtuse blade pitch and Figure 3.1h for the acute blade pitch. The intensity of the main peak for the obtuse blade pitch is higher than that of the acute blade pitch indicating a higher fluctuation amplitude.

The tangential velocity for both blade configurations is one order of magnitude higher than the radial and vertical velocities. Particle movement in this system is therefore dominated by the angular movement of the blade. Radial and vertical velocity values fluctuate around zero, while the tangential velocity does not. This indicates that the position of the particles relative to the blade determines if particles rise or fall or if they flow towards the cylinder wall or towards the impeller shaft. The amplitude of the radial and vertical fluctuations is higher for the obtuse blade pitch than for the acute blade pitch.

While the main flow of the particles in this system is in the tangential or angular direction, complex flow structures are observed. As the blades rotate, the granular bed deforms by forming heaps where the blades are present and valleys between blades passes. Figure 3.2 depicts time-averaged velocity fields for particles above the blades in the horizontal plane. Averaging was performed considering only the time-steps for which the blades were present at the position shown in Figure 3.2. Figures 3.2a and 3.2c show the horizontal plane velocity field for the obtuse and acute blade pitch respectively. The color of the vector represents the value of the vertical velocity. The velocity fields for the obtuse and acute cases are very similar with the main difference being the direction of flow. As expected, the magnitude of the velocity increases for particles close to the wall.

Additionally the velocity is higher for particles near the front of the leading blade than for particles behind the adjacent blade. For the vertical velocity, the magnitude is highest by the wall while particles near the shaft have a small vertical velocity component. This trend is observed for both blade orientations. The radial velocity fields are presented in Figure 3.2b for the obtuse blade pitch and 3.2d for the acute blade pitch. Particle radial movement is limited for the acute blade pitch, while higher radial velocities are observed for the obtuse blade pitch. Similar to the vertical velocity, the magnitude of the radial velocity is highest by the cylinder wall and smallest near the shaft.

The radial and vertical velocity trends shown in Figures 3.1 and 3.2 suggest the existence of 3-dimensional recirculation patterns. These patterns are observed in the velocity fields obtained in the vertical plane (Figure 3.3). Figures 3.3a through 3.3c show the time-averaged radial and vertical velocity fields for the obtuse blade pitch at 3 different positions. The magnitude of the tangential velocity is represented by the color of the vectors. For the obtuse blade pitch, the tangential velocity points out of the plane of the graph. In front of the blade (Figure 3.3a), a recirculation pattern develops analogous to the vortexing observed for liquid systems in cylindrical tanks agitated by pitch-blade turbines [160]. Experimental surface flow measurements suggested the existence of a 3D recirculation zone [106]. Our computational results confirm the existence of this zone and describe where and how the recirculation develops. A less prominent recirculation pattern was reported by Zhou et al. [110] for two flat blades. In particular the velocity for the particles near the bottom plate and the shaft was significantly smaller than what is observed in our system. In our system the recirculation is much stronger as due to the pitch of the blade, the particles by the wall flow upwards forming a heap. The particles on the top of the heap move radially inwards which forces the particles by the shaft to flow downwards and radially outwards, leading to the pronounced recirculation. The existence of such recirculation patterns becomes important during process design and scale-up, as such patterns could lead to enhanced mixing in monodisperse systems and potentially in polydisperse systems as well. Unlike liquid systems, this recirculation pattern is only present near the front of the blade. In between the blades, the particles on top of the blades now flow radially outwards (Figure 3.3b) while particles by the bottom plate and shaft move mainly in the tangential direction. Particles by the wall flow upward with a small radial velocity component. As the blade passes, particles on the top of the heap fall behind the blade (Figure 3.3c). Particles within the blade height flow downward as they fall from the front of the heap similar to forward flowing avalanches.

The acute blade pitch velocity profiles are shown in Figures 3.3d through 3.3f. In this case, the tangential velocity points into the plane of the graph and the magnitude is represented by the vector color. No recirculation pattern arises in front of the blade (Figure 3.3d) contrary to what is observed for the obtuse blade pitch. Particles by the cylinder wall flow downwards due to the blade's pitch. Particle on top of the blade flow radially inwards. A "dead zone" can be noticed near the shaft and bottom plate, as these particles have a small tangential velocity component and almost no vertical or radial movement. This "dead zone" is present in between the blades (Figure 3.3e) and behind the blade (Figure 3.3f). The presence of this "dead zone" has a significant effect on the mixing performance for the acute blade pitch, as will be demonstrated in Section 3.1.3. Particles by the wall follow the same behavior in between the blades and behind the blade as in the obtuse blade pitch case (Figures 3.3e and 3.3f).

3.1.2. Density and Granular Temperature Profiles

The bulk density of a system and the granular temperature profile are important macroscopic properties of a granular assembly. Knowledge of how these profiles develop in dynamic systems could assist in the development of continuum-like models analogous to classical fluid mechanics. Bulk density measurements provide insight into the system's compression and dilation states and can help determine other macroscopic properties such as pressure. Granular temperature profiles could be used to gauge the diffusive behavior of particles [161] and the tendency of the system to segregate as temperature gradients have been shown to produce segregation [23].

Periodic bulk density waves are seen within the mixer (Figure 3.4). As in the velocity case, the main density fluctuation frequency is that of the blades' rotation. This behavior indicates that the granular material compresses as the blade passes and dilates in between the blades. It is worth noting that qualitative differences in particle packing as a function of blade position were observed experimentally by Stewart et al. [105]. The DEM simulations allow us to quantify the frequency and magnitude of the density waves. Density profiles for the obtuse blade pitch as a function of mixer height and number of revolutions are shown in Figure 3.4a at r = 0.09 m. The average density and the amplitude of the fluctuations are a function of the mixer height. The power spectrums corresponding to these density profiles are shown in Figure 3.4b. The main peak height in the power spectrums shows that the amplitude of the fluctuations remains constant within the region that spans the height of the blades. In this region, the bulk density fluctuates between a maximum value of 1300 kg/m^3 and a minimum value of 1000 kg/m^3. This maximum value is close to the randomly close-packed density (~1400 kg/m^3 in this case).

Above the blades, the mean value and amplitude of these fluctuations change significantly. At h = 0.055 m, the density fluctuates between 1300 and 800 kg/m^3. The highest fluctuation amplitude occurs at h = 0.065 m, were density values range from 1200 to 300 kg/m^3. This region coincides with the top of the heaps. The granular material begins to compress at the leading edge of the heap and dilates as the particles fall in the wake of the blades. The magnitude of the density minima in this region suggests that the particle concentration in the wake of the blade is small. We may think of particles in this region as being fluidized for the period required for the wake of the blade to pass. The smallest density values are observed at the heap's summit (h = 0.075 m) since particle concentration here is at its lowest. The amplitude of these fluctuations is similar to that at h = 0.055 m.

A similar trend in density fluctuations is observed in the acute blade pitch case. However, differences in the average bulk densities were found. For the obtuse blade pitch, the total average bulk density was measured at ~ 900 kg/m^3 while for the acute blade pitch the total average bulk density was found to be ~ 1100 kg/m^3. The difference in bulk density can be explained by the blade configuration in each case. In the obtuse blade pitch configuration, the blade movement acts against gravity lifting the granular material up and causing dilation. On the other hand, the acute blade pitch acts in the same direction as gravity compressing the granular material as it gets pushed down. It should be noted that bed dilation relative to initial conditions (~ 1200 kg/m^3 initial density) also occurs for the acute blade pitch but to a lower extent than for the obtuse blade pitch. The difference in bulk density affects the stress profile within the granular bed, as will be shown in Section 3.3.

The time-averaged granular temperature profiles are shown in Figure 3.5. Figures 3.5a and 3.5c show contour plots of the granular temperature in the horizontal plane for the obtuse and acute blade pitch respectively. Vertical plane profiles are shown in Figures 3.5b and 3.5d. Granular temperature maximums are observed near the cylinder wall (Figure 3.5a) and above the top tip of the blades (Figure 3.5b). These high temperature regions correspond to the areas where the particle velocity is the highest (as shown in Figures 3.2 & 3.3). Additionally, frictional interactions between the particles and the cylinder wall leads to an increase in granular temperature. The resulting velocity of wall-colliding particles differs from that of the bulk flow due to wall friction. This behavior is also observed in granular flows down inclined chutes, where the granular temperature is highest by the rough chute wall [28]. Lower temperature regions exist near the impeller shaft and within the span of the blades. These colder regions represent areas of uniform particle flow and low velocity fluctuations. Similar granular temperature trends in the horizontal plane were observed experimentally by Lekhal et al. [107] *via* surface velocity measurements. The granular temperature for the acute blade pitch is much lower than for the obtuse blade pitch (Figures 3.5c and 3.5d). This is consistent with the velocity fluctuation results presented in Section 3.1.1. The acute blade orientation leads to more uniform flows where the bulk of the particles follow the angular motion of the blade. For this case, granular temperature is mostly generated by the frictional interactions with the cylinder wall and the bottom plate.

3.1.3. Mixing Kinetics – Obtuse vs. Acute Pitch

The difference in granular behavior observed between the obtuse and acute blade configurations lead to differences in mixing performance. We evaluate the degree of mixing obtained for each blade orientation by coloring particles on the left side of the horizontal plane differently from the particles on the right side prior to blade movement. The particles have identical properties except their color. We then follow the mixing pattern as blade motion begins.

Figure 3.6 shows snapshots of the top horizontal plane view for the obtuse blade pitch (Figure 3.6a) and for the acute blade pitch (Figure 3.6b) at different numbers of revolutions. Well-mixed zones in both cases are first observed by the cylinder wall, the area of highest granular temperature. Thus, the frictional characteristics of the wall facilitate mixing by increasing the fluctuation velocities. In contrast, areas of uniform flow and lower granular temperature remain unmixed for longer periods of time. Enhanced mixing is obtained for the obtuse blade pitch when compared to the acute blade pitch. This mixing difference is observed as early as after 1 revolution. After 4 revolutions, the obtuse blade pitch system is well mixed and mixing is down to the particle-particle level, while unmixed regions still remain in the acute blade pitch system. The velocity profiles showed that for acute blade pitch flows, “dead zones” appear and the 3-D recirculation found for the obtuse blade pitch is not present. Convective mixing is reduced by agitating with an acute blade pitch. Additionally, the acute blade pitch leads to a lower granular temperature within the particle bed. This decrease in granular temperature is associated with a decrease in particle diffusivity. Diffusive mixing is therefore hindered by acute blade pitch flows. The difference in mixing performance is confirmed with the calculation of the system’s RSD (Figure 3.7). After 5 revolutions, the RSD for the obtuse blade pitch is 0.45 while for the acute blade pitch is 0.51, indicating that a higher number of un-mixed regions exist in the acute blade pitch case. The difference in mixing performance is still present after 10 revolutions.

3.2. Effect of Microscopic Friction

Previous work done on bladed mixers with two flat blades showed that particle friction is an important parameter [108, 110]. In this section we look at the effect of sliding friction on velocity fields, density and granular temperature profiles and mixing kinetics. To reduce computational time, the results listed in this section were obtained using 10 mm particles. We find that similar flow patterns and trends are obtained for the 10 mm particle vs. the 5 mm particles. Unless stated otherwise, the simulations outlined in this section were carried out for an obtuse blade pitch and a rotational speed of 10 RPM.

From the system's frictional properties, the sliding friction coefficient (μ_s) was found to significantly affect velocity trends while the rolling friction coefficient (μ_r) had a negligible effect. Velocity fields at the front of the blade in the vertical plane are presented in Figure 3.8 for 3 different values of μ_s. Heap formation occurs for $\mu_s = 0.5$ and $\mu_s = 0.3$ (Figures 3.8a and 3.8b respectively) leading to the formation of the 3-dimensional recirculation zone. At these frictional conditions, stable contact force chains develop between particles [19], which cause the particle bed to deform by forming heaps where the blades are present. A force chain is a network of interparticle contacts in which force is transmitted along the contact path. Little difference is observed between the velocity fields shown in Figures 3.8a and 3.8b. Particles rise by the wall and fall by the impeller shaft. When μ_s is set to 0.1 (Figure 3.8c) a different behavior is observed. Due to the low friction, stable contact force chains do not form, particles slide past each other more often and no heap is formed. This in turn leads to low radial and vertical velocity values and the recirculation zone cannot develop. Particles move as a block solely in the tangential direction. A similar behavior was observed at low sliding friction coefficients for a flat two-blade impeller configuration [110]. However, experimental verification of the low friction results is still needed.

Bulk density differences were also observed. The vertical and radial movement of the particles for $\mu_s = 0.5$ and $\mu_s = 0.3$ allows the granular bed to dilate as the blade moves, leading to a total average bulk density value of ~ 900 kg/m^3. In contrast, little bed dilation is observed for the case of $\mu_s = 0.1$. The average bulk density in this case was measured at ~ 1200 kg/m^3. Density fluctuations similar to the ones shown in Figure 3.4 were observed for all values of μ_s. However, the mean and amplitude for the $\mu_s = 0.1$ case are not dependent on mixer height. The density in this case fluctuates between 1300 kg/m^3 and 1000 kg/m^3.

Fluctuation velocities are also affected by the value of μ_s. Figure 3.9 shows the time-averaged granular temperature profiles as a function of radial position for the three values of μ_s. Increasing the value of μ_s leads to an increase in the granular temperature of the system. Granular temperature gradients are observed for $\mu_s = 0.5$ and $\mu_s = 0.3$. However, a colder and uniform granular temperature profile is obtained for the $\mu_s = 0.1$ case. As a result, periodic velocity fluctuations are seen for $\mu_s = 0.5$ and $\mu_s = 0.3$ but not for $\mu_s = 0.1$ (not shown). Increasing the sliding friction coefficient leads to an increase in velocity fluctuations at frequencies higher than the rotation frequency of the blades. This behavior is analogous to the effect observed for wet systems in the experiments of Lekhal et al. [107] where higher velocity fluctuations were observed with increased moisture levels. These higher frequency fluctuations are associated with surface avalanching. The Fourier transform peak height for these fluctuations is significantly smaller than the main peak height indicating that, while present, avalanching is not a dominant effect in this system.

The effect of sliding friction on the mixing kinetics can be seen in Figure 3.10. Relative standard deviation trends as a function of revolution number are shown in Figure 3.10a. Figure 3.10b shows some top view snapshots for each μ_s value. As expected, increasing the friction coefficient leads to enhanced mixing. Almost no mixing occurs at $\mu_s = 0.1$. After 5 revolutions the RSD values are 0.45 for $\mu_s = 0.5$ and 0.6 for $\mu_s = 0.3$ while the value for $\mu_s = 0.1$ remains at 0.9. This poor mixing performance is explained by the absence of the 3-dimensional recirculation zone at $\mu_s = 0.1$. The presence of this vortex promotes convective mixing. However, in addition to convective mixing, diffusive mixing appears to play an important role in this system. While little difference is observed between the recirculation patterns for $\mu_s = 0.5$ (Figure 9a) and $\mu_s = 0.3$ (Figure 9b), the RSD trends show a difference in mixing kinetics. The enhanced mixing performance observed at the higher μ_s value is explained by the higher granular temperature. These higher fluctuation velocities are associated with an increase in particle diffusivity. Thus, higher friction coefficients promote diffusive mixing. While convective mixing is the dominant mechanism in this system, diffusive mixing becomes important when the homogenization process is down to the particle-particle level. However, the relative contribution of the diffusive and convective mixing components changes with particle/system size. The effect of system size on the observed mixing kinetics will be discussed in Chapter 4.

3.3. Shear and Normal Stress Profiles

In this section, we discuss the normal and shear stress profiles that develop inside bladed mixers. Figure 3.11 shows stress profiles at r = 0.09 m as a function of mixer height and number of revolutions for the obtuse blade pitch simulations at 20 RPM. The pressure profile is shown in Figure 3.11a and the $\tau_{\theta r}$ profile is shown in Figure 3.11c. These profiles document a periodic behavior similar to that of the velocity and density profiles. As demonstrated before, the main fluctuation frequency is equal to that of the blade rotation. The pressure profile implies that the material compresses when the blades are present and dilates in between blade passes. The mean and amplitude of the pressure fluctuations are a strong function of mixer height, as shown by the power spectrum (Figure 3.11b). Higher pressures are observed near the bottom plate and the pressure decreases monotonically with increased height, since the particles at the bottom sustain the weight of the particles at the top. This is similar to the behavior observed in silos [162, 163] for static systems. Higher fluctuation amplitudes are also observed near the bottom plate. In contrast to the density profiles, the pressure fluctuation amplitude reaches a minimum above the blade height, since these particles sustain lower weights than the bottom particles. The $\tau_{\theta r}$ fluctuations (Figure 3.11c) result from the formation of internal force chains when the material compresses near the blades and the subsequent breakage of these force chains as the material dilates in between blade passes. The value of the shear stress component $\tau_{\theta r}$ is roughly one order of magnitude lower than that of the normal stress or pressure. The mean and amplitude of the $\tau_{\theta r}$ fluctuations change little within the span of the blades, while these values decrease above the blade (Figure 3.11d). This indicates that most of the material shearing occurs within the span of the blade. Similar periodic behavior was observed for the remaining stress tensor components (not shown). However, the values for $\tau_{\theta y}$ and τ_{ry} fluctuate around zero, while the values for $\tau_{\theta r}$ do not.

The blade orientation affects the magnitude of the shear stress and pressure inside the mixer (Figure 3.12). Time-averaged pressure profiles are shown in Figure 3.12a as a function of radial position for both the obtuse and acute blade pitch orientations. Higher pressures are observed for the acute blade pitch. Pressure values vary little in the radial direction. The increase in pressure is explained by the increased bulk density observed for acute blade pitch (see Section 3.1.2). The acute blade pitch orientation compresses the granular bed by pushing it down as the blades rotate leading to higher pressures. On the other hand, dilation occurs for the obtuse blade orientation which reduces the pressure inside the particle bed. The effect of blade orientation is less pronounced for the shear stress $\tau_{\theta r}$ (Figure 3.12b). The values of $\tau_{\theta r}$ are highest near the cylinder wall and close to zero near the impeller shaft. This is due to the increased tangential movement observed near the wall and the increased strength of the force chains due to wall friction. The ratio of the shear stress to the normal stress is known as the bulk friction coefficient and is used to describe stresses at yield conditions in soil mechanics. This ratio is related to the internal angle of friction and is commonly assumed to be a constant material property when the material is at the critical state [41]. The critical state of a granular material is characterized by a constant bulk density. Figure 3.12c shows the time averaged value of the $\tau_{\theta r} / \tau_{\theta\theta}$ ratio. This ratio is far from constant with maximum values near the cylinder wall. Non-constant bulk friction coefficient values were also observed in computer simulations of 2-dimensional hopper discharge [164]. The non-constant bulk friction coefficient is most likely due to the changes in bulk density that occur within the particle bed as the blades rotate. These results suggest that the continuum models based on plasticity theory and soil mechanics may not provide an adequate description of granular flows in bladed mixers. The increase in bulk friction coefficient is a result of increased shear stresses near the cylinder wall. It should be noted that the highest value of the bulk friction coefficient is less than the particle-particle friction coefficient (0.3 for these simulations). This indicates that the particle bed yields at lower stresses than what is predicted by Coulomb's law. Identical friction coefficients are obtained from the $\tau_{\theta r} / \tau_{rr}$ ratio. The magnitude of τ_{yr} / τ_{rr} and $\tau_{\theta y} / \tau_{yy}$ is about 25% of the $\tau_{\theta r} / \tau_{\theta\theta}$ magnitude.

Despite the complex dynamics observed in the bladed mixer, we find that we can approximate the temporal averaged pressure as a function of mixer height with the simple hydrostatic pressure relationship

$$P = \rho_{bulk}\, g\left(h - H_{bed}\right) \qquad \textbf{(3-1)}$$

where ρ_{bulk} is the total average bulk density of the granular bed, g is the acceleration due to gravity, h is the vertical position and H_{bed} is the total height of the particle bed. The parenthesis term in equation 3-1 is needed to account for the bottom plate being located at h = 0.0 m. Figure 3.13 shows the fit between the pressure values obtained from the DEM simulations and the hydrostatic pressure curves for the obtuse and acute blade pitch cases. The bulk density values obtained from linear fitting of the hydrostatic pressure equation were 780 kg/m^3 for the obtuse blade pitch case and 1300 kg/m^3 for the acute blade pitch case. These values are close to the averaged densities calculated from the DEM simulations (~900 kg/m^3 for the obtuse case and ~ 1100 kg/m^3 for the acute case). This demonstrates that if the average bulk density during flow is known, the averaged normal stress in this dynamic system can be approximated by hydrostatics. This linear dependence of normal stresses with height has also been observed in fluidized systems [26, 43]. The effect of particle/system size on the observed pressure profiles will be discussed in Chapter 4.

Many of the stress trends observed in the bladed mixer are consistent with the behavior of slowly deforming, quasi-static systems. In quasi-static systems, momentum transfer is governed by the frictional contacts between particles. As such, the particle-particle friction coefficient has a significantly effect on the developed shear stresses. Figure 3.14a shows the effect of inter-particle friction on averaged values of $\tau_{\theta r}$ in the bladed mixer. Increasing the friction coefficient leads to an increase in shear stress. The $\tau_{\theta r} / \tau_{\theta\theta}$ ratio also increases with increased particle-particle friction (Figure 3.14b). The pressure profiles were found to be less sensitive to the particle's frictional characteristics. The strength and stability of the force chains that develop inside the mixer increase at higher friction coefficient. This result implies that the main source of stress in the bladed mixer is the formation of these force chains. On the other hand, shear stress profiles were found to be independent of shear rate (Figure 3.14c). From this we can conclude that increasing the shear rate in the bladed mixer leads to an increase in the shear stress fluctuation frequencies but has little effect on the mean and amplitude of these fluctuations. Momentum transfer is therefore governed by inter-particle contacts and for our simulations the bladed mixer operates in the quasi-static regime. Knowledge of the flow regime in which a process takes places could assist during process design and scale-up as it provides a fundamental basis for granular flow behavior and could assist in identification of critical process parameters.

3.4. Conclusions from Numerical Monodisperse, Cohesionless Flows

The discrete element method was used to characterize the flow of cohensionless, monodisperse spheres in a bladed mixer. The simulation results presented here are consistent with published experimental data and comparable to results obtained from previous numerical studies in similar systems. Instantaneous, averaged and fluctuating velocity fields show that the particle movement is governed by the angular motion of the blades. The granular bed deforms by forming heaps where the blades are present and valleys between blades passes. The presence of these heaps leads to the formation of a 3-dimensional recirculation zone in front of the blade, where particles flow upwards by the wall and downwards by the impeller shaft. This 3-D recirculation promotes radial and vertical mixing. When the blade orientation is changed from an obtuse blade pitch to an acute blade pitch, the recirculation zone is not present. As a result, the particles move mainly in the tangential direction with little radial and vertical mixing. Acute blade pitch flows were shown to lower the granular temperature within the particle bed. This decrease in granular temperature is associated with a decrease in particle diffusivity. Diffusive mixing is therefore hindered by acute blade flows.

Density fluctuations exits within the granular bed with a frequency equal to the rotation frequency of the blades. This behavior indicates that the granular material compresses as the blade passes and dilates in between the blades. The system's frictional characteristics were shown to strongly influence the flow structure and mixing kinetics observed within the mixer. At low friction coefficients the 3-D recirculation in front of the blade is not present, reducing the convective mixing. Higher friction coefficients lead to an increase in diffusive mixing. Collisional stresses showed a periodic behavior similar to the density trends. Normal stresses were found to be an order of magnitude larger than shear stresses. The average pressure was found to vary with mixer height with maximum values near the bottom plate and could be approximated by the simple hydrostatic pressure. A higher bulk density was observed for the acute blade pitch which led to an increase in pressure for this blade orientation.

A strong dependence between the magnitude of the shear stresses and the friction coefficient of the particles was found. Shear stress increases with higher particle-particle friction. Shear stresses were found to be independent of shear rate. These stress tensor characteristics indicate that for our simulations the granular flow in this bladed mixer occurs in the quasi-static regime. Momentum transfer in this system is therefore governed by inter-particle contacts. This observation implies that quasi-static theories could provide a first-principles approach to bladed mixer design, scale-up and operation for cohensionless systems. This chapter described the behavior of an idealized granular system (cohesionless, monodisperse glass spheres in the millimeter size range) in a bladed mixer. While simple in nature, it complements our understanding of granular flows in an industrially relevant geometry and represents an initial step towards understanding the granular behavior of more complex systems.

3.5. Figures for Chapter 3

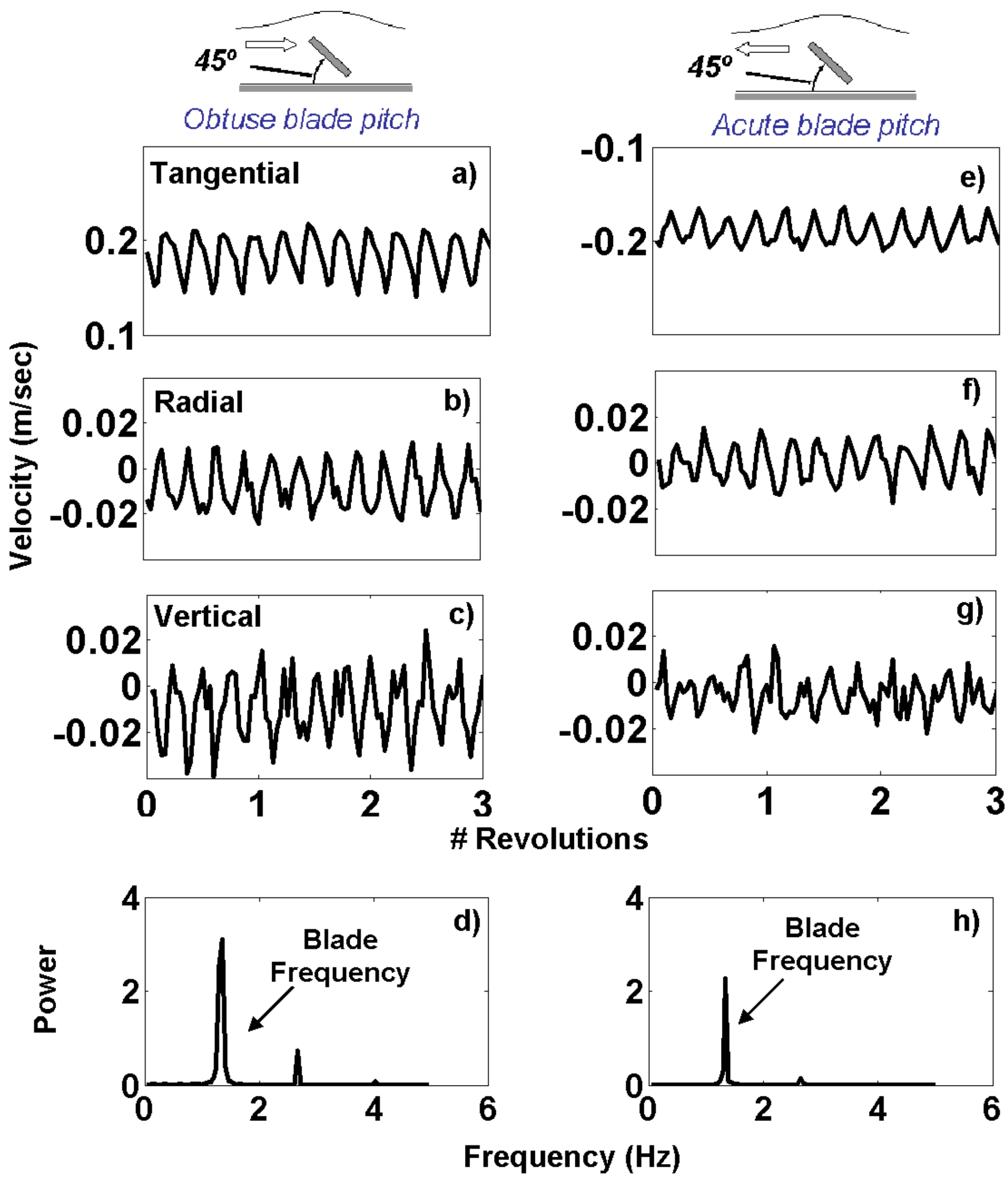

Figure 3.1. Velocity profiles at r = 0.09 m, h = 0.06 m. Obtuse blade pitch: a) tangential, b) radial, c) vertical velocity and d) tangential velocity power spectrum. Acute blade pitch: e) tangential, f) radial, g) vertical velocity and h) tangential velocity power spectrum.

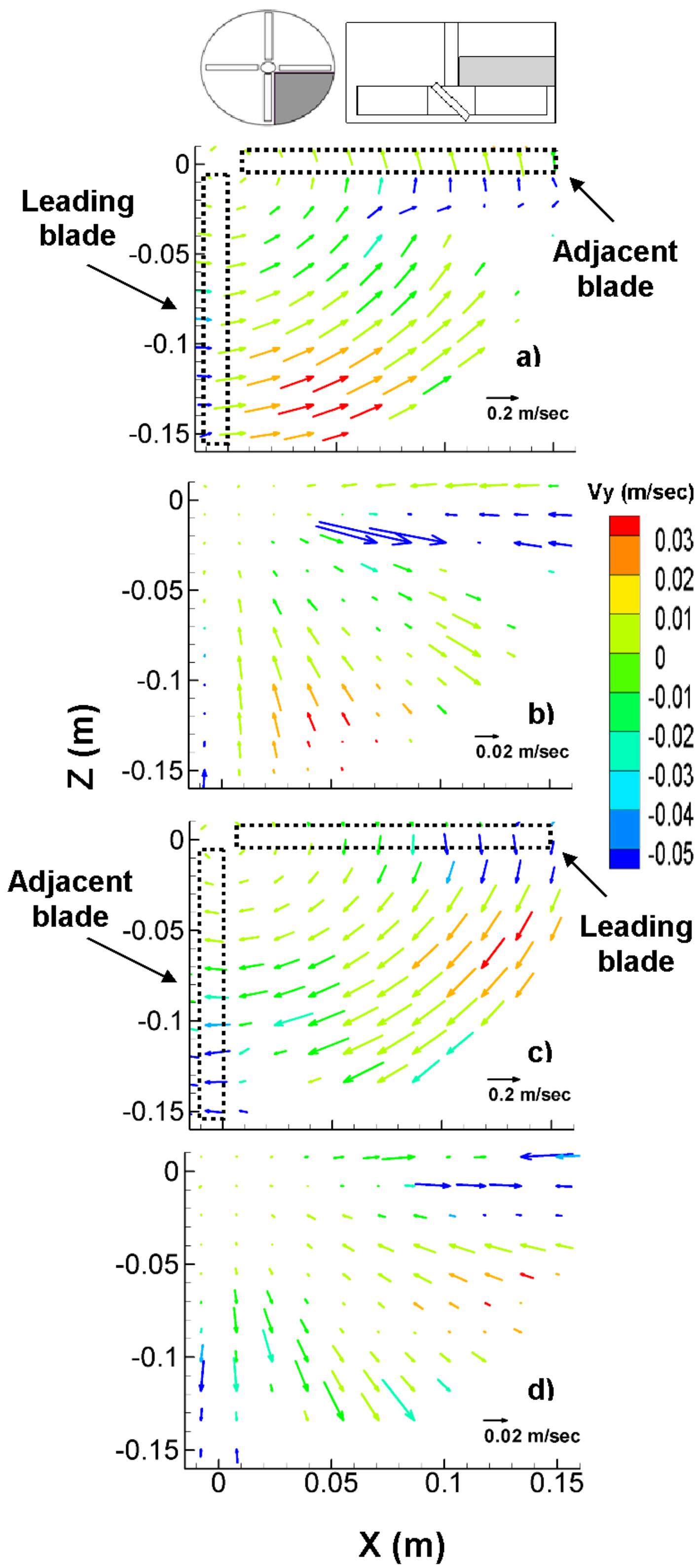

Figure 3.2. Time-averaged velocity fields on horizontal plane: Obtuse blade pitch: a) tangential velocity and b) radial velocity. Acute blade pitch: c) tangential velocity and d) radial velocity.

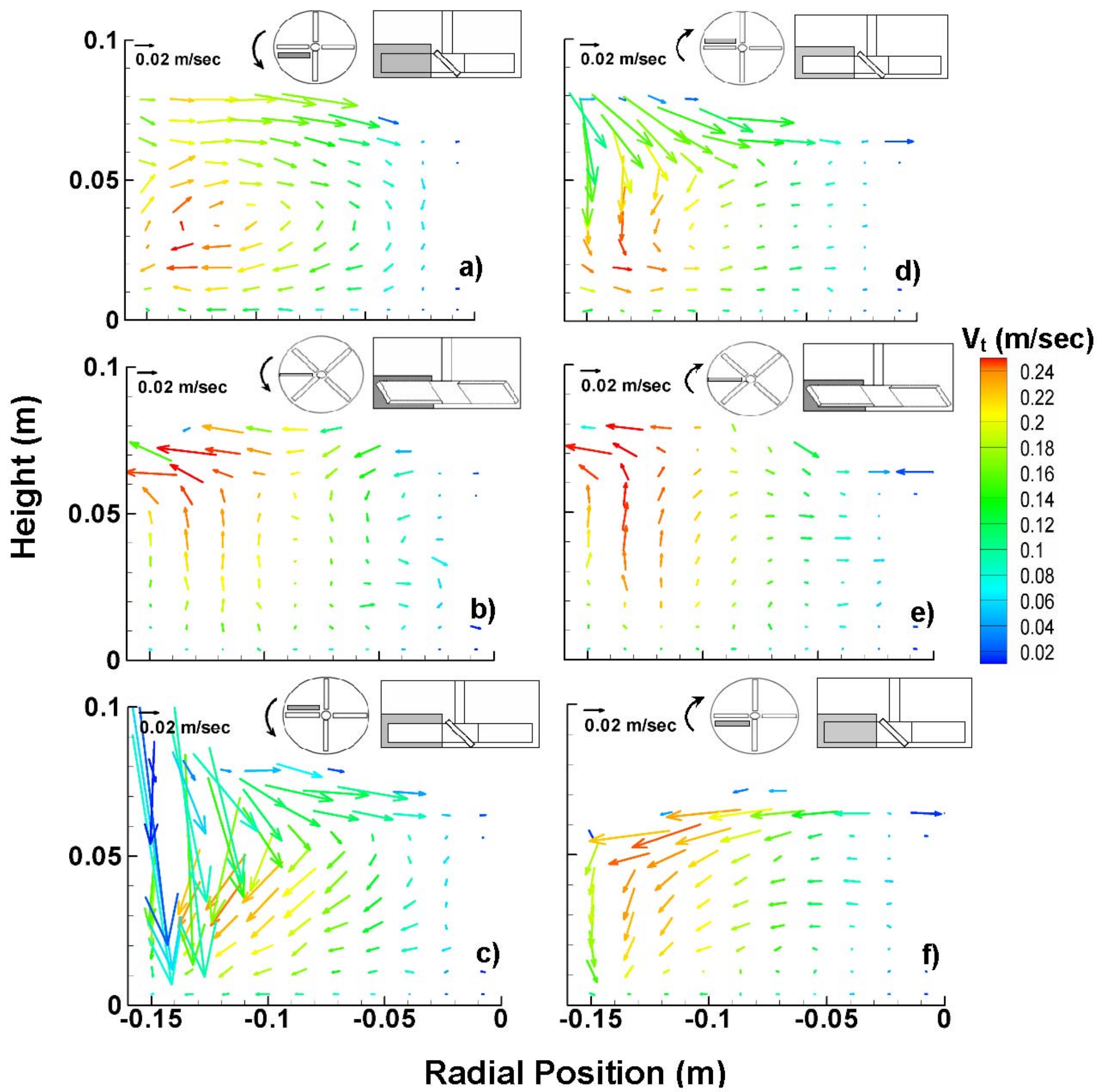

Figure 3.3. Time-averaged radial and vertical velocity fields in the vertical plane. Obtuse blade pitch: a) front of blade, b) in-between blades and c) behind the blade. Acute blade pitch: d) front of blade, e) in-between blades and f) behind the blade.

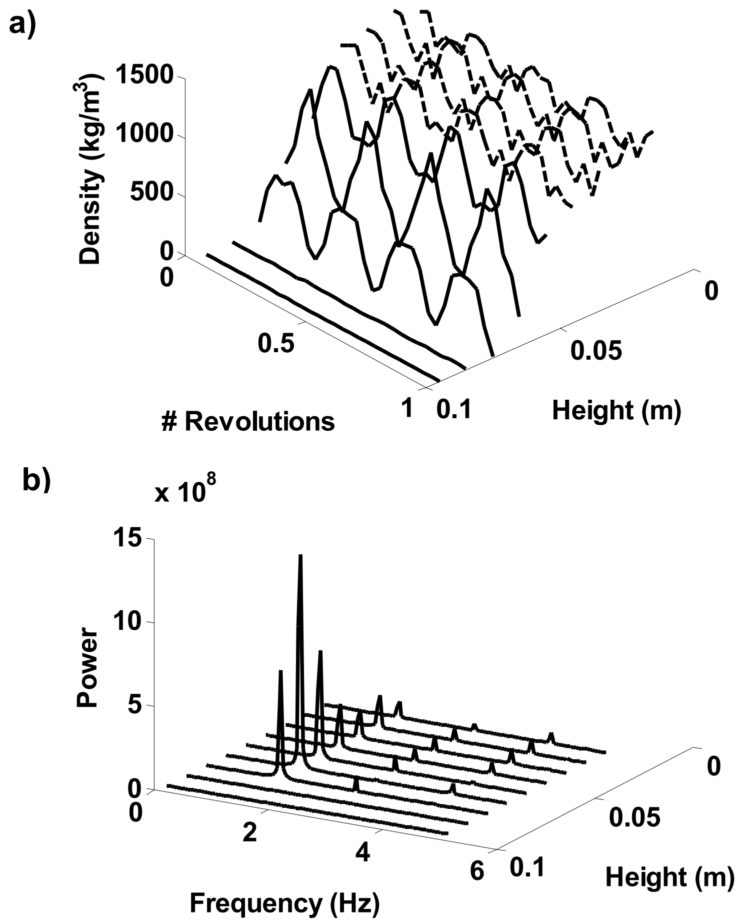

Figure 3.4. Density fluctuations at r = 0.09 m for the obtuse blade pitch. a) density profile as a function of revolution and height, b) density fluctuation power spectrum as a function of height.

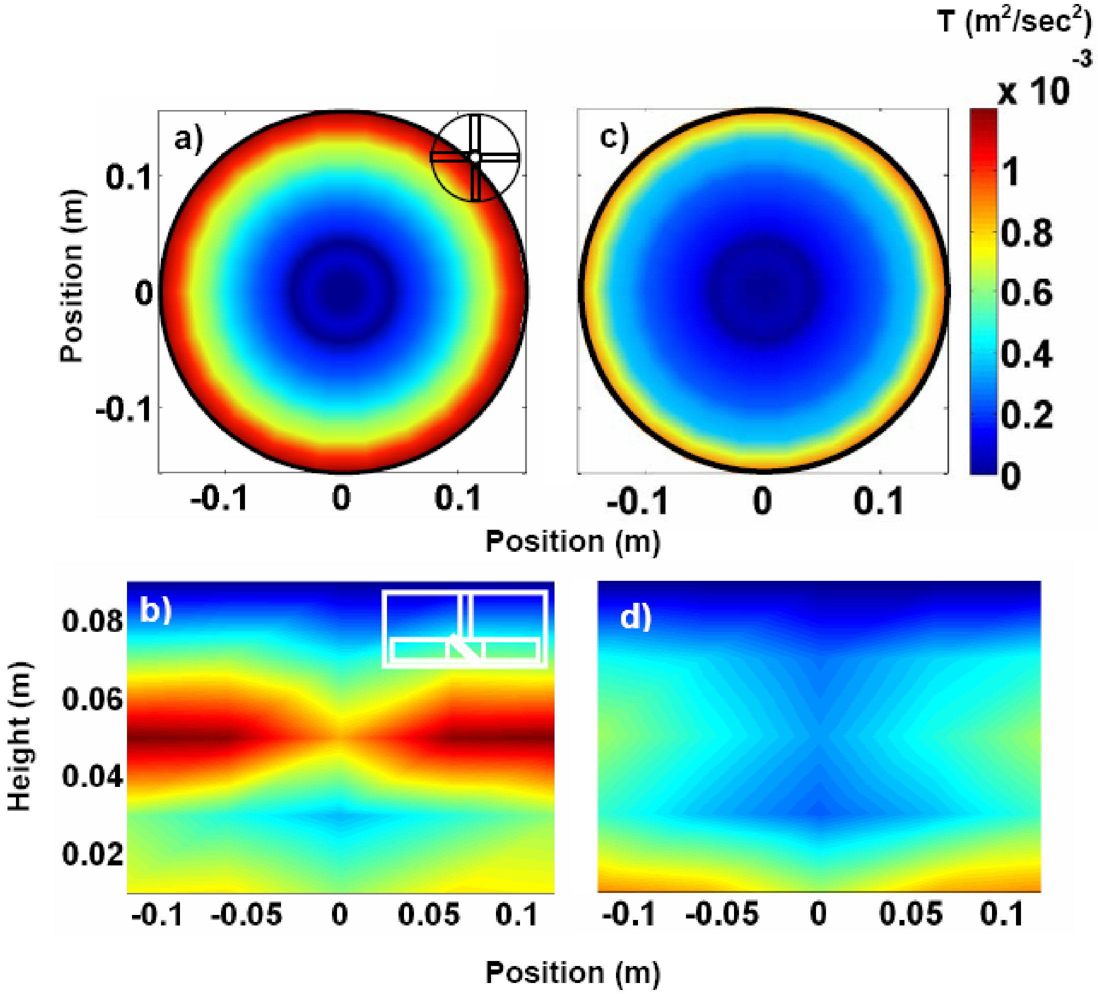

Figure 3.5. Time-averaged granular temperature profiles. Obtuse blade pitch: a) horizontal plane and b) vertical plane. Acute blade pitch: c) horizontal plane and d) vertical plane.

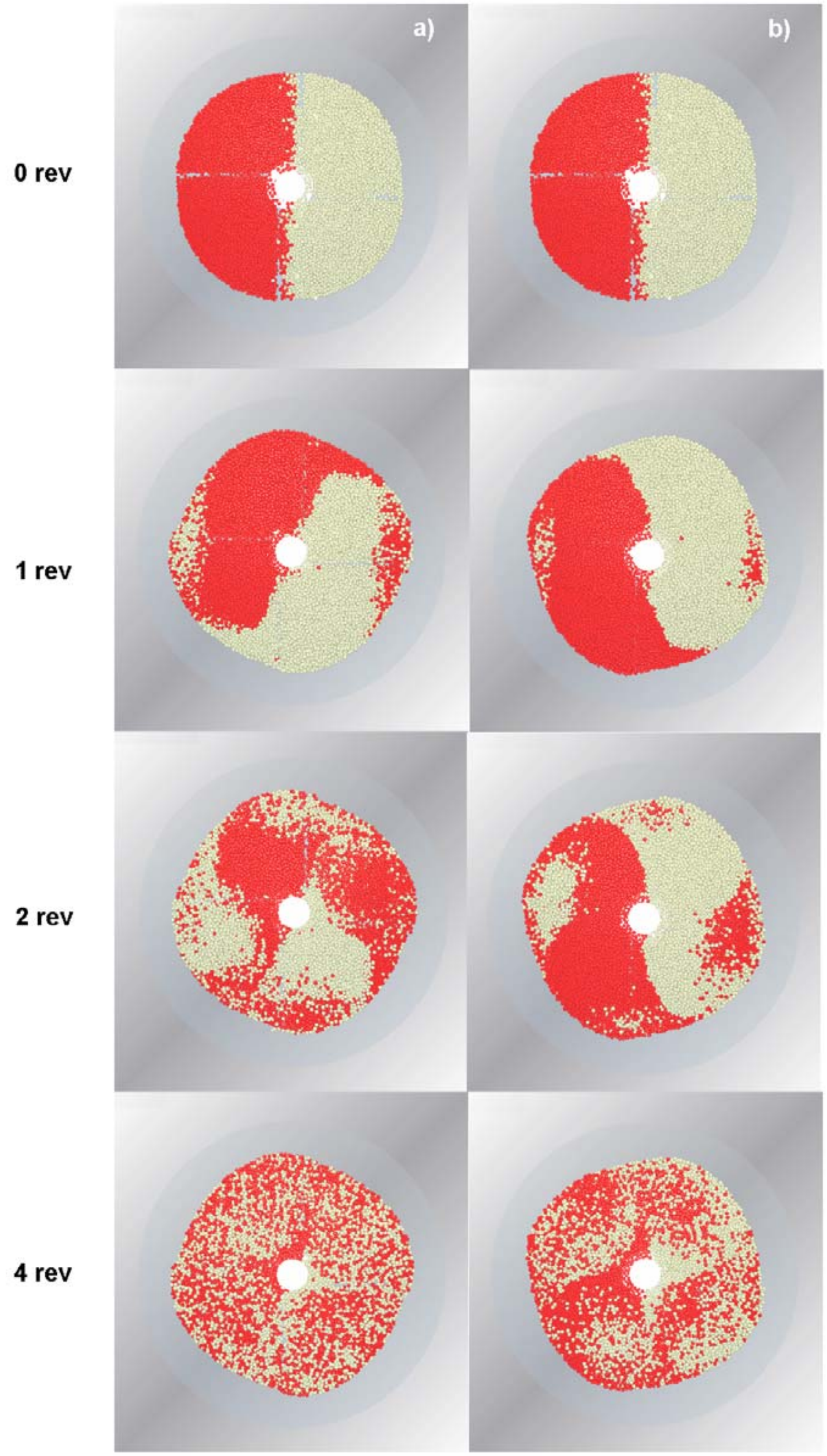

Figure 3.6. Top view of mixing for left-right segregated system at 20 RPM. a) obtuse blade pitch and b) acute blade pitch.

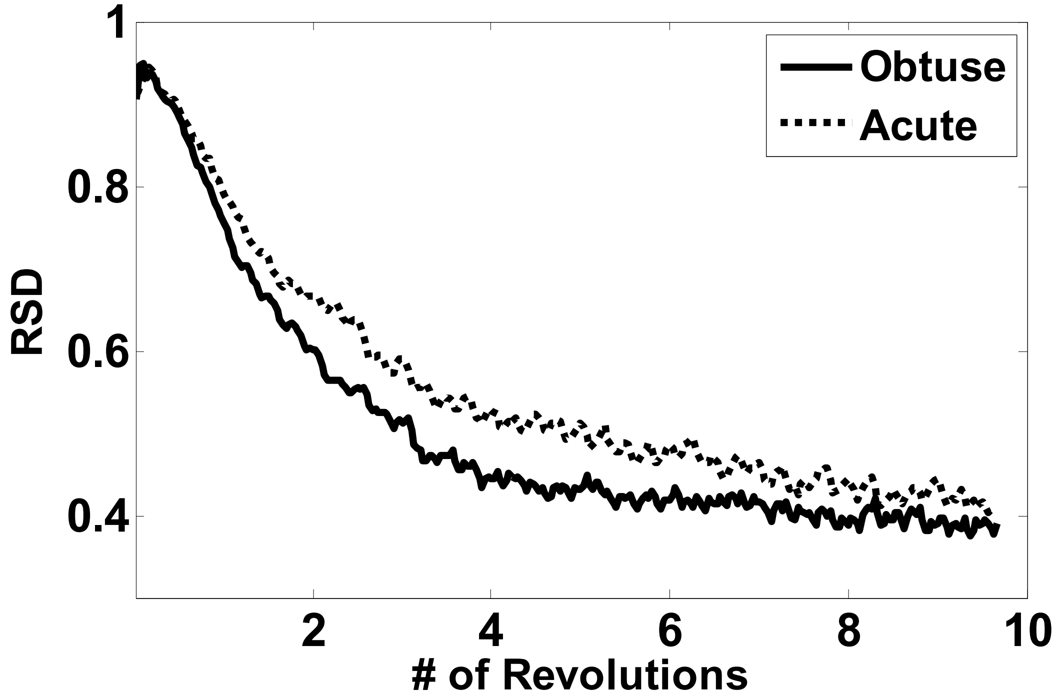

Figure 3.7. Effect of blade orientation on degree of mixing at 20 RPM.

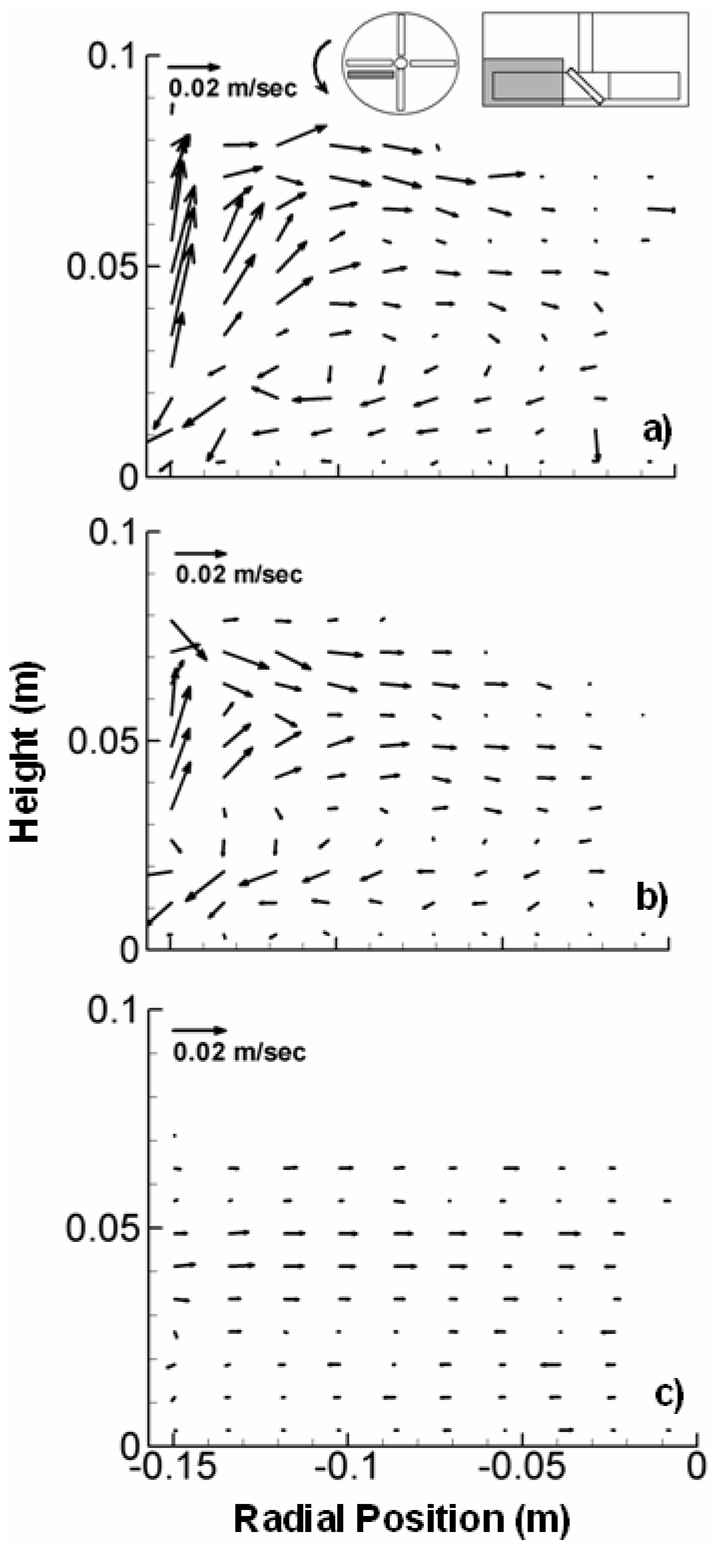

Figure 3.8. Time-averaged velocity fields in-front of blade. Obtuse blade pitch: a) μ_s = 0.5, b) μ_s = 0.3 and c) μ_s = 0.1.

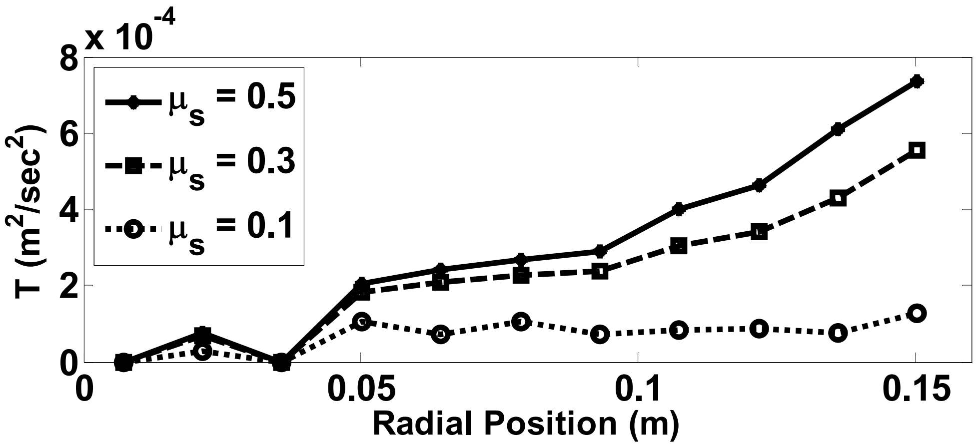

Figure 3.9. Time-averaged granular temperature profiles for different μ_s. Solid line with solid dots shows the granular temperature for μ_s = 0.5, dash line with squares μ_s = 0.3 and dotted line with circles μ_s = 0.1.

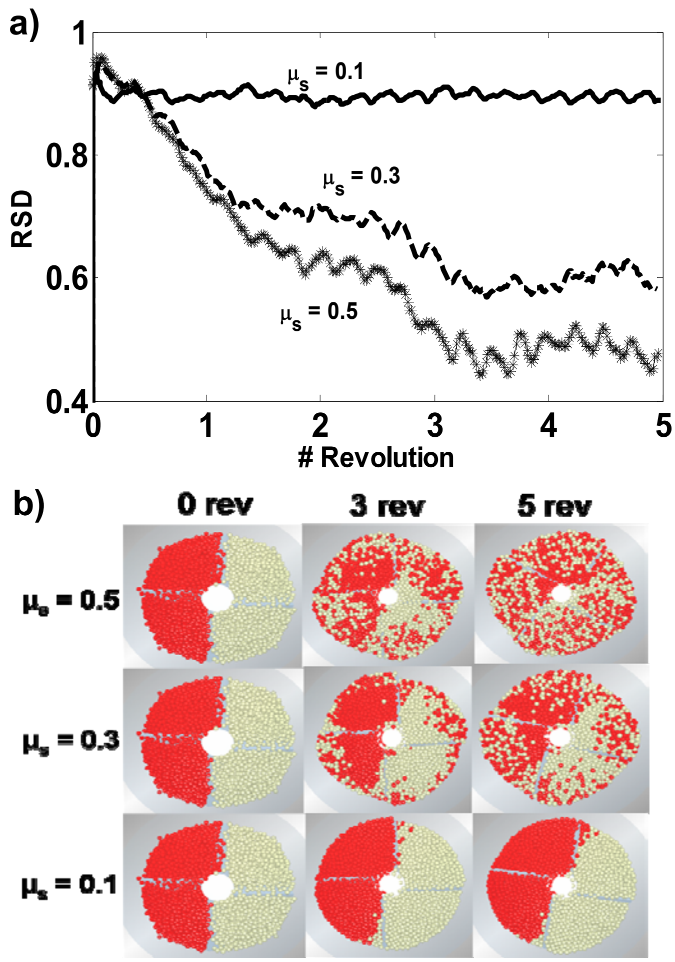

Figure 3.10. Effect of particle friction on mixing kinetics. a) relative standard deviation for red particle concentration and b) top view snapshot of mixing patterns for different friction coefficients.

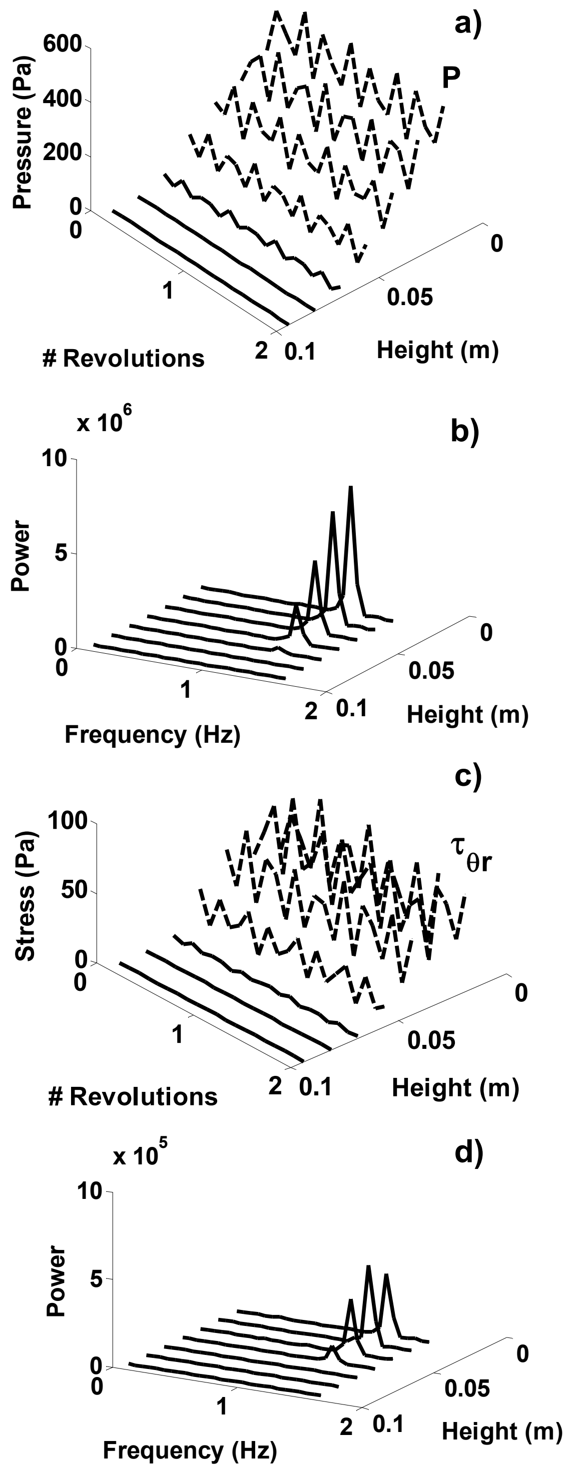

Figure 3.11. Pressure and shear stress fluctuations at r = 0.09 m for obtuse blade pitch flow at 20 RPM. a) pressure profiles, b) pressure power spectrum, c) shear stress $\tau_{\theta r}$ profile and d) $\tau_{\theta r}$ power spectrum. Particle diameter = 5 mm.

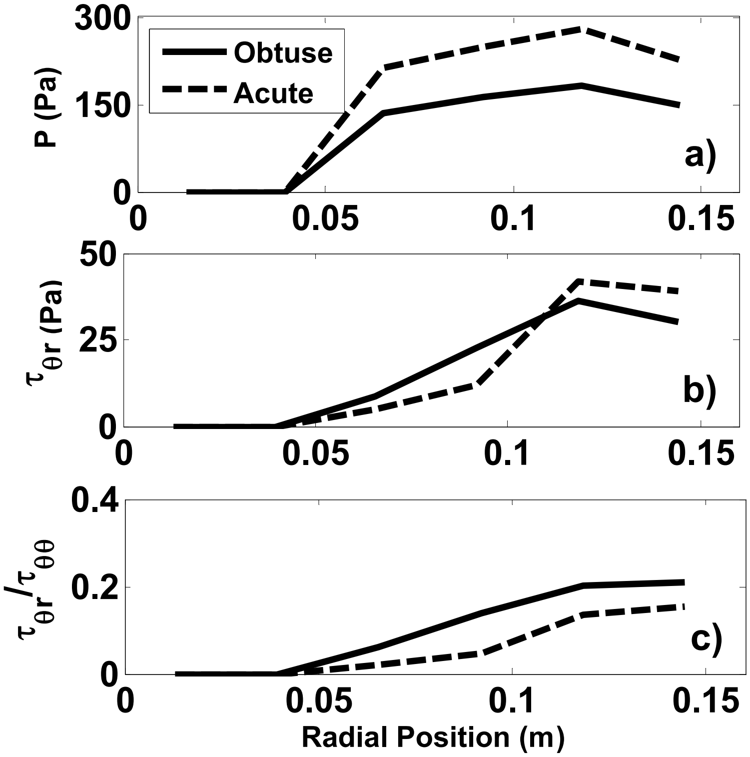

Figure 3.12. Comparison of time-averaged stresses for obtuse vs. acute blade pitch. a) Pressure, b) shear stress $\tau_{\theta r}$ and c) bulk friction coefficient $\tau_{\theta r} / \tau_{\theta\theta}$. Particle diameter = 5 mm.

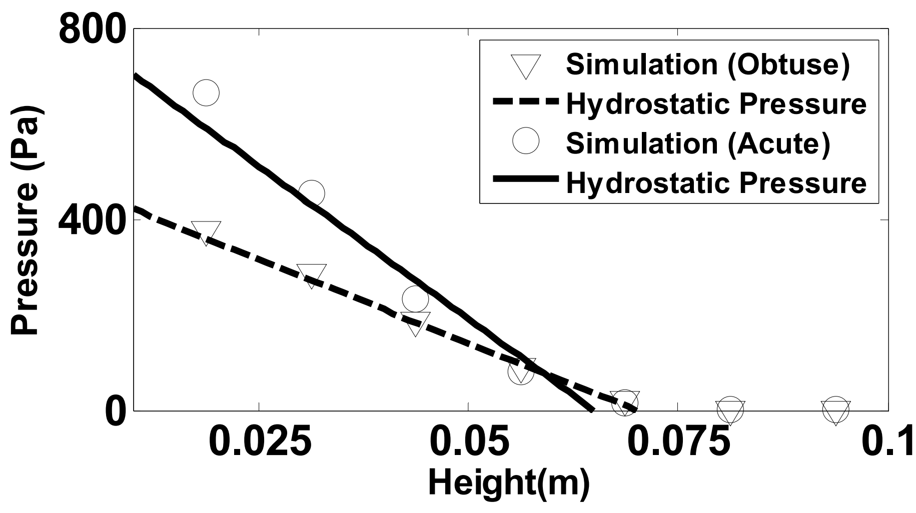

Figure 3.13. Time-averaged pressure as a function of height vs. hydrostatic pressure curves. Particle diameter = 5 mm.

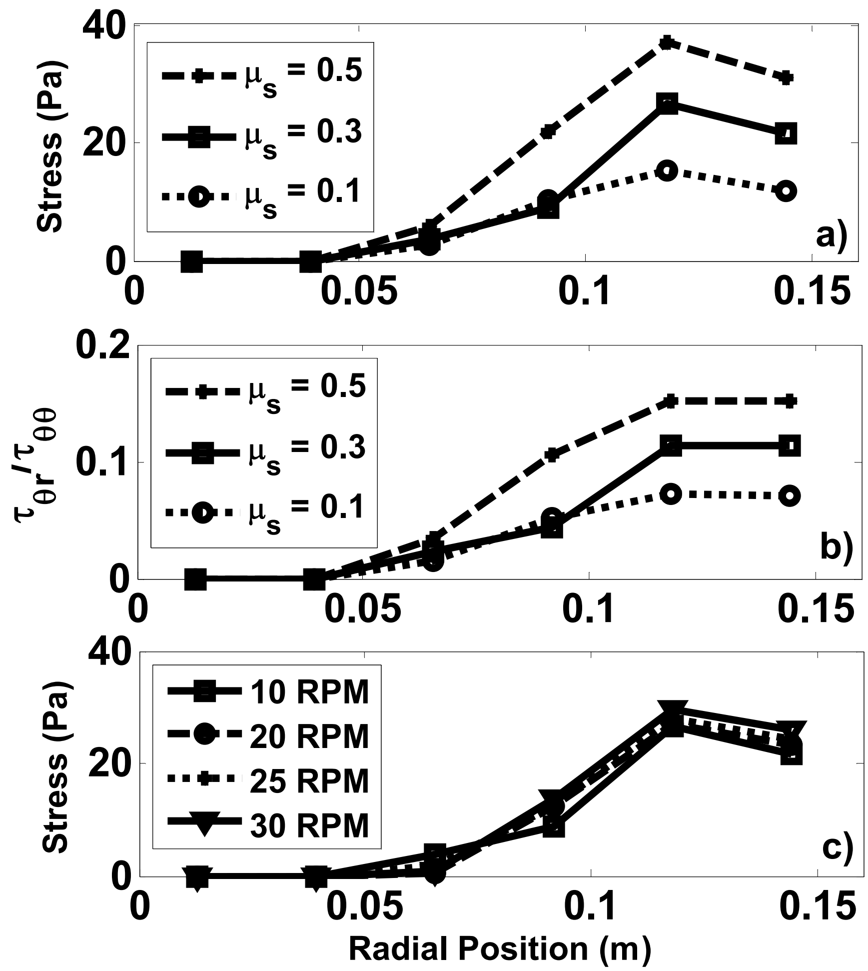

Figure 3.14. Effect of μ_s and shear rate on $\tau_{\theta r}$. Particle diameter = 10 mm.

Chapter 4. Effect of Mixer Properties, Fill Level and Mixer Scale

Mixer properties, mixer scale and fill level play an important role in the behavior of granular materials in bladed mixers. Often during the early stages of process development and design, laboratory or pilot plant experiments are carried out with different equipment configurations, at smaller scales or at different fill levels than what will ultimately be used at the manufacturing scale. The uncertainty surrounding the effects of mixer properties on granular flows opens up the door for complications to occur during scale-up. Thus, understanding the role of mixer parameters and operating conditions in agitated devices is critical for designing and engineering reliable processes. In this chapter, we examine the effect of these parameters on the flow of monodisperse, cohesionless particles with the use of DEM. The simulation results are first compared to the experimental data of Stewart et al. [105] obtained with two flat blades. The effect of fill level, particle-wall friction and blade position along the axis is then discussed for a base case system at the laboratory scale. The effect of mixer scale is then presented followed by some scaling relationships and general guidelines. Simulation results discussed in this chapter were obtained using blade speeds of 10 RPM (Section 4.1-4.3) and 20 RPM (Section 4.4). The particle size for all the simulations was 10 mm.

4.1. Comparison with Experimental Data from Stewart et al. [105]

In this chapter, we describe the fill level inside the mixer by taking the ratio of the particle bed height prior to blade movement (H) to the mixer diameter (D). H is measured from the bottom plate of the mixer. The mixer dimensions used here are listed in Table 2.1. For these mixer dimensions and the geometry presented in Figure 2.3, H/D = 0.17 represents an initial particle bed height covering just the top of the blades. We begin by comparing the particle velocities obtained from our simulations with the experimental results of Stewart et al.[105] obtained using glass beads and positron emission particle tracking (PEPT) in a mixer with two flat blades. Figure 4.1 shows the velocity frequency distributions for the normalized tangential, radial and vertical velocity components from the simulation with H/D = 0.17 vs. the PEPT experimental results at H/D = 0.12. The velocities presented in Figure 4.1 have been normalized by the blades' tip speed. The tangential velocities shown are relative to the angular movement of the blades, i.e. $V_t* = (V_t - V_{tip}) / V_{tip}$. As can be seen from Figure 4.1 the shape of the frequency distributions obtained from the simulation (Figures 4.1a-c) is very similar to those observed experimentally by Stewart et al. (Figures 4.1d-f). The tangential velocities in both cases have a left-skewed distribution with most particles having velocities lower than the tip speed of the blades (V* < 0) and a few particle possessing velocities above it (V* > 0). The radial velocities show a normal distribution centered at zero (Figures 4.1b and 4.1e) while the vertical velocities have right-skewed distributions (Figures 4.1c and 4.1f). For both the simulation case and the experimental case most particles possess radial and vertical velocities which are much lower than the tangential velocities. Some differences are observed between the simulation results and those obtained experimentally. The tails of the radial and vertical velocity distributions are longer than those obtained by Stewart et al. In our simulations we used four blades pitched at an angle and this blade configuration promotes vertical and radial mixing (see Chapter 3) vs. the two flat blades used by Stewart et al. Despite these differences, the general trends are remarkably similar.

4.2. Effect of Fill Level

A salient feature of granular flows in bladed mixers at fill levels just covering the span of the blades is the formation of heaps where the blades are present and valleys in between blade passes. The formation of these heaps leads to the development of a 3-dimensional recirculation zone in front of the blades which promotes radial and vertical mixing. The development of this recirculation zone leads to enhanced mixing kinetics as demonstrated in Chapter 3. This flow structure occurs near the front of the blades and is not present for the particles in between the blades and behind the blades. In this chapter we gauge the effect of the studied parameters on the convective particle motion by examining the flow structures that develop in front of the blades since the development of the recirculation zone is a key flow feature.

We find that, while present at all the fill levels studied, the size and intensity of the recirculation zone in front of the blades is dependent on mixer fill level. Velocity fields in front of the blade and granular temperature contour plots are presented in Figure 4.2 for different fill levels. The recirculation pattern that forms in front of the blades is most prominent for $H/D = 0.17$ (Figure 4.2a). Due to the pitch of the blades, particle rise by the wall forming a heap. The particles on the top of the heap then move radially inwards forcing the particles by the shaft to flow downwards and radially outwards, leading to the recirculation. The size of the recirculation zone decreases for $H/D > 0.17$ (Figures 4.2b and 4.2c) as heap formation does not occur at these fill levels and the free surface of the particle bed undergoes almost no deformation. Reduction in the size of recirculation zones as fill level is increased has also been observed experimentally in a mixer with two flat blades [105]. However, the velocity profiles within the span of the blades are very similar for H/D = 0.32 and H/D = 0.46. At H/D > 0.17, a mixing dead zone develops for the particles near the impeller shaft and above the blades. Almost no radial and vertical movement occurs in this zone and particles move mostly in the tangential direction. The size of the mixing dead zone increases with increased fill level. Granular temperature is highest for H/D = 0.17 with temperature maximums occurring at the top tip of the blades. Granular temperature profiles within the span of the blades are similar for H/D = 0.32 and H/D = 0.46. The mixing dead zone observed for H/D > 0.17 coincides with regions of low granular temperature.

Figure 4.3 shows time-averaged bulk density profiles as a function of bed height for different fill levels. Lower density values are observed for H/D = 0.17, i.e., the case with the highest granular temperature. At this fill level, bed dilation occurs when the blades rotate due to the development of heaps. Averaged density values increase for H/D > 0.17, since the weight of the particles above the blades hinders heap formation and bed dilation. However, bulk density values within the span of the blade change little between the H/D > 0.17 cases. This is similar to the behavior observed for the velocity and granular temperature profiles. Thus, for high fill levels, the portion of the particle bed within the blades' span dilates to a particular density value during flow and this value is independent of fill level. For fill levels significantly higher than the height of the blades (H/D > 0.32), the region above the blades undergoes almost no dilation and density values are close to the averaged bulk density prior to blade movement (~1200 kg/m^3). While bed dilation within the span of the blades is independent of fill level at H/D > 0.17, the amount of energy needed to induce flow does depend on fill level. Figure 4.4 shows the average impeller torque as a function of H/D. Impeller torque increases linearly with fill level as the average pressure within the span of the blades increases linearly with particle bed height. A similar behavior has been observed experimentally for impeller power measurements taken with glass beads at H/D < 2.5 [165]. Since impeller torque is independent of rotation rate in the quasi-static regime, our results suggest that a power per unit volume scaling relationship exists in bladed mixers. Therefore, the energy needed to induce flow at high fill levels could be predicted from torque measurements at lower fill levels.

We gauge particle motion at the microscopic level by calculating particle diffusivities which describe the mass flux rate due to the particles' "random walk". The convective and diffusive contributions to particle motion are compared by calculating the Peclet number. Table 4.1 lists diffusivity coefficients and Peclet numbers for the particles within the span of the blades at different H/D ratios. Particles diffusivities are the highest for H/D = 0.17 as granular temperature and bed dilation are highest for this case. $D_{\theta\theta}$ and D_{rr} values decrease for H/D > 0.17, but these values change little between the H/D = 0.32 and the H/D = 0.46 cases. The weight of the particles above the blades which leads to lower granular temperatures and lower degree of bed dilation hinders particle diffusivity in the radial and tangential direction. However, the D_{yy} value within the span of the blades appears to be independent of fill level. This behavior is explained by the pitch of the blades. When the energy needed to overcome the weight of the particle bed is supplied to the impeller, the 45° angle of the blades pushes material up as the blades rotate. As the particles rise following the convective flow, the frictional interactions add a random component to the particles' motion and diffusion occurs. Thus, the D_{yy} diffusion coefficient changes little with an increase in H/D for particles within the span of the blades. The Peclet numbers obtained for all the fill levels studied are significantly higher than unity indicating that convection is the dominating mechanism for particle transfer. The diffusive process is most significant in the vertical direction as Pe_{yy} values are lower than $Pe_{\theta\theta}$ and Pe_{rr}. Peclet numbers in the tangential and radial direction are the lowest for the H/D = 0.17 case. This indicates that the diffusive process contributing to particle motion is highest for fill levels just covering the height of the blades. However, Peclet numbers change little between H/D = 0.32 and H/D = 0.46 since bulk velocity profiles and particle diffusivities change little between these cases. These results are in agreement with the velocity and bulk density trends and demonstrate that flow kinematics within the span of the blades change little at high fill levels. The diffusion coefficients observed at H/D > 0.17 for the particles above the blades were 1-2 orders of magnitude lower than the values listed in Table 4.1.

The results presented thus far show that for H/D > 0.17, two different regions develop in the particle bed, each with different flow characteristics. The first region consists of the particles present within the span of the blades. In this region, dilation occurs and particles can move in the radial and vertical direction due to convective and diffusive motions. The second region consists of the particles above the blades. Here, particles move slowly as a block in the tangential direction and almost no dilation or diffusive movement occurs. These differences in behavior affect the particle mixing patterns obtained in each region. In order to evaluate the degree of mixing obtained for each case studied, particles are colored according to their position prior to blade movement. The cylindrical mixer is sliced in half axially and particles on the left side are colored red while particles on the right side are colored yellow. The particles have identical properties except their color. We then follow the mixing pattern as blade motion begins. Figure 4.5 shows some snapshots for the top horizontal view illustrating the mixing patterns obtained at different H/D ratios when the particles on the left and right sides of the impeller are colored differently prior to blade movement. Figure 4.5a shows snapshots of the mixing patterns obtained at the free surface of the particle bed. Enhanced mixing is obtained for the case of H/D = 0.17 compared to the H/D = 0.32 case. Little mixing is observed at the free surface for the H/D = 0.46 case. After 4.5 revolutions, the H/D = 0.17 system is well mixed and mixing is down to the particle-particle level, while unmixed regions still remain for the H/D = 0.32 and H/D = 0.46. However, enhanced mixing is observed for particles just above the span of the blades at high fill levels (Figure 4.5b). Mixing patterns in this region are similar for H/D = 0.32 and H/D = 0.46. This behavior is consistent with particle velocity and diffusivity analysis. Well-mixed zones are first observed by the cylinder wall, the area of highest granular temperature. Thus, the frictional characteristics of the wall facilitate mixing within the span of the blades by increasing the fluctuation velocities. The mixing kinetics of particles by the blades remain the highest for the case of H/D = 0.17 due to the higher particle diffusivities in the tangential and radial direction.

In addition to influencing flow kinematics, fill level affects the stresses that develop inside the mixer during flow. Figure 4.6 shows time averaged pressure profiles as a function of height at different H/D ratios. We find that for H/D = 0.17 and H/D = 0.32, the temporal averaged pressure inside the mixer can be approximated by the simple hydrostatic pressure relationship, $P = \rho_{bulk} g\left(h - H_{bed}\right)$. In this formula ρ_{bulk} is the overall time-averaged bulk density of the granular bed (determined from Figure 4.3), g is the acceleration due to gravity, h is the vertical position and H_{bed} is the total height of the particle bed. However, when the H/D ratio is above 0.46, two distinct regions develop in the pressure profile. The first region consists of a hydrostatic regime where the pressure is proportional to the height of the bed. The second region consists of a saturated regime where pressure is independent of bed height. The development of a saturated region in static systems is predicted by the classical Janssen equation [162]. However, in our system the height at which the saturated regime begins is the same for H/D = 0.46 and H/D = 0.75 and coincides with the height of the 3-D recirculation zone present in front of the blade. This is different from what the Janssen equation predicts. In static systems, the saturated regime begins at a height where the hydrostatic pressure is equal to a critical pressure value. At this height, normal stresses are transferred to the cylinder walls via stable contact chains and the walls begin to support the weight of the particle bed. The critical pressure value is a function of the particle-wall angle of internal friction and the cylinder's diameter [166, 167]. Thus, in static systems, the span of the saturated regime increases with total bed height. However, in our bladed mixer, the span of the saturated regime does not change when the total bed height is increased and it is independent of pressure. This suggests that the cylinder walls in the bladed mixers we have examined do not bear the load of the particle bed weight.

The saturated pressure regime observed for H/D > 0.46 develops as a result of two contributing factors; the decrease in bed dilation and the 45° angle of the blades. Since the expansion of the particle bed during flow is limited by the weight of the particles above the blades, the load associated with the weight of the particles within the span of the blade is transferred to the impeller. The pitched angle of the blades allows the impeller to support the weight of these particles leading to the almost constant pressure region. The linear relationship obtained between impeller torque and fill level (Figure 4.4) confirms that the particle bed weight is being carried by the impeller and not the cylinder walls. If the weight of the particle bed were supported by the cylinder wall at high H/D, the torque experienced by the impeller for the H/D = 0.46 case would the same as for the H/D = 0.75 case. The increase in impeller torque indicates that this is not case. Additionally, the Janssen equation predicts that much higher bed heights are needed for the saturated regime to be encountered for the frictional properties of our system. This behavior, while analogous to the Janssen effect in that a constant pressure is observed, is a result of the blade configuration and not the transfer of normal stress to the walls via stable contact chains.

Figure 4.7 shows the time-averaged shear stress to pressure ratio ${}^{\tau_{\theta r}}\!/\!{}_{P}$, also known as the bulk friction coefficient, for the particles within the span of the blade at different fill levels. As can be seen from Figure 4.7, the bulk friction coefficient is higher for the particle closes to the wall. As the averaged pressure remains constant in the radial direction [45], the increase in bulk friction is due to an increase in shear stress. Increased shear stress near the mixer walls has been observed experimentally by Watano et al. [122] in a high shear mixer. Figure 4.7 also shows that the ${}^{\tau_{\theta r}}\!/\!{}_{P}$ ratio decreases as H/D increases. The bulk friction is the highest for case where a hydrostatic pressure relationship is obtained within the span of the blades (H/D = 0.32). Bulk friction decreases for the cases where the pressure within the span of the blades is independent of height. The amount of momentum transferred in the shearing direction relative to the compression state of the system decreases when the impeller supports the weight of the particle bed. However, the decrease in the $\tau_{\theta r}/P$ ratio is ~ 22% between the values obtained for H/D = 0.32 and H/D = 0.75. This is a relatively small decrease when we consider that the average pressure increases by a factor of 3 between these two cases.

Figure 4.8 shows the temporal pressure and shear stress profiles that develop during flow at a radial position of r = 0.09 m. The pressure profile obtained for the H/D = 0.75 case is presented in Figure 4.8a as a function of height and number of revolutions. Periodic pressure fluctuations develop within the span of the blades with a main fluctuation frequency equal to the blade rotation. These pressure fluctuations exist in the saturated pressure regime region. Thus, the mean and amplitude of the pressure fluctuations are constant in this region. No fluctuations are observed for the region above the span of the blades. This is slightly different from the behavior observed for the bladed mixer flows for H/D = 0.17, where the pressure fluctuations are present throughout the span of the particle bed [45]. In Figure 4.8b, we compare the normalized pressure fluctuations obtained within the span of the blades at different H/D ratios at a radial position of r = 0.09 m. The normalized pressure is obtained by dividing the instantaneous pressure by the temporal averaged pressure at this position, $\langle P \rangle$. Figure 4.8b shows that the pressure fluctuates between $0.5\langle P \rangle$ and $1.5\langle P \rangle$ regardless of fill level. This suggests that the resulting pressure fluctuations within the span of the blades can be scaled according to fill level. If the average pressure is known, then the pressure fluctuations can be predicted. As shown in Figure 4.6, the average pressure can be determined from hydrostatics for low fill levels. For high fill levels, the average pressure within the span of the blades can be approximated by the hydrostatic pressure right above the blades.

Figure 4.8c shows the $\tau_{\theta r}$ fluctuations as a function of height and number of revolutions for H/D = 0.75. The shear stress profile shows a periodic behavior similar to the one observed for pressure. The mean and amplitude of the $\tau_{\theta r}$ fluctuations are relatively constant within the span of the blades. While $\tau_{\theta r}$ fluctuations are observed above the span of the blades, the mean and amplitude of these fluctuations decrease towards the top of the particle bed. Figure 4.8d present the normalized $\tau_{\theta r}$ fluctuations at different H/D ratios. Although the normalized $\tau_{\theta r}$ profiles show some scatter which was not observed in the pressure profiles, the maximum and minimum fluctuation values are similar for all the H/D ratios. $\tau_{\theta r}$ fluctuates between a minimum value of zero and a maximum value of $\sim 3\langle\tau_{\theta r}\rangle$. Since pressure profiles can be approximated by hydrostatics, our results suggest that if the value of the bulk friction coefficient inside the particle bed is known, then the $\tau_{\theta r}$ profiles could also be approximated from hydrostatics. Similar to pressure, the resulting $\tau_{\theta r}$ fluctuations can be scaled according to fill level. The trends reported in this section are applicable to monodisperse, cohesionless spheres in the quasi-static regime. A more comprehensive study is needed exploring the effect of polydispersity, particle shape and inter-particle cohesion on the results presented here.

4.3. Effect of Particle-Wall Friction

As mentioned earlier, the development of a 3-dimensional recirculation zone in front of the blades is a key flow feature in bladed mixers. As such, developing an understanding of the parameters leading to the formation of this flow pattern is critical for the design and operation of bladed mixers. In this section, the total height of the particle bed just covers the span of the blades (i.e., a fill level of H/D = 0.17). The influence of the particle-boundary frictional characteristics when they differ from those of the particle-particle interaction was examined. We find that the development of the 3D recirculation pattern is strongly dependent on the particle-cylinder wall sliding friction coefficient. Figure 4.9 shows the time-averaged velocity fields in front of the blade in the vertical plane for different combinations of particle-particle sliding friction (μ_s^{p-p}) and particle-cylinder wall sliding friction (μ_s^{p-w}). Heap and vortex formation occurs when wall friction is high (0.5) as can be seen from Figures 4.9a and 4.9b. Particles rise by the wall forming a heap as the impeller is moved. The formation of these heaps leads to the development of the recirculation zone. Lowering particle friction from 0.5 to 0.1 for high wall friction had a small effect on the velocity profile in front of the blade (Figure 4.9b). However, at high particle friction (0.5) and low wall friction (0.1) no heap or vortex formation occurs (Figure 4.9c). The absence of the heap leads to low radial and vertical velocities and the recirculation zone cannot develop. Particles move as a block solely in the tangential direction. Changing the particle-blade sliding friction coefficient had a negligible effect on the resulting velocity profiles.

We postulated in Chapter 3 that the formation of these heaps is due to the development of contact force chains when the granular bed is compressed in front of the blade. A force chain is a network of interparticle contacts in which force is transmitted along the contact path. The formation of stable contact chains has been demonstrated to be a function of wall friction in dynamic systems such as discharging silos [163]. At low particle-wall friction, stable contact force chains do not form, particles slide past the wall as they get pushed by the blade and cannot rise, and thus the heap and the recirculation zone can not develop. Slippage of the particles near the wall is decreased as wall friction is increased. For high wall friction values, we find that a particle layer 2 particle diameters in length forms at the wall which has an average velocity of 50 to 60% of the blades' tip speed. The reduced particle velocities are due to the stick-slip motion that occurs by the wall. This stick-slip behavior allows the formation of stable contact chains that lead to heap formation and consequently the 3D recirculation. However, at low wall friction values, the particles in contact with the wall flow at a velocity equal to the blade tip speed. A significant amount of friction at the cylinder wall appears to be necessary in bladed mixers to induce radial and axial flow.

Table 4.2 shows the particle diffusivity in the tangential direction ($D_{\theta\theta}$), the radial direction (D_{rr}) and the vertical direction (D_{yy}) at different values of wall friction and particle friction. Particle diffusivities are highest for the case of high wall friction and high particle friction. We have shown in Chapter 3 that frictional contacts in bladed mixers lead to an increase in fluctuating kinetic energy which is indicative of an increase in the random motion of the particles. When frictional collisions occur, the resulting particle velocities differ from that of the bulk flow. This effect increases with higher friction coefficients leading to higher particle diffusivities. When particle friction is decreased from 0.5 to 0.1 at high wall friction, diffusivity values decrease to about 40% of the observed values at $\mu_s^{p-p} = 0.5$. However, when wall friction is decreased to 0.1 at high particle friction, particle diffusivities drop by 2-3 orders of magnitude. These results show that the frictional cylinder walls act as the main source of fluctuating kinetic energy in the bladed mixer. Similar trends were observed for the cross diagonal terms of the diffusive stress tensor.

Table 4.2 also shows values for the Peclet number in the tangential, radial and vertical direction. The lowest Peclet numbers are obtained for the case of high wall friction and high particle friction. The diffusional contribution to particle transport is the highest for the most frictional system. Peclet numbers increase for the case of high wall friction and low particle friction. As can be seen from Figure 4.9b, the convective flow profile remains relatively unaffected by the decrease in particle friction while particle diffusivities are reduced. At high wall friction and low particle friction, the diffusive process all but shuts down. For this case, particles essentially move along the tangential direction in streamlines which the particles do not cross nor diffuse in and out of.

The effect of the convective and diffusive processes on mixing kinetics can be quantified by computing the relative standard deviation (RSD) of the red particle concentration for the entire system. As mentioned in Section 4.2, prior to blade movement the mixer is split in half along the axis of the impeller and the particles on the left side are colored yellow while the particles on the right are colored red. RSD curves for the different wall and particle friction cases are shown in Figure 4.10. Enhanced mixing is observed for high values of wall friction. No mixing occurs at μ_s^{p-p} = 0.5 and μ_s^{p-w} = 0.1. After roughly 3 revolutions the RSD curves for the high wall friction cases begin to level off indicating that the mixing process is down to the particle level. On the other hand, RSD values remain at 0.9 for the low wall friction case. This behavior is explained by the absence of the 3-dimensional recirculation zone at these frictional conditions. The presence of this vortex promotes convective mixing. However, in addition to convective mixing, diffusive mixing appears to play an important role in this system. While little difference is observed in the velocity patterns for the two cases of high wall friction (Figure 4.9a and Figure 4.9b), the RSD trends show a difference in mixing performance. The enhanced mixing kinetics observed for the higher particle friction case are explained by the higher particle diffusivities which promote diffusive mixing. While convective mixing is the dominant process in this system, diffusive mixing becomes important when the homogenization process is down to the particle-particle level.

Time-averaged values for the $\tau_{\theta r}$ shear stress are shown in Figure 4.11 for the cases of high wall friction. As can be seen from Figure 4.11a, $\tau_{\theta r}$ is the highest for the most frictional system (μ_s^{p-w} = μ_s^{p-p} = 0.5). Decreasing μ_s^{p-p} to 0.1 reduces $\tau_{\theta r}$ by roughly 50%. The values of $\tau_{\theta r}$ are highest near the cylinder wall in both cases and close to zero near the impeller shaft (Figure 4.11a). Increased shearing by the wall is a by-product of the stable force chains that form due to wall friction. $\tau_{\theta r}$ values for the case of high μ_s^{p-p} (0.5) and low μ_s^{p-w} (0.1) lie in between the two curves shown in Figure 4.11a. Shear stresses are strong functions of friction, since granular flows in bladed mixer occur in the quasi-static regime at low rotational speeds like the one used here. While momentum transfer is affected by the frictional characteristics of the cylinder wall, shear stresses inside the particle bed are most sensitive to changes in μ_s^{p-p}. Figure 4.11b shows the time averaged bulk friction coefficient, ${\tau_{\theta r}}/{P}$. We can see that the ${\tau_{\theta r}}/{P}$ ratio is a function of radial position and the system's frictional characteristics. This ratio is highest for the case of high wall friction and particle friction since pressure profiles are unaffected by changes in particle friction. The values obtained for ${\tau_{\theta r}}/{P}$ are much lower than the maximum sliding friction coefficient in the system (0.5). Bulk friction coefficients lower than the microscopic sliding friction coefficient have also been observed in quasi-static shear flows [19]. This implies that while momentum transfer is affected by friction at the microscopic level, the conditions at which the granular bed deforms are different from what is predicted by Coulomb's law for the particle-particle and particle-wall interactions.

4.4. Effect of Blade Position

In some industrial bladed mixer processes, such as in filter dryers, it is common to change the position of the blade when processing at high fill levels to enhance mixing and heat transfer. We now look at the effect of changing the position of the blades along the vertical axis at a fill level of H/D = 0.75. Simulations were performed for 3 different gap heights between the bottom of the blades and the bottom plate: a 10 mm gap (bottom blade position), a 110 mm gap (middle blade position) and 180 mm gap (top blade position). The apparent fill levels relative to the bottom of the blades are H/D = 0.22 for the top blade position, H/D = 0.44 for the middle and H/D = 0.75 for the bottom. Figures 4.12a through 4.12c show the velocity fields and granular temperature profiles obtained in front of the blade at the different blade position. For the top blade position, a strong recirculation zone develops where the blades are present (Figure 4.12a). Vertical and radial velocities are high and free surface of the bed deforms by forming heaps. High granular temperatures are achieved in this area. This behavior is analogous to what was obtained for the H/D = 0.17 case at the bottom blade position. However, the granular temperature obtained within the span of the blades is higher for the top blade position when compared to the H/D = 0.17 case. When the blades are in the top position, the particles just below the blades act as a rough bottom plate. In Section 4.3 we demonstrated that increasing wall friction leads to a higher fluctuating kinetic energy of the particles. We hypothesize that this “rough surface”, which is not present when the blades are in the bottom position, causes the increase in granular temperature. The region below the blades in Figure 4.12a is characterized by almost no particle movement and granular temperatures close to zero.

The size of the recirculation zone decreases when the blades are in the middle position (Figure 4.12b). The weight of the particle above the blades hinders heap formation decreasing the intensity of the recirculation zone. Granular temperature within the span of the blades is lower than for the top blade position case since the load from the particles on the top reduces bed dilation. These characteristics parallel the behavior observed for the H/D > 0.17 cases at the bottom blade position. The only difference between the H/D > 0.17 cases and the middle blade position case is the higher granular temperature within the span of the blade obtained in the latter. This is due to the “rough surface” formed by the particles just below the blade at the middle position. As in the top-blade-position case, the particles beneath the blades remain stationary as the blades rotate. When the blades are positioned at the bottom, the size of the recirculation zone decreases even further along with the granular temperature (Figure 4.12c). However, the granular temperature within the span of the blades in this case is the same as in the other H/D > 0.17 cases with the blades on the bottom. This confirms that the increase in granular temperature observed for the top and middle blade positions was due to the “rough surface” formed by the particles below the blades.

Figures 4.12d through 4.12f show side view snapshots after 5 revolutions demonstrating mixing patterns achieved for the different blade positions. Two zones developed in all the cases studied, a well-mixed zone and an unmixed region. For the top blade position, a well mixed region exists within the span of the blades which coincides with the region where the recirculation zone develops (Figure 4.12d). No mixing occurred below the blades. The majority of the particle bed remains unmixed when the blades are located at the top. When the blades are positioned in the middle, the size of the well-mixed zone increases as it includes the particles located within the span of the blades, as well as those above the blades (Figure 4.12e). No mixing occurs in the region below the blades. With this blade configuration, a little less than 50% of the particle bed remains unmixed. For the bottom blade position case (Figure 4.12f), the height of the well mixed zone is ~ 100 mm. No particle mixing occurs above this height, which represents roughly 50% of the particle bed. Based on these results, an efficient strategy to improve mixing in bladed mixers at high fill levels is to alternate between the bottom and the middle blade positions during processing. By doing this, the portions of the particle bed where particle velocities are low at these two blade positions get agitated and subsequently mixed. Placing the blades towards the top of the particle bed is very inefficient in terms of mixing, since a large portion of the particle bed remains unmixed.

The time-averaged pressure and shear stress profiles are presented in Figure 4.13 for the different blade positions for a fill level of H/D = 0.75. As was seen earlier, for the bottom blade position, the pressure within the span of the blades is independent of height, while a hydrostatic region exists above the blade (Figure 4.13a). A similar behavior is observed for the middle blade position. The pressure above and below the span of the blades follows a hydrostatic relationship while it is height independent where the blades are present (Figure 4.13b). This is not a surprising behavior, since the height of the particle bed above the blades is equivalent to an H/D = 0.44 case for a bottom blade position. The linear pressure profile observed below the span of the blades supports the conclusion that the weight of the particle bed in the saturated regime is supported by the impeller and not the cylinder wall. Two hydrostatic regions develop for the top blade position; one region below the blades with an average bulk density of ~ 1000 kg/m^3 and a second within the span of the blades with a bulk density of ~ 800 kg/m^3 (Figure 4.13c).

The $\tau_{\theta r}$ profile for the bottom blade position case is shown in Figure 4.13d. Shear stress is highest in the region spanning the blades. $\tau_{\theta r}$ is also fairly constant in this region. Above the blades shear stress is reduced and two regions can be distinguished, one region with a constant shear stress and another with a more or less linear relationship. The constant shear stress region develops as stresses get transferred via contact chains from the region within the blades. The linear region begins at the height where the contact chains end. The shear stress in this region follows the pressure trend. For the middle blade position, $\tau_{\theta r}$ increases linearly within the span of the blades and reaches a maximum at the top of the blades (Figure 4.13e). Below the blades, a fairly constant $\tau_{\theta r}$ region develops due to the transfer of stress via contact chains that originate within the span of the blades. Above the span of the blades, $\tau_{\theta r}$ decreases in a similar way to what is obtained for the bottom blade position in this region. The lowest values of $\tau_{\theta r}$ are achieved with the top blade configuration (Figure 4.13f). Here, shear stress is constant within the span of the blades and decreases linearly above the blades. Below the blades, a constant shear stress region develops as observed for the middle blade position. A third region arises towards the bottom plate. In this region, the shear stress exhibits large fluctuations with points of zero shear stress observed. The contact chains that originate within the span of the blades are not long enough to reach the region near the bottom plate. The randomness of the shear stress in this region is consistent with the stress profiles found in static piles, where stresses follow a random path depending on where particle contacts occur [166].

4.5. Effect of D/d Ratio

The ratio of mixer diameter to particle diameter (D/d) has been shown to be an important parameter in other granular processes, and it is one of the parameters that changes during scale-up. In this section, we study the effect of varying mixer diameter, while keeping a constant particle diameter. We compare the granular behavior observed in bladed mixers at D/d ratios of 31.5, 63.0 and 94.5. For the parameters used in this work, the range of D/d ratios studied includes mixer sizes ranging from 10 L to 300 L. The mixer dimensions for the D/d = 31.5 case are the ones listed in Table 2.1. The dimensions of the D/d = 63.0 system are a 2x linear scale-up of the values shown in Table 2.1. The D/d = 94.5 dimensions are 3 times the Table 2.1 values. The only dimension that is kept constant for all mixer sizes is H_2, the gap between the bottom plate and the bottom of the blades. The rotational speed of the blades was set at 20 RPM for all the mixer sizes. The fill level was set to H/D = 0.17 for all the D/d cases studied. In order to compare the results obtained at the different system sizes and to allow for plotting in the same axis, we normalized all particle velocities relative to the tip speed of the blades, V_{tip}. Particle positions are normalized by the total bed height (H) in the vertical direction and by the mixer radius (R) in the radial direction.

Normalized instantaneous velocity profiles at radial position r/R = 0.57 and height y/H = 0.6 are shown in Figure 4.14 for the different D/d ratios. A cubic control volume with dimensions of 6*d* x 6*d* x 6*d* was created at these coordinates. The velocity components were calculated by averaging over the control volume at a particular time-step. Since the control volume size was kept constant for all D/d ratios, the velocity values shown in Figure 4.14 were obtained by averaging over the same number of particles. Tangential velocity fluctuations are observed for all the D/d ratios (Figures 4.14a, 4.14d and 4.14g). These fluctuations develop since the particles in front of the blade have a higher tangential velocity than the particles behind the blades. The main frequency of the fluctuations is equal to the rotation frequency of the blades for each D/d case. While the fluctuation period is the same for all the D/d ratios, a difference is observed in the amplitude of the fluctuations. The amplitude of the tangential velocity fluctuation is the lowest for the D/d = 31.5 case, while higher amplitudes are obtained for the D/d = 63.0 and D/d = 94.5 cases. Little difference is seen between the tangential velocity curve for D/d = 63.0 and that for D/d = 94.5. The higher fluctuation amplitudes suggest that particle movement in the tangential direction is less uniform for D/d > 31.5.

Radial and vertical velocity profiles are shown in Figures 4.14b through 4.14i for each of the D/d cases. Both the radial and vertical velocity components fluctuate around zero and are much lower than the corresponding tangential velocity for all the D/d ratios. Periodic fluctuations of higher amplitudes are obtained at D/d = 63.0 and D/d = 94.5 for the radial (Figures 4.14e & 4.14h) and the vertical (Figures 15f and 15i) velocities. As with the tangential velocity, the curves obtained at D/d = 63.0 are very similar to the ones obtained at D/d = 94.5. The radial and vertical velocities at D/d = 31.5 show less of a periodic behavior and the fluctuation amplitude is much lower compared to the higher D/d ratios. The differences in radial and vertical velocities observed at D/d = 31.5 can be explained by the height of the heaps that develop in front of the blades. While heaps form at every D/d value, the total height of the heaps increases at the higher D/d ratios. The higher heap heights lead to an increase in the potential energy of the particles. This potential energy is then transferred into kinetic energy in the vertical and radial directions as particles flow in and out of the heaps at the larger D/d ratios.

Figure 4.15 depicts time-averaged radial and vertical velocity fields for the particles in front of the blades in the vertical plane at the different D/d values. The magnitude of the tangential velocity is represented by the color of the vectors. The flow pattern obtained in front of the blade is independent of the D/d ratio as the recirculation zone is present in all the D/d values studied. However, the recirculation zone is most prominent for D/d = 63.0 and D/d = 94.5 (Figures 4.15a and 4.15b). Lower radial and vertical velocities are observed near the bottom plate, cylinder walls and at the top of the heap for the D/d = 31.5 case (Figure 4.15c). The lower velocities near the boundaries are due to the effect of wall friction, which is stronger at the low D/d ratio. Boundary friction effects have been previously shown to be scale-dependent on dense granular flows [168]. The lower velocities at the top of the heap are a result of the reduced potential energy at D/d = 31.5, as previously explained. These results suggest that, if the system size is big enough so that the effects of wall friction are minimized, the convective particle motion is independent of system size and can be scaled by the rotational speed of the blades.

Particle diffusion has been previously shown to be dependent on system geometry and size in dense granular flows [169]. Table 4.3 presents the normalized diffusion coefficients in the tangential, radial and vertical direction obtained for the different D/d ratios. Particle diffusivities were normalized by the tip speed of the blades and the mixer diameter, i.e. $D_{\theta\theta}^{*} = D_{\theta\theta} / DV_{tip}$. Lower normalized particle diffusivities are obtained for the D/d = 31.5 in the tangential, radial and vertical direction, while higher values were observed at D/d = 63.0 and D/d = 94.5. The normalized diffusion coefficients values change little for D/d > 31.5, similar to the behavior observed for the convective particle motion. Therefore, above a certain system size (D/d ≥ 63.0 in our case), particle diffusivity scales linearly with mixer diameter and blade speed. Peclet numbers for the different D/d ratios are also shown in Table 4.3. All the Peclet numbers obtained are much higher than unity indicating that convection is the main mechanism for particle motion regardless of system size. While convection dominates the transport process, the diffusive contributions increase for the D/d = 63.0 and D/d = 94.5 cases as Peclet numbers decrease roughly by ½ from those observed at D/d = 31.5. The increase in particle diffusivity can be explained by the increase in velocity fluctuations observed at the higher D/d values.

Figure 4.16 shows the effect of system size on mixing. As a result of the enhanced convective and diffusive particle transport, faster mixing kinetics are observed for the D/d > 31.5 cases. The degree of mixing is very similar in all 3 system sizes during the early stages of the mixing process. However, the RSD curve for the D/d = 31.5 case (Figure 4.16a) begins to level off after 4 revolutions, while the RSD values for the other cases continue to decrease. As can be seen from the top view snapshots shown in Figure 4.16b, the mixing process after 5 revolutions is down to the particle level for D/d = 63.0 and D/d = 94.5 while regions of unmixed particles still remain at D/d = 31.5. Little differences is observed between the mixing kinetics obtained at D/d = 63.0 and D/d = 94.5. Since a constant blade rotational speed was used for all mixer sizes, the tip speed of the blades increases with D/d in our simulations. However, when the tip speed for the D/d = 63.0 case was set to that of the D/d = 31.5 and D/d = 94.0 cases, no difference in mixing was observed. These results imply that in the quasi-static regime, above a certain system size, the rotational speed of the blades provides the time scale for which the mixing process takes place. Further work is needed to investigate the effect of blade rotational speed on mixing kinetics when flow regime transition occurs.

Bed dilation is also affect by the D/d ratio. Figure 4.17 shows the time-averaged solids fraction ρ/ρ_p, where ρ is the bed bulk density during flow, and ρ_p is the density of the particles. The average solids fraction for the D/d = 31.5 case is roughly 40%, while at D/d > 31.5 a solids fraction of about 50% is observed. We hypothesize that the increase in bed dilation observed at the lower D/d ratio is a result of the frictional contact chains that develop by the cylinder wall. As the blades rotate, the contact chains force material to move upwards by the cylinder wall causing bed dilation. The maximum stable length of these contact chains is characterized by a certain number of particle diameters. The maximum number of particle diameters in a stable contact chain is a function of the system's frictional characteristics, but is independent of mixer size. As a result, the length of stable contact chains relative to the mixer diameter is larger at D/d = 31.5 causing the higher bed dilation.

We now look at the effect of system size on the stress profiles that develop inside the bladed mixer. We find that the time-averaged stresses increase as D/d is increased with the highest values obtained for the D/d = 94.5 case. The main reason for the increase in stresses is the increase in total weight of the particle bed at the higher D/d ratios (as the H/D ratio was kept constant in these simulations). Thus, we find that the normal and shear stress values obtained at each D/d ratio can be scaled by the quantity $\rho_p gH$. Figure 4.18 shows the scaled pressure ($P^* = P/\rho_p gH$) and shear stress ($\tau^*_{\theta r} = \tau_{\theta r}/\rho_p gH$) profiles as well as the bulk friction coefficient for the different D/d values. The pressure profiles obtained for all the D/d cases increase linearly with bed height (Figure 4.18a). The scaled pressure profile remains unchanged at D/d = 63.0 and D/d = 94.5, while a lower scaled pressure is obtained for the D/d = 31.5 case. The lower pressure is as a result of the increased bed dilation at this D/d ratio. It is interesting to note that the value of the scaled pressure at the bottom plate coincides with the average solids fraction at each D/d value. A similar behavior is observed for the scaled shear stress, $\tau^*_{\theta r}$ (Figure 4.18b). While it is reasonable to expect that pressure would scale with the system's mass, we find that shear stress also scales with this quantity. Identical scaled shear stress values are obtained at the higher D/d ratios while the D/d = 31.5 case is characterized by a lower scaled shear stress. This suggests that a larger amount of momentum is being transferred to the particle bed as a result of blade movement at the higher system sizes. The bulk friction coefficients obtained show the same trend (Figure 4.18c) with higher values at D/d > 31.5. Note that even at the high D/d ratios, the resulting bulk friction coefficient is lower than the value of the microscopic sliding friction coefficient (μ_s = 0.5 in these simulations).

Our analysis suggest that, while different flow kinematics and stress profiles were obtained at the lower D/d ratio, scaling relationships exists for systems with D/d ≥ 63.0. In particular, our results suggest that there is a critical D/d system size, and that simple scaling relationships exist above this critical system size. Above the critical D/d system size, the following scaling relationships were observed. Mean velocity profiles as well as velocity fluctuation amplitudes scale linearly with the blades' tip speed. Flow patterns are found to be independent of system size. Particle diffusivities scale linearly with system size and the blades' tip speed. Mixing kinetics are invariant of system size with the rotational speed dictating the mixing time scale. Bed dilation remains a constant as the system size is increased. The resulting pressure and shear stress profiles scale linearly with the total weight of the particle bed. While further work is needed to verify that the obtained scaling relationships are still applicable at higher D/d ratios, the results presented here suggest that granular flows in bladed mixer could be scaled according to system size and operating conditions. The scaling relationships shown here are applicable to monodisperse, cohesionless spheres in the quasi-static regime. The effect of granular regime transition on mixing and stress generation is presented in Chapter 4.

4.6. Conclusions from Effect of Mixer Properties, Fill Level and Mixer Scale

The discrete element method was used to analyze the effect of mixer properties and fill level on the observed granular behavior in bladed mixers. Fill level was demonstrated to influence granular flows in the bladed mixer. Higher convective and diffusive mixing was observed at the lower fill levels with the best mixing performance obtained when the height of the particle bed just covers the top of the blades. While the mixing kinetics of the entire system were affected by fill level, it was found that bed dilation, and convective and diffusive mixing within the span of the blades remains invariant of fill level above a certain fill level (H/D > 0.32 in our simulations). Impeller torque was found to increase linearly with fill level. Time averaged pressure profiles were found to vary linearly with height at low fill levels and are approximated by a simple hydrostatic relationship. However, at high fill levels, two regimes are obtained in the pressure profile. A hydrostatic region exists above the blades where pressure increases linearly with height, while a saturated region was obtained within the span of the blades where pressure is independent of blade height. The development of the saturated region was attributed to the 45° angle of the blades which causes the impeller to support the weight of the particles within the span of the blades. The saturated region is characterized by pressure and shear stress fluctuations with frequencies equal to the rotational speed of the blades. The amplitude of these fluctuations relative to the mean was found to be independent of fill level.

The frictional characteristics of the cylinder walls were shown to significantly affect flow patterns, particle diffusivities, mixing kinetics and shear stresses inside the mixer. At low particle-wall friction coefficients, secondary flow structures found in front of the blades at high frictional conditions do not develop, thus reducing convective mixing. High particle-wall friction leads to an increase in particle diffusivity and diffusive mixing. Shear stresses inside the particle bed decrease with a decrease in cylinder wall friction. Blade position in the vertical direction was shown to affect flow patterns and granular temperature and shear stresses within the particle bed.

The effect of scaling up the mixer while keeping constant the particle diameter and the fill level was also studied. The system scale was quantified by taking the ratio of the mixer diameter to the particle diameter, D/d. Lower convective and diffusive mixing was observed for the lowest D/d ratio studied (D/d = 31.5), while enhanced mixing kinetics were obtained for the larger systems (D/d = 63.0 & 94.5). Bed dilation was highest for the D/d = 31.5 system, while a higher solids fraction was observed as mixer size was scaled-up. Normal and shear stress profiles were found to increase with mixer size. While different results were obtained at D/d = 31.5, the resulting granular behavior at D/d $\geq$ 63.0 was found to scale according to system size. The difference in behavior observed at D/d = 31.5 was attributed to the effect of wall friction which is most prominent for smaller systems. Above a critical system size, the effect of wall friction is minimized and granular behavior could be predicted based on simple scaling relationships. Particle velocities and diffusivities vary linearly with the tip speed of the blades. The time averaged solids fraction remains a constant. Additionally, the rotational speed of the blades provides the time scale in which the mixing process occurs. Normal and shear stresses were found to scale linearly with the total mass of the system and could be scaled by the quantity $\rho_p gH$.

Despite the complex behavior observed in bladed mixers, our results suggest that granular flows in these types of mixers can be scaled according to system size when the size of the mixer relative to the particle size is large enough to overcome wall effects. The simple scaling relationships obtained from our analysis are summarized in Figure 4.19 for quasi-static flows with a middle blade position. This configuration was chosen as it captures the important flow features at the different fill levels. Many questions remain unanswered regarding the effect of the parameters studied here in more complex granular systems such as polydisperse mixtures, non-spherical particle beds and cohesive systems. Further work is needed to verify whether the trends reported here are applicable to these systems.

4.7. Figures for Chapter 4

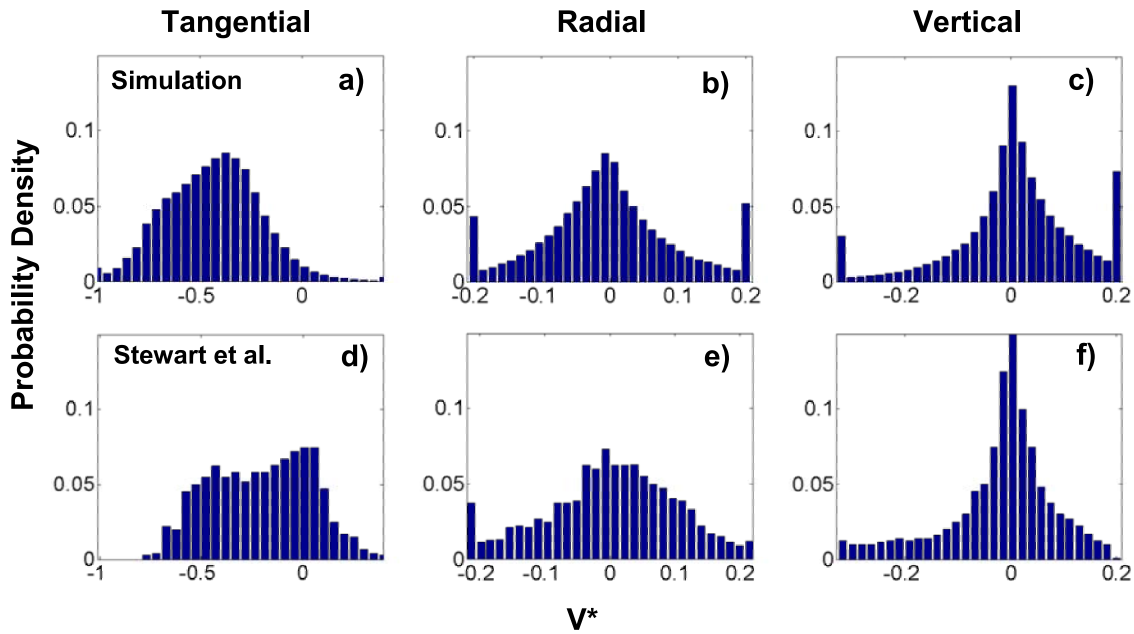

Figure 4.1. Normalized velocity frequency distributions obtained from simulations vs. experimental results from Stewart et al. [105]. a)–c) Simulation frequency distributions for the normalized tangential, radial and vertical velocity components, d)-f) PEPT experimental frequency distributions for the normalized tangential, radial and vertical velocity components. The tangential velocity values shown here are relative to the tip speed of the blades.

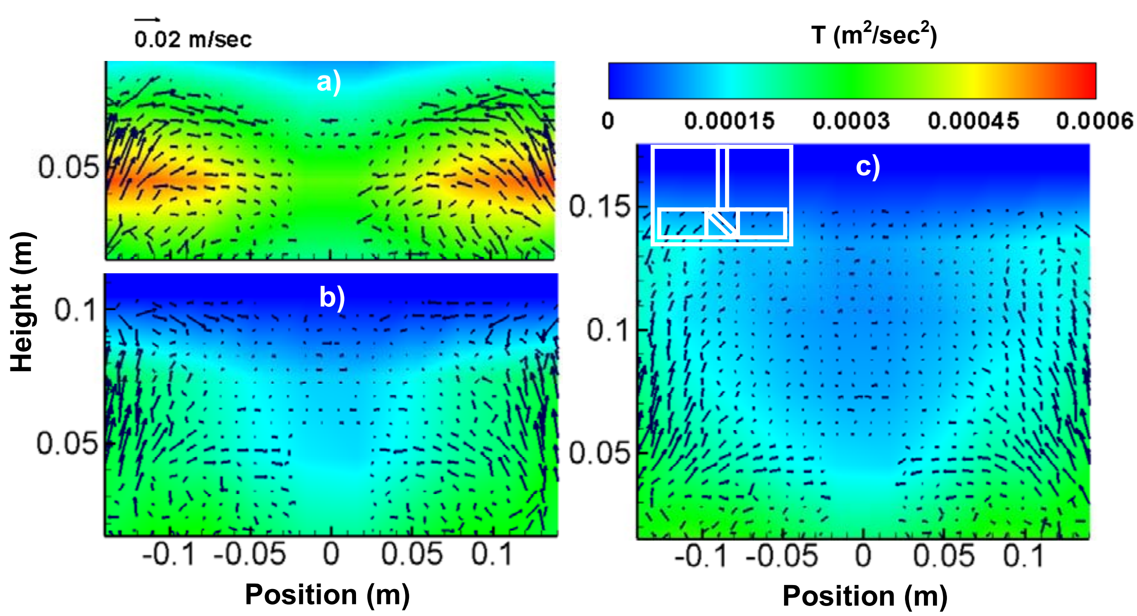

Figure 4.2. Velocity field in front of blade and granular temperature. a) H/D = 0.17, b) H/D = 0.32 and c) H/D = 0.46.

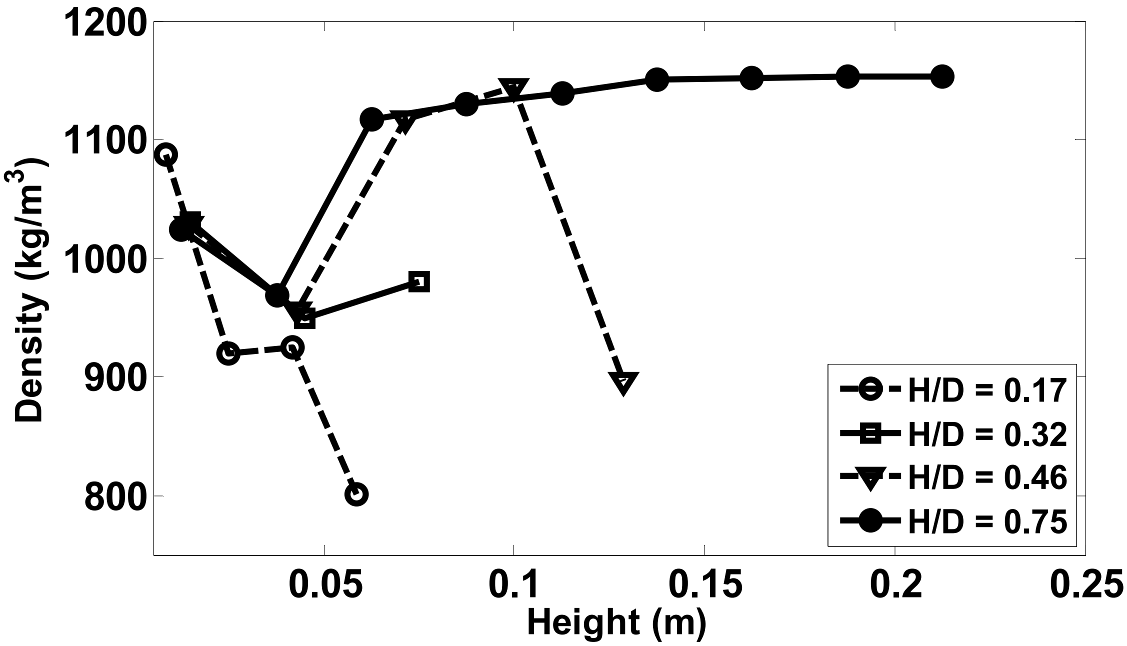

Figure 4.3. Effect of H/D on bulk density.

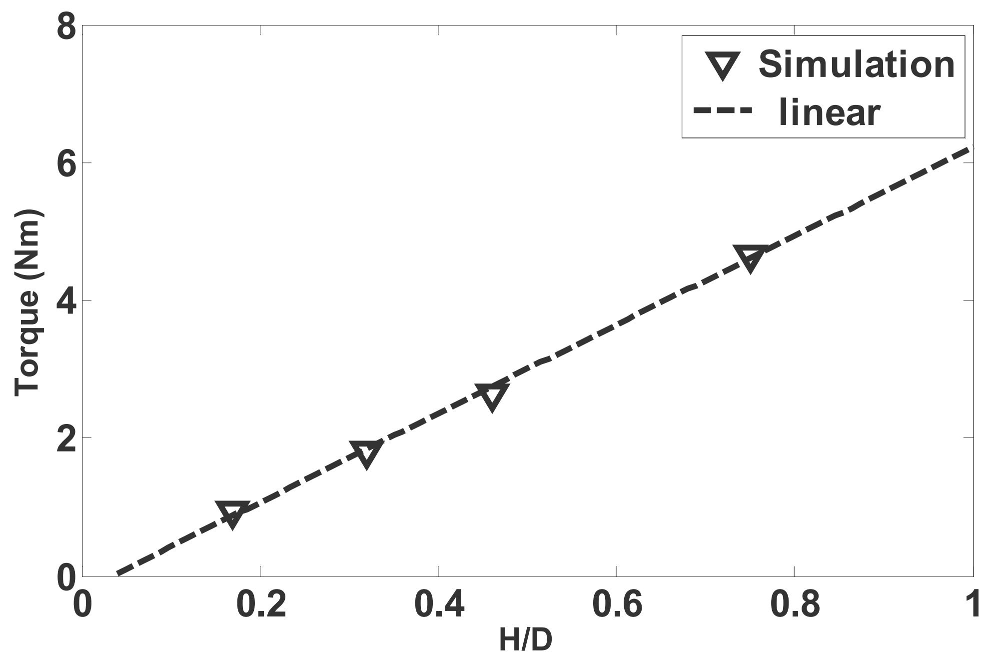

Figure 4.4. Effect of H/D on impeller torque.

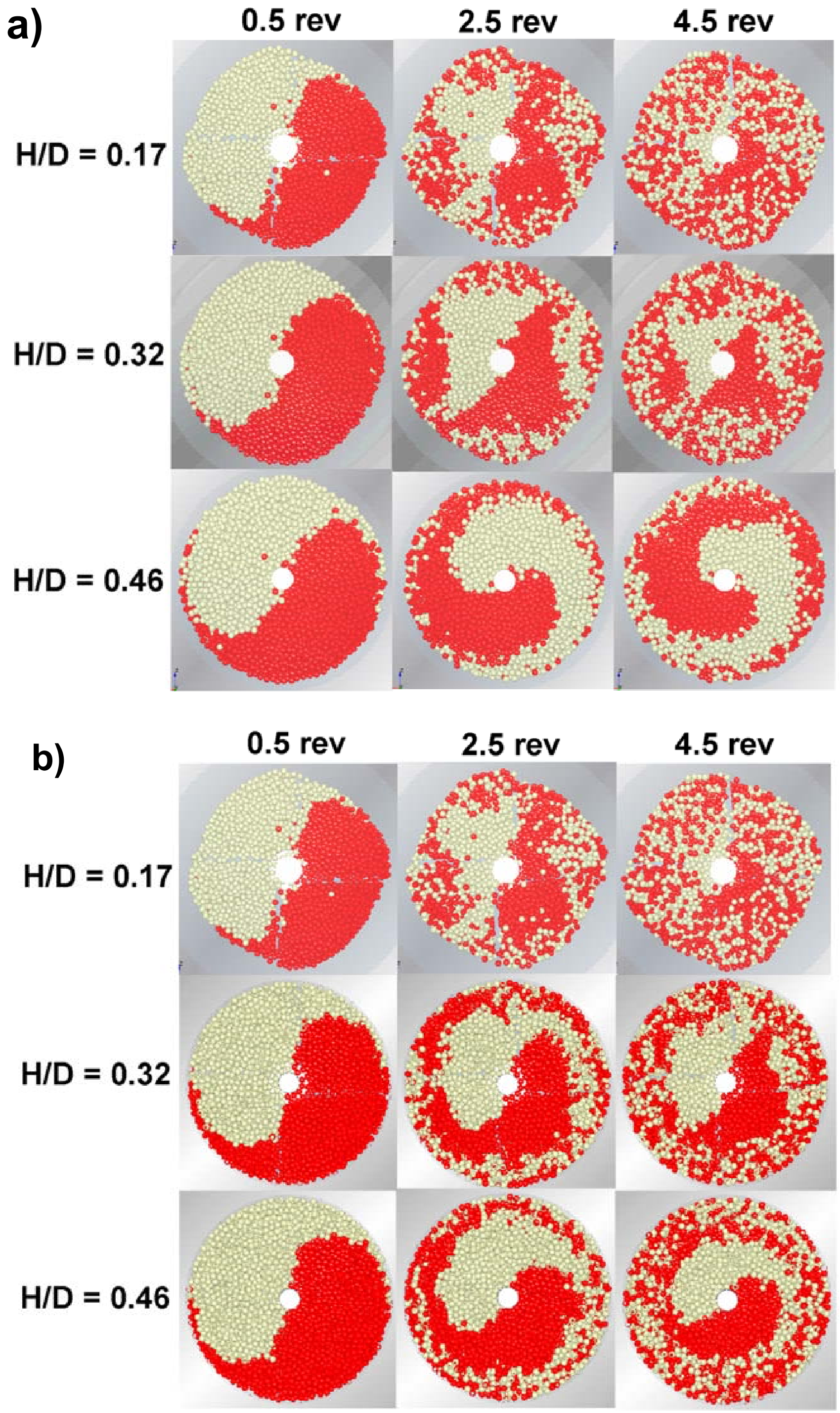

Figure 4.5. Effect of H/D on mixing. a) Snapshot of particles at the free surface and b) Snapshots of particles above the span of the blades.

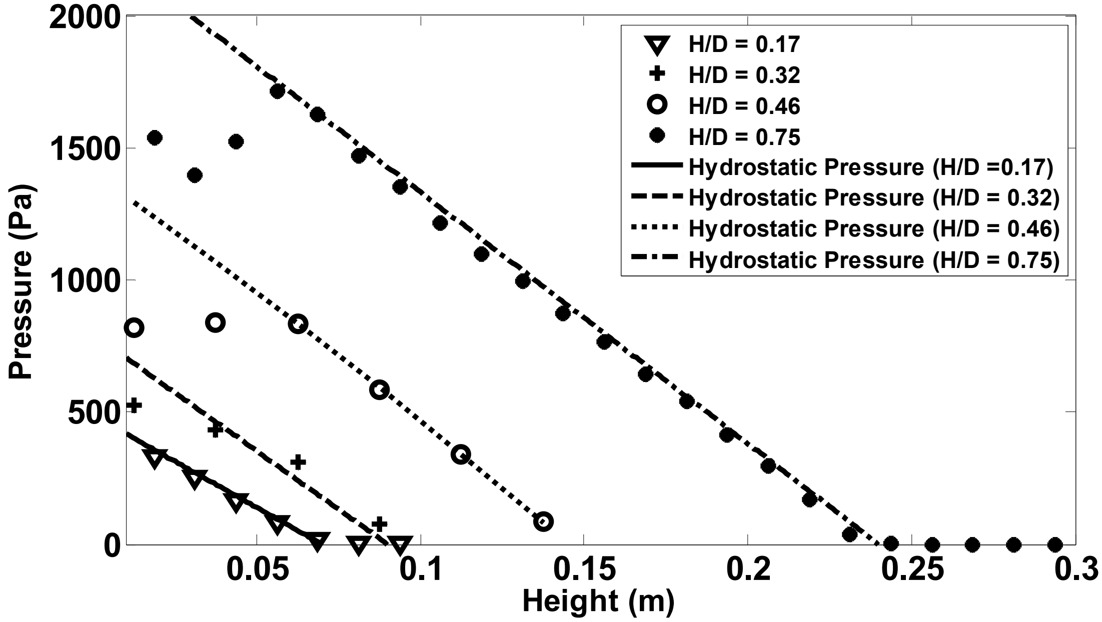

Figure 4.6. Time averaged pressure for particles within the mixer vs. height.

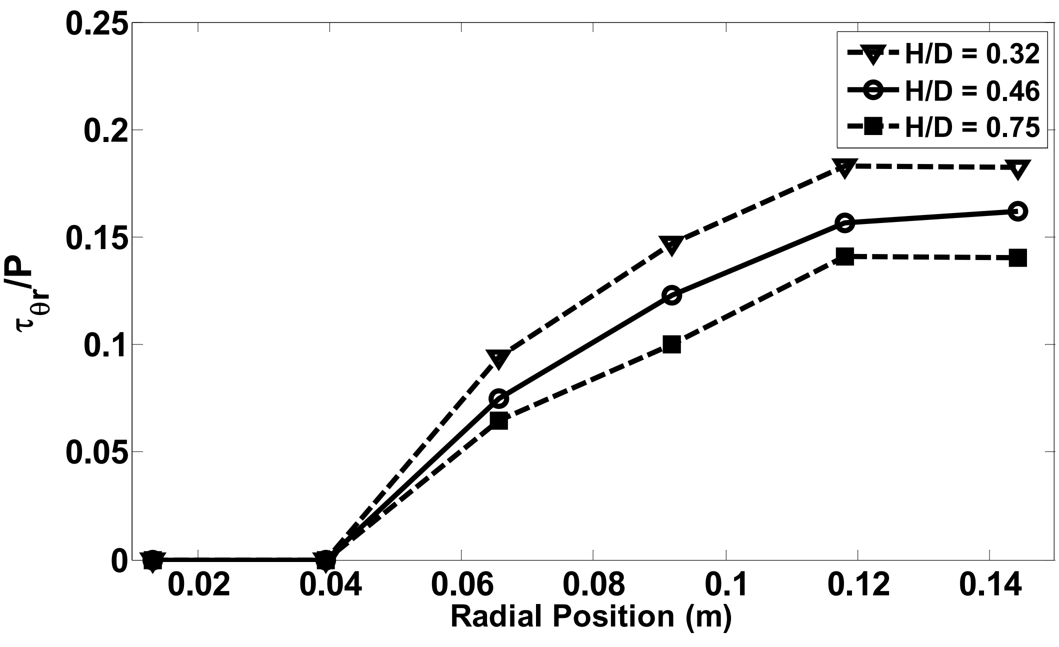

Figure 4.7. Time averaged bulk friction for particles within span of blade vs. height.

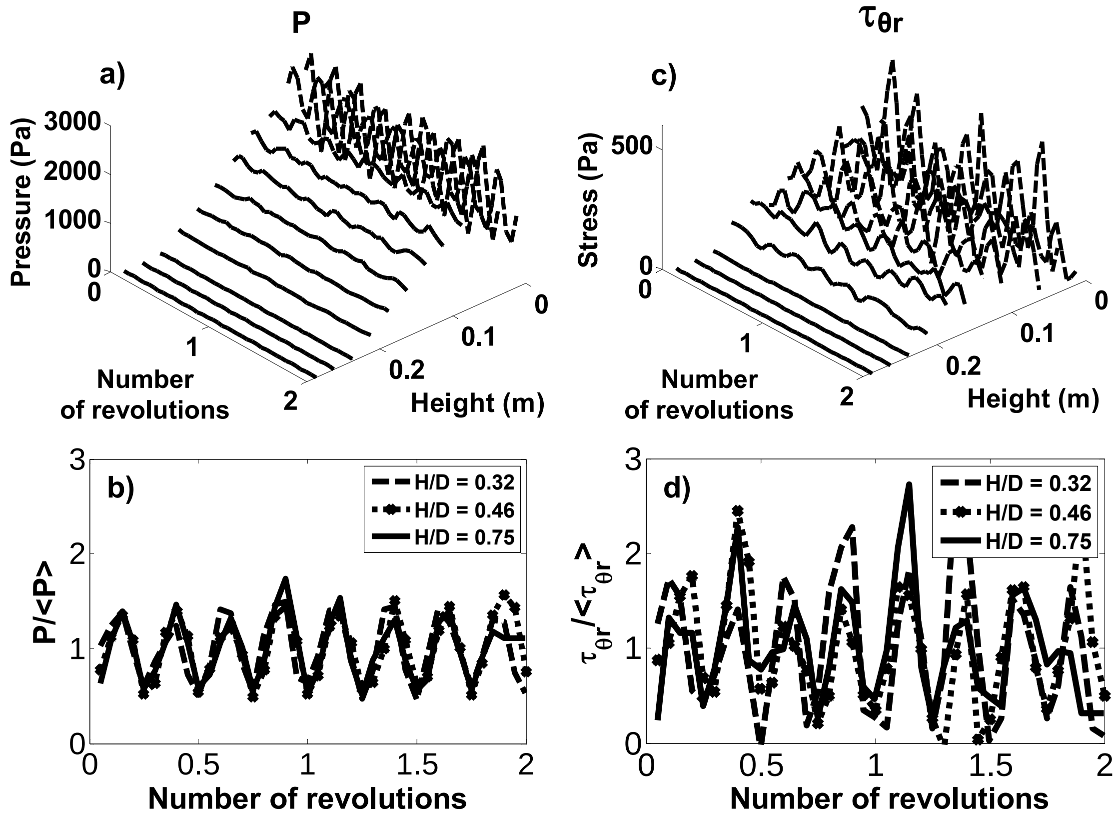

Figure 4.8. Pressure and shear stress fluctuations at r = 0.09 m. a) Pressure fluctuations as a function of height and number of revolutions for H/D = 0.75, b) Normalized pressure fluctuations for particles within span of blade, c) $\tau_{\theta r}$ fluctuations as a function of height and number of revolutions for H/D = 0.75 and d) Normalized $\tau_{\theta r}$ fluctuation for particles within span of blade.

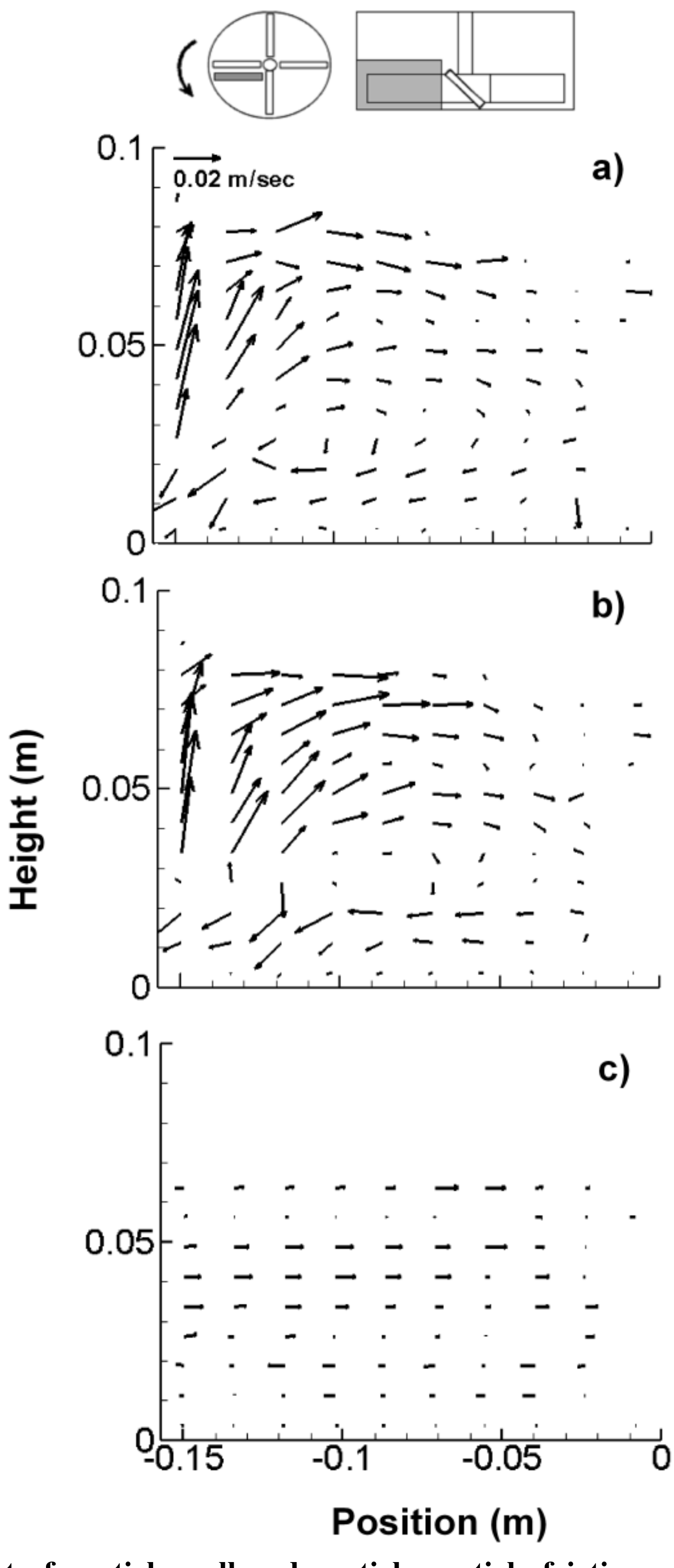

Figure 4.9. Effect of particle-wall and particle-particle friction on velocity field in front of the blades. a) $\mu_s^{p-p} = \mu_s^{p-w} = 0.5$, b) $\mu_s^{p-p} = 0.1, \mu_s^{p-w} = 0.5$ and c) $\mu_s^{p-p} = 0.5, \mu_s^{p-w} = 0.1$.

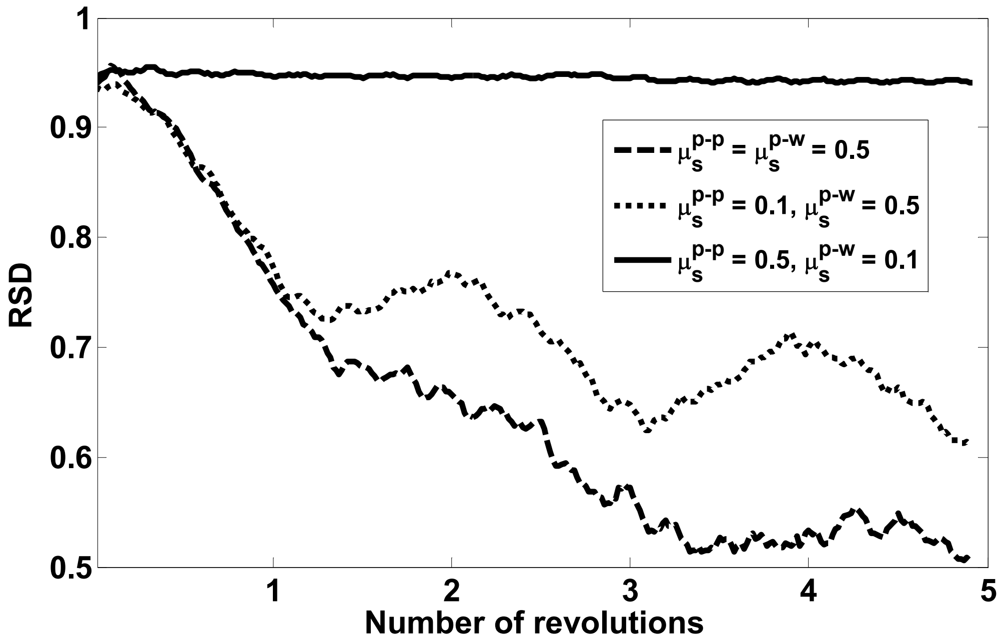

Figure 4.10. Effect of particle-wall and particle-particle friction on mixing. Relative standard deviation of red particle concentrations vs. number of revolutions.

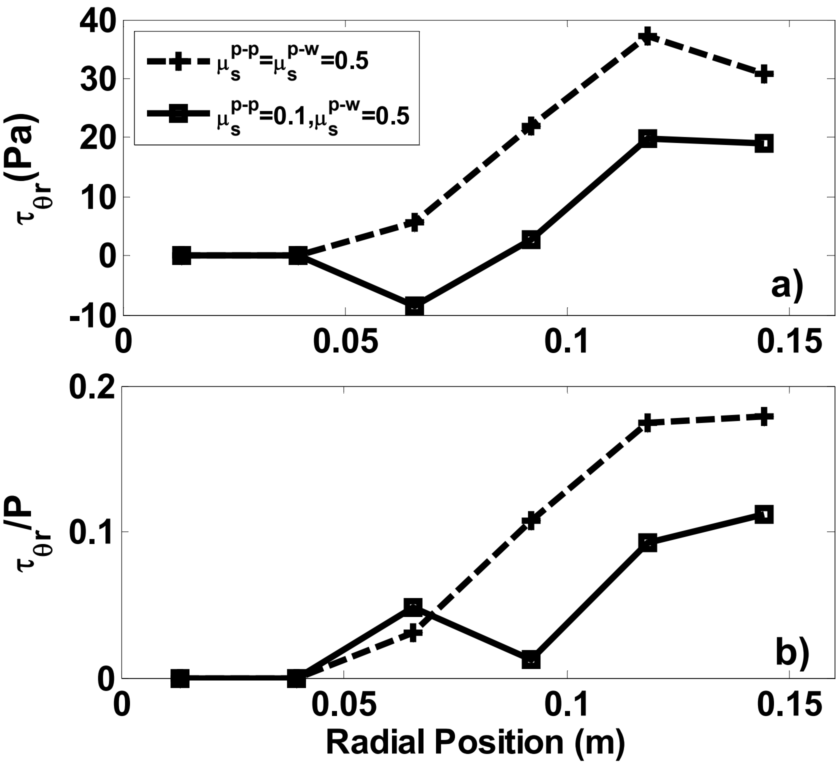

Figure 4.11. Effect of particle-wall and particle-particle friction on the time averaged shear stress and bulk friction coefficient. a) $\tau_{\theta r}$ and b) $\tau_{\theta r}/P$.

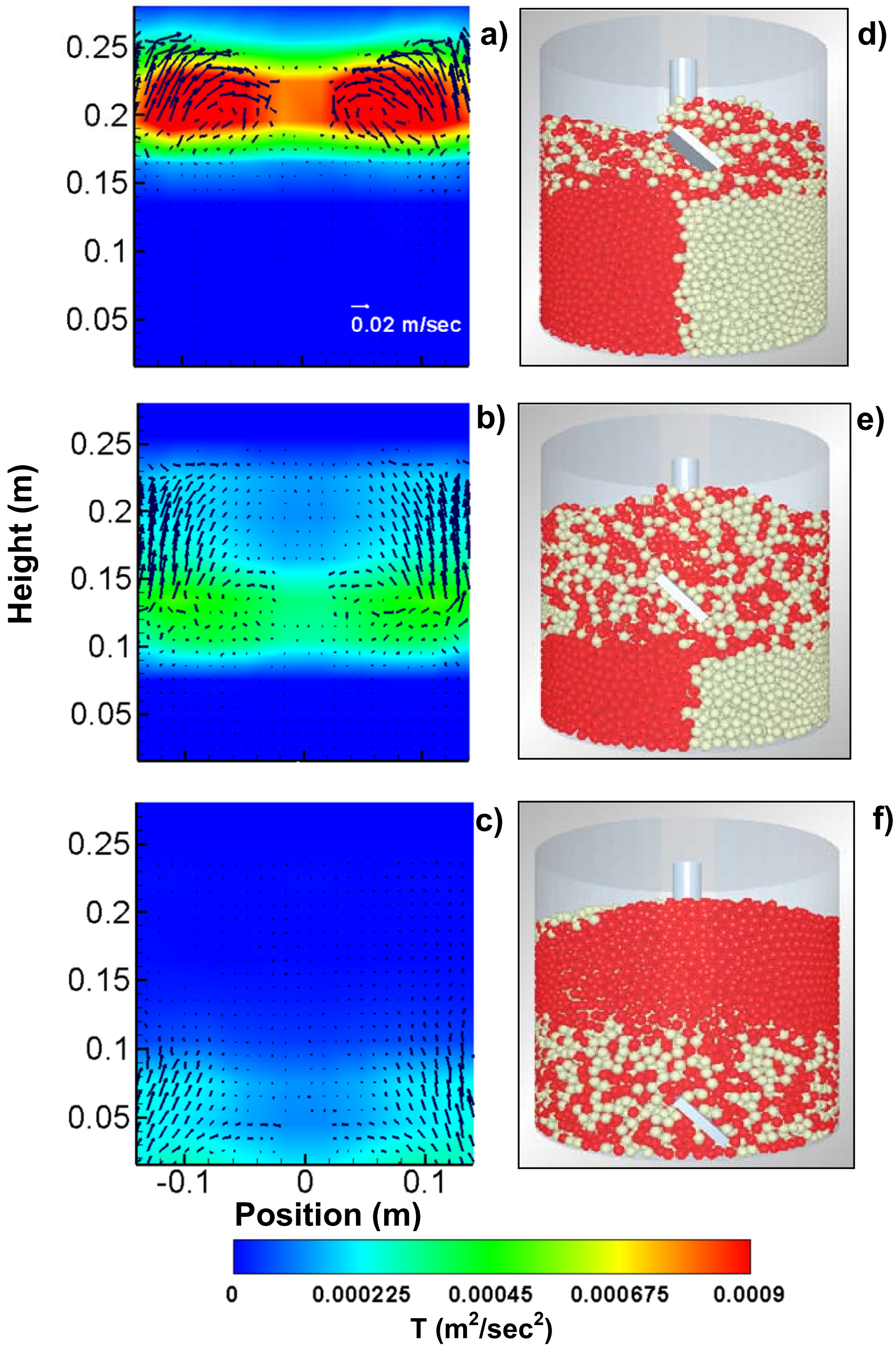

Figure 4.12. Effect of blade position on velocity fields, granular temperature and mixing patterns at H/D = 0.75. a)-c) Velocity fields in front of blade and granular temperature for different blade positions, d)-f) Side view snapshot of mixing after 5 revolutions.

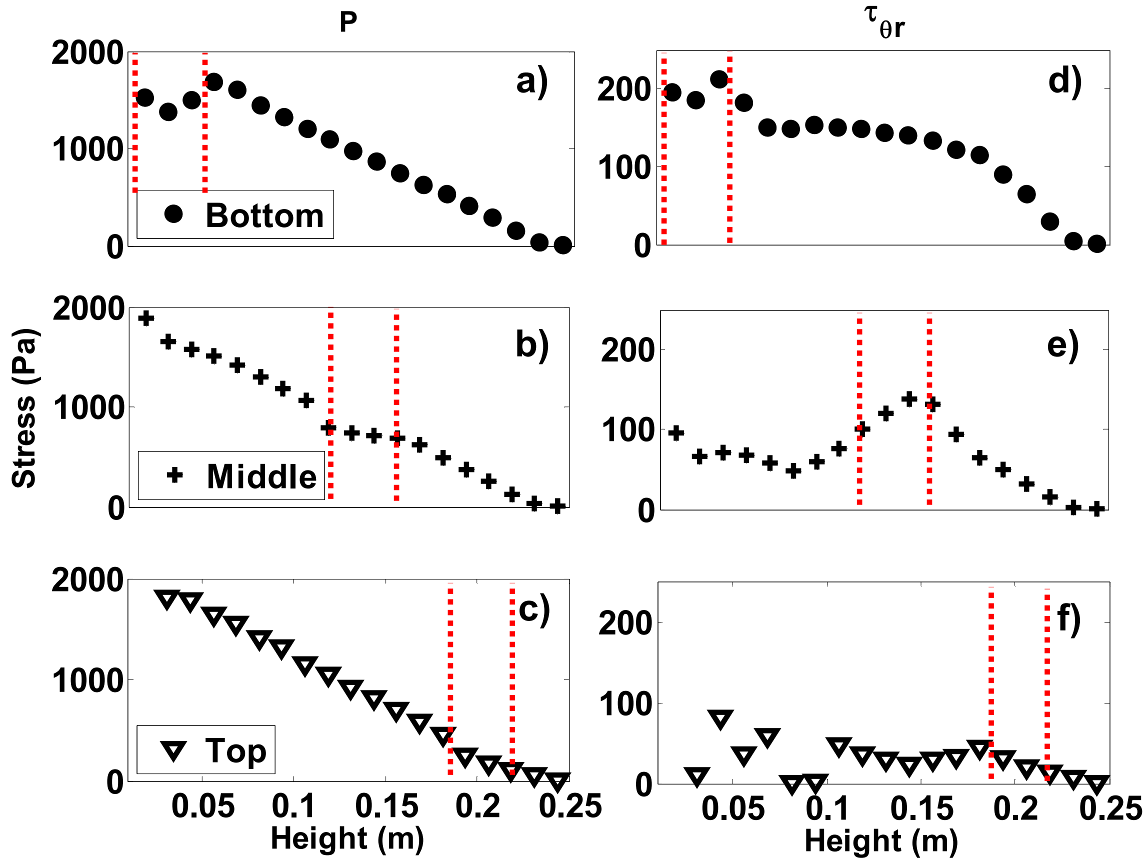

Figure 4.13. Time averaged pressure and shear stress profiles for different blade positions for H/D = 0.75. a)-c) pressure profiles as a function mixer height, d)-f) $\tau_{\theta r}$ profiles as a function of mixer height. The position of the blades is given by the dashed lines in each graph.

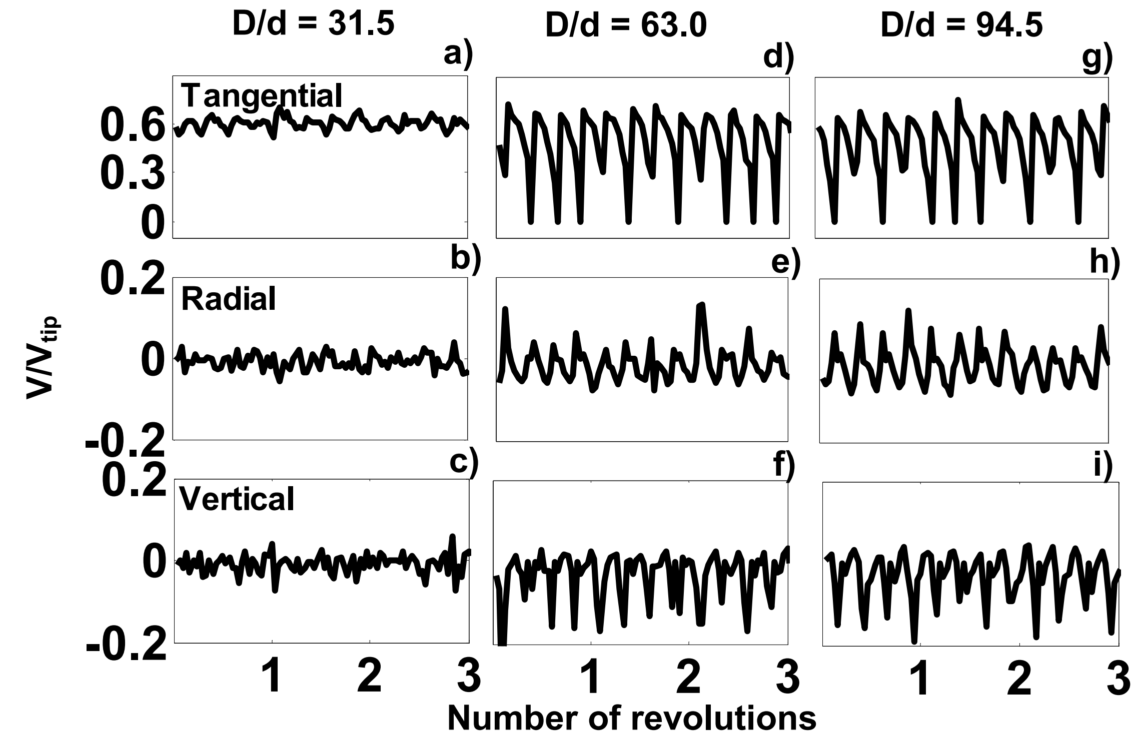

Figure 4.14. Velocity profiles at r/R = 0.57, y/H = 0.60. a)-c) for D/d = 31.5, d)-f) for D/d = 63.0 and g)-i) for D/d = 94.5.

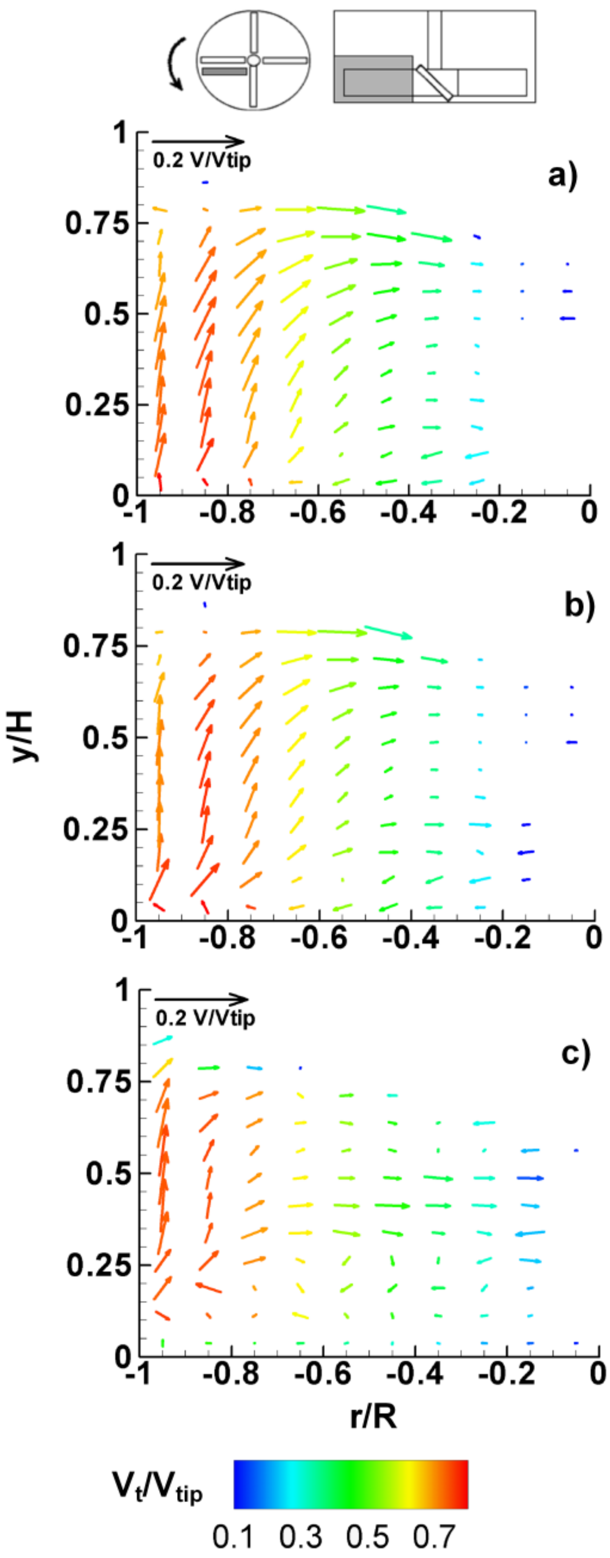

Figure 4.15. Velocity field in front of blade for different D/d. a) D/d = 94.5, b) D/d = 63.0 and c) D/d = 31.5.

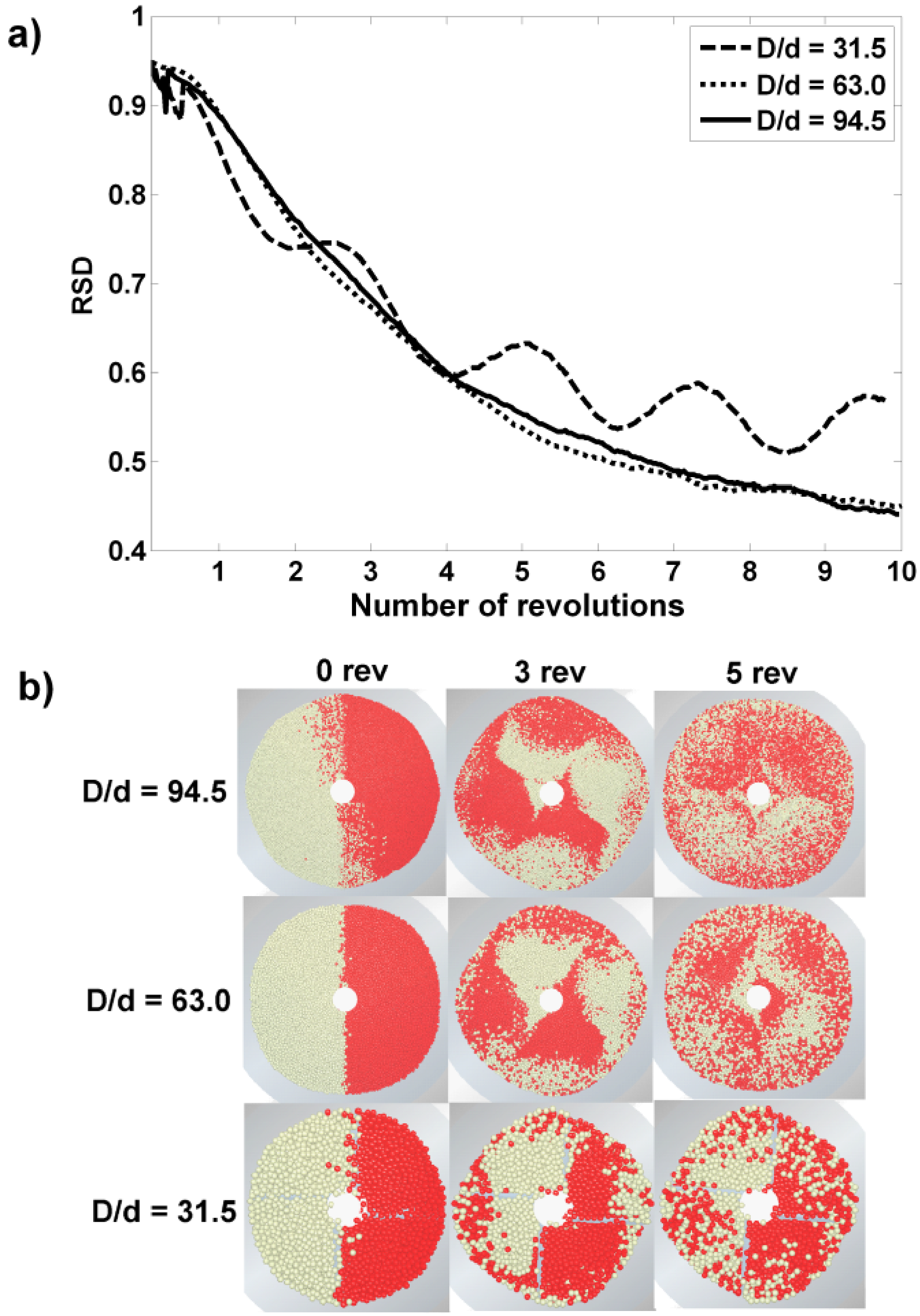

Figure 4.16. Effect of D/d on mixing. a) relative standard deviation of the red particle concentration vs. number of revolutions and b) top view snapshots of mixing patterns for different D/d ratios.

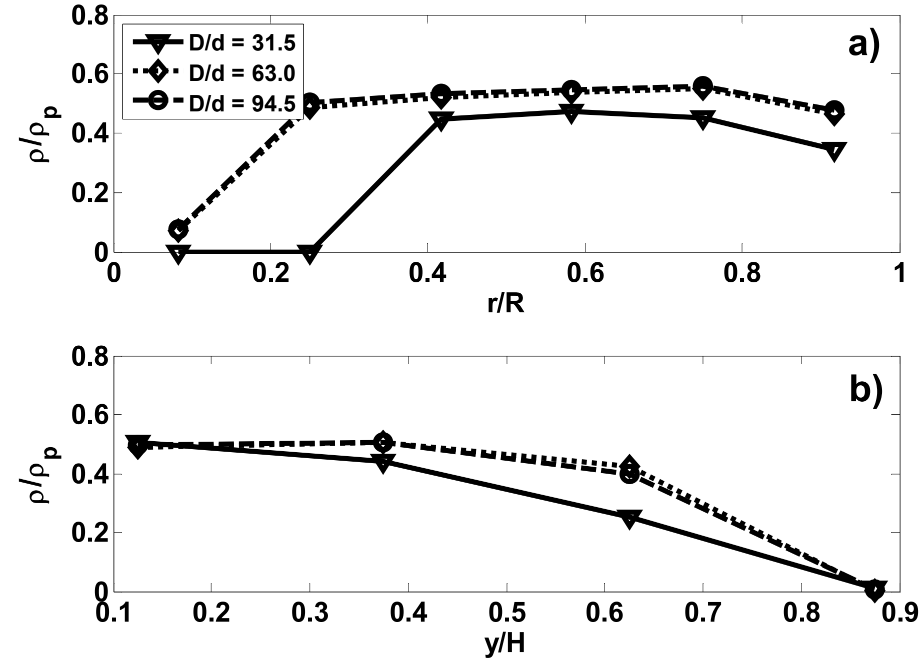

Figure 4.17. The effect of D/d on solids fraction. a) solids fraction vs. r/R and b) solids fraction vs. y/H.

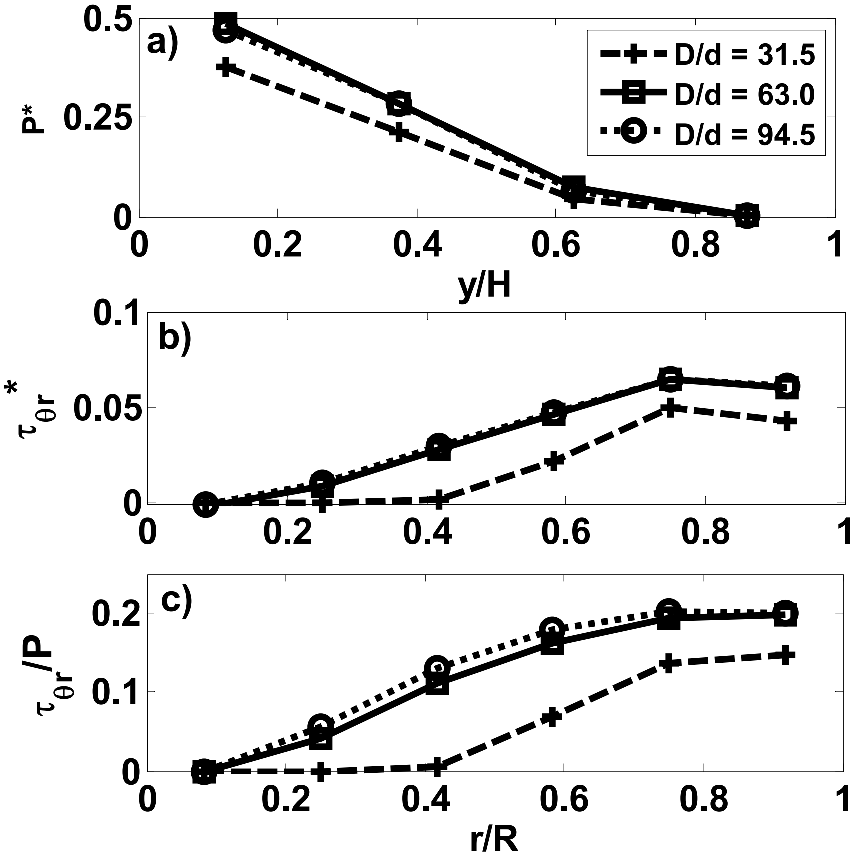

Figure 4.18. Scaled pressure, shear stress and bulk friction for different D/d ratios. a) Time averaged pressure vs. y/H, b) Time averaged $\tau^*_{\theta r}$ vs r/R and c) Time averaged $\tau_{\theta r}/P$ vs. r/R.

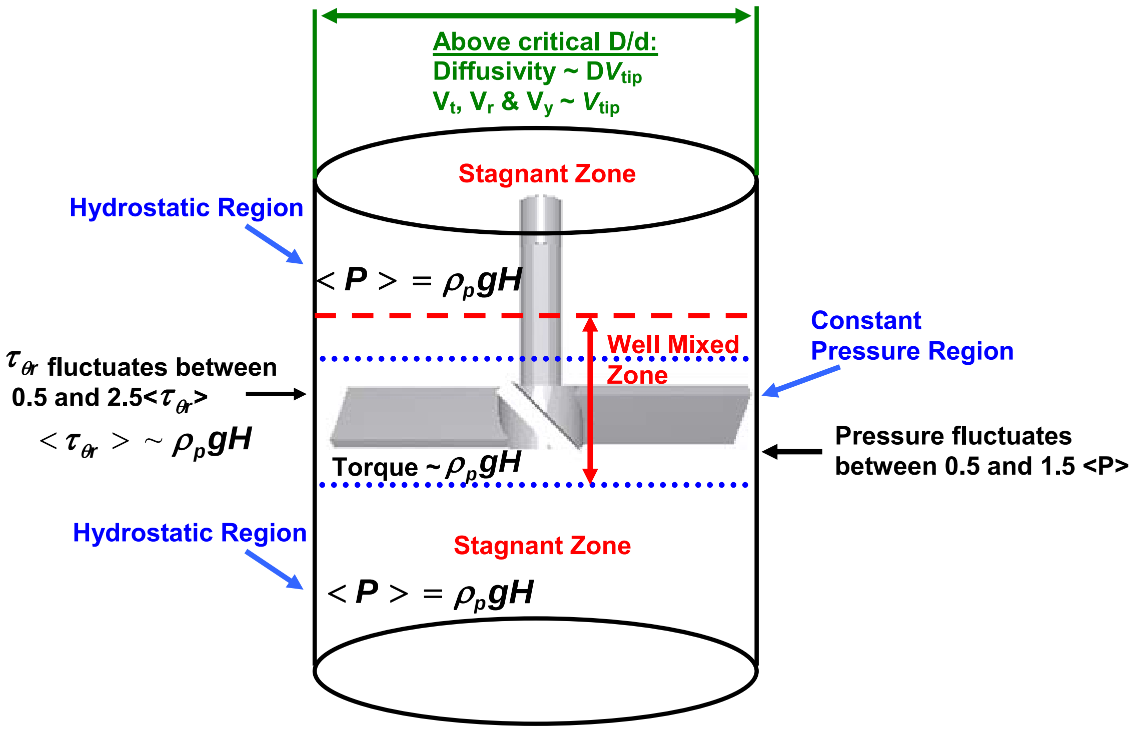

Figure 4.19. Scale-up of quasi-static flows in a bladed mixer with blades positioned below the surface of the particle bed.

4.8. Tables for Chapter 4

H/D	$D_{\theta\theta}$ (m^2/sec)	D_{rr} (m^2/sec)	D_{yy} (m^2/sec)	$Pe_{\theta\theta}$	Pe_{rr}	Pe_{yy}
0.17	4.0 x 10^{-5}	1.9 x 10^{-5}	5.4 x 10^{-5}	360	110	46
0.32	1.3. x 10^{-5}	7.2 x 10^{-6}	5.6 x 10^{-5}	1070	253	48
0.46	1.3 x 10^{-5}	7.1 x 10^{-6}	4.4 x 10^{-5}	1090	260	48

Table 4.1. Effect of H/D on particle diffusivity and Peclet number for particles within the span of the blades. Particle diffusivities were computed with a Δt of ¼ of a revolution.

$\mu^{p\text{-}p}$	$\mu^{p\text{-}w}$	$D_{\theta\theta}$ (m^2/sec)	D_{rr} (m^2/sec)	D_{yy} (m^2/sec)	$Pe_{\theta\theta}$	Pe_{rr}	Pe_{yy}
0.5	0.5	4.0 x 10^{-5}	1.9 x 10^{-5}	5.4 x 10^{-5}	360	110	46
0.1	0.5	1.7 x 10^{-5}	7. 5 x 10^{-6}	1.7 x 10^{-5}	900	217	117
0.5	0.1	4.6 x 10^{-8}	1.9 x 10^{-8}	2.3 x 10^{-8}	>300000	>10000	>5000

Table 4.2. Effect of particle-wall and particle-particle friction on particle diffusivity and Peclet numbers. Particle diffusivities were computed with a Δt of ¼ of a revolution and were averaged over all the particles in the computational domain.

D/d	$D_{\theta\theta}$*	D_{rr} *	D_{yy}*	$Pe_{\theta\theta}$	Pe_{rr}	Pe_{yy}
31.5	8.5 x 10^{-4}	3.3 x 10^{-4}	9.0 x 10^{-4}	720	152	70
63.0	1.3 x 10^{-3}	4.8 x 10^{-4}	2.2 x 10^{-3}	490	76	25
94.5	1.5 x 10^{-3}	5.9 x 10^{-4}	2.4 x 10^{-3}	400	56	23

Table 4.3. Effect of D/d on normalized particle diffusivity and Peclet number.

Chapter 5. Experimental Validation of DEM Results and Flow Regime Transitions for Monodisperse, Cohesionless Flows

In this chapter, a detailed comparison between DEM simulation results and experimental results is presented for near-monodisperse, cohesionless flows. The PIV technique was used to measure surface flow kinematics for the laboratory unit and these results are compared to the surface velocities obtained from the DEM simulations. Mixing kinetics and patterns are also compared. The effect of particle surface roughness and cylinder wall roughness is demonstrated experimentally and computationally. The effect of blade speed and particle surface roughness on flow regime transition is then discussed.

The experimental and computational results discussed in this chapter were obtained for fill levels just covering the top of the blades. In order to enable a one-to-one comparison between the experimental and numerical results, DEM simulations discussed in section 5.1 were carried out using the same mixer dimensions and the same number of particles as in the laboratory experiments. In order to reduce computational effort, the DEM results for the rest of this chapter (sections 5.2 to 5.4) were obtained for the mixer dimensions in Table 2.1 together with 10 mm particles. Experimental results listed in sections 5.1 to 5.3 were obtained for a blade speed of 50 RPM. Simulation results listed in section 5.1 were obtained at 50 RPM while the results in sections 5.2 and 5.3 were obtained at 25 RPM. The effect of blade speed is discussed in section 5.4.

5.1. DEM Results vs. Experimental Results

In this section, we compare the particle velocities and mixing kinetics from the DEM simulations to those obtained experimentally. The DEM simulations discussed in this section were performed with 2 mm particles and with the laboratory mixer dimensions (see Table 2.3). We showed in Chapter 3 that, for bladed mixer DEM simulations at low rotational speeds, the sliding friction coefficient (μ_s) is the input parameter that most significantly affects resulting velocities. Additionally, Stewart et al. [108] showed that good agreement can be reached between the simulation and experimental results by tuning the value of μ_s used in the simulations. We find that in our system, a μ_s of 0.5 provides the best fit with the experimental data. This value is within previously reported ranges for μ_s values of glass beads [170, 171] and within the range demonstrated by Stewart et al. [108].

Figure 5.1 shows instantaneous velocity profiles obtained at 50 RPM for the PIV experiments and the DEM simulations. Here, the velocities have been normalized by the tip speed of the blades, V_{tip}. For both the experiments and the simulations a 10 mm x 10 mm square control area was created at the top free surface at r/R = 0.5 and at the cylinder wall at y/H = 0.5. The instantaneous velocity components were calculated by averaging over the control area at a particular time. For the DEM simulation, only the velocities of the particles located 0.75 particle diameters away from each surface were included in the calculation. In general, good agreement is obtained between the experimental instantaneous velocities and the simulation velocities.

The tangential velocities at the top surface for the experiment (Figure 5.1a) and the simulation (Figure 5.1f) show a periodic behavior which has also been observed for bladed mixer flows of art sand [107] and calcium carbonate [172]. As the blades are rotated, the velocity of the particles in front of the blades increases from the interactions with the blades. The velocity of the particles in between the blades is lower, since the influence of the blades is not as strong in this region. A Fast Fourier Transform (FFT) analysis of the tangential velocity (V_t) showed that the main frequency of these fluctuations is that of the blade rotation (~3.2 Hz). The power spectrums obtained from this analysis are shown in Figure 5.1b (experimental) and 5.1g (DEM simulation). The intensity of the main peak is very similar for the DEM simulation compared to the experiment. The DEM simulation predicts reasonably well the maximum and minimum tangential velocity values at the top free surface. The radial velocity (V_r) profiles are shown in Figure 5.1c (experimental) and 5.1h (DEM simulation). Periodic fluctuations with a characteristic frequency equal to that of the blade rotation are obtained for both the experimental and simulation profiles. The radial velocity profiles fluctuate around zero indicating the existence of 3-dimensional recirculation zones within the particle bed. This is consistent with the simulation results presented in Chapters 3 and 4 in which recirculation patterns were shown to be present in front of the blades for counter-clockwise blade rotations (obtuse configuration).

The instantaneous tangential and vertical velocities at the cylinder wall are shown in Figures 5.1d and 5.1e for the experiment and in Figures 5.1i and 5.1j for the simulation. The periodicity in the tangential velocity (V_t) observed at the top free surface is less prominent near the cylinder walls. Additionally, tangential particle velocities near the wall are 50% of the tip speed of the blades. This is due to the frictional nature of the particle-wall interaction which lowers particle velocities and gives rise to slip-stick behavior. The simulated tangential velocities by the cylinder wall show almost no periodic behavior associated with the blade passes. This suggests that the frictional conditions by the cylinder wall are different between the experiment and the simulation.

The vertical velocity profiles (V_y) by the cylinder wall show a periodic behavior for both the experiment and simulation. As in the case of the V_r profile, the vertical velocity fluctuates around zero further confirming the existence of the previously reported recirculation patterns.

Time average velocity profiles and granular temperature trends are shown in Figure 5.2. Here the granular temperature values have been averaged in the azimuthal direction and normalized by V_{tip}^2. The average velocity field near the top free surface in the simulation (Figure 5.2c) is very similar to that of the experiment (Figure 5.2a), with particle velocities increasing near the cylinder wall. Granular temperature maximums are obtained at the top surface near the cylinder wall in both the experiment and the simulation. The increase in temperature is due to the higher particle velocities near the wall and to wall friction, which shears the material close to the wall and induces a degree of randomness to the velocities of the particles after hitting the wall. The region of high temperature near the wall is larger for the simulation than for the experiments. Additionally, lower average velocities and higher granular temperatures are obtained by the cylinder wall for the simulation (Figure 5.2d) when compared to the experiment (Figure 5.2b).

The differences observed between the experimental velocity fields and those obtained from the DEM simulations could be caused by a number of factors such as differences in particle properties, wall friction and slight polydispersity (present in the glass beads used, but not accounted for in the simulations). Despite the small discrepancies, the general trends obtained for both the experiments and the simulation are similar. The DEM simulations accurately capture the periodicity in the flow, the magnitude of the velocity components relative to the tip speed of the blades and the granular temperature gradients that exist within the particle bed. Since particle diffusivities are directly proportional to the granular temperature [155], we can conclude that the DEM simulations are also able to capture the qualitative diffusive behavior of particulate flows in bladed mixers.

In addition to accurately simulating particle velocities, the DEM simulations can also reproduce the mixing kinetics observed in the experiments. Figure 5.3 shows snapshots for the mixing of a bed initially loaded with particles of different colors to the left and to the right of the impeller. Figure 5.3a shows the experimental mixing profile while Figure 5.3b shows the simulation results. The simulation mixing profiles match reasonable well with the experimental results. In both cases, well-mixed zones start to appear near the cylinder wall as this is the area with highest bulk velocities and highest granular temperature. After 5 revolutions, the particle bed is well mixed in the simulation as well as in the experiment.

5.2. Effect of Particle Surface Roughness

The coating procedures outlined in section 2.2.3 were used to produce particles with different surface roughness. Figure 5.4 shows SEM pictures of the different particle types used in this study. The SEM pictures show that the glass beads (Figure 5.4a) have the smoothest surface at the 500 μm and the 50 μm scales. The MgSt coated beads (Figure 5.4b) have some surface irregularities at the 50 μm scale due to the shape of the MgSt particles. The sand coated beads (Figure 5.4c) posses the roughest surface with irregularities at the 500 μm scale. In order to quantify the degree of roughness of the particles, shear cell analysis was performed with a FT4 rheometer from Freeman

Technologies (Welland, Malvern UK). Shear cell analysis can be used to estimate the internal angle of friction of a material at the critical state [173]. While this analysis yields a value for a macroscopic friction coefficient (μ), this value is not the same as the microscopic sliding friction coefficient used as an input parameter in DEM simulations. This has been documented in various DEM studies of shear cells [174-176]. However, Baran et al. [177] and Theuerkauf et al. [178] have shown that the macroscopic friction coefficient obtained from shear cell analysis increases when the microscopic sliding friction coefficient of the particles is increased. Therefore, shear cell analysis provides an indirect measurement of microscopic friction. Table 5.1 list the macroscopic friction coefficient (μ) obtained from the shear cell analysis along with a standard deviation for each value. These friction coefficients were obtained following the procedure outlined by Freeman Technologies. The shear cell test was repeated 4 times for each particle type. The sand coated beads have the highest macroscopic friction, followed by the MgSt coated beads and the glass beads. The mass of the individual particles was also measured and these are listed in Table 5.1. The mass measurements were repeated 3 times for each particle type and a mean mass and standard deviation is reported. The mass of the coated particles is comparable to the mass of the glass beads. This shows that the main effect of the coating procedure was the modification of surface roughness.

The effect of surface roughness on instantaneous velocity profiles is shown in Figure 5.5. The tangential and radial velocities shown here were obtained on the top free surface at $r/R = 0.5$ while the vertical velocity was obtained by the cylinder wall at $y/H = 0.5$. Periodic velocity fluctuations are obtained for all particle types. However, as particle surface roughness is increased, the amplitude of the velocity fluctuations increases for all

3 velocity components. This suggests that, at higher frictional conditions, the flow inside bladed mixers becomes less uniform. In the tangential direction, the most notable effect of increasing surface roughness is the decrease of the minimum tangential velocity in between the blade passes (see Figures 5.5a, d and g). This implies that in between blade passes, the amount of energy dissipation in the tangential direction is larger for rougher particles.

It is also interesting to examine the effect of surface roughness on the deformation of the particle bed. As the granular material is sheared inside the mixer, the particle bed deforms by forming heaps where the blades are present and valleys in between the blade passes [110]. These heaps form due to the development of contact force chains which anchor themselves by the cylinder wall and cause the material to dilate where the blades are present. Figure 5.6 shows side view snapshots of the heaps that develop for each particle type. In all cases the material were poured into the laboratory mixer to achieve an initial bed height of ~ 27 mm. The height of the heaps in front of the blades increases with increased particle surface roughness. The heap height for glass beads is ~ 30 mm (Figure 5.6a). It increases to ~ 35 mm for the MgSt-coated beads (Figure 5.6b) and to ~ 40 mm for the sand-coated beads (Figure 5.6c). It has been shown that more frictional particles leads to an increased stability of the contact force chains [19] which could explain the development of higher heaps. As higher heaps are formed, the potential energy of the particles on top of the heaps increases. We hypothesize that this potential energy is then transferred into kinetic energy in the vertical and radial directions as particles flow in and out of the heaps leading to the increase in the radial and vertical velocities observed for the rougher particles (Figure 5.5).

Figure 5.7 shows the time average velocity profiles and granular temperature trends for the different particle types near the top free surface. Some differences are observed on the velocity fields of the sand coated particles (Figure 5.7c) when compared to the glass beads velocities (Figure 5.7a) and MgSt-coated beads (Figure 5.7b). The velocities of the sand-coated particles near the wall are lower than those of the MgSt-coated beads or the glass beads. This is due to the pronounced surface roughness of the particles, which increases the resistance to flow from interactions with the wall and from particle interlocking. Granular temperature profiles are also affected by the surface roughness of the particles. As can be seen from Figure 5.7, increasing particle surface roughness leads to an increase in granular temperature within the particle bed. This is consistent with the computational results present in Chapter 3. When two particles are in contact, surface friction will impart a degree of randomness in the resulting velocities of the particles acting as a source of fluctuating kinetic energy. This effect is more pronounced in particles with rougher surfaces leading to the increase in granular temperature.

The experimental results suggest that surface roughness significantly affects convective and diffusive particle motion in the bladed mixer. However, PIV is limited to the measurement of surface velocities. In order obtained a complete 3-dimensional picture, we explore the effect of surface roughness on resulting velocities within the particle bed via DEM simulations. Figure 5.8 shows time-averaged radial and vertical velocity fields for the particles located in front of the blades. Averaging was performed considering only the time-steps for which the blades were present at the position shown in Figure 5.8. The magnitude of the tangential velocity is represented by the color of the vectors. The resulting velocities for a particle μ_s value of 0.3 are shown on Figure 5.8a, while Figure 5.8b shows the velocities for a μ_s value of 0.5. In both cases, a recirculation zone develops in front of the blades as particles rise by the wall and fall near the impeller shaft. However, the magnitude of the radial and vertical velocities is higher for the more frictional case ($\mu_s = 0.5$). This is consistent with the results shown in Figure 5.5. Figure 5.8b shows that the increase in radial and vertical velocities occurs throughout the majority of the particle bed, though is most prominent near the top surface and by the cylinder walls.

In order to gauge particle motion at the microscopic level, we calculated particle diffusivities and Peclet numbers. Here, we normalize particle diffusivities by the tip speed of the blades and the mixer diameter, i.e. $D_{ij}^* = {D_{ij}}/{DV_{tip}}$. Table 5.2 lists the normalized particle diffusivities obtained for the different μ_s values. The values shown in Table 5.2 were obtained by averaging over all the particles in the computational domain with a Δt of ¼ revolution. The diffusivity in the tangential ($D_{\theta\theta}^*$), radial (D_{rr}^*) and vertical (D_{yy}^*) directions for the $\mu_s = 0.5$ case are nearly twice the value of the diffusivities obtained for the $\mu_s = 0.3$ case. This is consistent with the granular temperature trends obtained from the PIV experiments (Figure 5.7). Table 5.2 also lists Peclet number values at the different frictional conditions. In both cases, the Peclet numbers obtained are much higher than unity, indicating that convection is the dominating mechanism for particle transfer. However, Peclet numbers decrease for the $\mu_s = 0.5$ case. This result suggests that, in addition to increasing particle diffusivities, a high surface roughness increases the contribution of the diffusive mechanism relative to the convective mechanism for particle motion. The differences in convective and diffusive particle motion at higher particle surface roughness lead to enhanced mixing kinetics when compared to systems with smoother particles [110].

5.3. Effect of Cylinder Wall Roughness

In addition to particle surface roughness, we showed in Chapter 4 that cylinder wall roughness has a significant effect on flow behavior. In order to test the effect of wall roughness experimentally, the glass wall of the laboratory mixer was lined with sand paper (180 grit) and PIV measurements were then taken at the top free surface for beds of glass beads. The presence of the sand paper prevented the measurements of particle velocities at the cylinder wall. Instantaneous velocity fluctuations at $r/R = 0.5$ are shown in Figure 5.9 for the smooth (glass) wall mixer and the rough (sand paper lined) wall mixer. Similar to the effect of particle surface roughness, increasing wall roughness leads to an increase in the amplitude of the tangential and radial velocity fluctuations. This is attributed to the development of stronger contact force chains at higher wall roughness, which enable the transfer of energy from the moving blades to the particle bed. The strength of contact force chains has been demonstrated to be a function of wall friction in dynamic systems, such as discharging silos [163]. It is interesting to note that the influence of the rough wall on particle velocities is observed as far away from the wall as $r/R = 0.5$. This is probably due to the relatively small scale of the laboratory mixer and it is likely that the effect of wall roughness may not be as pronounced in larger units. However, the fact that this effect occurs at the laboratory scale could become important as bladed mixer processes are scaled from the laboratory/pilot plant scale to the manufacturing scale.

Average velocity fields and granular temperature are shown in Figure 5.10 for the smooth (Figure 5.10a) and rough wall (Figure 5.10b) experimental systems. Higher average velocities are observed at the top free surface for the rough wall system. This is consistent with the higher fluctuation amplitudes showed in Figure 5.9. Granular temperature profiles are also affected by wall roughness with higher temperature observed near the cylinder wall for the rough wall case. When particles collide with the wall, the resulting particle velocities differ from that of the bulk flow due to the frictional nature of the particle-wall interaction. This effect increases for the system with the rougher wall as this type of surface leads to slip-stick motion for the particles near the wall. The increase in granular temperature from wall roughness suggest that the frictional cylinder wall acts as an important source of fluctuating kinetic energy in the bladed mixer at the laboratory scale. However, this effect might be less pronounced in larger scale mixers. Further work is needed to explore the effect of wall roughness on granular temperature profiles at larger scales.

Figure 5.11 shows radial and vertical velocity fields obtained from DEM simulations for different particle-wall friction coefficients (μ_s^{p-w}) for the particles located in front of the blades. When the value of μ_s^{p-w} is increased from 0.3 (Figure 5.11a) to 0.5 (Figure 5.11b), the intensity of the recirculation zone increase due to higher radial and vertical velocities. This is consistent with the PIV results and with the computational results presented in Chapter 4. Figure 5.11 shows that the increase in velocities occurs not only at the top free surface but throughout the particle bed.

Table 5.3 lists values of normalized particle diffusivities and Peclet numbers obtained from DEM simulations at the different wall frictional conditions. Increasing the value of μ_s^{p-w} to 0.5 almost doubles the normalized particle diffusivities when compared to the $\mu_s^{p-w} = 0.3$ case. This is also consistent with the experimental granular temperature trends and it suggests that rough walls increase particle diffusivities not just for the particles located near the top free surface but throughout the bladed mixer bed. Increasing wall roughness also decreases Peclet number values, most significantly in the tangential direction but also in the radial and vertical directions. While these results indicate that at higher wall roughness, convection is still the dominating mechanism, they also suggest that increasing wall roughness increases the diffusive contribution to particle motion. The higher velocities and particle diffusivities obtained at higher wall roughness lead to enhanced mixing kinetics when compared to systems with smoother walls.

5.4. Effect of Blade Speed

Bladed mixer processes operate at a wide range of blade rotational speed. As such, it is important to understand the effect of blade speed on resulting particle velocities. Instantaneous velocity profiles at different rotational speeds are shown in Figure 5.12 for our experimental system. Two main effects are observed when blade speed is increased from 25 RPM to 200 RPM. The first is the loss of periodicity in all 3 velocity components. While strong periodicity is observed for the 25 RPM and the 50 RPM profiles, the fluctuation period at 100 RPM is less defined and at 200 RPM is almost completely lost. The loss of periodicity suggests that as blade speed is increased, particulate flows in bladed mixers become less correlated. A similar behavior was reported by Conway et al. [106] for art-sand flows in a four-bladed mixer. The second effect of increasing blade speed is to decrease the amplitude of the velocity fluctuations. As blade speed is increased, the height of the heap that forms in front of the blades also increases, which suggest that dilation of the particle bed has occurred. The heap height was measured at ~ 27 mm for 25 RPM, at ~ 30 mm for 50 RPM and at ~ 38 mm for 100 RPM. As heap height increases, the distance between the top of the blades and the particles near the surface of the bed becomes large enough that the influence of the blades on surface velocities is reduced. The decrease in vertical velocity fluctuations is attributed to the dilation of the particle bed which leads to a flatter vertical velocity profile.

When the normalized average speed (U_{avg} / V_{tip}) of the particles near the top free surface is plotted against the rotational speed of blades, two distinct flow regimes are observed (Figure 5.13). At lower rotational speeds (below ~ 50 RPM), the quasi-static regime is obtained where the value of U_{avg} / V_{tip} is independent of RPM. This implies that the resulting particle speeds near the top free surface increase linearly proportional to the tip speed of the blades in the quasi-static regime. The behavior in this region is similar to the bumping flow reported by Litster et al. [121]. The PIV results suggest that in the quasi-static regime, the blade rotational speed provides the time scale for momentum transfer within the particle bed. As blade speed is increased (above 50 RPM), the intermediate regime is reached where the value $\boldsymbol{U_{avg}}$ at the surface reaches a constant value (independent of V_{tip}); thus the normalized quantity, U_{avg} / V_{tip}, decreases as V_{tip} is increased (see Figure 5.13). This is similar to the roping flow reported also by Litster et al. [121]. It is interesting to note that the transition from the quasi-static to intermediate flow regime reported in the study mentioned above occurred at rotational speeds above 200 RPM for dry lactose flows in a granulator with a diameter of 0.4 m. Here, we observed a transition from the quasi-static to intermediate regime at ~ 50 RPM for glass bead flows in a mixer with a diameter of 0.1 m. This implies that the conditions leading to flow regime transition are dependent on system size and particle properties (i.e., free flowing grains vs. cohesive powders).

Dimensionless average velocity fields and granular temperature profiles obtained from the experiments at the different rotational speed near the top free surface are shown in Figure 5.14. The normalized velocity fields are very similar for the 25 RPM and 50 RPM cases (Figures 5.14a and b). Above 50 RPM, the normalized velocities decrease with increased blade speed due to a change in flow regime. A different effect is observed on the granular temperature profiles. In general, normalized granular temperature values decrease with blade speed, even for the cases in the quasi-static regime (25 and 50 RPM). We showed in sections 5.2 and 5.3 that resulting granular temperature profiles in our bladed mixer are dependent on the frictional contacts between the particles and between the particles and the wall. The increased dilation of the particle bed that occurs at higher RPM decreases the number of frictional contacts at the surface of the mixer, causing a drop in the normalized granular temperature. In addition, as the bed dilates the distance between the top of the blades and the particles near the surface increases leading to a reduced influence of the blades on the surface fluctuation velocities. It should be noted that the unscaled value of granular temperature does increase with blade speed. However, the increase in the fluctuating velocity (u') is small when compared to the increase in V_{tip}.

DEM simulations were also carried out at different blade rotational speed to analyze the velocity profiles that develop within the particle bed. Figure 5.15 shows time average radial and vertical velocity profiles that develop in front of the blades at different rotational speeds. At 3 RPM (Figure 5.15a) and 20 RPM (Figure 5.15b), the normalized velocity profiles are very similar indicating that at these rotational speed, resulting velocities are linearly proportional to V_{tip}. This is consistent with the quasi-static regime identified in Figure 5.13. The DEM results show that particle velocities throughout the entire bed are proportional to V_{tip}. A different behavior is observed for the velocities obtained at 55 RPM (Figure 5.15c) and at 120 RPM (Figure 5.15d). For these two cases, significant dilation of the particle bed occurs, resulting in the flow transition from the quasi-static regime to the intermediate regime. Analysis of the average particle coordination number within the mixer confirms that dilation of the bed does occur as blade speed is increased. The average coordination number at 20 RPM fluctuated between 5 and 6 versus an average coordination number between 3 and 2 for 120 RPM. Similar to the results obtained via PIV, the normalized particle velocities at the top free surface decrease with an increase in blade speed. However, the DEM results show that while normalized tangential velocities decrease with the rotational speed, the normalized radial and vertical velocities actually increase. This effect is particularly strong for the particles within the span of the blades (y/H < 0.5). Figure 5.15c and 5.15d show that the velocities for the particles above the blade (and near the free surface) are much lower than the particles within the span of the blades. The DEM simulations indicate that while normalized surface velocities decrease in the intermediate regime, the normalized radial and vertical velocities within the particle bed increase.

Table 5.4 lists normalized particle diffusivities and Peclet numbers obtained from the DEM simulations at the different blade speeds. At low RPM (3 & 20 RPM), normalized particle diffusivities change little with blade speed and are significantly higher than the values obtained at higher RPM. These results are consistent with the granular temperature trends obtained from PIV measurements. Peclet numbers at 3 & 20 RPM are also lower indicating that the contribution of diffusive mechanism at lower rotational speeds is larger. At 55 and 120 RPM, normalized diffusivities decrease and Peclet numbers increase due to the dilation of the particle bed. While the strength of bulk convection increases with blade speed in the intermediate regime, particle diffusion decreases in this regime.

The differences in convective and diffusive particle motion observed lead to differences in mixing performance. We evaluate the degree of mixing obtained for each blade speed by coloring particles on the left side of the blade impeller differently from the particles on the right side prior to blade movement in our DEM simulations. The particles have identical properties except their color. We then we perform statistical analysis on particle concentration for a specific color particle. At a particular time step, we compute the relative standard deviation (RSD) of particle concentration within the mixer. RSD values as a function of number of revolutions are shown in Figure 5.16 for the different blade speeds for the DEM simulations. The RSD curves for the 3 RPM and 20 RPM cases lay on-top of each other. These results imply that in the bumping regime, the blade rotational speed provides the time scale for the mixing process. This is consistent with the proportionality observed between the average particle velocities and V_{tip}. As normalized radial and vertical particle velocities increase in the roping regime, increasing blade speed in this regime leads to enhanced mixing kinetics as shown in Figure 5.16 by the RSD curves for the 55 RPM and the 120 RPM cases. It should be noted that Conway et al. [106] observed enhanced mixing at 3 RPM vs. the mixing observed at 30 RPM for art sand particles. The authors characterized the degree of mixing by calculating interface stretching via image analysis of top free surface snapshots. The differences in the mixing behavior observed by Conway et al. and the trend reported here could be due to the differences in particle properties (i.e., particle shape, size and degree of polydispersity). This suggests that the effect of regime transition on mixing is dependent on material properties.

We now look at the effect of blade speed on the average shear stresses that develop inside the particle bed at different values of microscopic friction. Average $\tau_{\theta r}$ values for the particles located within span of blades are plotted on Figure 5.17a vs. the dimensionless shear rate, γ^*. Here, the dimensionless shear rate is calculate from the expression proposed by Tardos et al. [43], $\gamma^* = \gamma \circ (d/g)^{1/2}$, where $\gamma \circ$ is the shear rate, d is the particle diameter and g is the acceleration due to gravity. $\gamma \circ$ is assumed to be equal to the blade rotational speed in rad/s. Figure 5.17a shows the existence of two distinct regimes, similar to what is obtained from the flow kinematics data. At low values of γ^* (below 0.1), the quasi-static regime is obtained where the average value of $\tau_{\theta r}$ is not a function of γ^* but is significantly affected by microscopic friction.

The rate independence of $\tau_{\theta r}$ can be explain by considering the dominant mechanism for momentum transfer in the quasi-static regime. In this regime, momentum transfer is governed by the generation of contact force chains that arise from sustained particle contacts. At low blade rotational speeds (i.e. low γ^* values), the average number of contact force chains inside the particle bed does not change as blade speed is increased. This is confirmed by the calculating the average coordination number for the particles in the quasi-static regime which is a constant value of ~ 5.5. Contact chains are created and destroyed as the blades are rotated, but the average number of contact chains stays the same leading to a constant value of $\tau_{\theta r}$. This behavior further indicates that in the quasi-static regime, the blade speed provides the time scale for the mixing process. Figure 5.17a also shows that in the quasi-static regime, shear stresses are only a function of the amount of friction in the system (for a given particle size). As explained before, the stability and strength of contact force chains increases with friction in the quasi-static regime leading to the higher values of $\tau_{\theta r}$.

For $\gamma^* > 0.1$ (blade speeds > 50 RPM), the intermediate regime is encountered where $\tau_{\theta r}$ increases linearly with γ^*, a behavior similar to that of liquids. The value of γ^* at which the transition from the quasi-static to the intermediate regime occurs is consistent with the regime map proposed by Tardos et al. [43]. This regime transition occurs when the dilation of the particle bed increases and number of sustained particle contacts becomes a function of blade speed. In the intermediate regime a second mechanism for momentum transfer arises; momentum transport due to the apparent random velocities of particles flowing across moving layers. We also find that the behavior of the intermediate regime in our bladed mixer resembles that of visco-plastic fluids such as Bingham fluids, where shear stress is related to shear rate by

$$\tau_{\theta r} = \tau_y + \kappa \gamma^\circ \qquad \textbf{(5-1)}$$

where τ_y is the yield stress and κ the apparent viscosity. In our bladed mixer, a yield stress needs to be overcome in order to induce flow (due to the frictional inter-particle contacts). Once flow has been achieved, the shear rate is linearly proportional to the shear rate times a proportionality constant (i.e., an apparent viscosity). Similar behavior has been observed for chute flows [53] and mechanically agitated beds [54] in the intermediate regime. From a least-square fitting of the data presented on Figure 5.17a for $\gamma^* > 0.1$, yield stresses and apparent viscosities can be calculated. These values are listed in Table 5.5 along with the R^2 statistic. In general, the R^2 values are high indicating a good fit of the data with the Bingham model. The lines in Figure 5.17a show the least square fitting of the model. Yield stress and apparent viscosity increase as microscopic friction is increased. This relationship has also been observed for Taylor-Couette flows in the intermediate regime [179]. Increasing microscopic friction increases the resistance to flow as one would expect. The apparent viscosities are also high compare to that of Newtonian fluids, a behavior analogous to Bingham fluids. Our results suggest that constitutive equations based on visco-plastic models can accurately describe the behavior of cohesionless granular flows in bladed mixers. It also shows that the visco-plastic parameters are strong functions of particle properties. These values are also expected to be dependent on the amount of cohesion and polydispersity present in the system along with system size.

Figure 5.17b shows blade torque as a function of γ^* for different microscopic friction values. Similar trends are obtained between the average $\tau_{\theta r}$ values and blade torque values. At low shear rates, blade torque is independent of blade speed. Above a critical value ($\gamma^* > 0.1$), blade torque increases linearly with blade speed. The lines in Figure 5.17b show the linear fit. The minimum torque required to induce flow increases with increased microscopic friction as well as the slope of the fitted line in the intermediate regime, a behavior similar to the one observed for $\tau_{\theta r}$. These results suggest that blade torque can be used to estimate the average shear stress within the span of the blades in bladed mixers and that torque can used to detect flow regime transition.

Finally, we look at the effect of surface roughness on the amount of power drawn by the blade motor experimentally. The amount of power drawn by the blades during agitation is proportional to the blade torque times the blade rotation speed. In order to remove the effect of blade rotational speed, we compute an adjusted blade power parameter by subtracting the power drawn by the blade motor when the cylinder is empty from the power drawn by the motor under load (i.e. when the granular material is agitated in the cylinder). Here, we assume that the power efficiency of the blade motor does not change significantly when the motor is under load (a reasonable assumption for a small motor, like the one used here). Adjusted power measurements for the different types of beads are shown in Figure 5.18 as a function of γ^*. The behavior observed in Figure 5.18 is very similar to the behavior obtained from the simulations. Here again we see the development of two distinct flow regimes, a quasi-static regime and an intermediate regime. Flow regime transition occurs for $\gamma^* > 0.11$ (blade rotational speeds above 50 RPM), which is consistent with the particle velocity data shown in Figure 5.13. The lines shown in Figure 5.18 show the linear fit of blade power in the intermediate regime. The minimum power needed to induce flow increase with particle surface roughness along with the slope of the lines in the intermediate regime. These results are consistent with the DEM simulation results.

Our analysis showed that two different flow regimes occur in bladed mixer and that the resulting flow kinematics and stress profiles change significantly between the two regimes. The changes in particle velocities lead to differences in mixing kinetics.

However, comparison of our results to previously reported data suggests that the conditions leading to flow regime transitions are scale and material property dependent. Care should be taken during the scale-up and design of bladed mixer processes to avoid operating at different flow regimes.

5.5. Conclusions from Experimental Validation and Effect of Blade Speed

Experimental and computational methods were used to study the kinematics of particulate flows in bladed mixers. The ability of DEM simulations to accurately capture experimental behavior was demonstrated. Particle velocities and granular temperature profiles obtained from the simulations are in good agreement with those obtained experimentally using the PIV technique. The simulation mixing kinetics were also in agreement with the mixing kinetics observed experimentally. The small discrepancies observed between the simulation results and the experimental results could be due to differences in particle properties, wall friction and the slight polydispersity present in the glass beads used (but not accounted for in the simulations). Further work is needed to develop methods for measuring particle and boundary properties that could be used as input parameters for DEM simulations.

PIV and DEM results showed that particle surface roughness and cylinder wall roughness significantly influence flow kinematics in bladed mixers. Increasing particle roughness leads to an increase in the velocity fluctuation amplitudes, bed dilation and granular temperature. DEM simulations showed that the contribution of the diffusive mechanism in the momentum transport process increases with particle roughness. Similar results were obtained when cylinder wall friction was increased. However, the influence of wall roughness is expected to be scale dependent. Further work is needed to explore the effect of surface roughness at larger scales.

The effect of blade speed on resulting particle velocities and mixing kinetics was also studied. Two distinct flow regimes were observed as blade speed was increased. Below 50 RPM, the particle flow inside the mixer occurred in the quasi-static regime. This regime is characterized by particle velocities and diffusivities which are linearly proportional to the tip speed of the blades. Because of this relationship, the rotational speed of the blades provides the time scale for momentum transfer and for the mixing process in the bumping regime. Above 50 RPM, the intermediate regime was observed. This regime is characterized by radial and vertical velocities which increase with blade speed but are no longer proportional to the tip speed of the blades. Dilation of the particle bed occurs in the intermediate regime which leads to a decrease in particle diffusivities when compared to the tip speed of the blades. The increase in radial and vertical velocities within the particle bed leads to enhanced mixing kinetics in the intermediate regime. The conditions leading to regime transition appear to be dependent on system scale and the properties of the granular material based on the data previously reported in the literature.

The effect of blade speed on average shear stress was also shown. In the quasi-static regime, average shear stress is independent of blade speed but increases with microscopic friction. In the intermediate regime, the relationship between average shear stress and shear rate was demonstrated to be similar to that of visco-plastic or Bingham fluids. A yield stress needs to be overcome in order to induce flow and further shearing of the material increases the average stress linearly. Yield stress and apparent viscosities were shown to be a function of microscopic friction in bladed mixers. Similar trends were observed for blade torque measurements from the simulations and blade torque power from the experiments.

The results shown here elucidate some of the mechanisms leading to particle motion and mixing kinetics in bladed mixers. Specifically, they highlight the sensitivity of resulting flow kinematics on particle properties, mixer properties and operating conditions. Further work is needed to explore the effect of particle size distribution, particle shape and inter-particle cohesion on the trends reported here.

5.6. Figures for Chapter 5

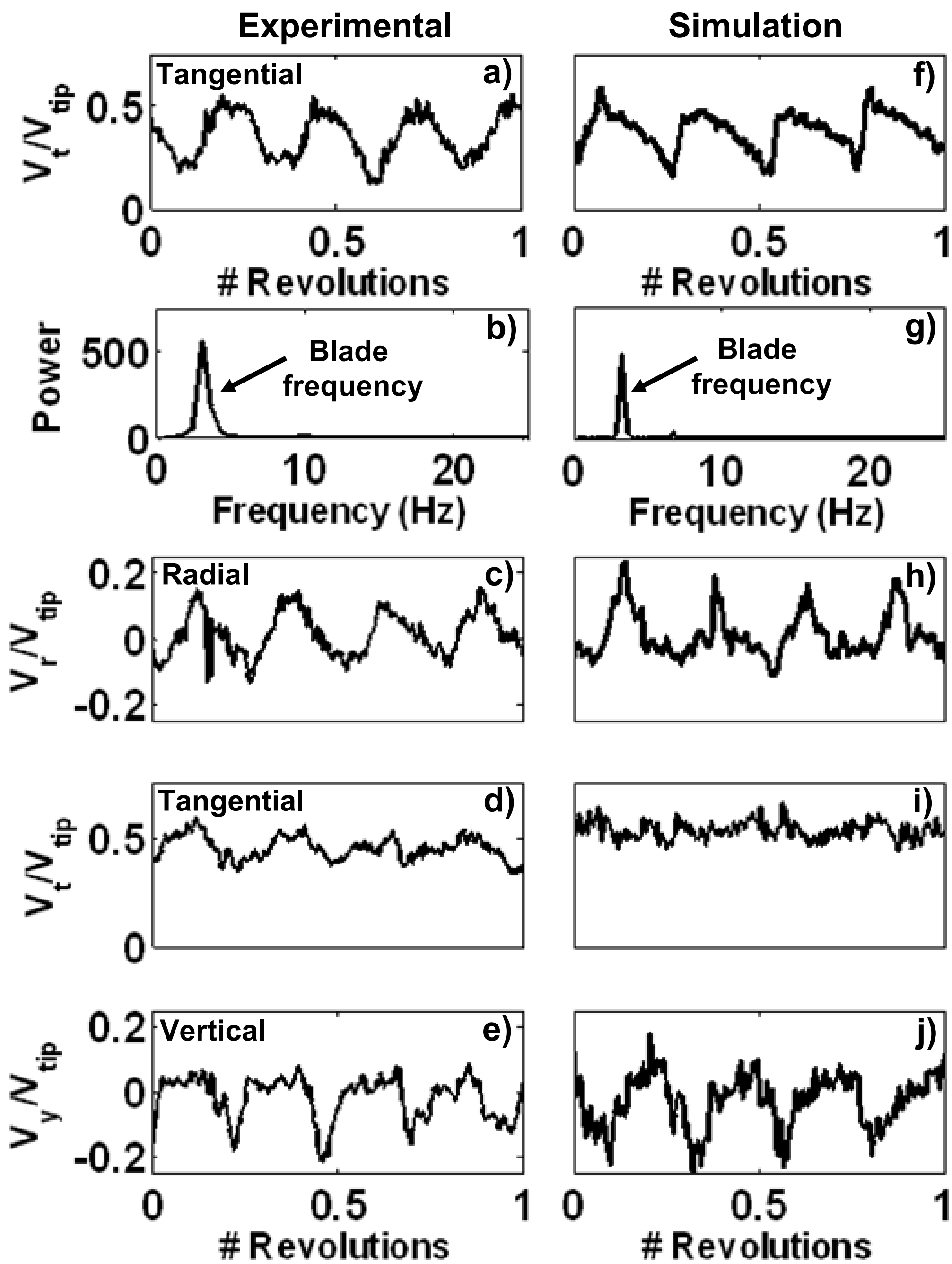

Figure 5.1. Velocity fluctuations near free top surface at r/R = 0.5 and by the cylinder walls at y/H = 0.5. Experimental results: a) top free surface tangential velocity, b) tangential velocity power spectrum, c) top free surface radial velocity, d) cylinder wall tangential velocity and e) cylinder wall vertical velocity. Simulation results: f) top free surface tangential velocity, g) tangential velocity power spectrum, h) top free surface radial velocity, i) cylinder wall tangential velocity and j) cylinder wall vertical velocity. Results obtained for a blade speed of 50 RPM.

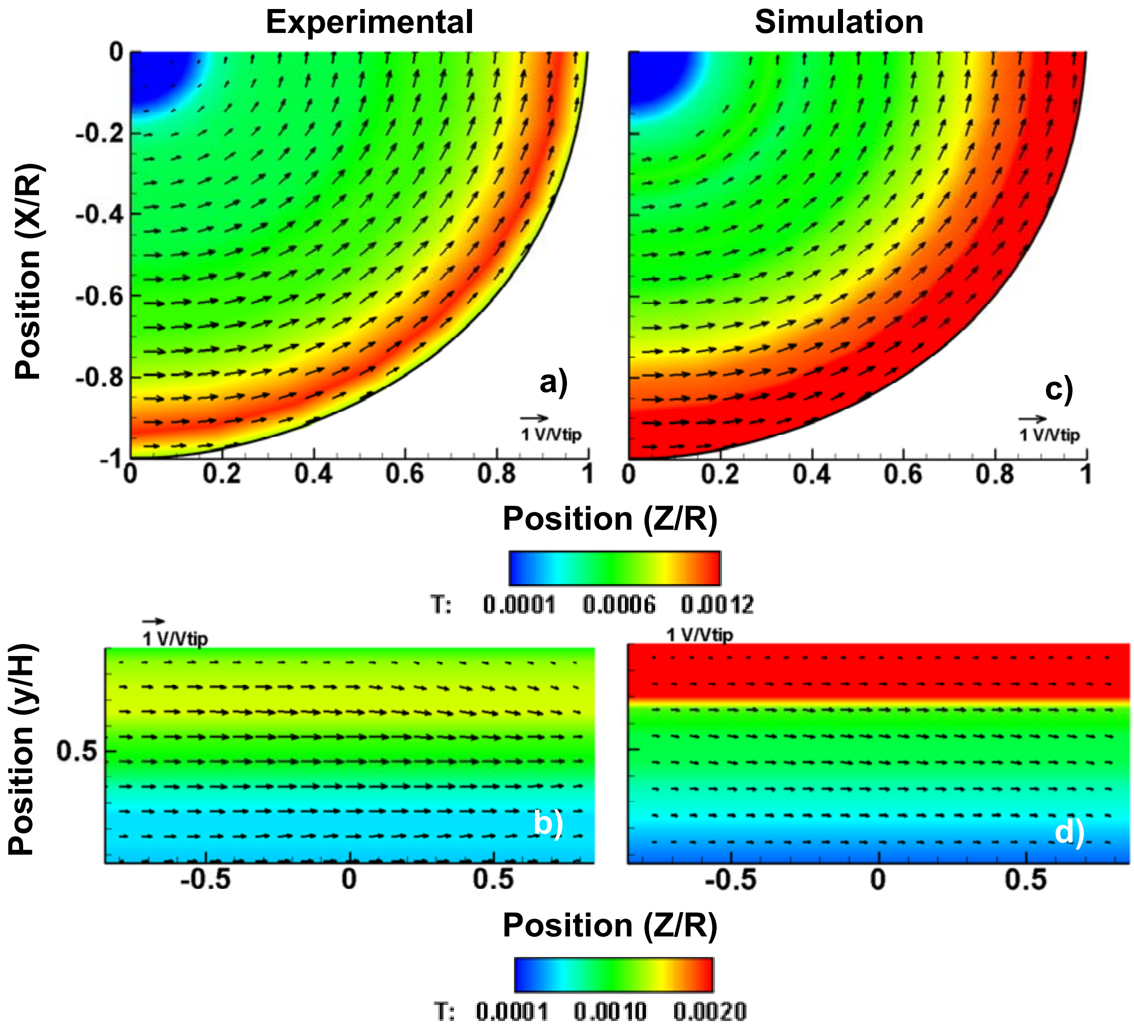

Figure 5.2. Time average velocity profile and granular temperature. a) experimental results at the top surface, b) experimental results at the cylinder wall, c) simulation results at the top surface and d) simulation results at the cylinder wall. Granular temperature shown here has been averaged in the azimuthal direction and normalized by V_{tip}^2. Results obtained for a blade speed of 50 RPM.

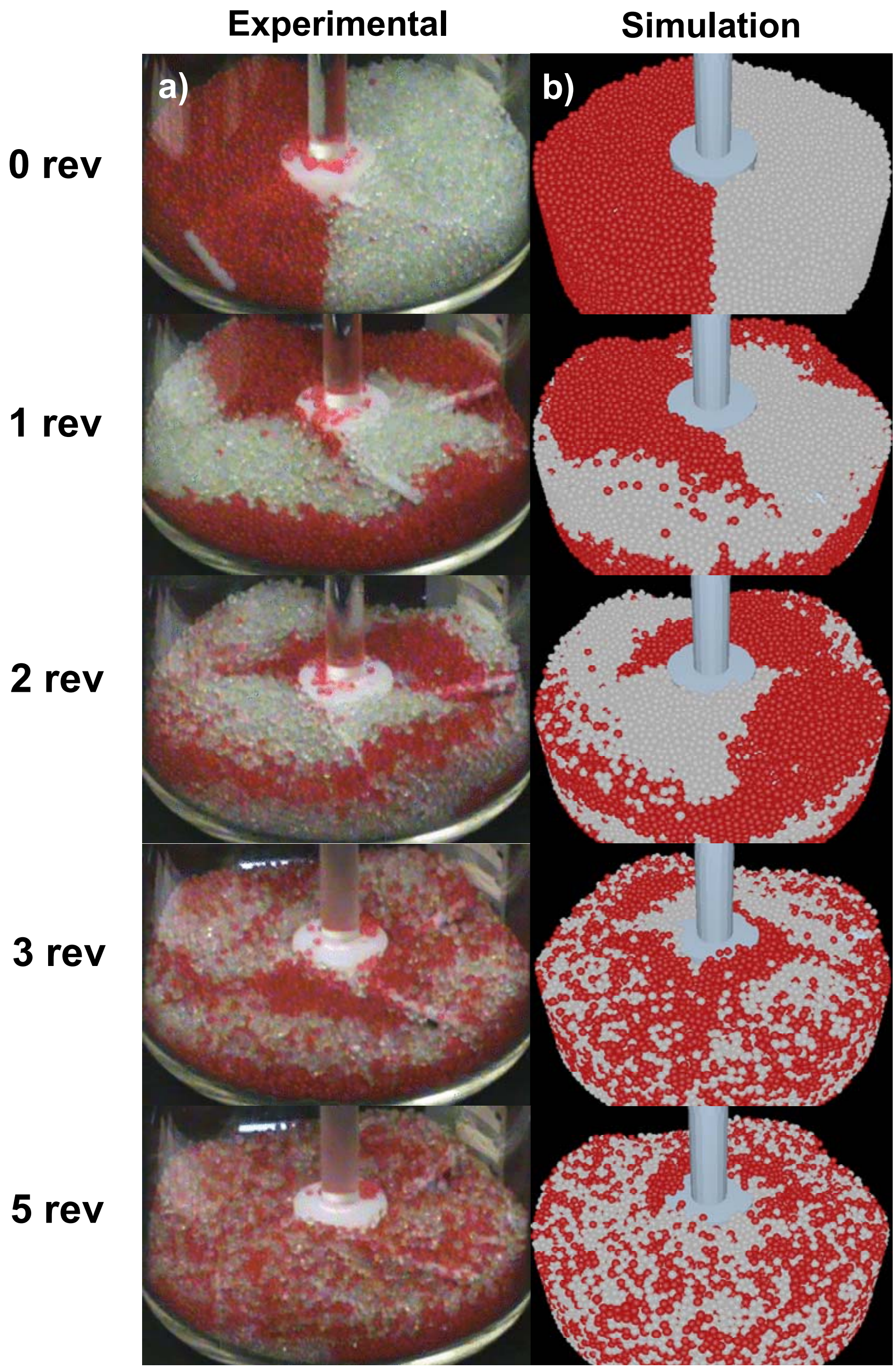

Figure 5.3. Mixing performance for left-right segregated bed. a) experimental results and, b) simulation results. Results obtained for a blade speed of 50 RPM.

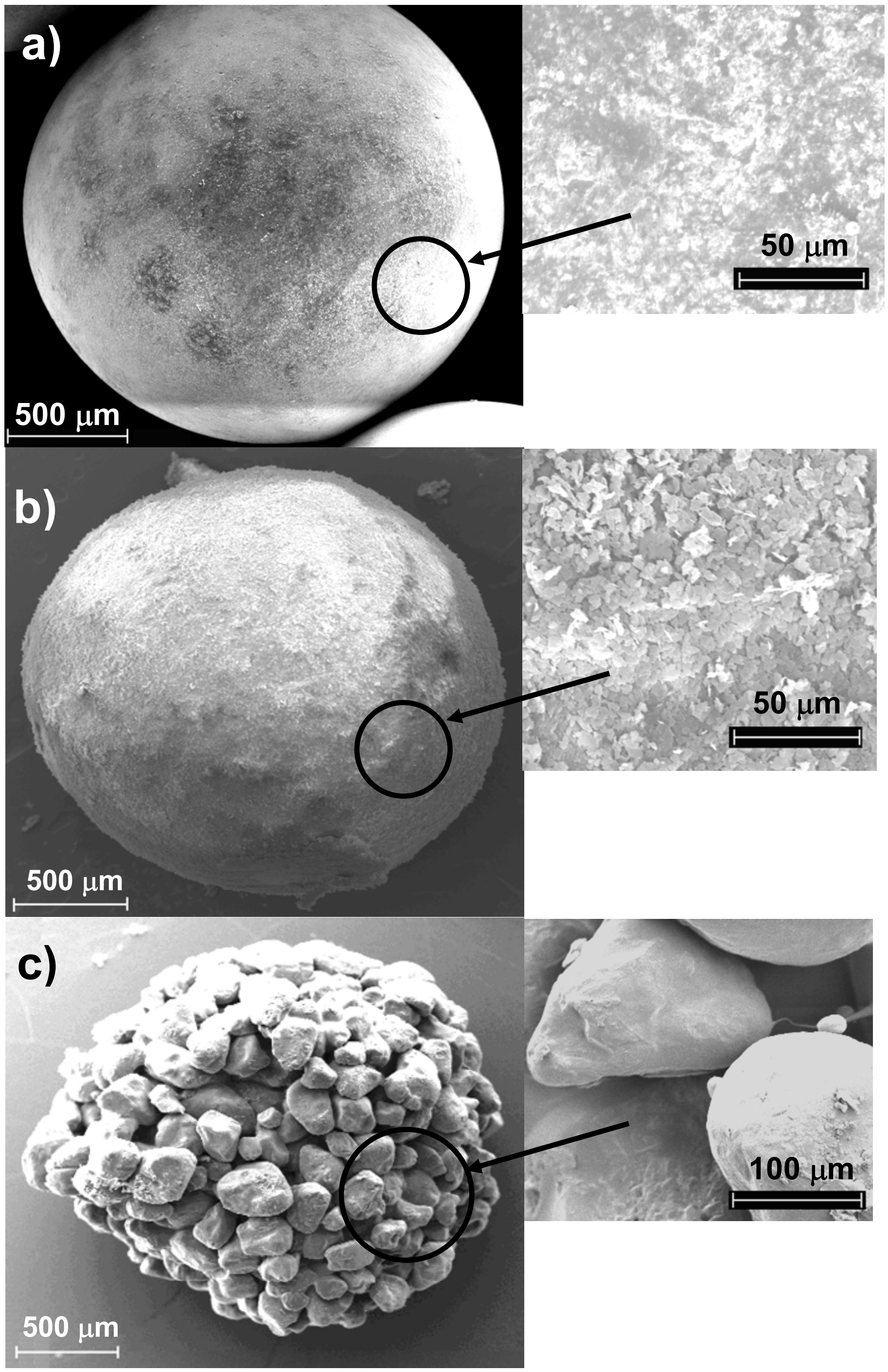

Figure 5.4. SEM pictures of particle surfaces. a) blue glass bead, b) MgSt coated bead and c) sand coated bead.

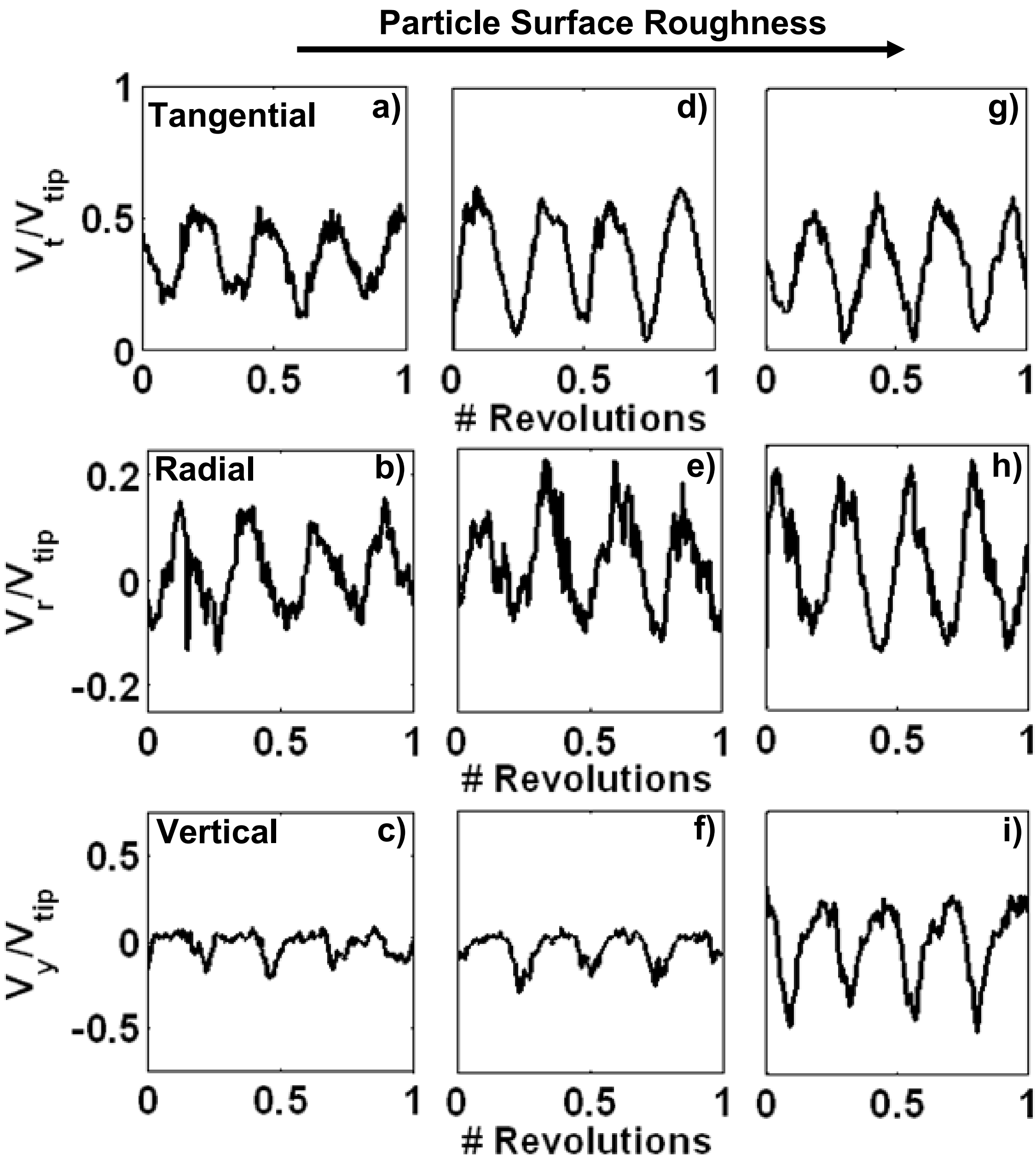

Figure 5.5. Effect of surface roughness on tangential, radial and vertical velocity fluctuations. a)-c) glass beads, d)-f) MgSt coated beads and g)-i) sand coated beads. The tangential and radial velocities were obtained on the top free surface at r/R = 0.5. The vertical velocity was obtained by the cylinder wall at y/H = 0.5. Results obtained for a blade speed of 50 RPM.

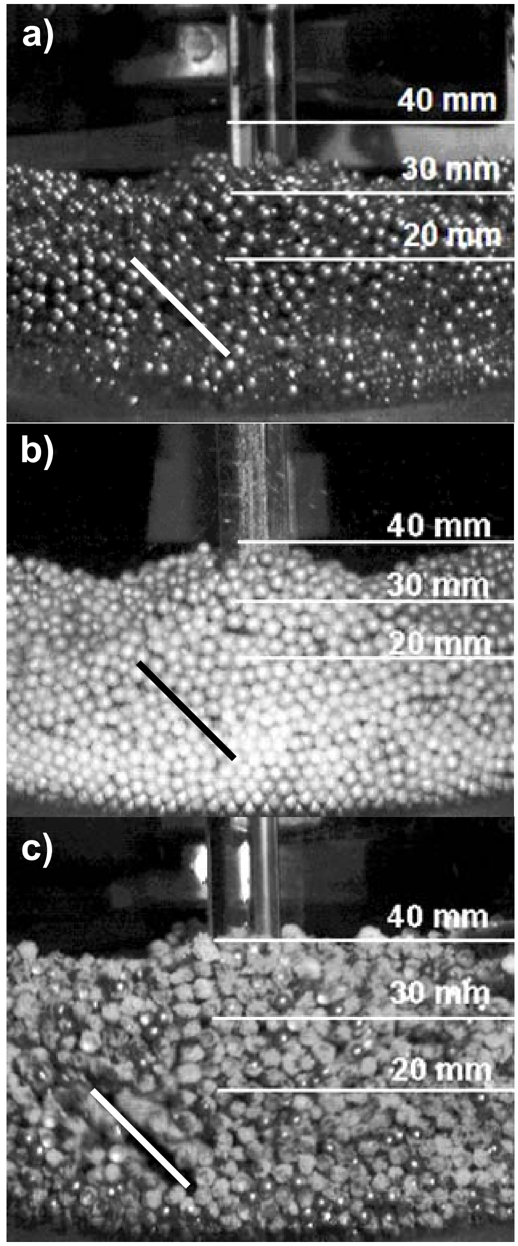

Figure 5.6. Effect of surface roughness on heap height. a) glass beads, b)MgSt coated beads and c) sand coated beads. The solid line shows the position of the blade. Results obtained for a blade speed of 50 RPM.

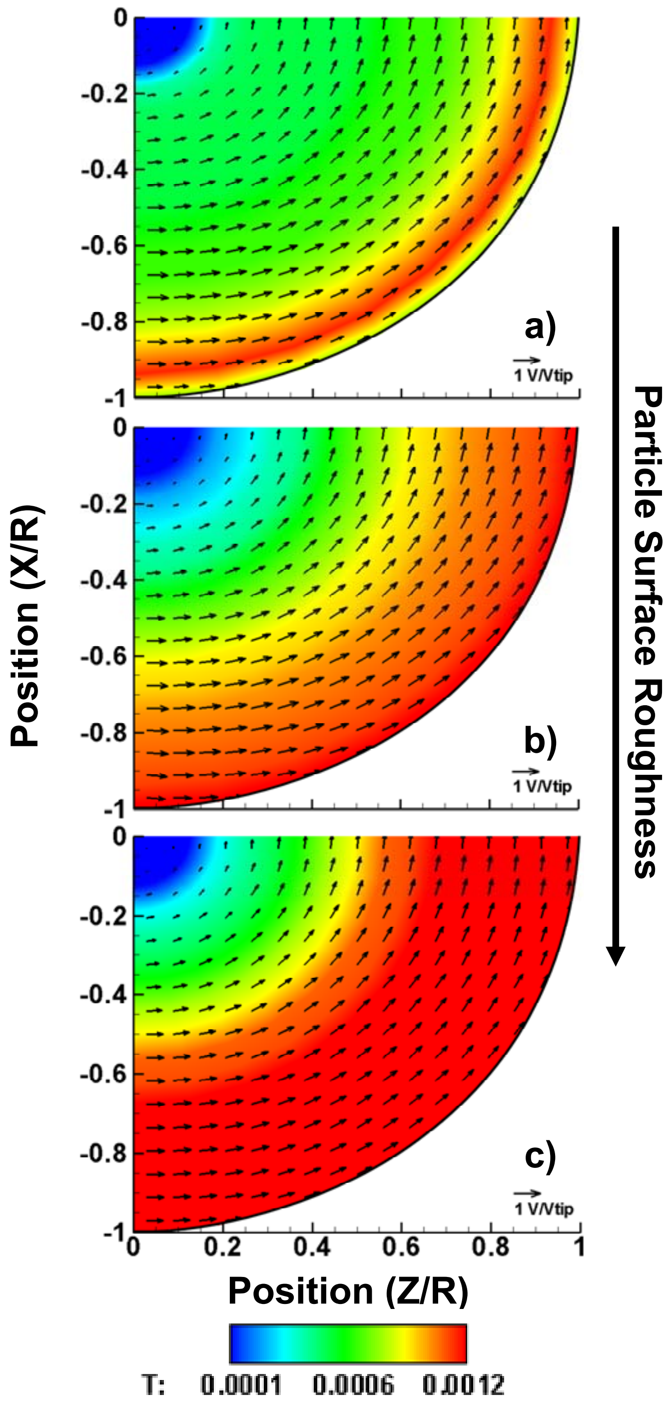

Figure 5.7. Effect of surface roughness on average velocity fields and granular temperature. a) glass beads, b) MgSt coated beads and c) sand coated beads respectively. Granular temperature shown here has been averaged in the azimuthal direction and normalized by V_{tip}^2. Results obtained for a blade speed of 50 RPM.

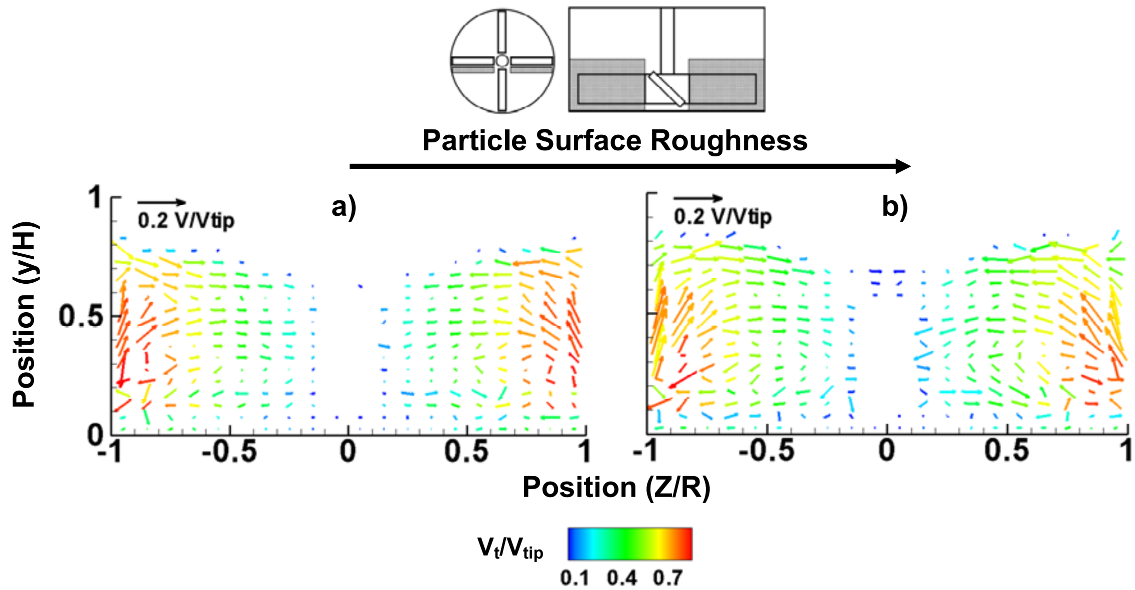

Figure 5.8. Simulation velocity field in front of the blades for different particle friction parameters. a) $\mu_s = 0.3$ and b) $\mu_s = 0.5$. In this figure the top tip of the blades is located at y/H = 0.5. Results obtained for a blade speed of 20 RPM.

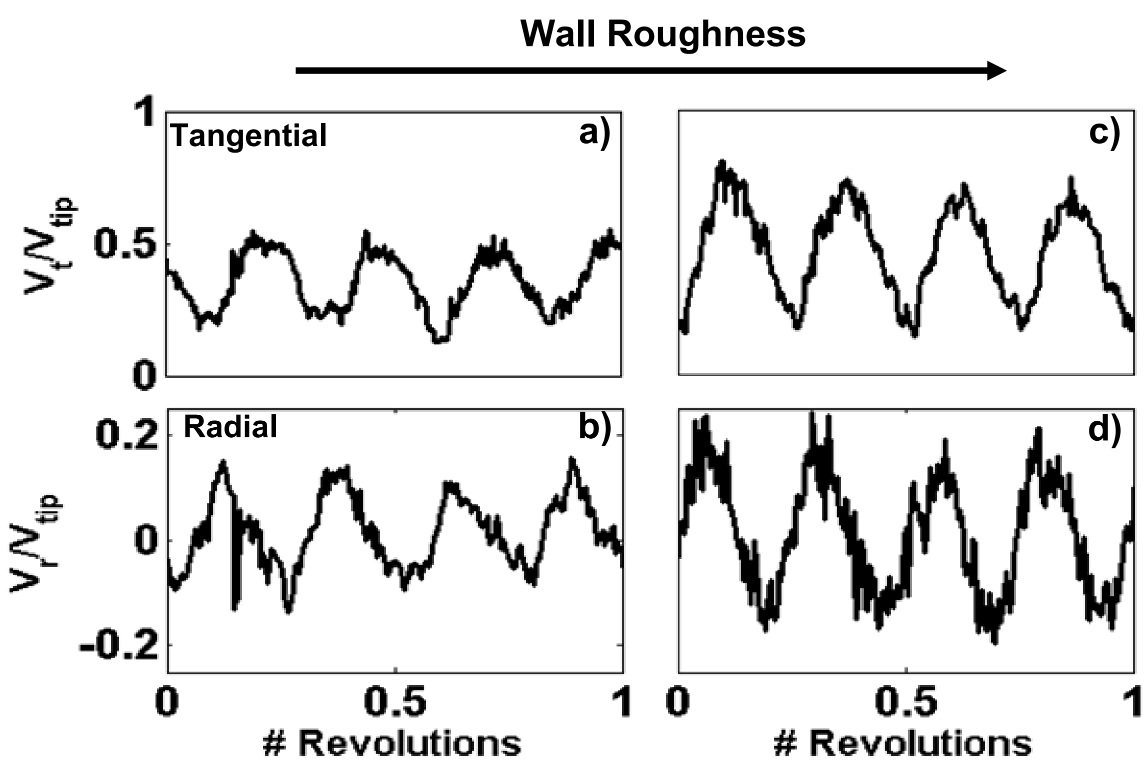

Figure 5.9. Effect of cylinder wall roughness on tangential and radial velocity fluctuations near free top surface at r/R = 0.5. a) Smooth wall tangential velocity, b) smooth wall radial velocity, c) rough wall tangential velocity and d) rough wall radial velocity. Results obtained for a blade speed of 50 RPM.

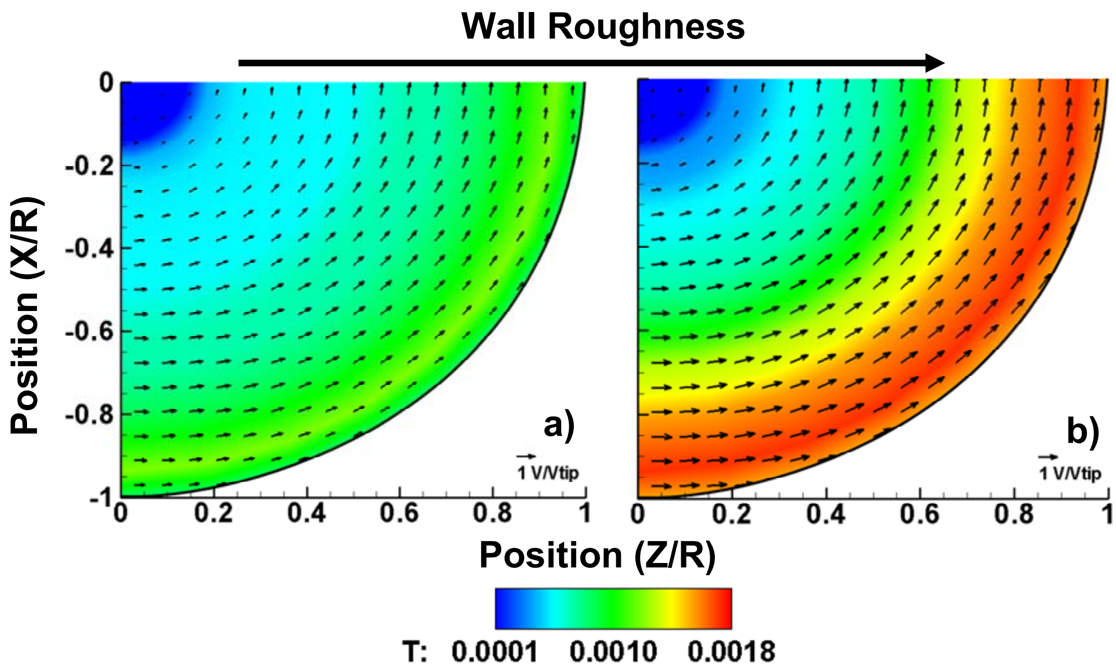

Figure 5.10. Effect of cylinder wall roughness on average velocity field and granular temperature near free top surface. a) smooth wall and b) rough wall. Granular temperature shown here has been averaged in the azimuthal direction and normalized by V_{tip}^2. Results obtained for a blade speed of 50 RPM.

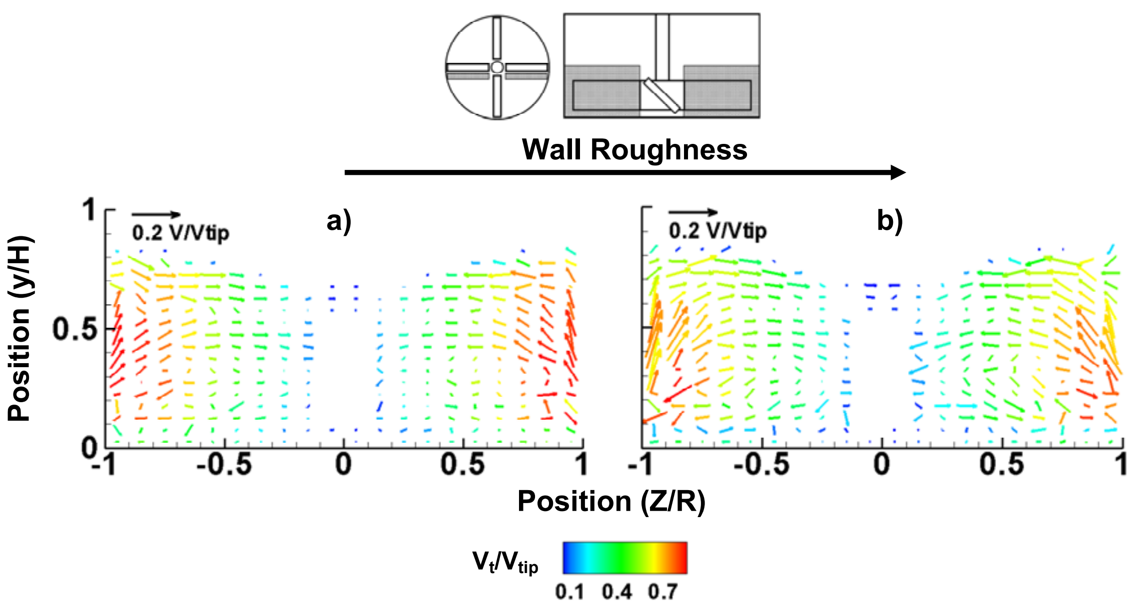

Figure 5.11. Simulation velocity field in front of the blades for different wall friction parameters. a) $\mu_s^{p-p} = 0.5, \mu_s^{p-w} = 0.3$ and b) $\mu_s^{p-p} = \mu_s^{p-w} = 0.5$. In this figure the top tip of the blades is located at y/H = 0.5. Results obtained for a blade speed of 20 RPM.

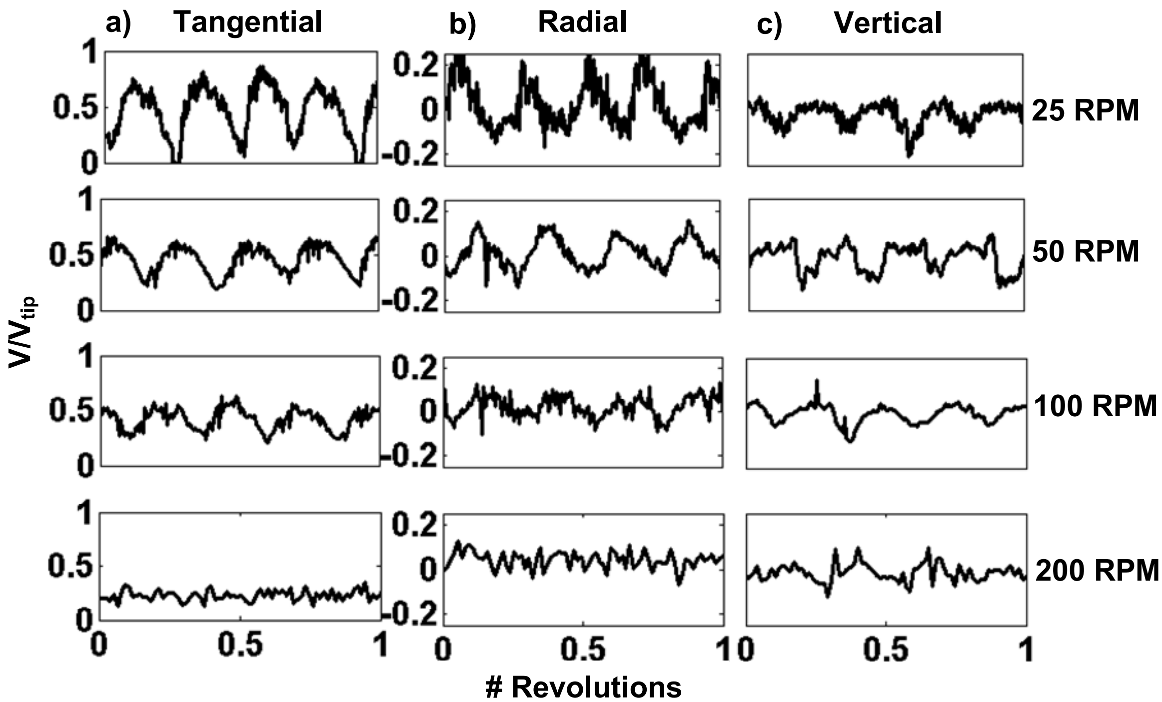

Figure 5.12. Effect of blade speed on tangential, radial and vertical velocity fluctuations. a) tangential velocity fluctuations, b) radial velocity fluctuations and c) vertical velocity fluctuations. The tangential and radial velocities were obtained on the top free surface at r/R = 0.5. The vertical velocity was obtained by the cylinder wall at y/H = 0.5.

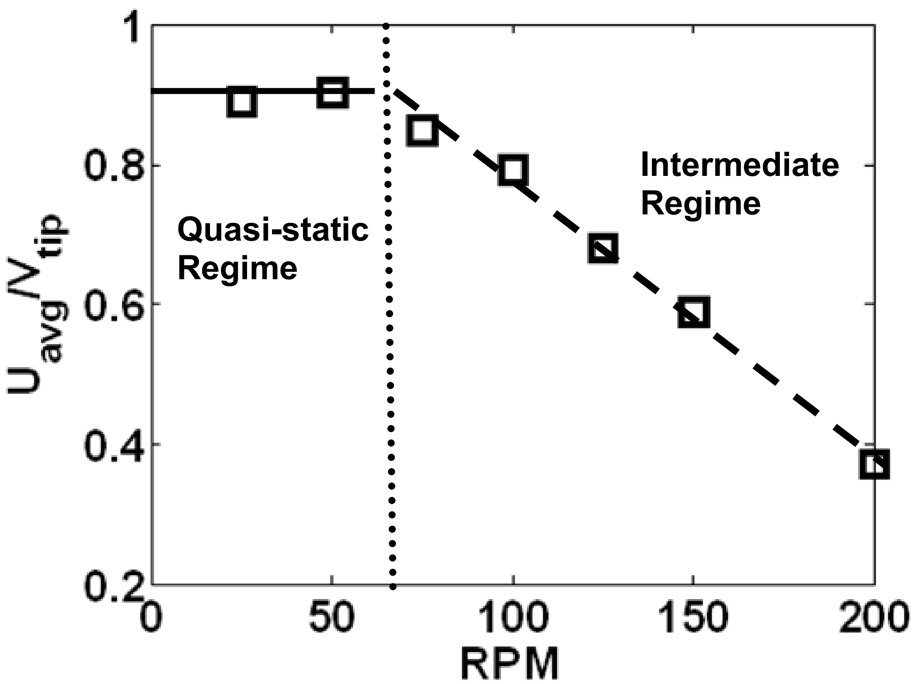

Figure 5.13. Effect of blade speed on average speed near the top surface.

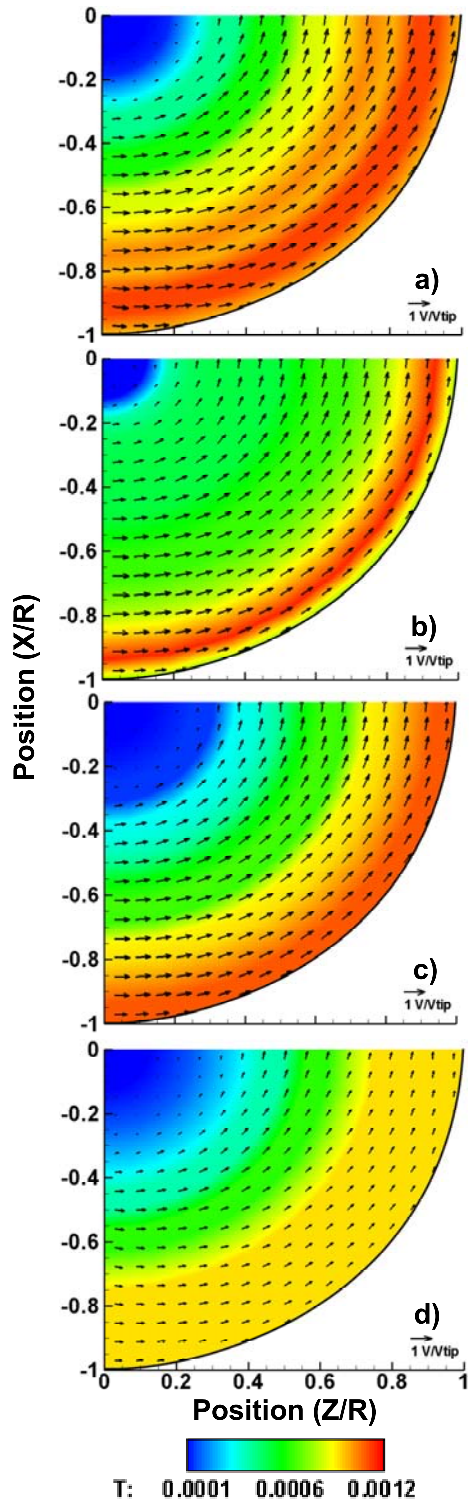

Figure 5.14. Effect of blade speed on time average velocity field and granular temperature. a) 25 RPM, b) 50 RPM, c) 100 RPM and d) 200 RPM. Granular temperature shown here has been averaged in the azimuthal direction and normalized by V_{tip}^2.

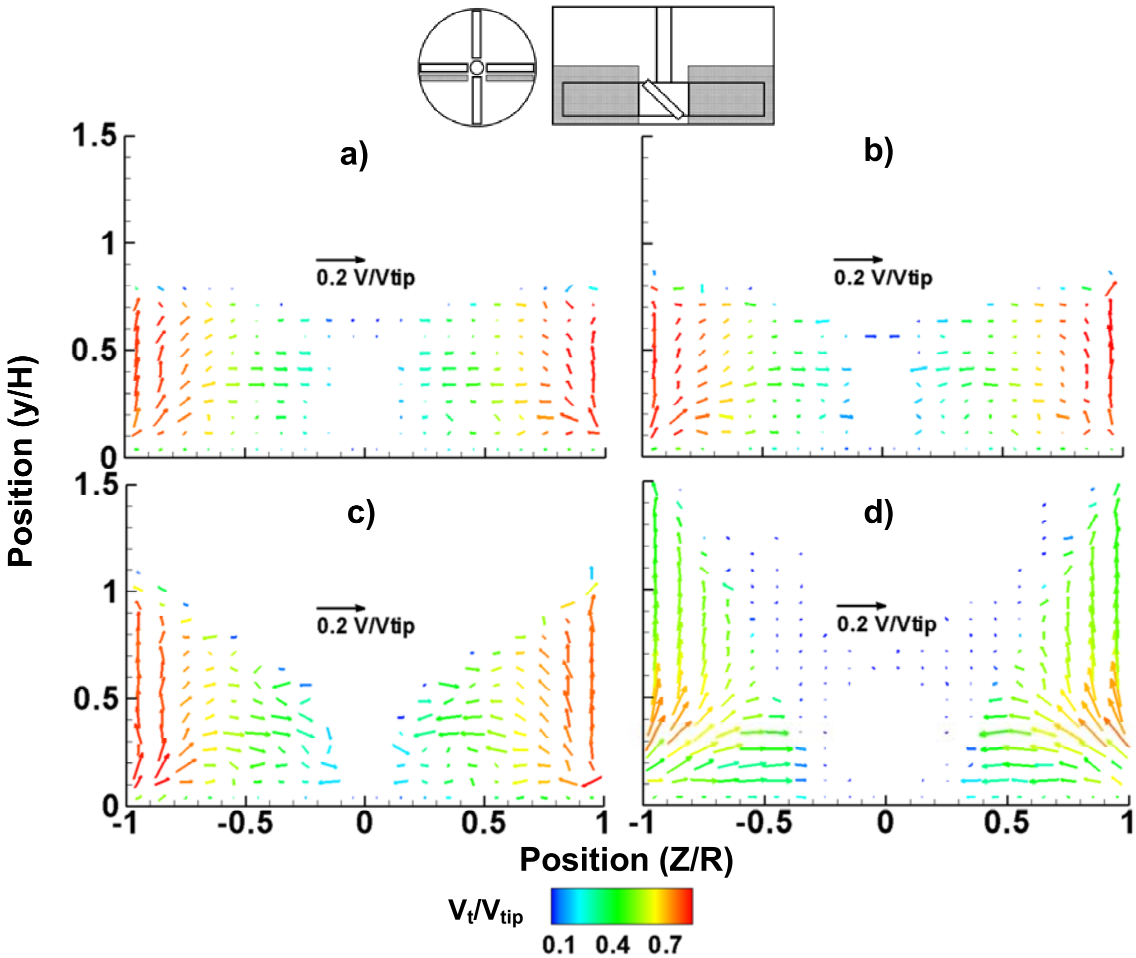

Figure 5.15. Simulation velocity field for different blade speeds. a) 3 RPM, b) 20 RPM, c) 55 RPM, and d) 120 RPM. In this figure the top tip of the blades is located at y/H = 0.5.

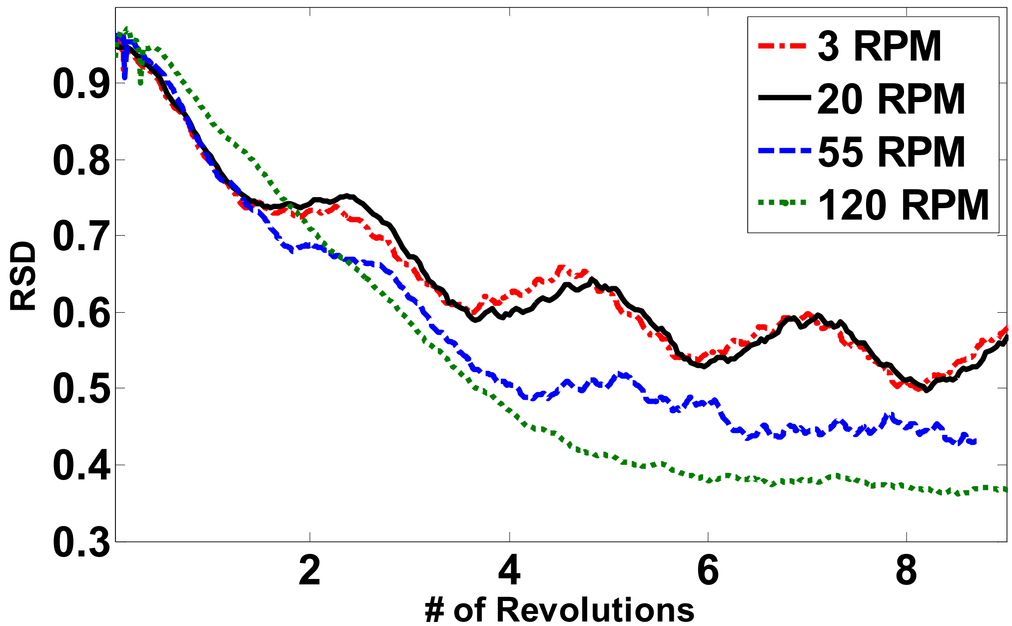

Figure 5.16. Effect of blade speed on mixing kinetics from simulations.

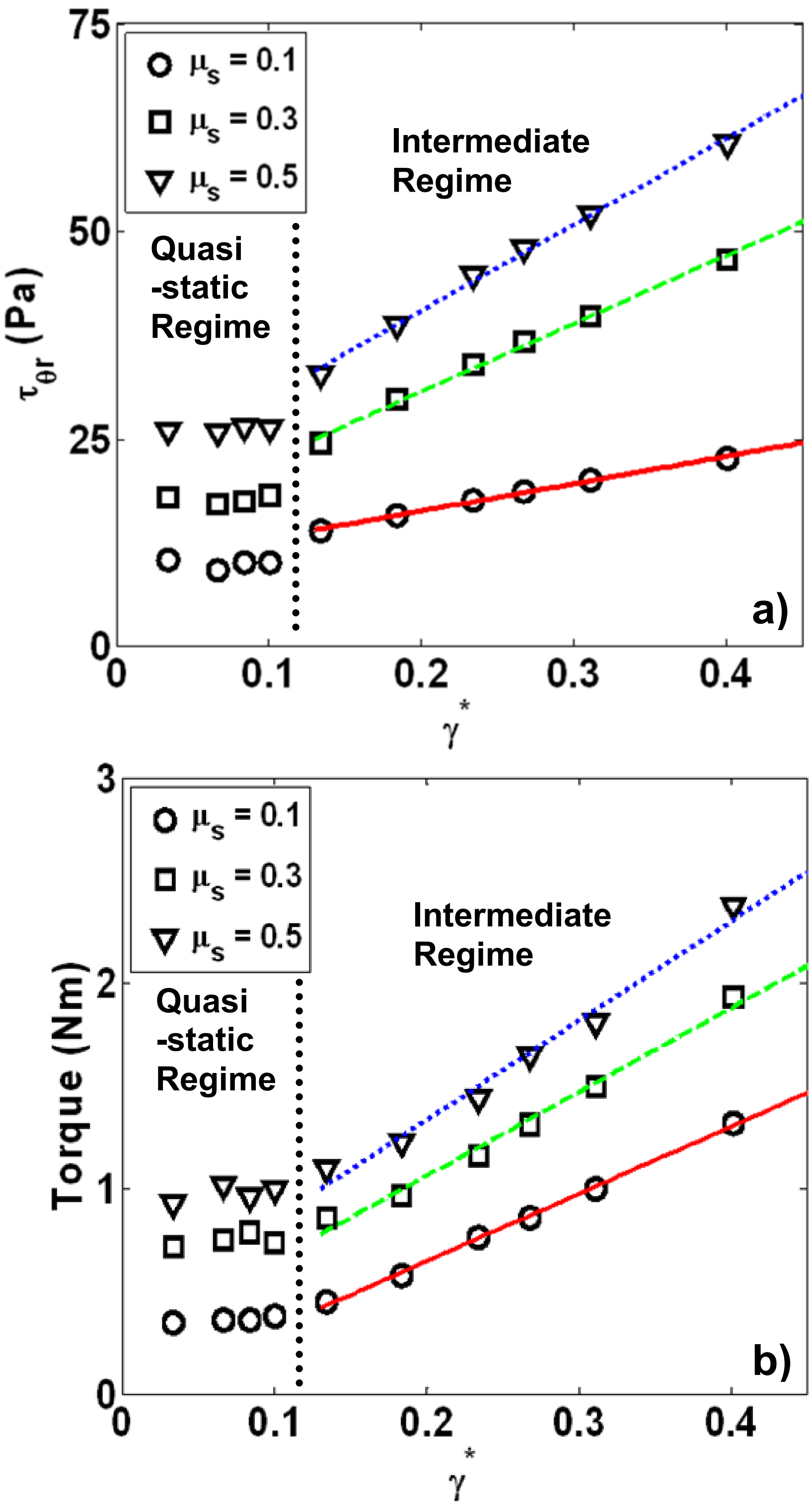

Figure 5.17. Effect of blade speed on average shear stress and blade torque from simulations. a) average $\tau_{\theta r}$ for particle located within span of blades vs. γ^* and b) average impeller torque vs. γ^*.

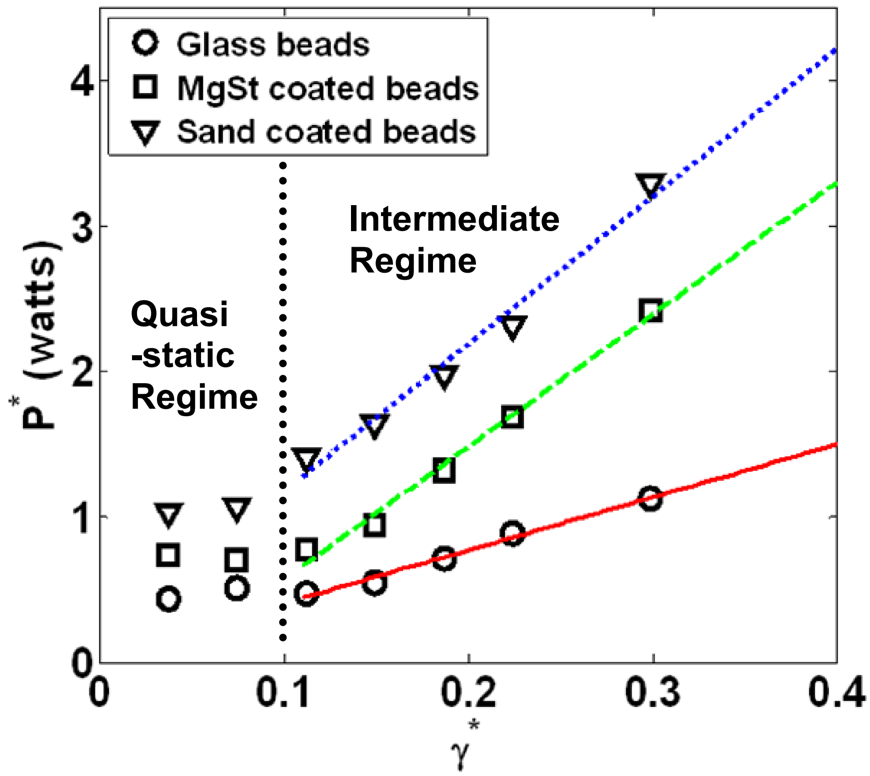

Figure 5.18. Effect of blade speed on adjusted blade power draw from experiments. The adjusted impeller power is obtained by subtracting the power draw at a specific RPM for the empty cylinder from the power draw for the impeller for the charged cylinder.

5.7. Tables for Chapter 5

Material	Mean μ	Standard deviation	Mean mass (mg)	Standard deviation (mg)
Glass beads	0.32	0.009	13.4	0.63
MgSt coated beads	0.38	0.008	13.8	0.68
Sand coated beads	0.55	0.013	15.6	0.42

Table 5.1. Experimentally determined particle properties. Macroscopic friction values were obtained via shear cell analysis.

μ_s	$D_{\theta\theta}$*	D_{rr} *	D_{yy}*	$Pe_{\theta\theta}$	Pe_{rr}	Pe_{yy}
0.3	7.3×10^{-4}	3.3×10^{-4}	9.6×10^{-4}	842	191	69
0.5	1.6×10^{-3}	7.5×10^{-4}	2.1×10^{-3}	360	110	46

Table 5.2. Effect of particle friction on normalized particle diffusivity and Peclet number from simulations.

$\mu^{p\text{-}p}$	$\mu^{p\text{-}w}$	$D_{\theta\theta}$*	D_{rr} *	D_{yy}*	$Pe_{\theta\theta}$	Pe_{rr}	Pe_{yy}
0.5	0.3	2.3×10^{-5}	1.0×10^{-5}	3.3×10^{-5}	617	164	56
0.5	0.5	4.0×10^{-5}	1.9×10^{-5}	5.4×10^{-5}	360	110	46

Table 5.3. Effect of wall friction on normalized particle diffusivity and Peclet number from simulations.

RPM	$D_{\theta\theta}$*	D_{rr} *	D_{yy}*	$Pe_{\theta\theta}$	Pe_{rr}	Pe_{yy}
3	6.7 x 10^{-4}	3.1 x 10^{-4}	9.1 x 10^{-4}	910	210	78
20	8.5 x 10^{-4}	3.3 x 10^{-4}	9.0 x 10^{-4}	719	151	69
55	2.0 x 10^{-4}	8.5 x 10^{-5}	4.8 x 10^{-4}	3550	587	207
120	1.1 x 10^{-4}	7.0 x 10^{-5}	2.1 x 10^{-4}	4726	671	330

Table 5.4. Effect of blade speed on normalized particle diffusivities and Peclet number from simulations. Particle diffusivities were computed with a Δt of ¼ of a revolution.

μ_s	Yield Stress (Pa)	Viscosity (Pa s)	R^2
0.1	9.7	1.1	0.996
0.3	14.5	2.6	0.995
0.5	19.7	3.3	0.996

Table 5.5. Effect of microscopic friction on apparent visco-plastic parameters from simulations. These values were obtained by fitting a visco-plastic model to the data plotted on Figure 5.17a for $\gamma^* > 0.1$.

Chapter 6. Polydisperse, Cohesionless Flows

Industrial bladed mixer operations often involve components with different particle sizes or with size distributions. Few studies are found in the literature which investigate the effect of particle size differences on flow and segregation in bladed mixers. Thus far, the segregation studies performed in bladed mixers have focused on the behavior of binary mixtures of small and large particles [106, 109]. In this chapter, the effect of increasing polydispersity on flow and segregation in bladed mixers is discussed. Experiments and DEM simulations were performed to investigate the flow, segregation patterns, mixing kinetics and stresses that develop in granular beds containing multiple particle sizes. A detailed comparison between the experimental results and the DEM results is included for a base case consisting of a binary mixture. DEM simulations were used to study the effect of increasing the amount of intermediate particle sizes in the system while keeping the small to large particle size ratio the same.

The experimental and computational results discussed in this chapter were obtained for fill levels just covering the top of the blades. The total mass of the particle bed was divided equally among the number of species in the mixture in both the experiments and the simulations (i.e. equal mass fractions for each component). Since densities of the particle species were the same, the equal mass fractions correspond to equal volume fractions. DEM simulations discussed in section 6.1 were carried out using the same mixer dimensions (Table 2.3) and the same number of particles as in the laboratory experiments to enable a one-to-one comparison. The DEM results for the rest of this chapter (sections 6.2 to 6.3) were obtained for the base case mixer dimensions (Table 2.1) in order to facilitate the comparison of the polydisperse results with the monodisperse results discussed in previous chapters. Experimental results were obtained for a blade speed of 25 RPM. Simulation results listed in section 6.1 were obtained at 25 RPM while the results in sections 6.2 and 6.3 were obtained at 10 RPM.

6.1. Binary mixtures - DEM Results vs. Experimental Results

In this section, the behavior of a binary mixture with equal mass fractions of 2 mm and 4 mm particles in the laboratory bladed mixer unit (Table 2.3 dimensions) is discussed. Previous bladed mixer studies performed with monodisperse particles highlighted several flow features which are known to cause size segregation in other granular systems such as granular temperature gradients, heap formation [45] and the occurrence of avalanches at several frequencies [106]. Figure 6.1 shows the segregation patterns observed at the top surface and by the sidewalls for the experiments and simulations. Starting from an initial, well mixed state, the particle bed begins to segregate as the blades are set to rotate. The small particles accumulate near the impeller shaft and the cylinder's bottom plate while the large particles accumulate near the top free surface and by the cylinder walls. This segregation pattern is consistent with the patterns observed by Conway et al. [106] and Zhou et al. [109] for conditions similar to the ones used here. In general, good qualitative agreement is obtained between the experimental segregation patterns and those obtained from the DEM simulations. These patterns indicate that sieving is the dominant segregation mechanism in this system. In sieving segregation, the smaller particles fall through the gaps that are formed between larger particles during flow as a result of localized shearing [62]. In effect, the shearing action of the blades which is intended to promote mixing causes the segregation of the particle bed.

The rate of segregation in this system is fast, with some signs of segregation appearing after 1 revolution and with a fully segregated statistical steady state obtained after just 5 revolutions. It is interesting to note that for monodisperse systems, a well mixed state is reach after 5 revolutions for similar system conditions (see Chapter 3). Further shearing of the particle bed does not result in mixing as can be observed from the snapshots taken at 10 revolutions. As the small particles percolate through the bed, they form close-packed structures near the bottom plate and in front of the blades. These packed structures reduce the probability of large particles finding a void of sufficient size that would allow them to penetrate to the bottom of the bed. Thus, the large particles remain near the top surface. After segregation occurs, the blades pick up some of the small particles located at the bottom moving them towards the top. However, these particles flow past the blades and fall to the bottom behind the blades leading to no significant change in their vertical position in between blade passes.

Normalized large particle concentration profiles at the sidewalls and top surface for the experiments and the simulations are displayed in Figure 6.2 at different revolutions. The local large particle concentration, C_{large} has been normalized by $\left\langle C_{large} \right\rangle$, the average large particle concentration in the whole system: $C^*_{large} = C_{large} / \left\langle C_{large} \right\rangle$. Side view concentrations are shown in Figures 6.2a-6.2c and top surface concentrations in Figures 6.2d-6.2f. After 1 revolution, a gradient in the C^*_{large} profile emerges along the vertical direction (Figure 6.2a) and the radial direction (Figure 6.2d). The large particle concentration at the top is more uniform after 1 revolution (Figure 6.2d) when compared to the side view concentration profile (Figure 6.2a). It should be noted that the y-axis scales in Figures 6.2a and 6.2d are different.

Larger $C*_{large}$ gradients along the radial direction are obtained after 10 revolutions (Figures 6.2f). Additionally, the extent of segregation is most significant along the vertical direction with local concentration values ~ 8 times the total average concentration near the top of the particle bed for the fully segregated state (Figures 6.2b and 6.2c). This behavior is expected for systems in which sieving segregation occurs. Some differences are obtained between the experimental profiles and the simulation profiles. The large particle concentration near the middle of the bed in Figure 6.2b is higher for the simulation than for the experiment causing the concentrations at the top to be slightly lower. Additionally, the extent of radial segregation after 10 revolutions is higher in the simulation. However, the simulation results show the same general trends as the experimental results.

Average surface velocity profiles and granular temperature trends are shown in Figure 6.3 for the experiments and the simulations. Experimental velocity measurements were obtained using PIV. For the DEM simulation, only the velocities of the particles located 0.75 particle diameters away from each surface were included in the calculation. The size of the control area used for the calculation of granular temperature was 5 mm x 5 mm. Here, granular temperature values are normalized by V_{tip}^2 and have been averaged in the azimuthal direction. The average velocity field near the top free surface in the experiment (Figure 6.3a) is qualitatively very similar to that of the simulation (Figure 6.3c), with particle velocities increasing near the cylinder wall. Side view particle velocities near the wall are roughly 50% of the tip speed of the blades (Figures 6.3b and 6.3d). This is due to the frictional nature of the particle-wall interaction which lowers particle velocities and gives rise to slip-stick behavior.

Granular temperature maximums are obtained near the cylinder wall and at the top surface in both the experiment and the simulation. High temperatures by the cylinder wall and the top free surface have also been observed for monodisperse bladed mixer flows (see Chapter 3). The high temperature by the wall is due to wall friction, which shears the material close to the wall and induces a degree of randomness to the velocities of the particles after hitting the wall. Granular temperature gradients lead to increases in the thermal diffusion and pressure diffusion forces, two of the main driving forces for segregation [23]. For densely packed systems, kinetic theory predicts that large particles will accumulate near high temperature regions and that small particles will migrate towards lower temperature regions [180]. Our results are consistent with the kinetic theory predictions and further indicate the occurrence of sieving segregation. A stronger temperature gradient is obtained in the DEM simulations near the top surface and by the side walls when compared to the experiment. This increase might explain some of the differences observed in the large particle concentration profiles.

The differences observed between the experiments and the DEM simulations could be caused by a number of factors such as differences in particle properties, wall friction and slight polydispersity (present in each glass bead type used, but not accounted for in the simulations). Despite the small discrepancies, the general trends obtained for both the experiments and the simulation are similar. The DEM simulations qualitatively capture the segregation patterns obtained experimentally, the magnitude of the particle velocity relative to the tip speed of the blades and the granular temperature gradients that exist within the particle bed.

6.2. Effect of Increasing Polydispersity

Most granular materials are characterized by a higher degree of polydispersity than that of a binary mixture. Understanding the effect of increased polydispersity on flow and segregation is necessary for the design and scale-up of reliable bladed mixer processes. Figure 6.4 compares the experimental segregation profiles at the sidewalls observed for a binary system to those obtained for a ternary system. The ternary system consists of 2 mm, 3 mm and 4 mm beads at equal mass fractions. The degree of polydispersity in the system has been increased by adding an intermediate particle size while keeping the large (4 mm) and small (2 mm) particles the same as in the binary system. The total mass of the ternary system is equal to the total mass of the binary system. While segregation occurs in both the binary and ternary mixtures, Figure 6.4 shows that the extent of segregation is lower for the ternary system. The presence of the intermediate particle size reduces the large particle concentrations towards the top of the particle bed. During the early stages of shearing the effect is not as pronounced (Figures 6.4c and 6.4d). However, after 10 revolutions, the normalized concentration of large near the top is reduced by ~25%. Introduction of intermediate particle sizes has been shown to reduce segregation in vibrated beds [66, 181] and fluidized beds [182]. The experimental results suggest that this trend also occurs in bladed mixers and that segregation can be reduced by increasing the degree of polydispersity.

Experiments with additional number of intermediate particles sizes are difficult to implement as glass beads are only available in a limited number of sizes. However, DEM simulations can easily include the effect of multiple particle sizes. Simulations were performed for 4 different systems: binary, ternary, a 5 particle size system and an 11 particle size system. The last system can be viewed as possessing a pseudo-continuous particle size distribution. The mixer dimensions listed in Table 2.1 were used for the simulations discussed in the remainder of the paper. The largest and smallest particle sizes were 10 mm and 5 mm. The ratio of the mixer diameter to the particle diameter for the small and large in the simulations is similar to the experimental ratio. In each case the total mass charged to the cylinder was divided equally among the number of species in the mixture i.e. equal mass fractions of each component. In addition, the sizes of the intermediate particles were evenly spaced between 5 mm and 10 mm. The binary system consists of 5 mm and 10 mm particles. The ternary system consists of equal masses of 5, 7.5 and 10 mm particles. The 5 particle system consists of equal masses of 5, 6.25, 7.5, 8.75 and 10 mm particles. The 11 particle size system consists of equal masses of 5, 5.5, 6, 6.5, 7, 7.5, 8, 8.5, 9, 9.5 and 10 mm particles.

Initial and final snapshots for the 4 different systems are shown in Figure 6.5. The final snapshots were taken after 5 revolutions, as the degree of mixing analysis (discussed later in this section) showed that the mixing (or de-mixing) curves level off within 5 revolutions. Here the particles have been colored according to their size. For the binary system, the top surface of the particle bed consists of mostly large particles, with a limited amount of small particles located where the blades are present. Similar to what was observed in the experiments; these particles flow past the bed and acquire no net vertical movement in-between blade passes. However, as polydispersity is increased, larger amounts of small and intermediate particles are observed at the top surface of the bed. Table 6.1 lists the normalized large particle concentrations at the top surface and cylinder wall. For the values listed in Table 6.1, only the particles located 1 large particle diameter away for each surface were included in the calculation. The C^*_{large} top surface values were averaged along the radial direction while the C^*_{large} cylinder wall values were averaged along the height of the bed. It should be noted that $\langle C_{large} \rangle$, the average particle concentration in the whole bed, changes as the degree of polydispersity changes. However, by normalizing the concentration of large particles by $\langle C_{large} \rangle$, we can compare the relative amounts of segregation. Increasing the number of particle sizes to 11 decreases the large particle concentration by ~35% from the binary case value. The final side view snapshot for the binary system shows the formation of two distinct particle layers. As intermediate sizes are added to the system, the formation of segregated particle layers is reduced. Normalized large particle concentrations are reduced by ~30% by going from a binary system to an 11 particle size system. While segregation still occurs in all the systems studied, the extent of segregation is reduced by increasing the degree of polydispersity.

The mitigation of segregation with increased polydispersity can be explained by close examination of particle kinematics and packing densities. For monodisperse systems, a 3 dimensional recirculation zone develops in front of the blades which promotes vertical and radial mixing [45]. As the intensity of the recirculation zone increases, monodisperse mixing kinetics increase. Figure 6.6 shows normalized mass flux fields that developed in front of the blades for each of the systems studied. Mass fluxes have been normalized by the density of the particles and the tip speed of the blades, $\dot{M}_{flux} = M_{flux} / \rho_p V_{tip}$, and have been averaged in time. In Figure 6.6, the impeller shaft is located on the right hand side of the graphs and the cylinder wall on the left hand side.

The lengths of the vectors in Figure 6.6 have been capped to an upper limit of 0.01 in order to examine the motion of the particles within the center of the bed (the area of lowest particle movement in monodisperse systems). The magnitude (uncapped) of the vector is represented by the color of the vectors. For all cases, mass flux values are highest by the wall and lowest by the impeller shaft, similar to what is observed in monodisperse systems. In the binary system, very little particle movement is observed near the center of the bed (Figure 6.6a). This region is characterized by a large concentration of small particles. Additionally, the particles located by the walls have very little radial movement, indicating that these particles flow past the blades and cannot penetrate the center of the particle bed. As the amount of polydispersity is increased (Figures 6.6b-6.6d), the movement of the particles near the center of bed increases. Particles flow down by the impeller shaft and then move radially outward towards the cylinder wall. Particles near the wall are able to flow radially towards the center of the bed. Figure 6.6 shows that increasing polydispersity promotes particle convection within the bladed mixer leading to an increase on the intensity of the recirculation zone.

In addition to affecting convective particle motion, the degree of polydispersity also affects diffusive particle motion. The diffusivities values discussed in this chapter have been normalized by the tip speed of the blades (V_{tip}) and the particle diameter (*d*). Table 6.2 lists normalized particle diffusivities and Peclet numbers for all the particles present in the different cases. Increasing the degree of polydispersity leads to an increase in particle diffusivities which suggest that diffusive mixing is enhanced by the presence of intermediate particle sizes. Particle diffusivities increase by ~ 50% for the 11 particle sizes system vs. the values obtained for the binary system. In all cases, the Peclet numbers obtained are much higher than unity, indicating that convection is the dominating mechanism for particle transfer. This is consistent with the behavior observed in monodisperse systems [183]. However, Peclet numbers decrease with increasing polydispersity indicating an increase on the contribution of the diffusive mechanism relative to the convective mechanism.

Table 6.3 and Table 6.4 list particle diffusivities and Peclet numbers for the 5 and 10 mm particles respectively. Diffusivities increase for both types of particles and Peclet numbers decrease as the number of particle sizes is increased. These results indicate that both the 5 mm and 10 mm particles experience increased diffusive motion as the number of intermediate particle sizes is increased, and that the results listed in Table 6.2 are not an artifact of the change in the particle size distribution. For all the cases studied, normalized diffusivities are higher for the 5 mm particles when compared to the 10 mm particles. However, Peclet numbers are lower for the 10 mm particles. While the 5 mm particles have larger diffusivities relative to their size, particle diffusion plays a more important role in the transport of the 10 mm particles.

As more intermediate particle sizes are introduced into the system, particle flow kinematics is improved. This increase in convective and diffusive motion promotes a mixing mechanism which reduces the effect of segregation via the sieving mechanism. Sieving forces drive the small particles to accumulate near the cylinder bottom plate and by the impeller shaft. For a binary system, the small particles become trapped as these areas are characterized by low particle movement. Particle movement near the bottom plate and the impeller shaft increases as the degree of polydispersity is increased. The presence of intermediate particle sizes enhances particle transport for the all species present in the bed allowing the small (and large) particles to mix as the blades are rotated.

The changes in particle motion are accompanied by changes in the packing structure of the particle bed. Figure 6.7 displays time averaged void fraction profiles in front of the blades as a function of normalized radial position (r/R). Void fractions were calculated by creating spherical control volumes in front of the leading edge of the blades. The volume of the particles inside the control sphere plus the overlap volume of particles near the edges are subtracted from the volume of the control sphere to give the local void fraction. These values are then averaged in time and along the radial direction. The diameter of the spherical control volumes was 27 mm. As the polydispersity is increased, void fraction in front of the blade increases. It has long been demonstrated that the packing of spheres is a function of particle size distribution [184, 185]. Our previous computational work on monodisperse spheres showed that the highest particle densities are obtained in front of the blades [45]. Here, we see that addition of intermediate particle sizes (without increasing the maximum size ratio) leads to a less dense packing in front of the blade. The void fraction increases by ~ 6% for the 11 particle size system from the binary case value. Decreases in packing density with the addition of intermediate particle sizes have been reported in the literature for static packing of spheres [186-188]. These studies showed that for spherical particle mixtures with a 2:1 large to small size ratio, addition of an intermediate particle size at equal volume can increase void fraction by up to 2%. In the bladed mixer case, addition of intermediate particle sizes decreases void fraction during flow. For flow to occur in dense granular systems, the particle bed needs to expand or dilate as steric hindrances must be overcome to achieve particle motion

[189]. A higher degree of dilation in the bladed mixer allows the particles to move more freely throughout the particle bed, with a corresponding increase in convective and diffusive particle motion.

Figure 6.8 shows probability frequency distribution for the void fraction within the bladed mixer for the binary and 11 particle sizes beds. Frequency distributions were calculated by creating spherical control volumes throughout the particle bed and calculating the void fraction in each control volume over a period of 1 revolution. The diameter of the spherical control volumes was 27 mm. Figure 6.8 shows a shift to the right of the graph for the 11 particle size distribution when compared to the binary frequency distribution. This indicates that a larger portion of the particle bed is characterized by higher void fractions. Larger voids increase the probability of a large particle finding an accommodating void, allowing it to penetrate deeper into the particle bed thus reducing the effect of sieving segregation.

We have demonstrated that mixing mechanisms become more prominent in bladed mixers as the degree of polydispersity is increased from that of a binary system. The final extent of segregation depends on the competition between the mixing and segregation mechanisms. As discussed by Metzger et al. [181], in order for particles to segregate, different sized particles must move at different velocities in the system which leads to a segregation flux [190]. If all particles always moved at the same velocity, segregation would not occur. If a particle is surrounded by other particles of very different sizes then one would expect a higher segregation flux than if a particle is surrounded by other particles that are close to its own size. However, if we only have segregation (and no mixing) then given enough time the system would evolve to a completely segregated state, which is not what is observed in this work.

To characterize the extent of mixing (or de-mixing) across the different cases, we perform statistical analysis on the particle concentrations throughout the entire particle bed. For polydisperse systems, a metric capable of characterizing mixing in systems composed of multiple particle sizes is required for a fair comparison across systems. The mixing metric, M [156], is used to calculate degree of mixing for polydisperse systems. This metric considers the variation in concentration of each particle size in the system. A perfectly mixed system would yield $M = 1$ while a fully segregated system would yield $M = 0$.

Figure 6.9 shows the extent of mixing as a function of number of revolutions for the 4 cases studied. Plotted along with the mixing profiles are the initial slopes of the curves. The slopes represent the rate of segregation (or de-mixing) during the transient period before the systems reach their final statistical steady state. As the number of intermediate particle sizes is increased, the system becomes less segregated, or better mixed. The rate of segregation during the transient period is also significantly reduced. The binary system segregates 5 times faster than the 11 particle size system. This analysis shows that the concentrations of all particles species (not just the large ones) within the mixer become more uniform as polydispersity is increased. Therefore, the importance of the mixing mechanism relative to the segregation mechanism increases as polydispersity is increased.

6.3. Normal and Shear Stress Profiles

In this section, we discuss the effect of polydispersity on the normal and shear stress profiles that develop inside the mixer. We focused our attention on the average normal stress and the shear stress component in the plane of the blade rotation, $\tau_{\theta r}$. Normal and shear stress values obtained for each simulation were normalized by the quantity $\rho_p gH$, where ρ_g is the particle density and H is the maximum height of the particle bed.

Figure 6.10 shows the normalized pressure ($P^* = P/\rho_p gH$) and shear stress ($\tau^*_{\theta r} = \tau_{\theta r}/\rho_p gH$) profiles at r/R = 0.5 as a function of mixer height and number of revolutions for the binary case once the system has reached a statistical steady state. Figures 6.10a-b show the total values of P^* and $\tau^*_{\theta r}$. Figures 6.10c-d show the portion of the P^* and $\tau^*_{\theta r}$ values which are generated by the 5 mm particles while Figures 6.10e-f show the portion generated by the 10 mm ones. When a contact involved both a 5 mm and 10 mm particle, the stress generated was divided so that 50% of the stress generated was added to the 5 mm stress values and the remaining 50% to the 10 mm stress values. All the profiles shown in Figure 6.10 display a periodic behavior with the main fluctuation frequency equal to that of the blade rotation. The pressure profiles show that the particle bed is compressed in front of the blades and dilates in between blade passes. The mean and amplitude of the pressure fluctuations are a strong function of mixer height while the shear stress fluctuations are invariant of height within the span of the blades (y/H < 0.5). This behavior is analogous to what was observed in monodisperse systems [45]. Figure 6.10c shows that the 5 mm particles generate a larger amount of pressure than the 10 mm particles (Figure 6.10e). As the small particles accumulate near the bottom plate due to sieving segregation, these particles sustain the weight of the particles above leading to the more pronounced pressure fluctuations. These results suggest that smaller particles would experience higher compression forces within bladed mixers for systems in which sieving segregation occurs. The pressure fluctuations generated by the 10 mm particles are ~ 50% that of the 5 mm particles. A similar trend is observed for $\tau^*_{\theta r}$ profiles; the 5 mm particles (Figure 6.10d) generate higher shearing forces than the 10 mm particles (Figure 6.10 f). Smaller particles therefore experience higher shearing forces within bladed mixers due to the occurrence of segregation. Similar periodic behavior was observed for the remaining stress tensor components (not shown). However, the values for $\tau_{\theta y}$ and τ_{ry} fluctuate around zero. Differences in stresses between particle species would result in different rates of agglomeration and breakage for bladed mixer operations such as wet granulation or agitated drying. In addition to affecting quality of mixing, sieving segregation would also affect the ability to control the particle size distribution through breakage and agglomeration.

Figure 6.11 shows time averaged P^* and $\tau^*_{\theta r}$ for all the different cases studied. The P^* profiles are displayed in Figure 6.11a as a function of normalized height. Normalized pressure increases linearly towards the bottom of the mixer for all the cases studied. The solid line in Figure 6.11a represents the hydrostatic pressure line for an average solids fraction of 0.55. This shows that, despite the complex dynamics observed in polydisperse systems, at low fill levels the average pressure inside the bladed mixer can be approximated by hydrostatics. This is consistent with the behavior observed in monodisperse systems [45]. Figure 6.11a also shows that the pressure for the 11 particle size system is slightly lower than for the other systems. This is attributed to the higher void fraction observed in the 11 particle size case. While differences in void fraction were observed for the other polydisperse systems, these differences do not appear to affect the time averaged pressures or stress.

The $\tau^*_{\theta r}$ profiles are displayed in Figure 6.11b as a function of normalized radial position. Average stress values for all the cases studied are one order of magnitude lower that the pressure values, a behavior consistent with that of monodisperse systems. This trend suggests that the polydisperse flows occur in the quasi-static or slowly deforming regime for the range of operating conditions studied here. Shear stress is highest by the cylinder wall and close to zero near the impeller shaft. This is due to the increased tangential movement of the particles near the wall and due to wall friction. The $\tau^*_{\theta r}$ values for the 11 particle size system are smaller than the $\tau^*_{\theta r}$ values for the other systems. As shear stress values scale with the total pressure in the quasi-static regime [183], the lower $\tau^*_{\theta r}$ values are due to the increased dilation observed in the 11 particle size system.

The effect of particle size distribution on the partial pressure and shear stress generated by the 5 mm and 10 mm particles is shown in Figure 6.12. The values shown in Figure 6.12 were calculated by taking the total average pressure and stress generated by each particle type and dividing them by the average pressure in the bed (P / P^{total} and $\tau_{\theta r} / P^{total}$ respectively). Figure 6.12a shows P / P^{total} values for the 5 mm and 10 mm particles as a function of number of particle species in the mixer. The partial pressure of both particle species decreases as the number of particle species is increased. Stresses in bladed mixers at the conditions studied here are generated by sustained particle contacts, and the number of contacts for each particle species is reduced as more intermediate particle sizes are introduced (i.e. equal mass systems). However, this decrease does not follow a linear relationship and values appear to level off for the 11 particle size system. The 5 mm particles generate a higher amount of pressure than the 10 mm particles for all the examined cases. This is due to the accumulation of small particles towards the bottom plate and the increased number of 5 mm particle contacts. However, as the number of intermediate particle sizes is increased, the differences in partial pressure between the 5 mm and the 10 mm particles decrease. According to Zhou et al. [109], differences in the forces (i.e. stresses) experienced by each particle size lead to a driving force that leads to segregation as different forces result in different velocity profiles. Figure 6.12a shows that the magnitude of this driving force is reduced as intermediate particle sizes are added to the system. Similar trends are observed for the values of $\tau_{\theta r} / P^{total}$ (Figure 6.12b). The 5 mm particles generate a higher amount of stress than the 10 mm particles. The difference in $\tau_{\theta r} / P^{total}$ between the particle types decrease as the number of particle species is increased, although this effect is not as pronounced as for the pressure values.

In addition to affecting average stress values, increasing polydispersity leads to changes in the distribution of forces throughout the particle bed. In quasi-static flows, the main mechanism for momentum transfer comes from the formation of contact force chains [19]. A force chain is a network of interparticle contacts in which force is transmitted along the contact path. Figure 6.13 shows instantaneous normal contact force networks in the horizontal plane for the binary and 11 particle size systems. Here, each line represents the contact vector connecting the center of the particles and the thickness of the line represents the magnitude of the normal force associated with that contact. Higher forces are represented by thicker lines and vice versa.

The normal contact force network obtained for the binary system is shown in Figure 6.13a along with the distribution of the particles in Figure 6.13b. Two different regions are observed in Figure 6.13a. The region near the blade (where the small particles accumulate) is characterized by many short contacts chains each carrying a lower amount of load. In contrast, the region behind the blade (where the large particles accumulate) is characterized by fewer, longer contacts, but each of these contacts carries a higher amount of load. This disparity in force distribution prevents the transfer of energy from the blades deep into the particle bed. It has been shown that in static granular systems, contact chains posses a characteristic length of a few particle diameters [191]. As the small particles cannot form long contact chains, momentum transfer into the center of the bed is hindered. A different force distribution is observed for the 11 particle size system. In general, there is a smaller number of contacts for the 11 particle size case. However, the two distinct regions observed in the binary case are no longer present leading to a more uniform force distribution. As small, intermediate and large particles are present in front of the blades; longer contact chains that carry higher amounts of loads can develop. These contacts chains enable the transfer of energy from the blades into the center of the particle bed.

To demonstrate that the length and amount of force carried by contact chains is a function of particle size in bladed mixers, we show normal contact forces networks in Figure 6.14 for monodisperse beds of 5 mm and 10 mm particles. The 5 mm contact network (Figure 6.14a) is comprised of a larger number of interparticle contacts, but each contact carries a relatively small amount of load. The average length of contact chains in the 5 mm system is also smaller. In contrast, the 10 mm force network (Figure 6.14b) is characterized by a smaller number of contacts but each contact carries a higher amount of load. These high load contacts lead to the formation of longer contact chains which penetrate deeper into the particle bed. Comparing the monodisperse networks to the binary case network, one can see that the region in front of the blade is very similar to the contact force structure for the 5 mm monodisperse case, while the region behind the blade resembles that of the 10 mm monodisperse case. The addition of intermediate particle sizes enables the formation of longer contact chains which carry a higher amount of load since the number of small particle contacts is reduced while the number of intermediate and large particle contacts is increased.

6.4. Conclusions for Polydisperse Flows

Experimental and computational methods were used to study the flow and segregation of polydisperse systems in bladed mixers. The ability of DEM simulations to accurately capture experimental behavior for polydisperse systems was demonstrated. Segregation patterns, particle velocities and granular temperature profiles obtained from the simulations are in good qualitative agreement with those obtained experimentally. For a binary system with a size ration of 2:1, segregation by size occurs as the blades are rotated due to a sieving mechanism. Small particles accumulate near the bottom plate of the mixer while large particles accumulate near the top free surface and the cylinder walls. Segregation in the binary system is fast, with a fully segregated system observed after just 5 revolutions.

DEM simulation results showed that the extent of segregation is reduced as the degree of polydispersity is increased while the maximum size ratio is kept constant (2:1). Introducing additional intermediate particle sizes in between the smallest and the largest particles leads to increases in the convective and diffusive motion of the particles in the system. This increase in convective and diffusive motion promotes a mixing mechanism which reduces the extent of segregation via the sieving mechanism. The enhancement of flow kinematics is accompanied by differences in packing structure within the particle bed. As the degree of polydispersity is increased, higher void fractions develop in front of the blades which allow the particles to move more freely. Higher void fractions also increase the probability of larger particles finding accommodating voids in the particle bed reduced the extent of sieving of the small particles.

Normal and shear stress profiles are also affected by the degree of polydispersity within the mixer. While total stress values show similar trends to what is observed in monodisperse systems, lower stresses were observed for the system with the highest degree of polydispersity (11 particle sizes). Differences in the amount of stress generated by each particle species were also observed. In general, the small particles generate a higher amount of stress than the large ones as they accumulate near the bottom plate, the region of highest pressure within the mixer. However, the differences in stress are reduced as the number of particle species in the system is increased leading to a reduction in the segregation driving force. Finally, it was shown that the addition of intermediate particle sizes leads to the development of larger and longer force contact chains which enable the transfer of energy from the blades into the center of the particle bed.

The results presented here show that the behavior of polydisperse systems can be different from what is observed in binary systems. Most realistic granular materials are characterized by some degree of polydispersity. The findings from this study are relevant to the operation and optimization of industrial bladed mixer processes as they provide insight into the role of polydispersity on flow and segregation. They suggest that reduction of segregation rates can be achieved by tailoring the particle size distribution of the system. Many questions still remain regarding the effect of particle size distributions on flow and segregation in bladed mixers. Additional work is needed to investigate how changing the width of the particle size distribution affects flow kinematics and the effect of cohesion on polydisperse flows.

6.5. Figures for Chapter 6

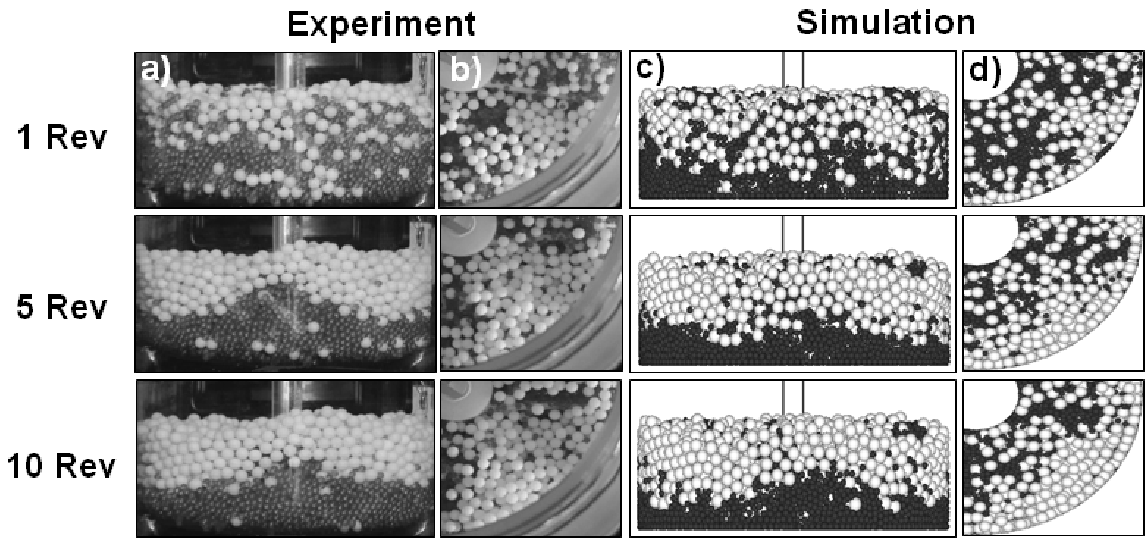

Figure 6.1. Particle segregation for binary system – experiment vs. simulation. Experiment: a) side view snapshots and b) top view snapshots. Simulation: c) side view snapshots and d) top view snapshots.

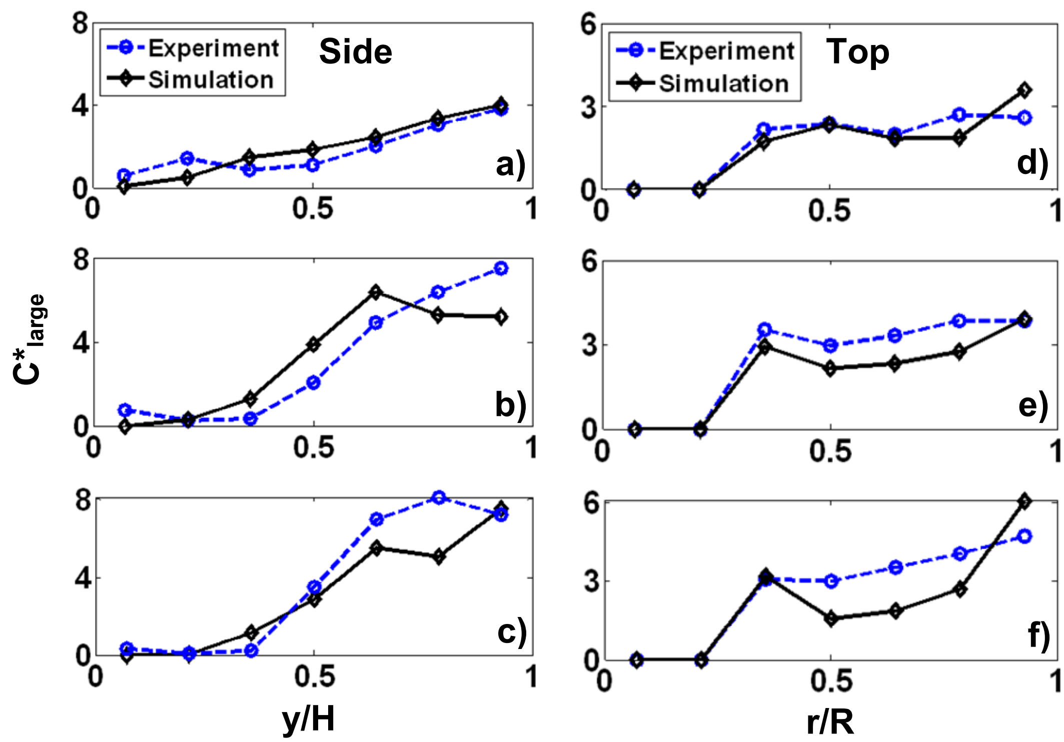

Figure 6.2. Normalized large particle concentration for binary system – experiment vs. smulation. Side view: a) C^*_{large} at 1 revolution, b) C^*_{large} at 5 revolutions and c) C^*_{large} at 10 revolutions. Top view: d) C^*_{large} at 1 revolution, e) C^*_{large} at 5 revolutions and f) C^*_{large} at 10 revolutions.

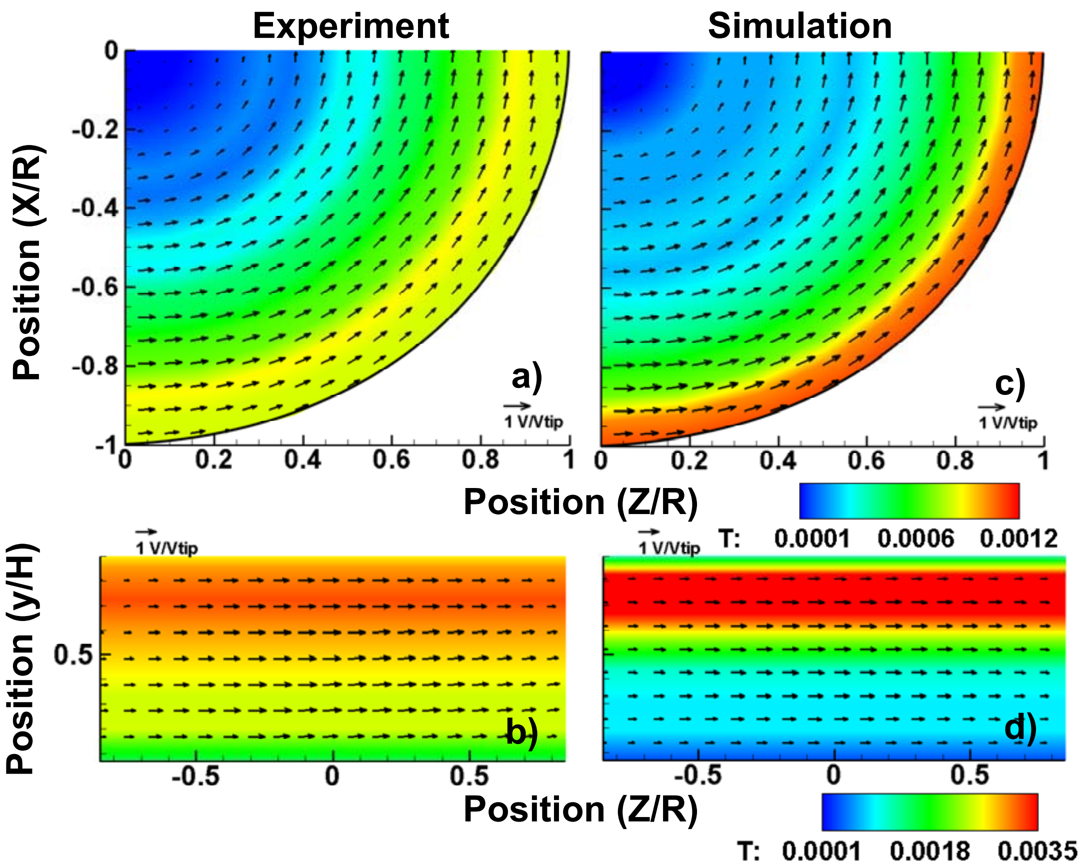

Figure 6.3. Time average velocity profile and granular temperature – binary system. a) experimental results at the top surface, b) experimental results at the cylinder wall, c) simulation results at the top surface and d) simulation results at the cylinder wall. Granular temperature shown here has been averaged in the azimuthal direction and normalized by V_{tip}^2.

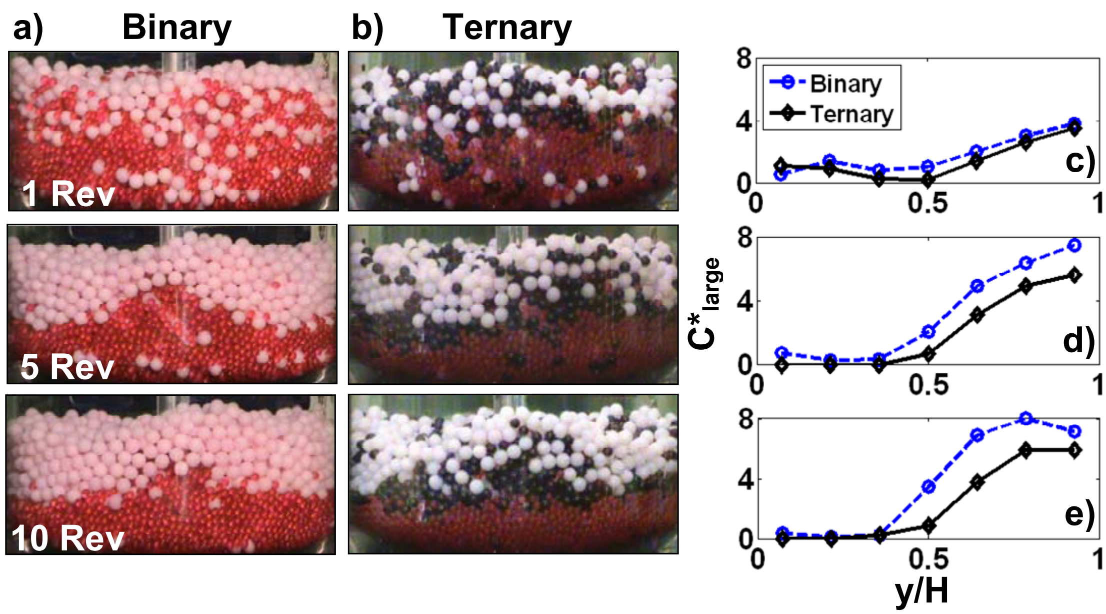

Figure 6.4. Particle segregation for binary and ternary systems. a) binary side view snapshots, b) ternary side view snapshots, c) C^*_{large} for side view at 1 revolution, d) C^*_{large} for side view at 5 revolutions and e) C^*_{large} for side view at 10 revolutions.

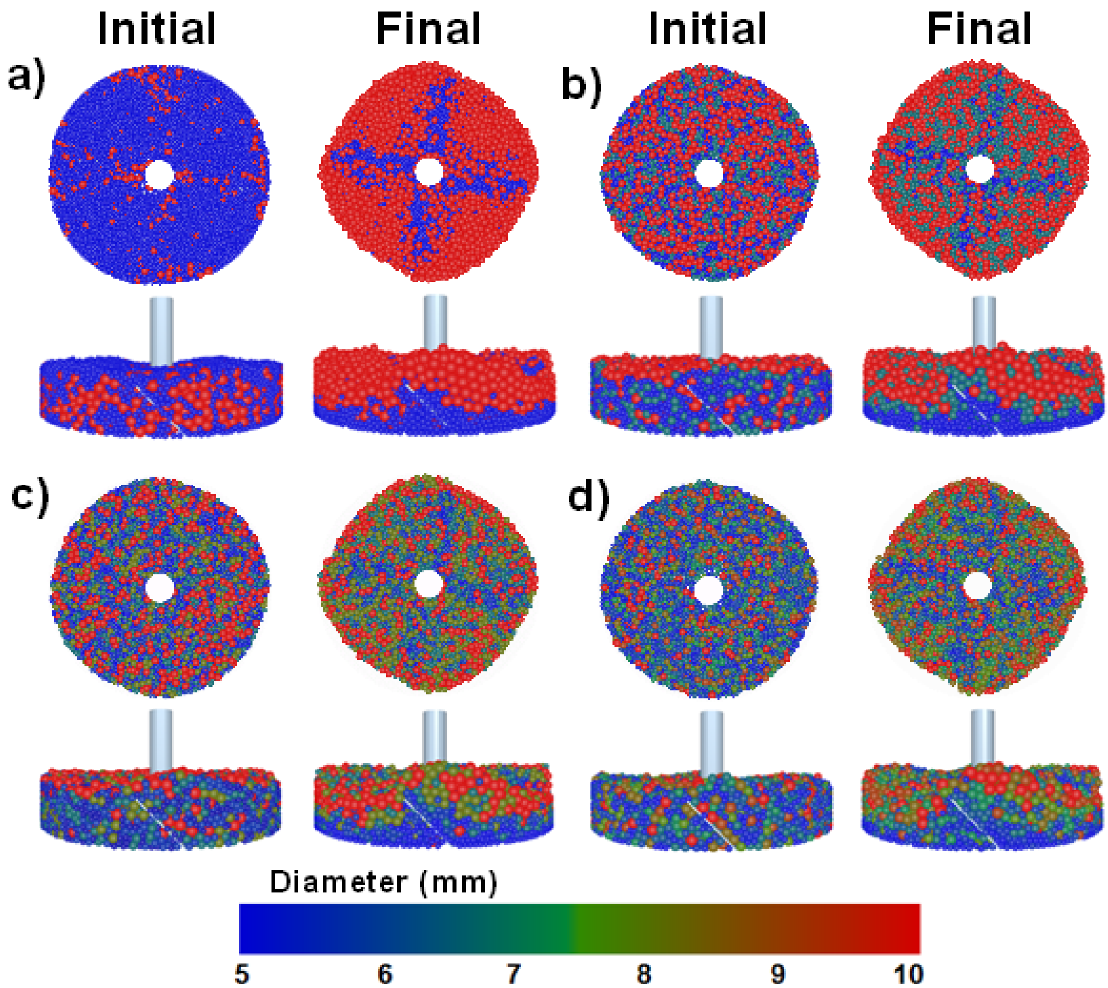

Figure 6.5. Effect of polydispersity on particle segregation. a) binary, b) ternary, c) 5 particle sizes and d) 11 particle sizes.

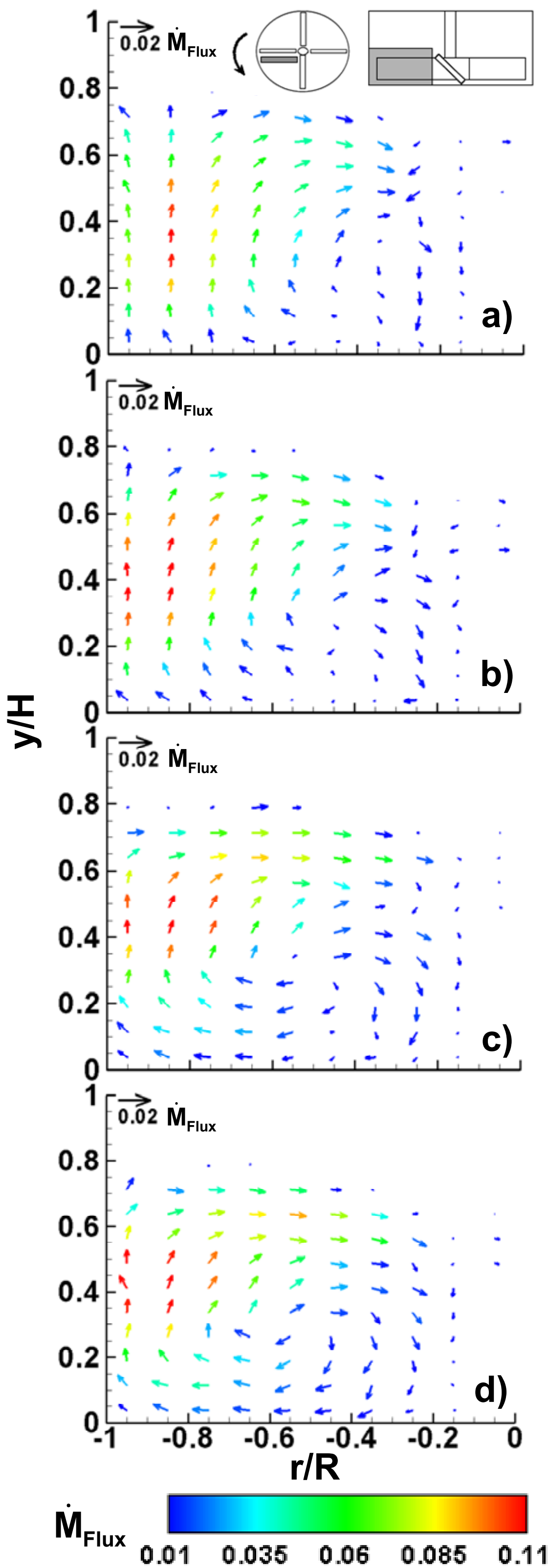

Figure 6.6. Normalized mass flux in front of blades. a) binary, b) ternary, c) 5 particle sizes and d) 11 particle sizes.

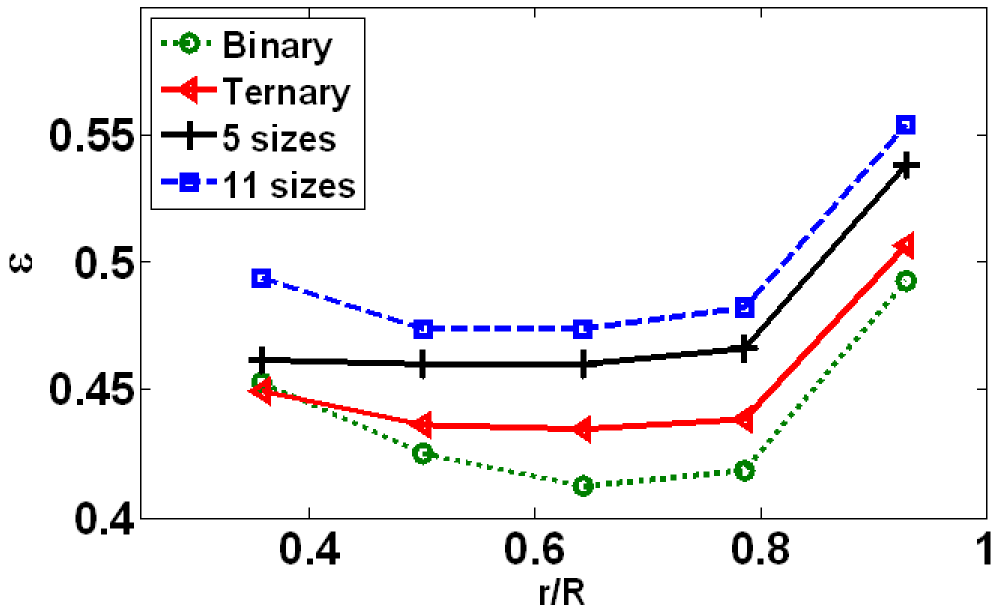

Figure 6.7. Effect of particle size distribution on void fraction in front of the blades.

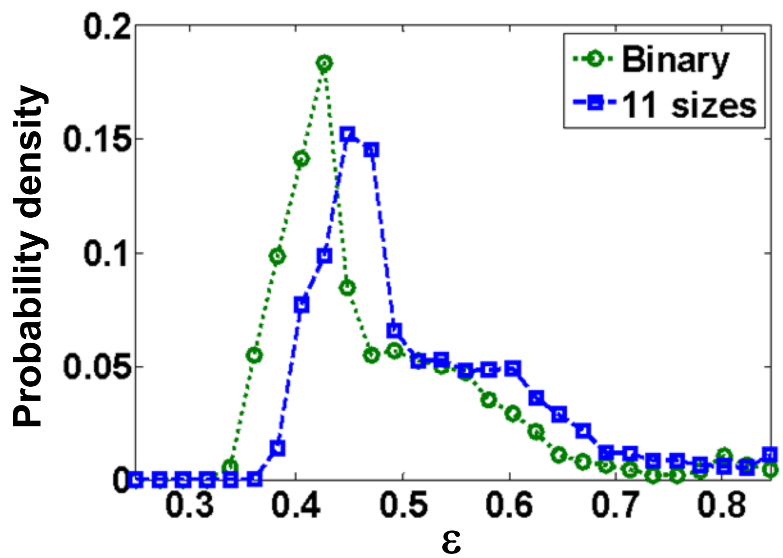

Figure 6.8. Void fraction frequency distribution - binary vs. 11 particle sizes.

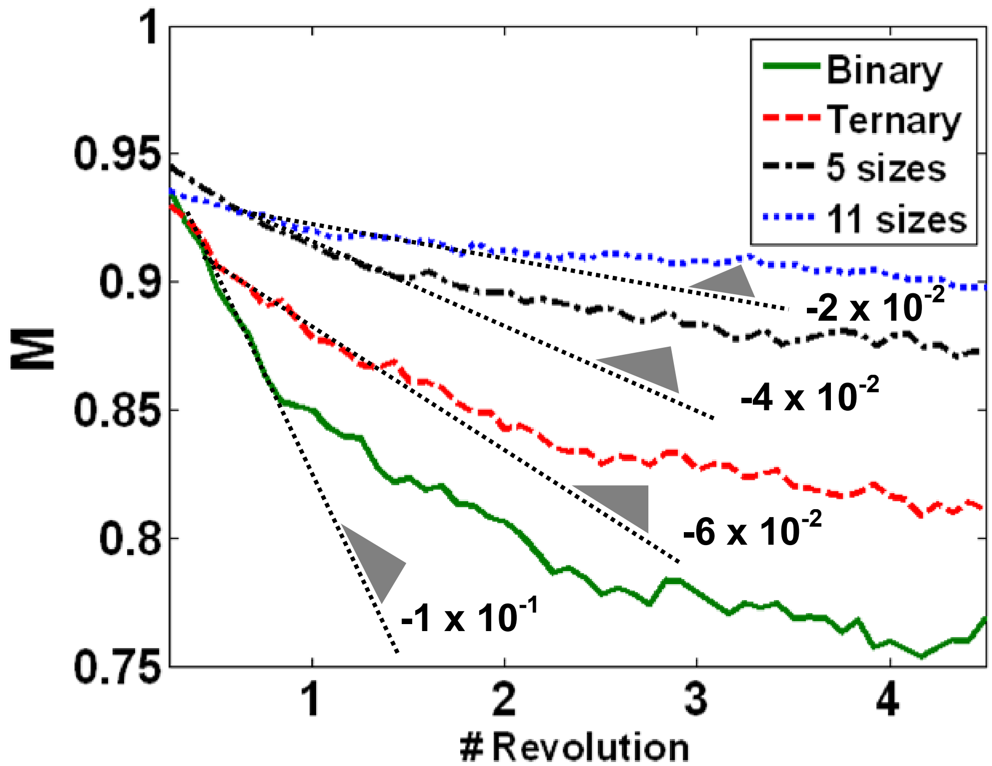

Figure 6.9. Effect of particle size distribution on degree of segregation and segregation flux.

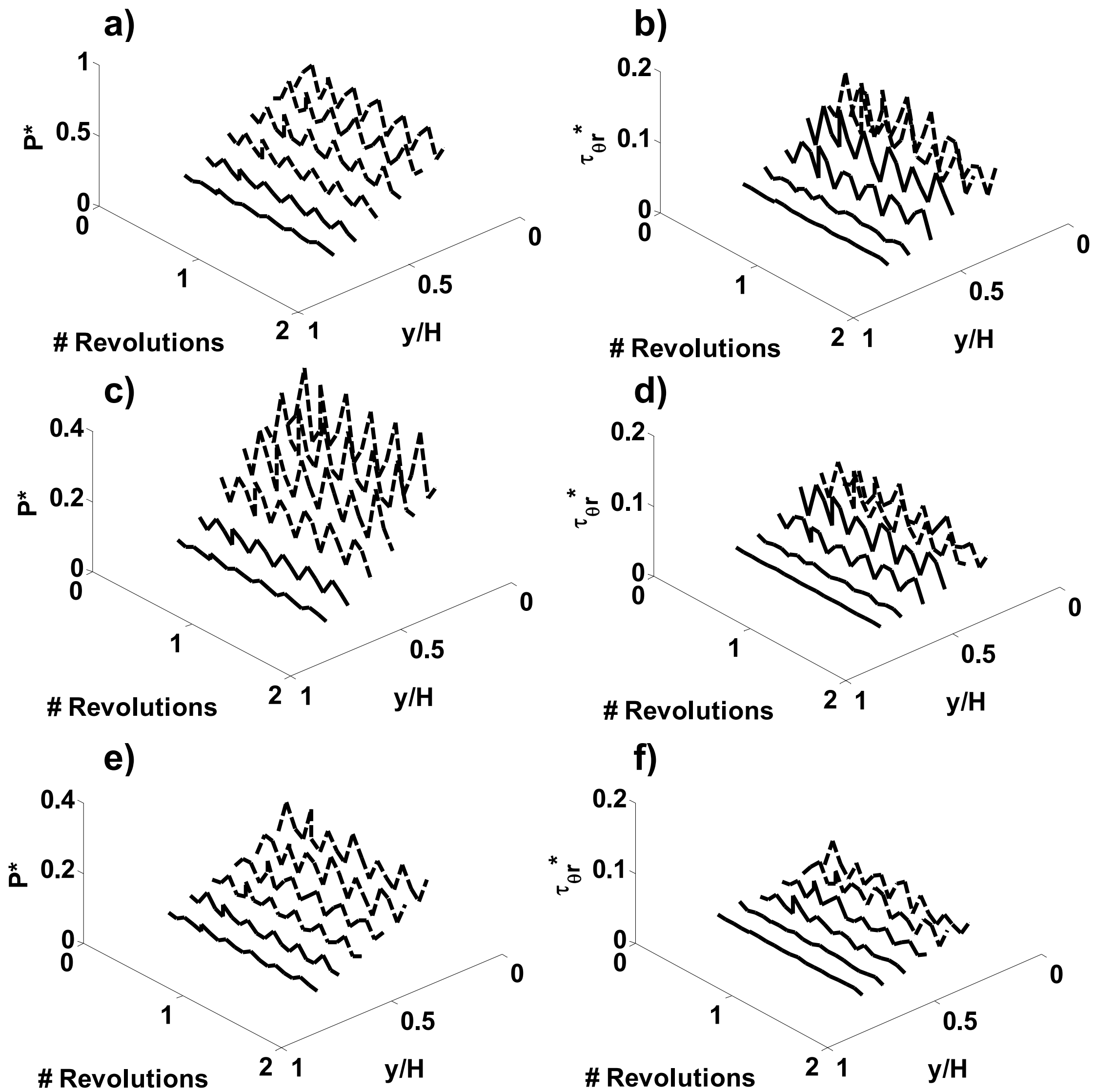

Figure 6.10. Normalized pressure and shear stress fluctuations at r/R = 0.5 - binary system. a) total P^* fluctuations, b) total $\tau_{\theta r}{}^*$ fluctuations, c) P^* fluctuations from 5 mm particles, d) $\tau_{\theta r}{}^*$ fluctuations from 5 mm particles, e) P^* fluctuations from 10 mm particles and f) $\tau_{\theta r}{}^*$ fluctuations from 10 mm particles.

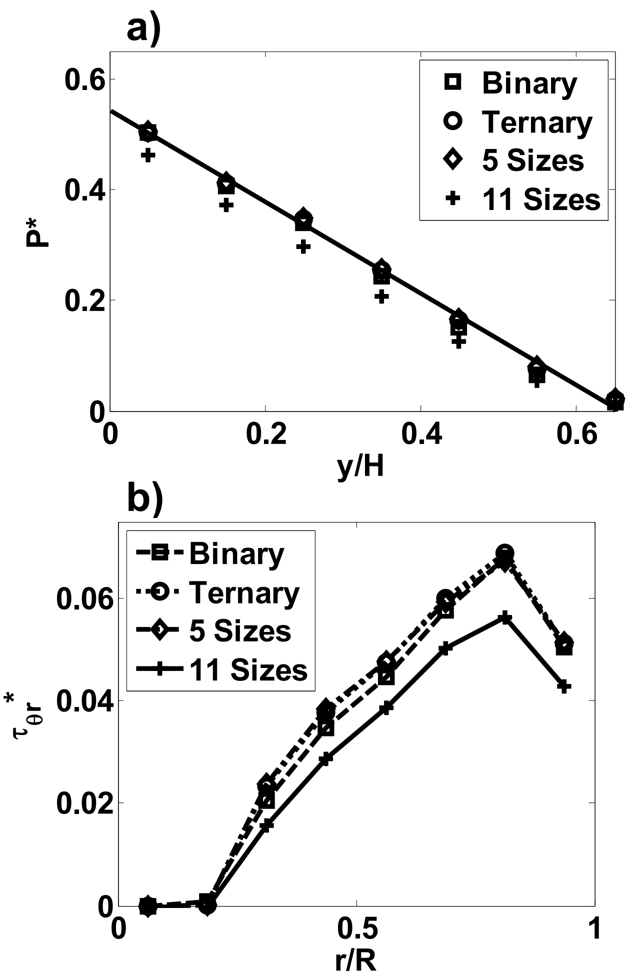

Figure 6.11. Effect of particle size distribution on normalized pressure and shear stress. a) Time average P^* vs. normalized height and b) Time average $\tau_{\theta r}{}^*$ vs. normalized radial position.

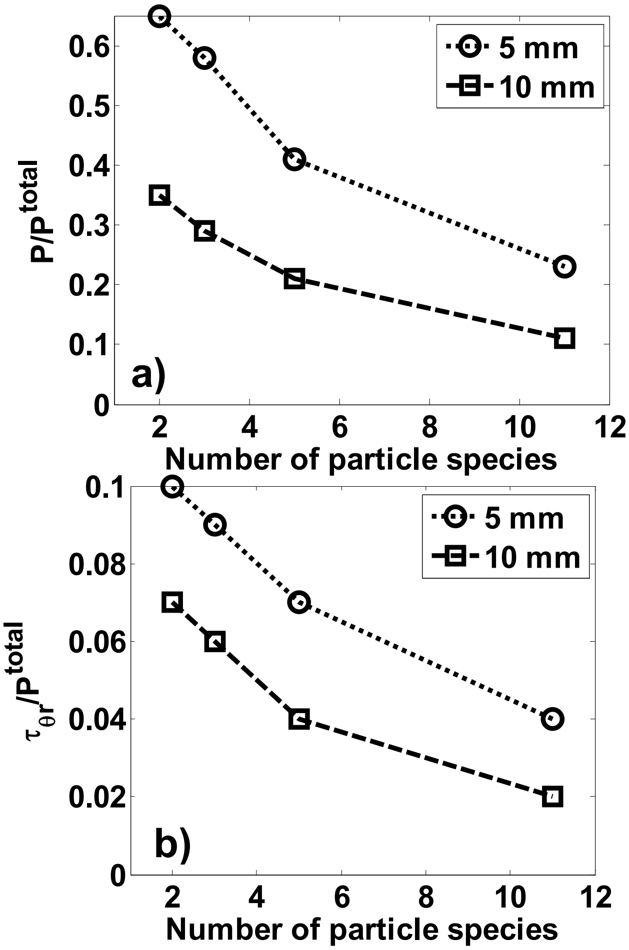

Figure 6.12. Effect of particle size distribution on partial pressure and shear stress for 5 and 10 mm particles. a) P/P^{total} vs. number of particle species and b) $\tau_{\theta r}/P^{total}$ vs. number of particle species.

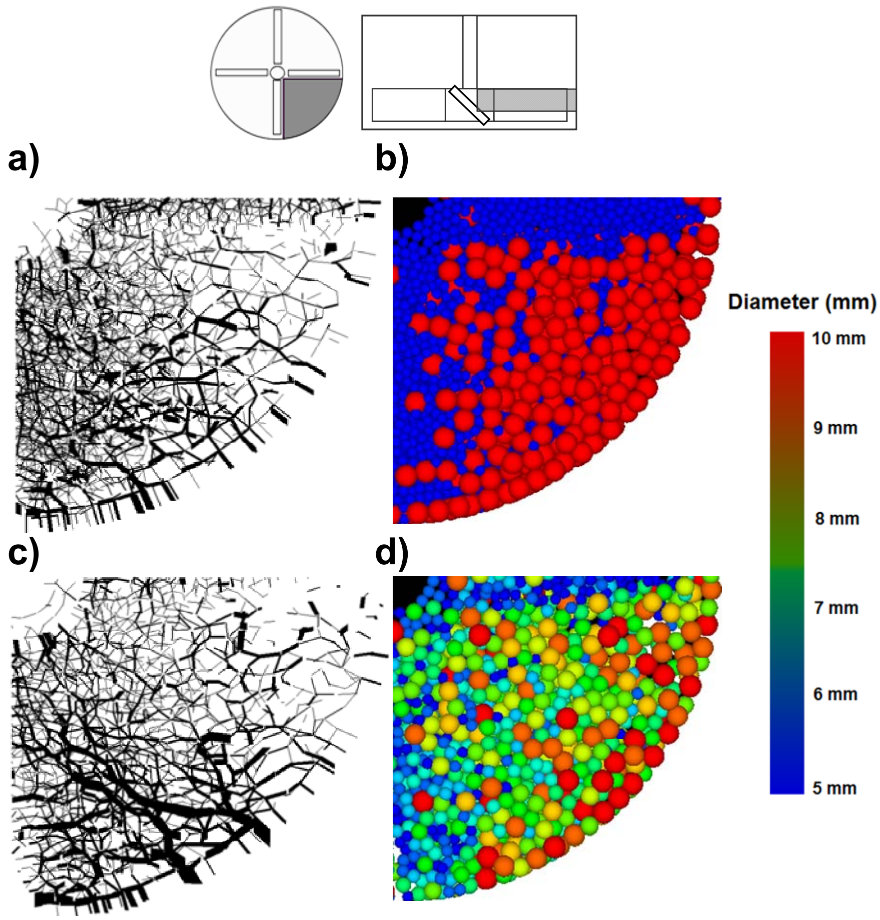

Figure 6.13. Effect of particle size distribution on normal contact force network near top of the blades. Binary: a) contact force network and b) particle distribution. 11 sizes: c) contact force network and d) particle distribution.

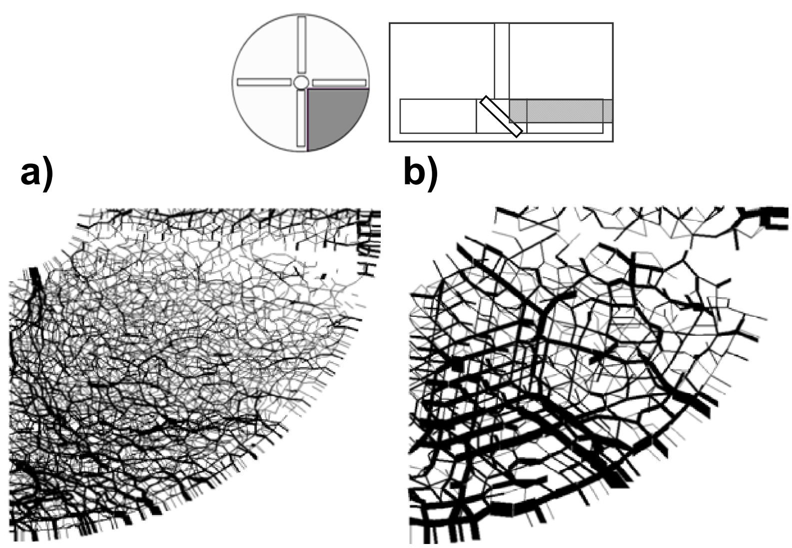

Figure 6.14. Normal contact force network near top of the blades - monodisperse systems. a) 5 mm monodisperse and b) 10 mm monodisperse.

6.6. Tables for Chapter 6

Case	**C^*_{large} (top surface)**	**C^*_{large} (cylinder wall)**
Binary	4.0	2.2
Ternary	3.6	1.9
5 Sizes	3.3	1.7
11 Sizes	2.6	1.5

Table 6.1. Effect of polydispersity on final large particle concentration near the top surface and by the cylinder wall.

Case	**$D_{\theta\theta}$***	**D_{rr} ***	**D_{yy}***	**$Pe_{\theta\theta}$**	**Pe_{rr}**	**Pe_{yy}**
Binary	6.6×10^{-2}	3.4×10^{-2}	1.3×10^{-1}	257	73	25
Ternary	6.9×10^{-2}	3.6×10^{-2}	1.5×10^{-1}	224	71	24
5 Sizes	7.1×10^{-2}	3.7×10^{-2}	1.6×10^{-1}	215	66	23
11 Sizes	1.0×10^{-1}	5.1×10^{-2}	2.1×10^{-1}	147	51	16

Table 6.2. Effect of particle size distribution on normalized particle diffusivities and Peclet number for all species. Particle diffusivities were computed with a Δt of ¼ of a revolution.

Case	$D_{\theta\theta}$*	D_{rr} *	D_{yy}*	$Pe_{\theta\theta}$	Pe_{rr}	Pe_{yy}
Binary	6.2×10^{-2}	3.2×10^{-2}	1.4×10^{-1}	280	81	26
Ternary	6.3×10^{-2}	3.4×10^{-2}	1.5×10^{-1}	248	78	24
5 Sizes	6.7×10^{-2}	3.6×10^{-2}	1.6×10^{-1}	234	74	24
11 Sizes	8.8×10^{-2}	4.6×10^{-2}	1.8×10^{-1}	182	60	20

Table 6.3. Effect of particle size distribution on normalized particle diffusivities and Peclet number for 5 mm particles. Particle diffusivities were computed with a Δt of ¼ of a revolution.

Case	$D_{\theta\theta}$*	D_{rr} *	D_{yy}*	$Pe_{\theta\theta}$	Pe_{rr}	Pe_{yy}
Binary	3.6×10^{-2}	1.8×10^{-2}	6.6×10^{-2}	241	70	28
Ternary	4.2×10^{-2}	2.2×10^{-2}	7.5×10^{-2}	186	58	24
5 Sizes	4.2×10^{-2}	2.3×10^{-2}	7.6×10^{-2}	187	59	24
11 Sizes	6.8×10^{-2}	3.2×10^{-2}	8.0×10^{-2}	118	43	23

Table 6.4. Effect of particle size distribution on normalized particle diffusivities and Peclet number for 10 mm particles. Particle diffusivities were computed with a Δt of ¼ of a revolution.

Chapter 7. Flow and Agglomeration of Wet, Monodisperse Particles

The work presented thus far has focused on the behavior of cohesionless particles in bladed mixers. However, several industrial bladed mixer processes are carried out with some amount of moisture present in the system (i.e. wet granulation and agitated drying). The presence of moisture in a particle bed leads to an increase in interparticle cohesiveness, which directly impacts the bulk flowability of the granular materials. In this chapter we discuss the effect of moisture content on the flow of non-porous monodisperse particles in the bladed mixer geometry. We focus on the effect of moisture for systems in the pendular state (i.e. low moisture contents). Moisture contents ranging from 1.0 v/v% to 4.5 v/v% were examined experimentally and computationally. This range was chosen to ensure that the liquid bridges exist in the pendular regime [192, 193]. The wet system results are compared to the results obtained for dry systems. The effect of moisture content and microscopic friction on macroscopic quantities like flow patterns, mixing kinetics, bulk density, stress and particle diffusivities is discussed. We compare our results to previously reported experimental and computational results. The effect of moisture content on particle agglomeration is then discussed.

The experimental and computational results shown in this chapter were obtained using the laboratory mixer dimensions (Table 2.3) along with the 2 mm glass beads. The fill level in the experiments and the simulations was enough to cover the top of the blades. All the results discussed in this chapter were obtained using a blade speed of 25 RPM. This blade speed yields bladed mixer flows in the quasi-static regime for dry systems (as shown in Chapter 5).

7.1. DEM Results vs. Experimental Results

In this section, we compare the particle velocity profiles obtained from the DEM simulations to those obtained experimentally. DEM simulations discussed here were carried out using the same mixer dimensions (Table 2.3) and the same number of particles (2 mm particles) as in the laboratory experiments. The particle input parameters for the simulations were the same as the ones used in Chapter 5, which were demonstrated to afford results in good agreement with the experiments for dry systems. The input parameters used for the capillary liquid bridge model are listed in Table 7.1. The liquid properties are those of water. A contact angle of 0 ° was used as this simulates the formation of liquid bridges in hydrophylic materials [194] . The amount of liquid in the system is characterized by the liquid volume fraction, ϕ_{liq}, which is defined as the ratio of total volume of liquid in the system to the total volume of the particles. A Bond number of 5 was used for all the wet particle simulations.

The PIV technique was used to measure surface particle velocities in the laboratory unit. Experimental velocities were measured only near the top free surface. We were not able to obtain side view velocity measurements due to particles sticking to the cylinder wall in the presence of moisture. For the wet particle experiments, the particles were first loaded into the mixer. The blades were then set to rotate and water was added from the top at different locations with the use of a small spraying device. The wet particle bed was allowed to mix for 5 minutes prior to taking the PIV measurements. This water addition procedure was found to yield reproducible results in the laboratory and is consistent with the procedure used by Lekhal et al. [107].

Figure 7.1 shows instantaneous tangential velocity profiles obtained for the PIV experiments and the DEM simulations at different moisture contents. Here, the tangential velocities have been normalized by the tip speed of the blades, V_{tip}. For both the experiments and the simulations, a 10 mm x 10 mm square control area was created at the top free surface at r/R = 0.5. The instantaneous velocity components were calculated by averaging over the control area at a particular time. For the DEM simulation, only the velocities of the particles located 0.75 particle diameters away from the top surface were included in the calculation. In general, good qualitative agreement is obtained between the experimental instantaneous velocities and the simulation velocities. For the dry velocity profiles (Figures 7.1a for the experiment and 7.1d and for the simulation), periodic velocity fluctuations are observed with a main frequency equal to that of the blade rotation. Normalized tangential velocity values fluctuate between 0.75 and 0.1 for both the experiment and the simulation.

Addition of water changes the tangential velocity profiles significantly. Figures 7.1b (experiment) and 7.1e (simulation) show the tangential velocities obtained for ϕ_{liq} = 0.024. The presence of water leads to an increase in the amplitude of the velocity fluctuations. Maximum tangential velocity values are close to the tip speed of the blades for both the experiment and the simulation. Negative tangential velocities are also observed. Similar results were observed by Lekhal et al. [107] for the flow of wet art sand in a four-bladed mixer at similar moisture contents. The increase in velocity fluctuations suggest that particle movement in the tangential direction is therefore less uniform for the ϕ_{liq} = 0.024 system compared to the dry system. In the wet systems, particle agglomeration occurs due to the presence of cohesive forces. The formation of these agglomerates leads to a less correlated flow field in wet systems.

Further addition of water leads to a different effect in the tangential velocity. Figures 7.1c (experiment) and 7.1f (simulation) show the tangential velocities obtained at ϕ_{liq} = 0.045. At this moisture content, the periodicity displayed is less than what's observed in the dry and ϕ_{liq} = 0.024 profiles. The amplitude of the velocity fluctuation is also significantly reduced. A similar behavior was observed by Lekhal et al. [107] at high moisture contents. Inspection of the video footage obtained from the PIV experiment and the DEM simulation showed that the reduction in velocity fluctuations is due to the agglomeration of a large portion of the particle bed in front of the blades. These agglomerated particles follow the movement of the blades leading to a more uniform tangential velocity profile inside the mixer.

While the wet particle DEM simulations are able to capture the qualitative behavior observed in the experiments, some differences are observed. In particular, the amount of periodicity and the amplitude of the velocity fluctuations in the experimental results (Figures 7.1b and 7.1c) are higher than what is observed in the simulation results (Figures 7.1e and 7.1f). The differences are more pronounced for the ϕ_{liq} = 0.045 simulation. These differences could be caused by a number of factors such as differences in particle properties, wall friction and slight polydispersity (present in the glass beads used, but not accounted for in the simulations). Additionally, in the simulations the water present in the system is assumed to uniformly coat the particles and to be perfectly mixed within the particle bed leading to a constant liquid volume in all the capillary bridges. Visual inspection of the particle bed during the experiments suggest that, while a good distribution of the water within the mixer is achieved, water is not perfectly dispersed in the mixer. In particular, water accumulates toward the bottom plate of the cylinder and this effect is more pronounced at the higher moisture contents. This is due to the effect of gravity which causes some of the water to drain out of the liquid bridges due to the low viscosity of water. Donahue et al. [195] demonstrated the reduction of volume in a liquid bridge due to gravity for two 1 inch steel spheres wetted with oil. In this work, additional experiments were conducted for particles wetted with water/glycerin mixtures at different viscosities (but equivalent liquid contents and surface tension). These experiments showed that the amount of liquid that accumulated towards the bottom was reduced as viscosity was increased. The velocity fluctuations obtained for the higher viscosity experiments resemble those obtained for the ϕ_{liq} = 0.045 water simulation.

Figure 7.2 shows the experimental and simulation instantaneous radial velocity profiles obtained at different moisture contents. The radial velocity profiles show similar trends to the tangential velocity profiles. For the dry cases (Figure 7.2a for the experiment and 7.2d for the simulation) radial velocities oscillate between positive and negative values with a frequency equal to that of the blade rotation. These fluctuations arise from the development of secondary flow structures within the mixer as demonstrated in Chapter 3. The amplitude of these fluctuations increases for the cases with ϕ_{liq} = 0.024 (Figure 7.2b for the experiment and 7.2e for the simulation). A similar trend was observed by Lekhal et al. [107] at low moisture contents. These results suggest that the intensity of the secondary flow structures increases at low moisture contents. However, Figures 7.2c (experiment) and 7.2f (simulation) show that for ϕ_{liq} = 0.045, the amplitude of the radial velocity fluctuations decreases. While addition of a small amount of water promotes the formation of stronger secondary flow patterns, too much water could hinder the formation of such flow features. The ϕ_{liq} = 0.045 simulation over-predicts the reduction in radial velocity fluctuations when compared to the experimental results. This is most likely due to the accumulation of water towards the bottom of the cylinder during the experiments at higher moisture contents which is not accounted for in the simulations.

For dry systems with fill levels just covering the height of the blades, the granular bed deforms by forming heaps where the blades are present and valleys in between blade passes. The formation of these heaps is a key feature for dry flows in the quasi-static regime. The effect of moisture on the deformation of the particle bed near the top free surface is shown in Figure 7.3. Experimental snapshots are displayed in Figures 7.3a (dry) and 7.3c (ϕ_{liq} = 0.045). Simulation snapshots are presented in Figures 7.3b (dry) and 7.3d (ϕ_{liq} = 0.045). The dashed lines show the position of the blade. The particles in the simulation snapshots are colored according to their potential energy. For the dry cases, a smooth surface is obtained as the particles rise in front of the blade to form a heap. The free surface of the bed remains relatively flat on each side of the heap. However, at ϕ_{liq} = 0.045, a rough surface develops due to the formation of particle agglomerates. A large portion of the particle bed forms agglomerates in front of the blades in the presence of moisture leading to the formation of larger voids on both sides of the heap. This effect is observed in both the experiment and the simulation. Additionally, the presence of moisture causes the particles closest to the side wall to stick to the cylinder walls as the blades rotate. The DEM simulation is able to capture this behavior well. Due to the high surface tension of water, the cohesive force between the particles and the wall is higher (about 5 times higher) than the weight of the particles causing them to stick to the walls.

Normalized average velocity profiles and granular temperature trends are shown in Figure 7.4 for the PIV experiments and DEM simulations at different moisture contents. The average velocity field near the top free surface for the dry simulation (Figure 7.4d) is similar to the dry experimental field (Figure 7.4a), with particle velocities increasing near the cylinder wall. Granular temperature maximums are observed near the cylinder wall for both the experiment and the simulations. For the ϕ_{liq} = 0.024 cases, average velocities near the top surface decrease. This effect is more pronounced in the experimental profile (Figure 7.4b) when compared to the simulation profile (Figure 7.4e). The average velocity of the particles near the cylinder wall is significantly reduced in both the experiment and the simulation due to particles sticking by the wall. Granular temperatures near the top surface increase for the ϕ_{liq} = 0.024 cases indicating that the motion of the particles is less correlated. Increases in granular temperature at small moisture contents were also observed by Radl et al. [196] from numerical simulations of wet bladed mixer flows with 3 mm particles. At lower moisture content, small agglomerates form due to cohesive forces. Small agglomerates can be considered as "rough" particles which increase the frictional conditions in the particle bed and induce a higher degree of randomness in the particle velocities. A different behavior is observed for the ϕ_{liq} = 0.045 cases (Figures 7.4c and 7.4f). Here average particle velocities increase (compared to the ϕ_{liq} = 0.024 cases) and are close to the tip speed of the blades. Granular temperature decreases at this moisture content as the formation of larger agglomerates prevents individual particles from flowing independently from each other.

Decreases in granular temperatures at higher moistures contents were also observed experimentally by Lekhal et al. [107]. The ϕ_{liq} = 0.045 simulation over-predicts the reduction in granular temperature near the top surface when compared to the experiment.

Despite the discrepancies observed, the general trends obtained for both the experiments and the simulation are similar. The DEM simulations accurately capture the effect of moisture at different levels on the instantaneous and average particle velocities, on the deformation of the particle bed and on the granular temperature gradients that exist within the bladed mixer. The remainder of this chapter focuses on the examination of moisture content effects via DEM simulations.

7.2. Effect of Moisture Content

Particle surface velocities are significantly affected by the moisture content in the particle bed. The DEM simulations show that particle motion throughout the entire bed (and not just near the free surface) is affected by the amount of moisture in the system. Average radial and vertical velocity fields in front of the blades are displayed in Figure 7.5 for different moisture contents. The color of the vectors in Figure 7.5 represents the value of the tangential velocity component. A secondary flow structure consisting of a recirculation zone forms in front of the blades for all the different moisture contents studied. Particles rise by the wall forming a heap and flow downwards near the impeller shaft. The particles near the top of the heap flow radially towards the impeller while the particles near the bottom plate flow towards the cylinder wall. The intensity of the recirculation zone changes with moisture content. For ϕ_{liq} = 0.01 (Figure 7.5b) and ϕ_{liq} = 0.024 (Figure 7.5c), the intensity of the recirculation zone increases when compared to the dry velocity field (Figure 7.5a) as radial and vertical velocities in these systems are higher. This is consistent with the PIV results presented in section 7.1. The increase in the intensity of the recirculation zone leads to enhanced vertical and radial mixing. The small agglomerates that form at lower moisture contents increase the frictional conditions within the bed. Similar to the effect of microscopic friction in cohesionless systems, addition of water at low moisture contents promotes convective particle motion. At high moisture contents (ϕ_{liq} = 0.045), radial and vertical velocities decrease as can be seen in Figure 7.5d when compared to the dry and the lower moisture content systems. Here, the radial and vertical movement of the particles is limited by the formation of large agglomerates in front of the blades. This is also consistent with the velocity surface measurements. At this moisture content, convective particle movement is hindered by the presence of water.

Particle diffusive movement is also affected by moisture content. Normalized particle diffusivities and Peclet numbers are listed in Table 7.2 at different moisture contents. Here, we normalized particle diffusivities by the tip speed of the blades and the mixer diameter, i.e. $D_{ij}^{*} = D_{ij} / DV_{tip}$. The values shown in Table 7.2 were obtained by averaging over all the particles in the computational domain with a Δt of ¼ revolution. The presence of water at low levels (ϕ_{liq} = 0.01 and ϕ_{liq} = 0.024) leads to an increase in particle diffusivities when compared to the dry case diffusivities. This is consistent with the granular temperature results presented in Figure 7.4. The particle diffusivities in the tangential direction ($D_{\theta\theta}^{*}$) increase by ~ 30% while the diffusivities in the radial direction (D_{rr}^{*}) increase by ~ 45%. Diffusivities in the vertical direction increase the most, with the low moisture content D_{yy}^{*} values increasing by ~ 100% relative to the dry values. As moisture is added to the system, the spherical particles agglomerate to form clusters with non-spherical shapes and rough surfaces. Similar to the effect of microscopic friction observed in dry systems (see Chapters 3-5), the rough surfaces of these agglomerates impart a degree of randomness in the particles' motion. The pronounced increase in D^*_{yy} values is due to an increase in the total height of the heaps that form in front of the blades. Increases in heap height for bladed mixer flows of wet particles have been observed experimentally by Lekhal et al. [107] and computationally by Radl et al. [196]. The higher heap heights lead to an increase in the potential energy of the particles. This potential energy is then transferred into kinetic energy in the vertical direction as particles flow in and out of the heaps leading to the increase in particle diffusivities. A small increase in particle diffusivities is observed for the ϕ_{liq} = 0.024 case when compared to the ϕ_{liq} = 0.01 case.

At higher moisture contents (ϕ_{liq} = 0.045), a different behavior is observed. The $D^*_{\theta\theta}$ and D^*_{rr} values decrease and are lower than the dry simulation values. The D^*_{yy} value decreases compared to the low moisture content cases (ϕ_{liq} = 0.01 and ϕ_{liq} = 0.024); but this value is higher than for the dry simulation due to the increased heap height at ϕ_{liq} = 0.045. These trends are consistent with the granular temperature trends observed in Figure 7.4. These results show that, while a small amount of water promotes diffusive mixing in bladed mixers, high moisture contents hinders the particles' diffusive motion.

Peclet numbers are also listed in Table 7.2. In all the cases studied, the Peclet numbers obtained are much higher than unity, indicating that convection is the dominating mechanism for particle transfer. However, Peclet numbers decrease for the ϕ_{liq} = 0.01 and ϕ_{liq} = 0.024 cases when compared to the dry cases. This result suggests that a small amount of water in the system increases the contribution of the diffusive mechanism relative to the convective mechanism for particle motion. The smallest Peclet numbers for the low moisture content simulations are achieved in the vertical direction. At ϕ_{liq} = 0.045, the Peclet numbers in the tangential and radial direction increase when compared to the other cases. However, the vertical direction Peclet number is similar to the values obtained at the lower moisture contents. These results demonstrate that the diffusive behavior of particles in wet systems is complex and highly sensitive to the amount of moisture present. But, in general, high moisture contents reduce the contribution of the diffusive mechanism to particle motion.

The effect of moisture content on bed porosity is shown in Figure 7.6. Average void fractions at different moisture contents are plotted in Figure 7.6a as a function of r/R. As the moisture content in the system is increased, the void fraction within the particle bed also increases. The increase of bed porosity with moisture content was also observed in the static packing of wet spheres by Yang et al. [192]. As agglomerates form in wet systems, the irregular shape and rough surfaces of the agglomerates prevent the formation of dense packed zones within the mixer increasing the overall porosity of the particle bed. The void fraction for the ϕ_{liq} = 0.045 case increases by 13% when compared to the dry case. This is a significant change in void fraction for granular systems, where density changes of a couple of percents have been shown to cause significant differences in behavior [179]. It should be noted that the average void fraction profile obtained for the ϕ_{liq} = 0.01 case was similar to the ϕ_{liq} = 0.024 profile. While differences in bed porosity may be expected between these two cases, the method for determining void fraction used here was not able to detect these differences.

The addition of water increases not only the mean void fraction within the particle bed but also the probability of larger gaps occurring in between particles. Figure 7.6b shows the void fraction probability frequency distributions within the bladed mixer at different moisture levels. Frequency distributions were calculated by creating spherical control volumes throughout the particle bed and calculating the void fraction in each control volume over a period of 1 revolution. The diameter of the spherical control volumes was 13 mm. For the dry system, two peaks are observed in the probability frequency distribution, one at $\varepsilon = 0.45$ and the other at $\varepsilon = 0.6$. The peak at $\varepsilon = 0.45$ represents the particles located in front of the blade, which get compressed into a denser state as the blades rotate. The peak at $\varepsilon = 0.60$ represents the particles located in the wake of the blades which are in a dilated state. Figure 7.6b shows a shift to the right of the graph for the wet frequency distributions when compared to the dry frequency distribution. This indicates that a larger portion of the particle bed is characterized by higher void fractions. The frequency distribution for the $\phi_{liq} = 0.045$ case shows a third peak at $\varepsilon \sim 0.75$. This peak represents the agglomerated particles located above the blades. These agglomerates posses a higher void fraction as they experience lower shearing forces above the blades.

The differences in convective and diffusive particle motion as moisture content is increased lead to differences in mixing kinetics. Degree of mixing at the different moisture contents was evaluated by coloring particles on the left side of the blade impeller differently from the particles on the right side prior to blade movement. A statistical analysis of particle concentration for a specific color particle is then performed. At a particular time step, the relative standard deviation (RSD) of the particle concentration within the mixer is computed. RSD values as a function of number of revolutions are shown in Figure 7.7a for the different cases studied. Better mixing is observed for the lower moisture content cases (ϕ_{liq} = 0.01 and ϕ_{liq} = 0.024) when compared to the dry, base case simulation. At these moisture contents, the formation of small agglomerate increases convective and diffusive particle motion leading to enhanced mixing. This effect is analogous to the enhancement observed in mixing kinetics for cohesive flows in rotating drums at low Bond numbers (i.e. lower amount of cohesion) [94, 197]. The RSD curves for the ϕ_{liq} = 0.01 and ϕ_{liq} = 0.024 cases lie on top of each other indicating that similar mixing kinetics are obtained for these systems. Mixing in these systems is fast with RSD values leveling off after ~ 5 revolutions. A decrease in mixing performance is observed for the ϕ_{liq} = 0.045 case. For this case, larger agglomerates form which are less mobile than the smaller agglomerates and hinder convective and diffusive particle motion. The formation of these larger agglomerates leads to a decrease in the degree of mixing. This effect is analogous to the decrease in mixing kinetics observed in rotating drums at high Bond numbers (i.e. higher amount of cohesion) [94, 197].

Figure 7.7b shows the localized RSD values for the different cases as a function of r/R after 10 revolutions. Close to the wall (r/R > 0.8), the RSD values are the lowest with similar values obtained for all the different cases. This is due to the shearing action of the blades and the cylinder wall which leads to faster mixing in this region. Away from the wall however, RSD values increase and differences in the local RSD values are observed between the different cases. The low moisture content cases are characterized by a higher degree of mixing than the dry and high moisture content cases. RSD values are the highest for the ϕ_{liq} = 0.045 case. This analysis shows the main effect of moisture content on mixing is to alter localized mixing rates for the particles located far away from the walls. It is interesting to note that Radl et al. [196] did not observed significant differences in the overall mixing rates of dry systems vs. wet systems at ϕ_{liq} = 0.007 and Bond numbers of 2. The authors did observe differences in the localized mixing rates. Here we show that systems with a higher degree of cohesion (higher Bond numbers and higher moisture contents) mix at different rates, both locally and globally, when compared to dry systems.

7.3. Effect of Microscopic Friction

In Chapter 3 we showed that microscopic friction significantly influences the flow behavior of dry, monodisperse particles in the quasi-static regime. In this section, we discuss the effect of microscopic friction on wet systems at high moisture contents. All the simulation results discussed in this section were obtained for ϕ_{liq} = 0.045. Here, we vary the amount of microscopic friction by changing the value of the sliding friction coefficient (μ_s) for both the particle-particle and particle-wall interactions. Velocity fields in the front of the blades are presented in Figure 7.8 for 3 different values of μ_s. Heap formation occurs for μ_s = 0.3 and μ_s = 0.5 (Figures 7.8b and 7.8c respectively) leading to increased vertical and radial velocities. However, for the μ_s = 0.1 (Figure 7.8a), particles slide past each other as the blades are rotated and no heap is formed. This in turn leads to low radial and vertical velocity values at these frictional conditions. This is similar to the behavior observed in dry systems. For dry systems, we have demonstrated that the increase in friction leads to the formation of stable contact force chains which enable the transfer of energy from the blades into the particle bed. The results presented in Figure 7.8 suggest that the formation of stable contact force chains is important in achieving secondary flow structures, even for wet systems.

Differences in the porosity of the particle bed are also observed at different μ_s values. Figure 7.9 shows average void fractions vs. r/R for the three cases studied. Increasing μ_s leads to an increase in the void fraction of the particle bed, a behavior similar to that of dry systems. The formation of stronger contact force chains at high μ_s values enables the dilation of the particle bed as the blades are rotated. The average void fraction at $\mu_s = 0.5$ is 10 % higher than at $\mu_s = 0.1$. A small difference in void fraction is observed between the $\mu_s = 0.5$ and the $\mu_s = 0.3$ cases. The increase in bed dilation allows the particles to move more freely and enables the formation of secondary flow structures by increasing the radial and vertical particle velocities.

Microscopic friction also affects particle diffusive motion at $\phi_{liq} = 0.045$. Table 7.3 list particle diffusivities and Peclet numbers obtain for the different μ_s values. As μ_s is increased particle diffusivities increase and Peclet numbers decrease. This shows that increasing microscopic friction at $\phi_{liq} = 0.045$ increases the random motion of the particles and leads to a less correlated velocity field within the mixer. A similar trend is obtained for dry systems.

The effect of microscopic friction on mixing kinetics can be seen in Figure 7.10. Top view snapshots are presented at different revolutions for each μ_s value. As expected, increasing microscopic friction leads to enhanced mixing kinetics. Very little mixing occurs at μ_s = 0.1. This poor mixing performance is explained by the absence of the secondary flow structure at μ_s = 0.1. Mixing improves for the μ_s = 0.3 with the best mixing obtained at μ_s = 0.5. This behavior is similar to the behavior observed in dry systems. However, it should be noted that for dry systems at μ_s = 0.1, the particle bed moves as a solid mass with particles moving in streamlines along the tangential direction. In these systems, no mixing occurs. At ϕ_{liq} = 0.045, a small amount of mixing is observed by the cylinder walls for μ_s = 0.1. The particles that stick to the cylinder walls at this moisture content act as a "rough" wall which allows a small amount of mixing to occur in this region. These results suggest that the effect of friction may not be as pronounced at moisture contents above ϕ_{liq} = 0.045. Further work is needed to explore the effect of friction at higher moisture contents.

7.4. Pressure and Shear Stress Profiles

In this section, we discuss the normal and shear stress profiles that develop inside bladed mixers for systems at different moisture contents. Pressure and shear stress values shown here have been normalized by the quantity $\rho_p gH$. Figure 7.11a shows the normalized pressure ($P^* = P/\rho_p gH$) values as a function of y/H at different moisture contents. For all the cases studied, normalized pressure increases linearly towards the bottom of the mixer since the particles at the bottom sustain the weight of the particles at the top. Similar to what is observed in dry systems, at low fill levels, the pressure profile in wet systems can be approximated by hydrostatics. Figure 7.11a also shows that for the ϕ_{liq} = 0.045, the normalized pressure is lower towards the bottom of the mixer and higher towards the top. This is due to the increase in bed porosity at this moisture content. The pressure profile for the ϕ_{liq} = 0.024 is very similar to the dry pressure profile. Although differences in bed porosity were observed at ϕ_{liq} = 0.024, the method used to calculate stresses is not able to detected differences in the pressure profile at this moisture content vs. the dry case.

Figure 7.11b shows normalized shear stress ($\tau^*_{\theta r} = \tau_{\theta r} / \rho_p g H$) profiles as a function of r/R at the different moisture contents. In all cases the values of $\tau^*_{\theta r}$ are highest near the cylinder wall and close to zero near the impeller shaft. This is due to the increased tangential movement observed near the wall and the increased strength of the force chains due to wall friction. At a low moisture content (ϕ_{liq} = 0.024), $\tau^*_{\theta r}$ values increased when compared to the dry values. This effect is more pronounced by the cylinder wall, where $\tau^*_{\theta r}$ values are ~50% higher than the dry case values. The formation of small agglomerates increases the roughness of the particle bed leading to an increase in shear stress. Increases in shear stress in wet systems have been previously observed experimentally by Pierrat et al. [78, 198] via shear cell analysis and Karmakar et al. [54] via use of a soil rheometer. The shear stress analysis indicates that the addition of water at low levels enables the transfer of energy from the blades into the particle bed. This explains the increase in particle velocities observed at low moisture contents. A different behavior is observed at ϕ_{liq} = 0.045. In this case, $\tau^*_{\theta r}$ values by the walls are similar to the ϕ_{liq} = 0.024 values. However, the $\tau^*_{\theta r}$ values decrease towards the center of the particle bed and are similar to the dry case values. The decrease in mixing rates towards the center of the particle bed at high moisture contents can also be explained in the context of the shear stress profiles. As larger agglomerates are formed at higher moisture contents, a larger amount of energy is needed to break the agglomerates and to promote mixing. Since a lower amount of energy is transferred from the blades to the particle bed in this region, the large agglomerates remain and mixing is decreased.

In addition to affecting average stress values, moisture content affects the distribution of forces throughout the particle bed. Figure 7.12 shows instantaneous normal contact force networks in the horizontal plane for the dry case (Figure 7.12a) and the ϕ_{liq} = 0.045 case (Figure 7.12b). In Figure 7.12, each line represents the contact vector connecting the center of the particles and the thickness of the line represents the magnitude of the normal force associated with that contact. Higher forces are represented by thicker lines and vice versa. Here, only the particle contacts located near the top half of the particle bed are displayed, as shown by the side view drawing in Figure 7.12. The contact force network for the dry simulation is fairly homogeneous while the network for the ϕ_{liq} = 0.045 simulation is very heterogeneous. Stronger contact chains which extend further into the particle bed are observed for the wet case. A similar behavior was observed by Yang et al. [192] in the static packing of wet spheres. At high moisture contents, the magnitude of the capillary forces increases which causes the increase in normal forces and, consequently, the formation of large agglomerates. The white areas shown in Figure 7.12b represent areas of high bed porosity where no particles are present. Thus, the contact force network for the ϕ_{liq} = 0.045 simulation displays the roughness of the particle bed surface while the dry case network shows the smooth surface of the bed.

The effect of microscopic friction in shear stress at ϕ_{liq} = 0.045 is shown on Figure 7.13. $\tau^*_{\theta r}$ values increase with μ_s close to the cylinder wall which explains the increase in mixing kinetics at higher friction. This is consistent with the behavior observed in dry systems in the quasi-static regime. Towards the center of the particle bed, shear stress values become insensitive to the μ_s value. This is not the case in dry systems. In dry systems, shear stress values increase throughout the entire particle bed as μ_s is increased. The presence of moisture reduces the effect of friction on shear stress development in the center of the particle bed. The shear stress profiles suggest that at very high moisture contents, shear stress values may be completely independent of the amount of microscopic friction in the system. Further work is needed to determine whether this is the case.

7.5. Effect of Moisture Content on Particle Agglomeration

In this section, we discuss the effect of moisture content on the formation of agglomerates in bladed mixers. A method was developed to evaluate the extent of agglomeration that occurs in the bladed mixer at different moisture contents. In this method, the contact time (t_c) for each particle-particle contact is tracked during shearing. In the wet simulations, particles are considered to be in contact if the distance between the surfaces of the particles is less than the rupture distance of the liquid bridge ($\hat{h}_c R$). Tracking of contact time is started after the system has reached steady state (~ 2-3 sec after the blades are set to rotate). From the dry simulation, a characteristic time-of-contact breakage is determined (t_{break}^{dry}). t_{break}^{dry} represents the amount of time that it takes the shearing action of blades to break all the particle-particle contacts that were present at a particular time step in the dry system. If a particle-particle contact in the wet simulation is characterized by $t_c > t_{break}^{dry}$, then this contact is classified as an enduring wet contact and these particles are considered to be agglomerated. Groups of agglomerated particles are then determined from the list of enduring wet contacts. For the simulation conditions used here, t_{break}^{dry} was determined to be one revolution. This is equal to 4 blade passes for the blade configuration shown in Figure 2.3.

Figure 7.14 shows the weight percent of the particle bed which is agglomerated at different moisture contents based on the method described above. With this method, no agglomeration is obtained for the dry system (i.e. ϕ_{liq} = 0) as can be seen from Figure 7.14. As moisture content is increased, the weight percent of the particle bed which is agglomerated increases. For ϕ_{liq} = 0.045, roughly 50% of the particle bed is agglomerated. This shows that a significant amount of agglomeration can occur in bladed mixers at high Bond numbers and modest moisture contents despite the significant amount of shearing provided by the blades. It should be noted that the values listed in Figure 7.14 do not change at steady state since, for the wet simulations, we assume a perfect liquid distribution within the mixer.

The effect of moisture content on the size of the agglomerates at steady state is shown in Figure 7.15. As expected, increasing moisture content increases the size of agglomerates as a higher amount of energy is needed to break the liquid bridges that exist between particles. Average agglomerate size vs. r/R is shown in Figure 7.15a at the different moisture contents. Larger agglomerates are obtained close to the impeller shaft and agglomerate size decreases towards the cylinder wall. Figure 7.11b shows that stresses are higher near the cylinder wall leading to the formation of smaller agglomerates in this region. This is consistent with the agglomeration behavior observed in wet shear flows, where the extent of agglomeration is reduced when the amount of shearing is increased [199, 200]. Similar agglomerate sizes are observed near the cylinder wall at the different moisture contents since similar $\tau_{\theta r}{}^{*}$ values are obtained in this region. The differences in agglomerate size along the radial direction explain the reduction in mixing rates for the ϕ_{liq} = 0.045 case. Close to the wall, the majority of the agglomerates formed are small (between 2-4 particles in size). These small agglomerates increase the roughness of the particle bed leading to enhanced mixing in this region. Towards the center of the particle bed, agglomerates with an average size of ~ 35 particles are formed. These large agglomerates hinder particle motion in the radial and vertical direction (as shown in Figure 7.5) leading to a decrease in mixing.

Average agglomerate size vs. y/H is shown in Figure 7.15b at the different moisture contents. Here again we see that increasing moisture content increases the average size of the agglomerates. Smaller agglomerates are observed near the cylinder's bottom plate and agglomerate size increases towards the top of the particle bed. The formation of small agglomerates towards the bottom is due to the increased pressure in this region. As the particles near the bottom sustain the weight of the particles near the top, the agglomerates that form towards the bottom experience higher normal and shear stresses and therefore large agglomerates cannot form.

Differences in the size distribution of the agglomerates at steady state were also obtained. Figure 7.16 displays the agglomerate size distributions obtained at different locations within the particle bed with the different moisture contents. The lower limit of the abscissa for the graphs shown in Figure 7.16 is 2 since only the agglomerated particles are considered in this analysis. Figure 7.16 shows that the shape of the agglomerate size distribution is not constant throughout the particle bed. Near the impeller shaft (Figure 7.16a), right-skewed size distributions are obtained while towards the center of the bed (Figure 7.16b) and near the cylinder walls (Figure 7.16c), lognormal distributions are obtained. The agglomerate size distribution near the impeller shaft shifts to the right and becomes broader as moisture content is increased. As can be seen from Figure 7.16a, agglomerates containing more than 150 particles are obtained for the ϕ_{liq} = 0.045 case even though the average agglomerate size is ~35. The presence of these large agglomerates coupled with the lower shear stresses lead to reduced mixing in this region. For the remainder of the particle bed, lognormal agglomerate size distributions are obtained. The amount of agglomerates composed of two particles is reduced as moisture content is increased leading to broader distributions in the center of the particle bed and near the cylinder walls. For the ϕ_{liq} = 0.045 case, ~5 wt% of agglomerates contain 150 particles or more in the center of the particle bed. The agglomerate particle size distributions are smallest near the cylinder wall. Here, the majority of the agglomerates are composed of two particles although agglomerates composed of > 20 particles are observed for the ϕ_{liq} = 0.045 case.

Finally, we look at the effect of moisture content on agglomerate shape. Figure 7.17a displays the average agglomerate aspect ratio as a function of r/R. Aspect ratio is defined as the ratio of the length of the major axis to the length of the minor axis. For agglomerates composed of multiple particles, the aspect ratio is calculated by determining the distance between each particle and the center of mass of the agglomerate. From these distances the length of the major and minor axis is determined. A lower aspect ratio represents a more symmetrical shape (as spheres have an aspect ratio of 1) while a larger aspect ratio represents a more elongated particle shape. As can be seen in Figure 7.17, the average aspect ratio of the agglomerates increases as moisture content is increased. This means that agglomerates with more elongated, needle-like shapes are formed at higher moisture contents. Figure 7.17a also shows that the shape of the agglomerates is not constant throughout the particle bed. Aspect ratio is highest by the impeller shaft and decreases towards the cylinder walls since higher stresses in this region prevent the formation of longer agglomerates.

In Figure 7.17b, the morphology of some agglomerates that form in the different regions of the particle bed is displayed. These agglomerates have a size and aspect ratio which is similar to the average values obtained at the different moisture contents. The size of the agglomerates increases as moisture content is increased which is consistent with the results presented in this section. Near the impeller shaft, elongated agglomerates are observed while shorter agglomerates are formed closer to the cylinder walls. The smaller agglomerates form as elongated agglomerates are broken along the major axis by the shearing action of the blades into shorter agglomerates. This is similar to the fracture of needle-like particles due to shearing.

The results presented here show that while a more complex behavior is obtained in wet flows, many of the trends observed are consistent with the behavior observed in dry systems. At low moisture contents, the formation of small agglomerates increases the roughness of the particle bed. These “rough”, wet particle beds show a behavior similar to that of frictional, dry particle beds. At higher moisture contents however, the behavior differs. Larger agglomerates are formed reducing the mobility of the particles within the mixer and significantly affecting the distribution of stress within the particle bed.

7.6. Conclusions for Wet, Monodisperse Flows

Experimental and computational methods were used to study the behavior of wet particle flows in bladed mixers. The ability of DEM simulations to accurately capture experimental behavior was demonstrated. Particle velocities and granular temperature profiles obtained from the simulations are in good qualitative agreement with those obtained experimentally using the PIV technique. The discrepancies observed between the simulation results and the experimental results could be due to differences in particle properties, wall friction and the slight polydispersity present in the glass beads used (but not accounted for in the simulations). Additionally in the simulations the water is assumed to uniformly coat the particles and be perfectly mixed within the particle bed. Some of the discrepancies observed at higher moisture contents are the result of water accumulation near the bottom of the cylinder in the experiments due to the low viscosity of water. While this effect is not accounted for in the simulation, the general trends observed in the simulations are similar to the experimental trends. Further work is needed to study the effect of liquid viscosity on liquid dispersion in bladed mixers.

DEM simulation results showed that addition of water at low moisture contents leads to an increase in the radial and vertical velocities of the particles located in front of the blades leading to a stronger recirculation pattern than what’s observed in the dry system. Particle diffusivities also increase at low moisture contents. The increase in convective and diffusive particle motion at low moisture contents leads to enhanced mixing kinetics when compared to the dry case. However, at higher moisture contents the behavior changes. In this case, the presence of water leads to lower radial and vertical particle velocities in front of the blades. Particle diffusivities also decrease. This decrease in particle motion leads to lower mixing rates at high moisture contents. Bed porosity was shown to increase as moisture content is increased. Void fraction increases by 12% for the high moisture content simulation when compared to the dry simulation.

Microscopic friction was shown to affect the behavior of particle flows at high moisture contents. Increasing microscopic friction leads to an increase in convective and diffusive particle motion. As a result, systems with a higher amount of microscopic friction experience enhanced mixing. This behavior is similar to that of dry systems as microscopic friction is increased. Bed porosity also increased as microscopic friction was increased.

Pressure and shear stress profiles are significantly affected by moisture content. The average pressure inside the particle bed at different moisture contents was shown to be linear and approximated by hydrostatics. Shear stress was highest near the cylinder wall and lowest by the impeller shaft for all the cases studied. At low moisture contents, higher shear stresses were obtained compared to the dry systems. For high moisture contents, the stresses near the cylinder wall are high. However, shear stress decreases towards the center of the particle bed with values similar to those obtained for the dry case.

The cohesive forces that develop in wet systems lead to the formation of particle clusters or agglomerates. A method for examining the extent of agglomeration in the wet particle simulations was developed. Our analysis showed that the portion of the particle bed which is agglomerated increases as moisture content is increased. At the highest moisture content examined, close to 50% of the particles in the system were agglomerated. Agglomerate size is highest near the impeller shaft and towards the top of the particle bed, regions characterized by lower stresses. A strong dependence between the aspect ratio of the agglomerates and moisture content was found. Aspect ratio increases with moisture content indicating the formation of elongated, needle-like agglomerates.

This chapter described the behavior of an idealized, wet granular system (non-porous monodisperse spheres with a perfect liquid distribution) in a bladed mixer. While simple in nature, it represents an initial step towards understanding the behavior of wet granular systems as it pertains to flow, mixing and agglomeration. Further work is needed to examine the effect of mixer size and other operating parameters on the trends reported here.

7.7. Figures for Chapter 7

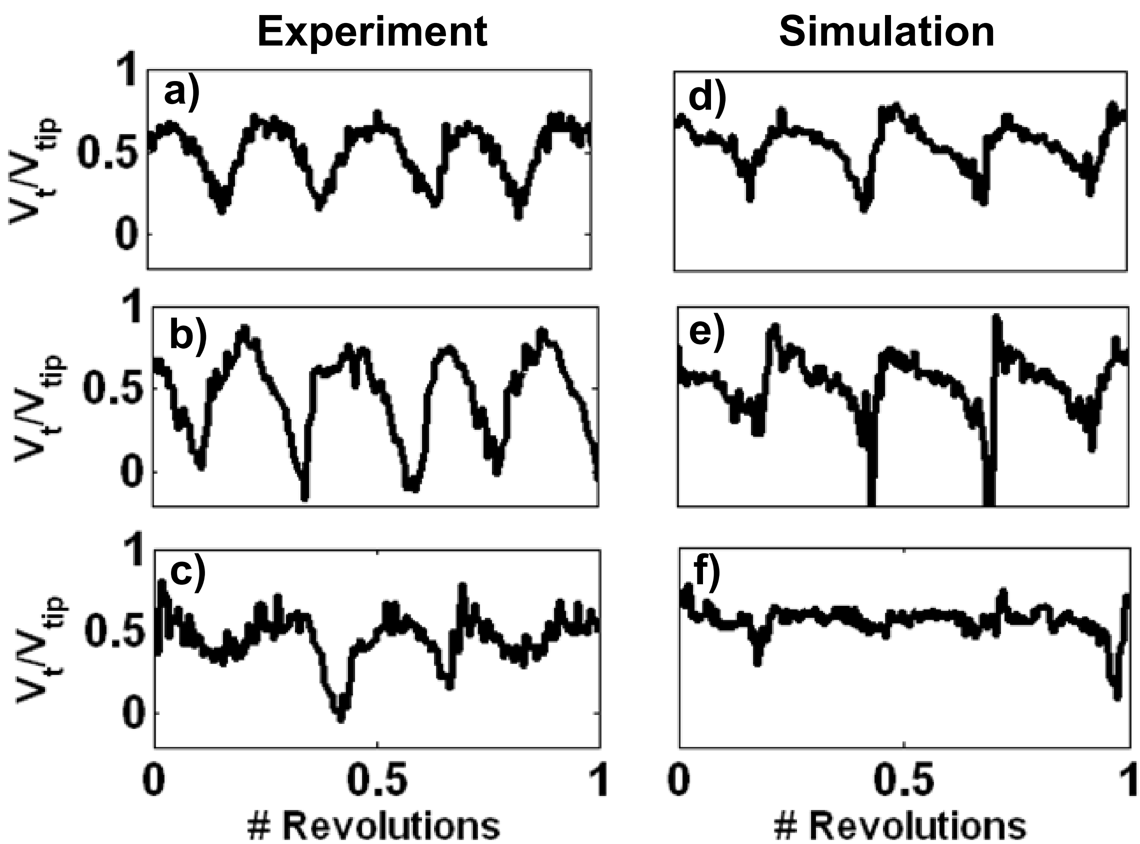

Figure 7.1. Tangential velocity fluctuations near top free surface at r/R = 0.5. Experimental results: a) dry, b) ϕ_{liq} = 0.024 and c) ϕ_{liq} = 0.045. Simulation results: d) dry, e) ϕ_{liq} = 0.024 and f) ϕ_{liq} = 0.045.

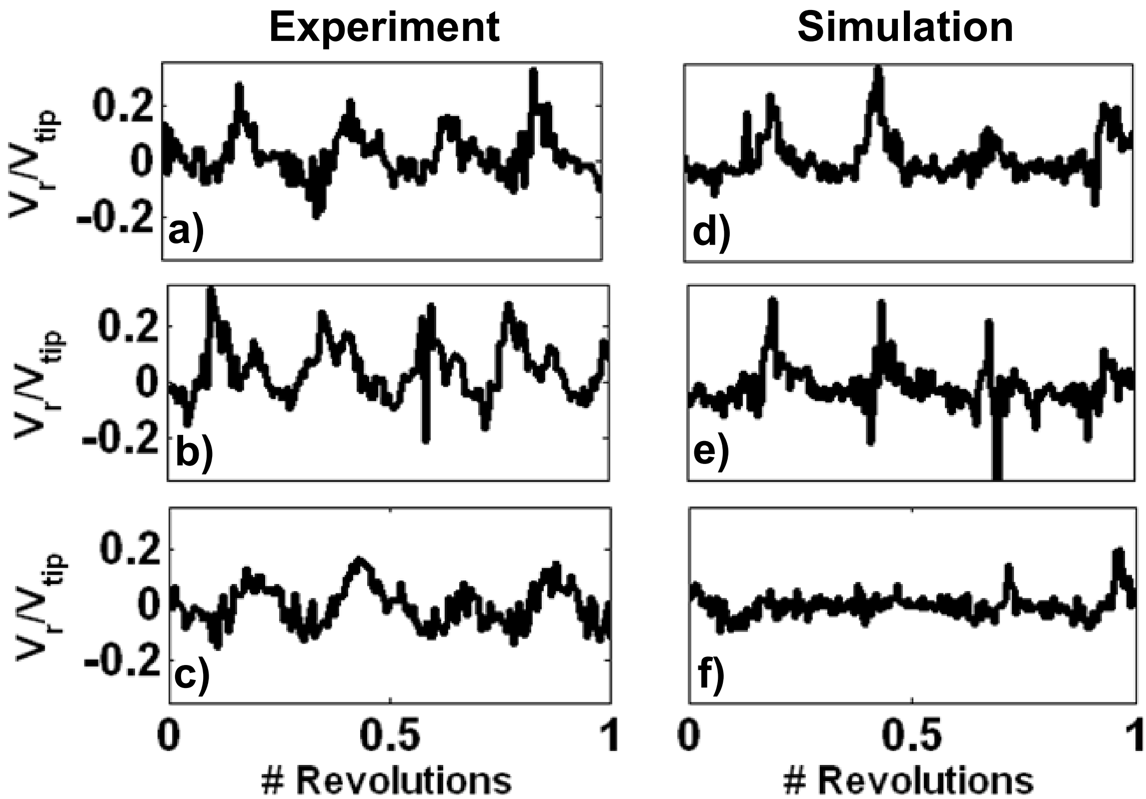

Figure 7.2. Radial velocity fluctuations near top free surface at r/R = 0.5. Experimental results: a) dry, b) ϕ_{liq} = 0.024 and c) ϕ_{liq} = 0.045. Simulation results: d) dry, e) ϕ_{liq} = 0.024 and f) ϕ_{liq} = 0.045.

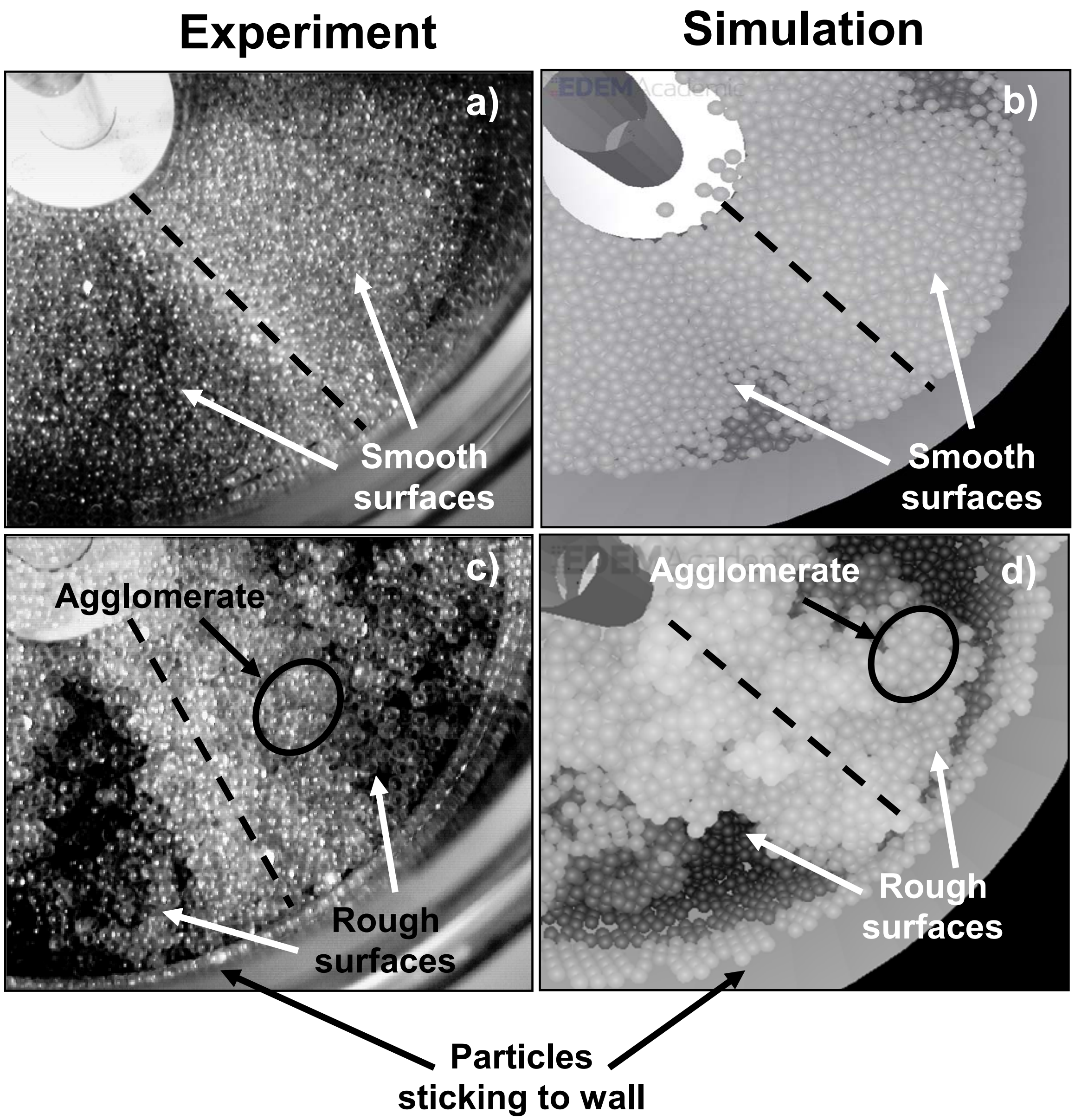

Figure 7.3. Deformation of particle bed near top free surface. Dry: a) experiment and b) simulation. ϕ_{liq} = 0.045: c) experiment and d) simulation. The dash lines show the position of the blade. The particles in the simulation snapshots are colored according to their potential energy.

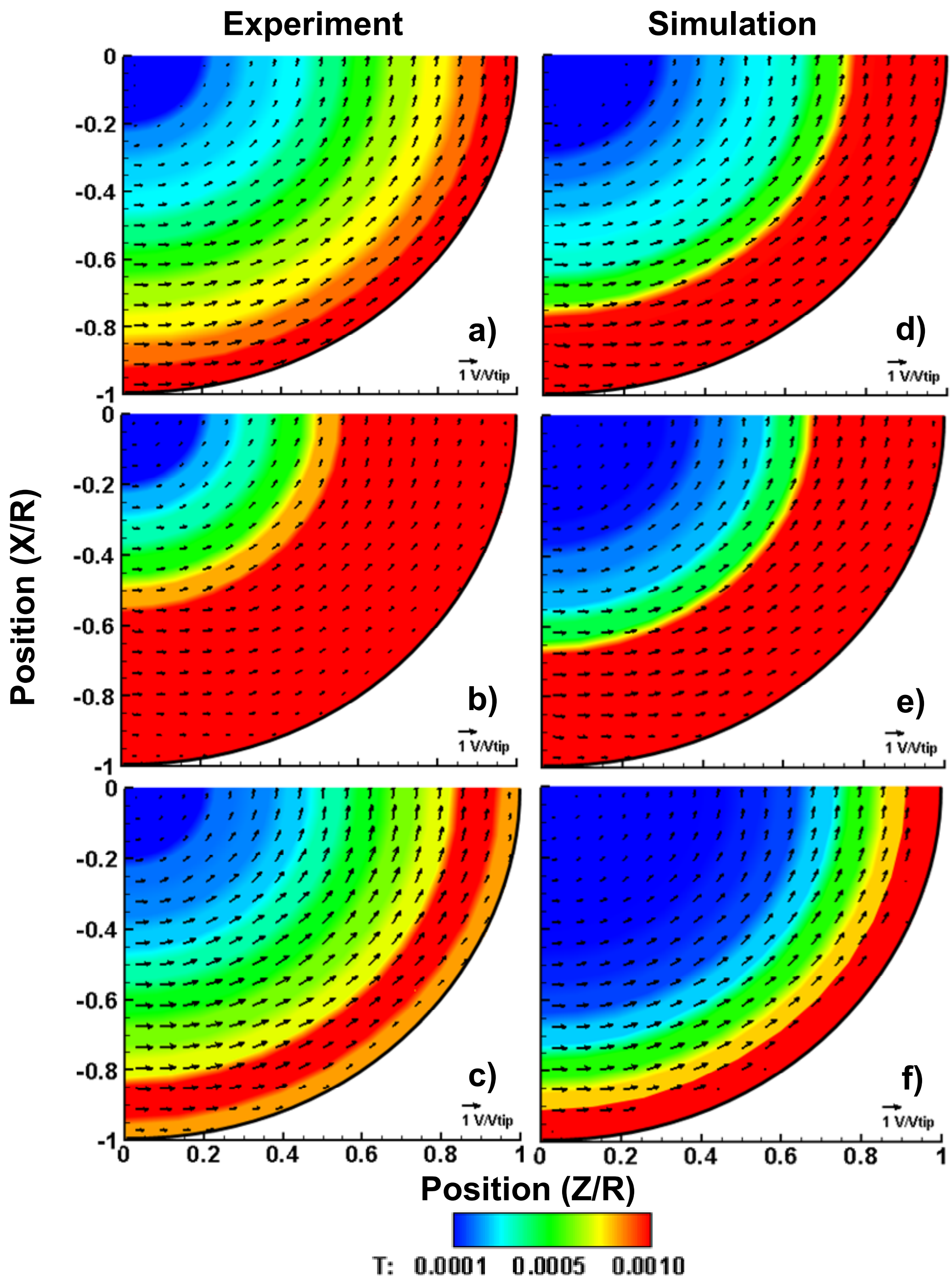

Figure 7.4. Time average velocity fields and granular temperature profiles. Experimental results: a) dry, b) ϕ_{liq} = 0.024 and c) ϕ_{liq} = 0.045. Simulation results: d) dry, e) ϕ_{liq} = 0.024 and f) ϕ_{liq} = 0.045.

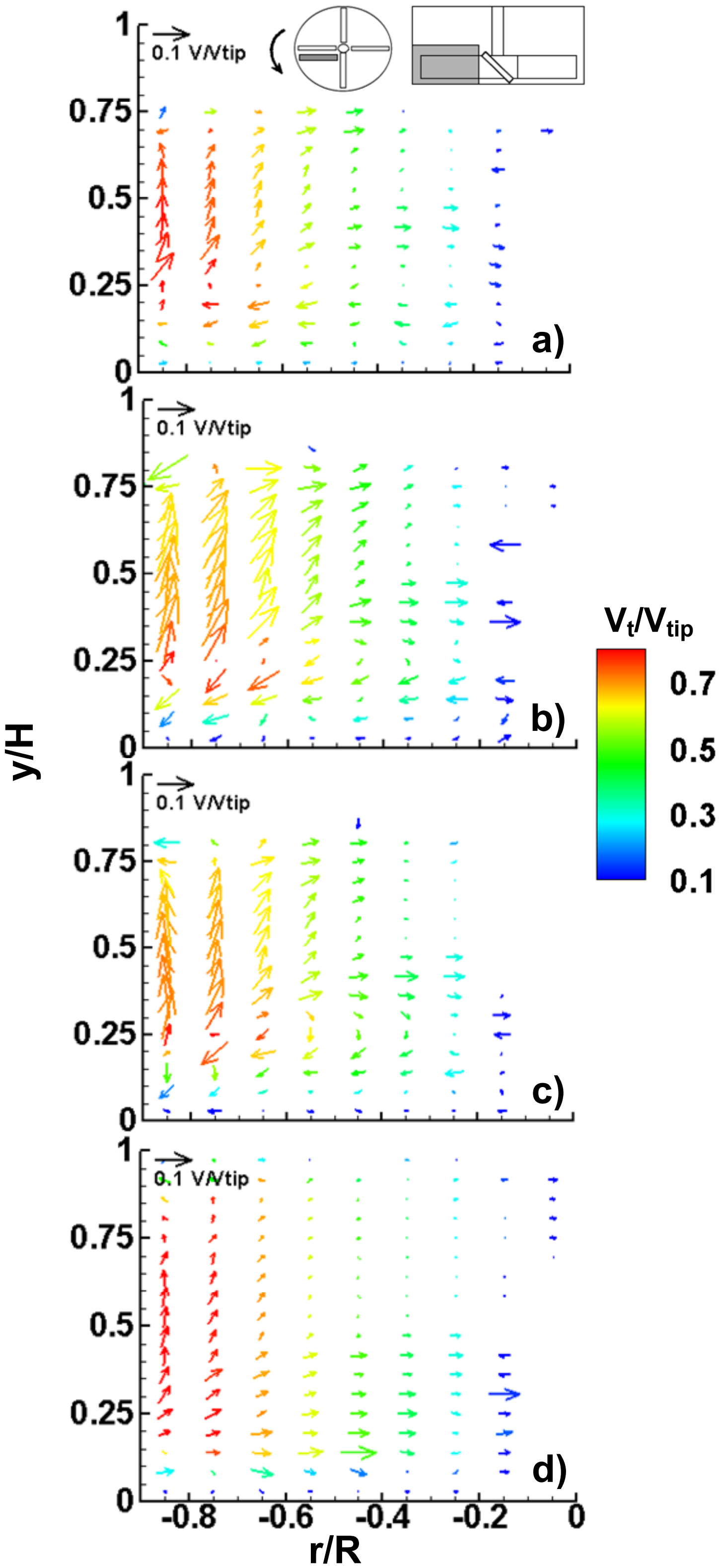

Figure 7.5. Effect of moisture content on velocity fields in front of the blades. a) dry, b) ϕ_{liq} = 0.01, c) ϕ_{liq} = 0.024 and d) ϕ_{liq} = 0.045.

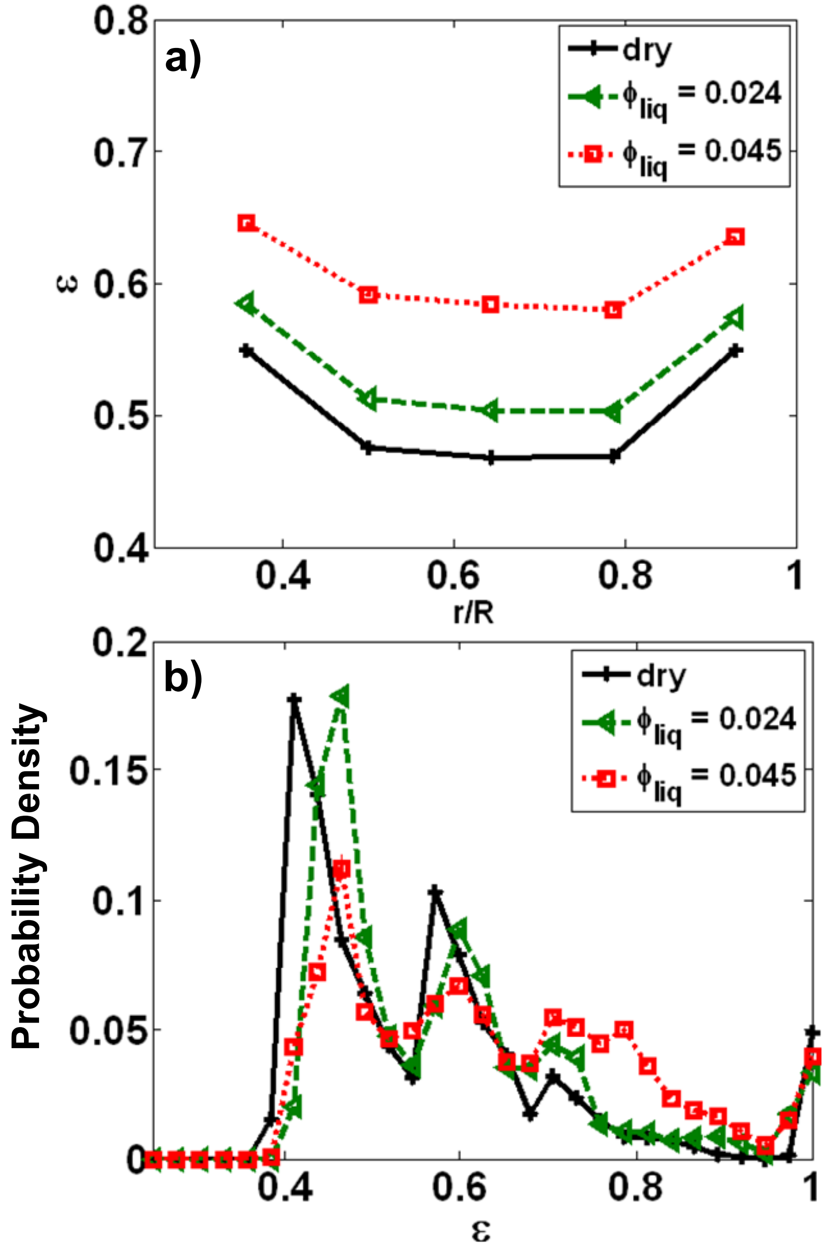

Figure 7.6. Effect of moisture content on void fraction within particle bed. a) average void fraction vs. r/R and b) void fraction frequency distribution at steady state.

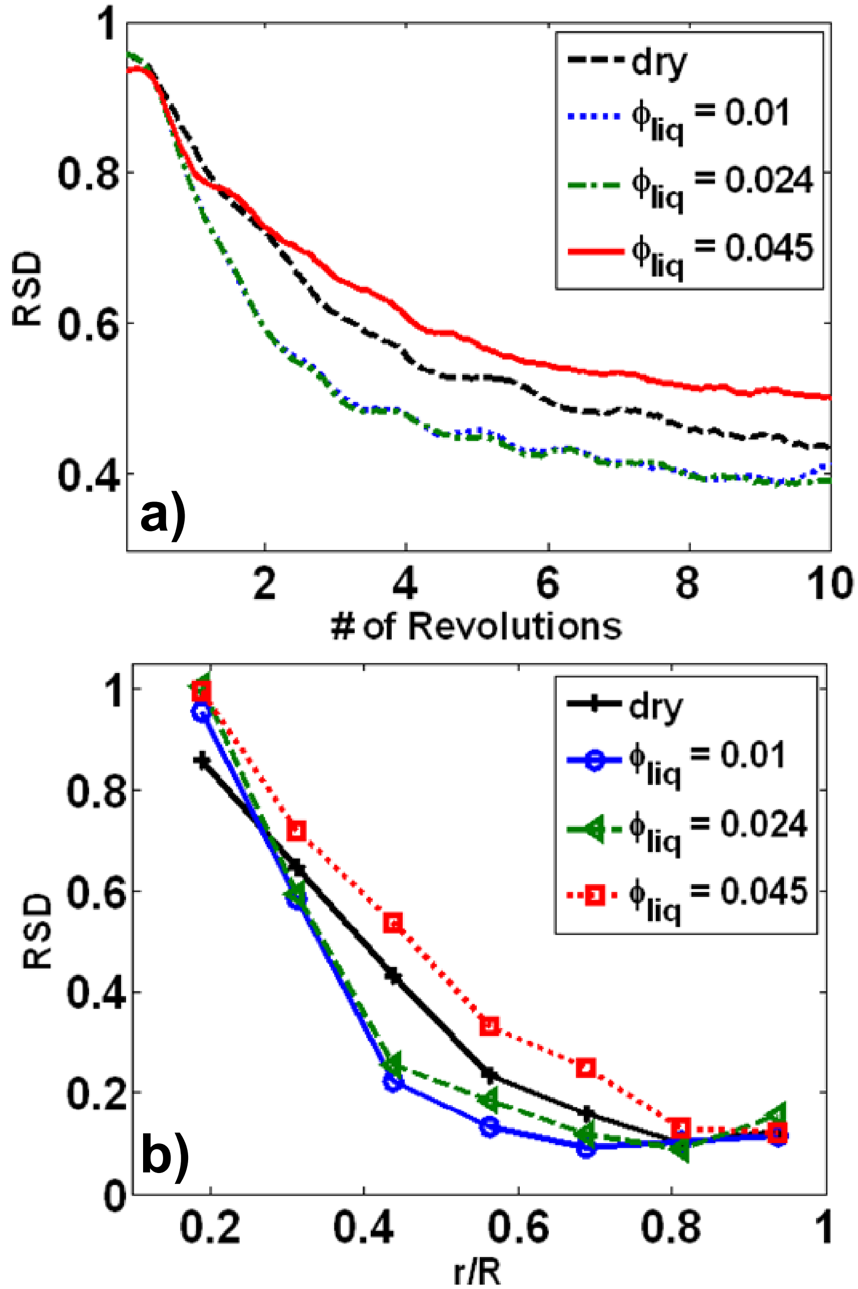

Figure 7.7. Effect of moisture content on mixing. a) RSD vs. number of revolution and b) RSD vs. r/R after 10 revolutions.

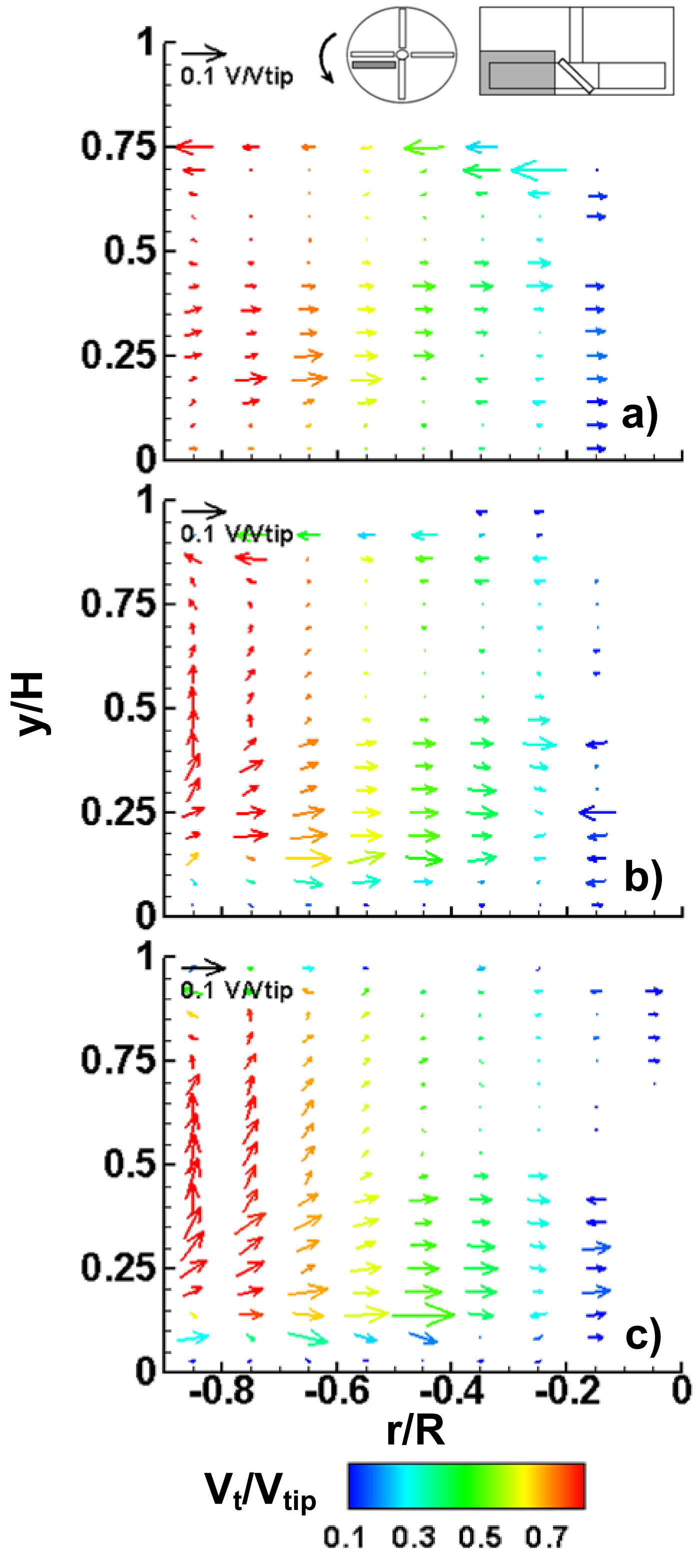

.

Figure 7.8. Effect of microscopic friction on velocity fields in front of the blades for wet systems. a) μ_s = 0.1, b) μ_s = 0.3 and c) μ_s = 0.5. Results obtained for ϕ_{liq} = 0.045 moisture content.

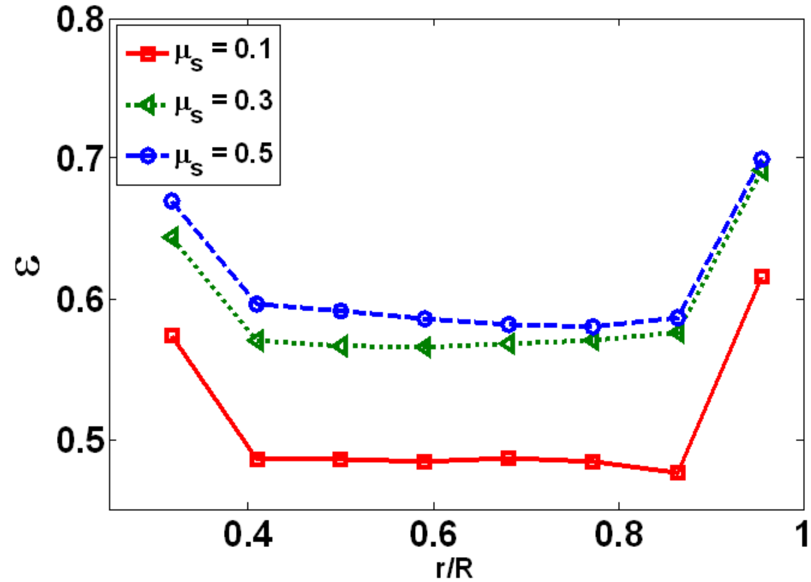

Figure 7.9. Effect of microscopic friction on average void fraction. Results obtained for ϕ_{liq} = 0.045 moisture content.

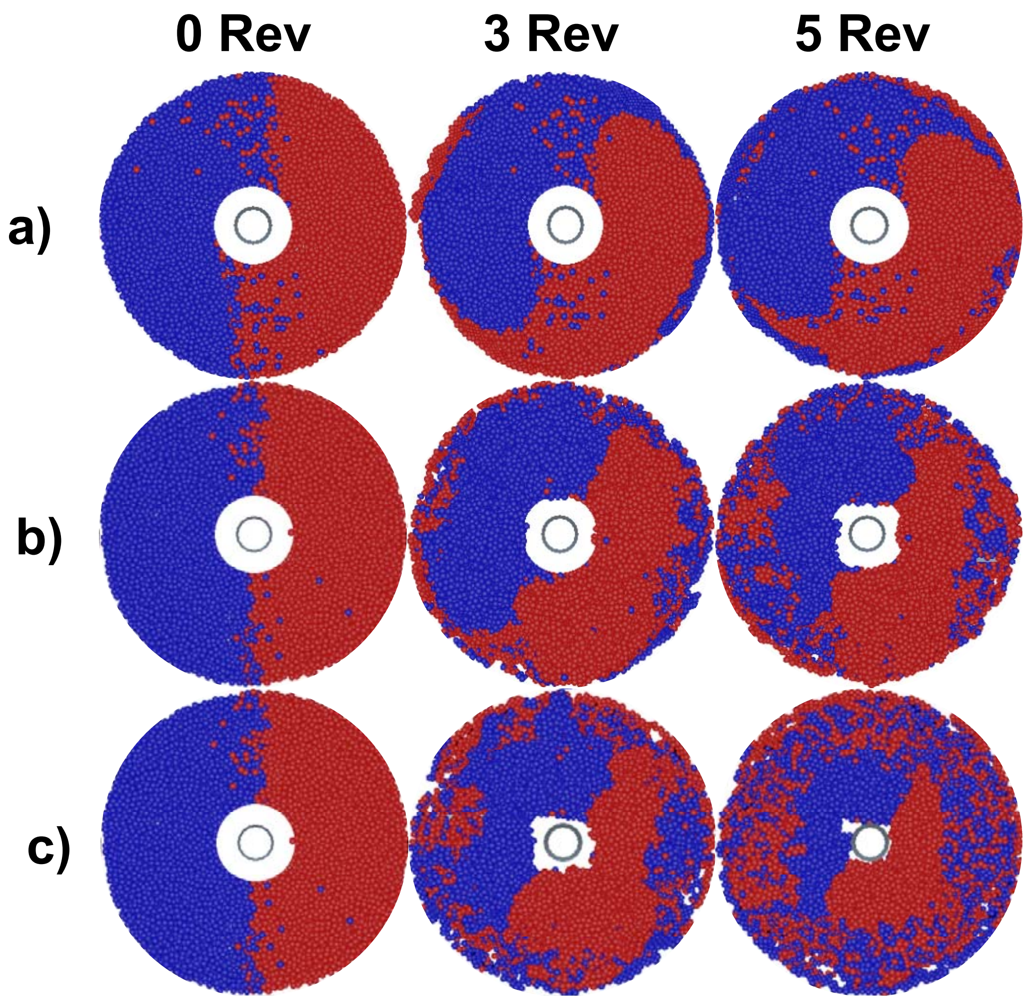

Figure 7.10. Effect of microscopic friction on mixing. a) μ_s = 0.1, b) μ_s = 0.3 and c) μ_s = 0.5. Results obtained for ϕ_{liq} = 0.045 moisture content.

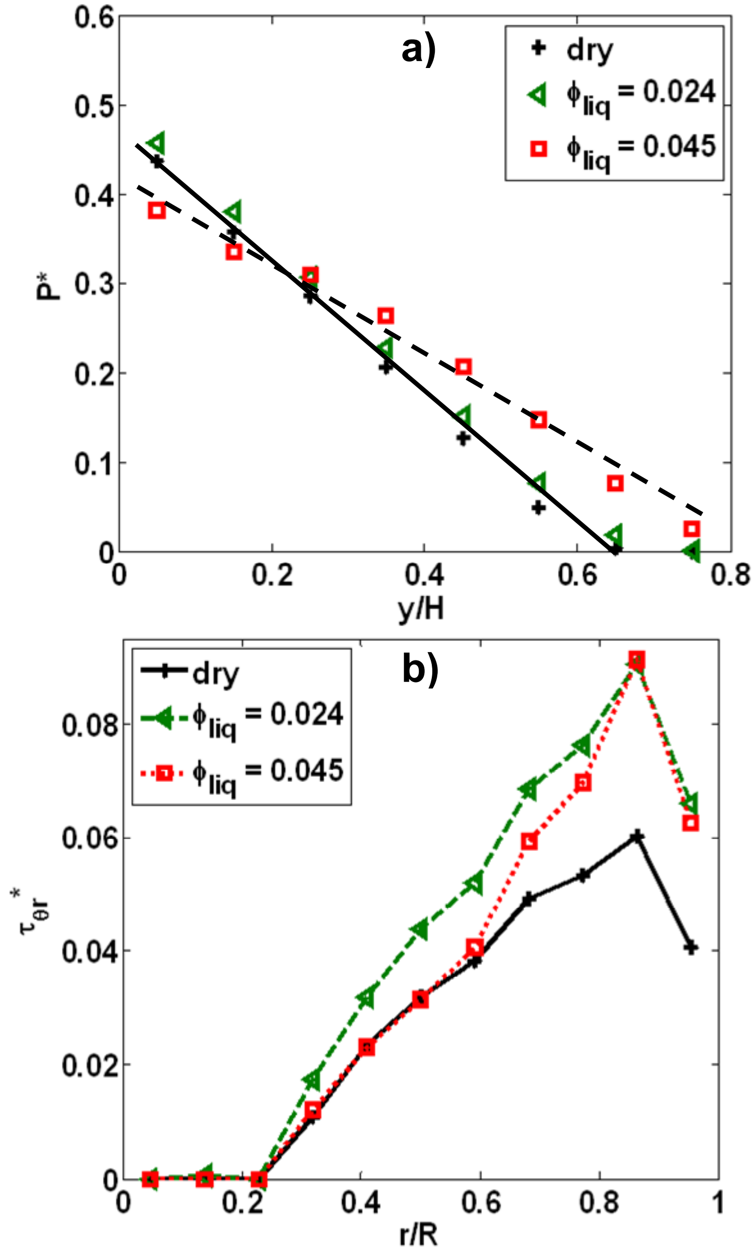

Figure 7.11. Effect of moisture content on normalized pressure and shear stress. a) time average P^* vs. normalized height and b) time average $\tau_{\theta r}{}^*$ vs. normalized radial position.

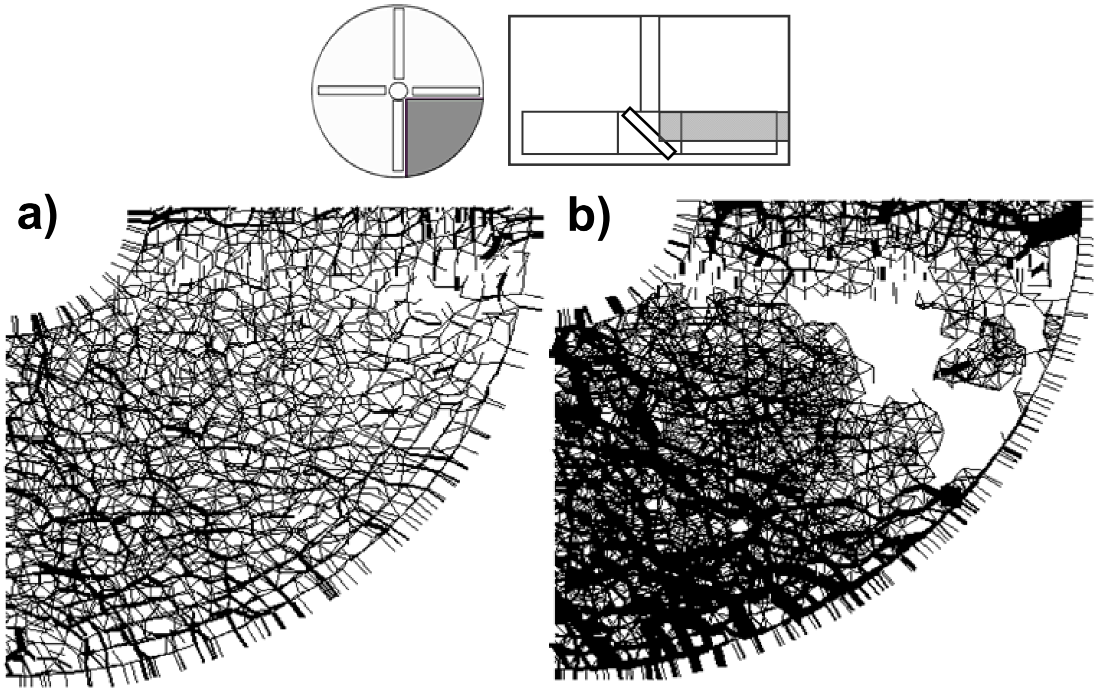

Figure 7.12. Effect of moisture content on normal contact force network near top of the blades. a) dry and b) ϕ_{liq} = 0.045.

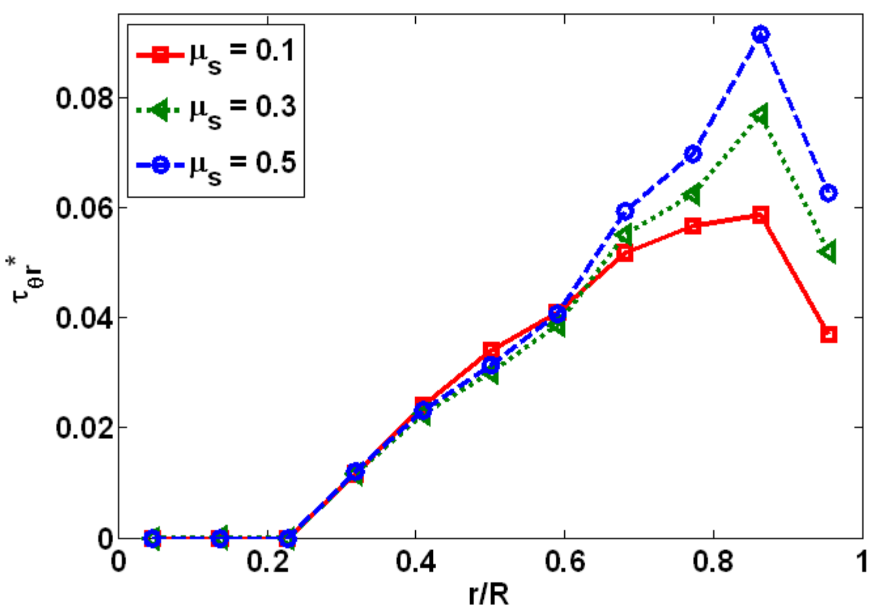

Figure 7.13. Effect of microscopic friction on normalized shear stress. Results obtained for ϕ_{liq} = 0.045 moisture content.

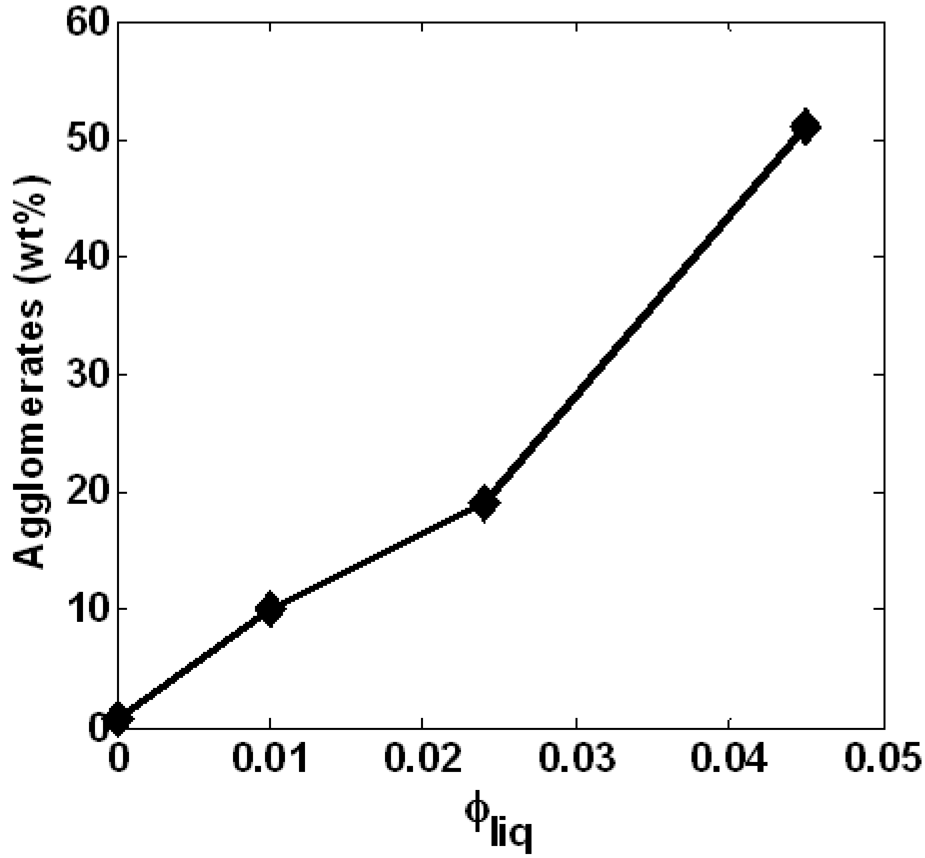

Figure 7.14. Weight percent of particle agglomeration vs. moisture content at steady state.

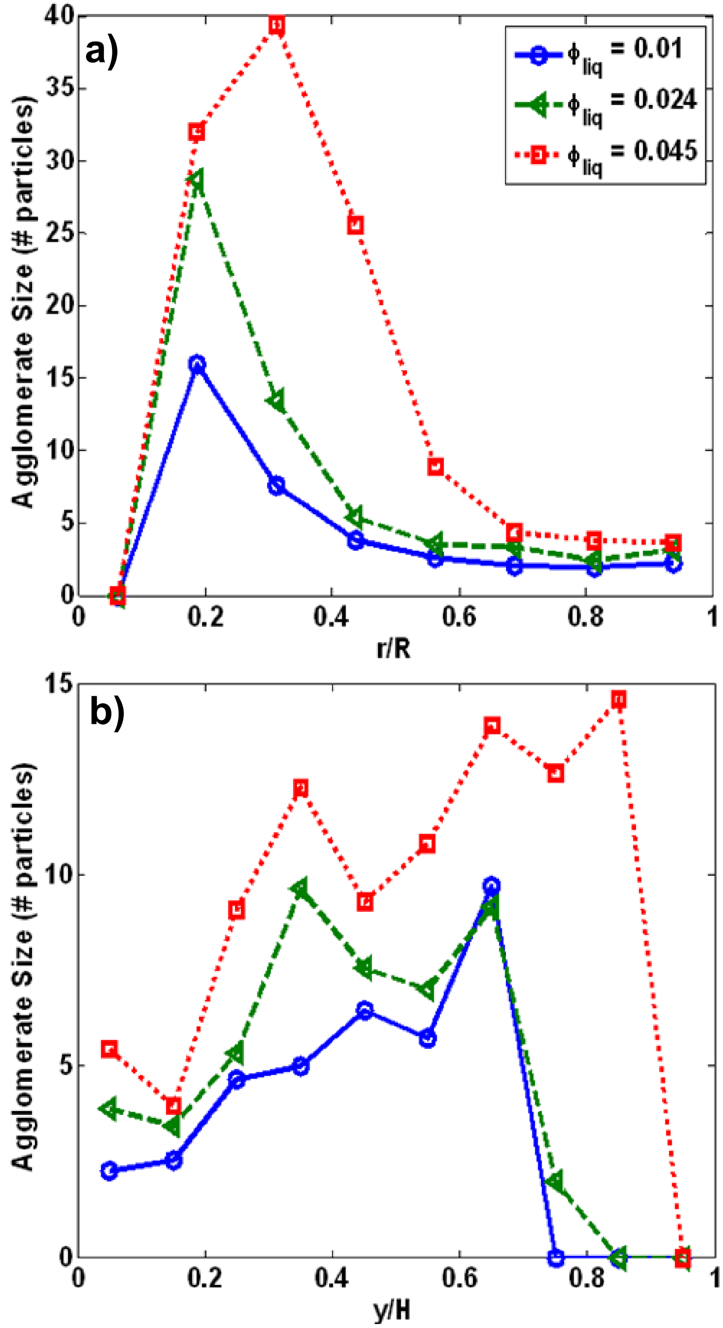

Figure 7.15. Effect of moisture content on average agglomerate size. a) agglomerate size vs. r/R and b) agglomerate size vs. y/H.

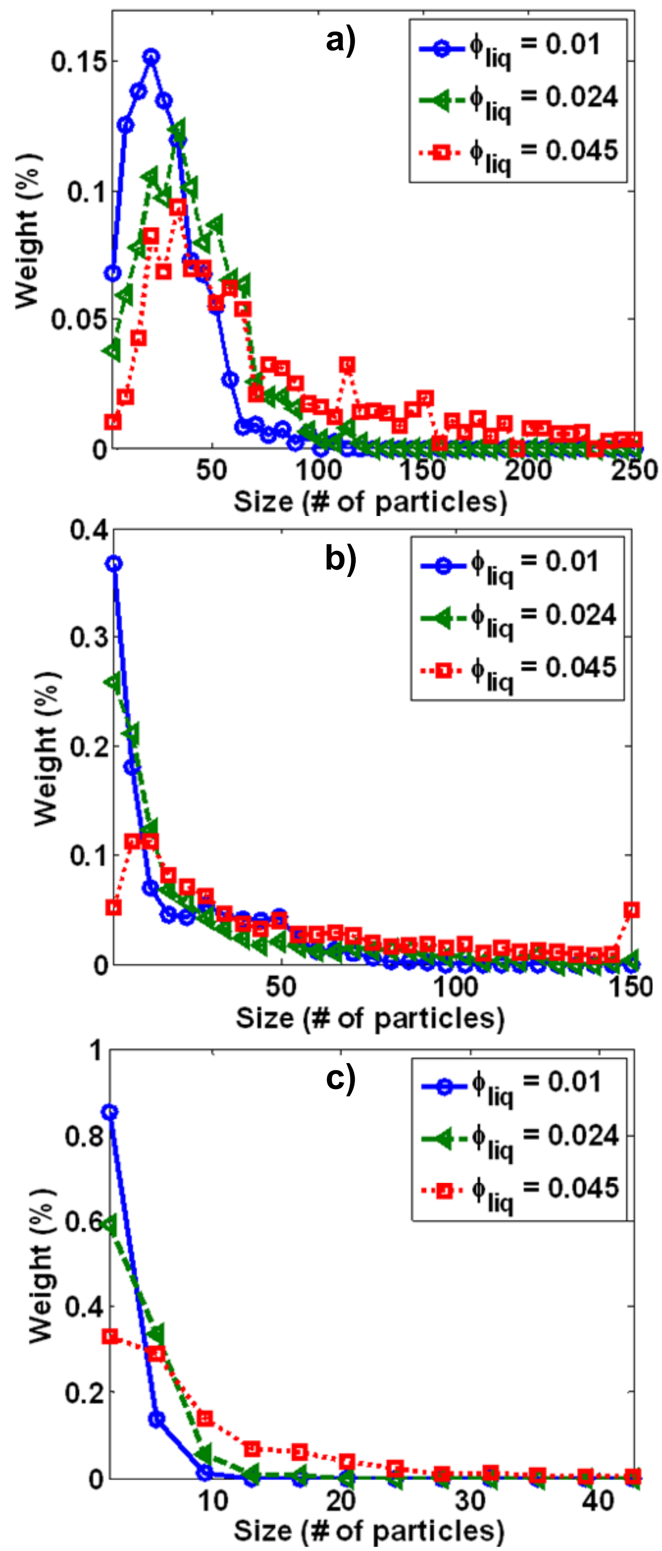

Figure 7.16. Effect of moisture content on agglomerate particle size distribution. a) size distribution near impeller shaft, b) size distribution in the center and c) size distribution near cylinder wall. Note: The lower limit of the abscissa for these graphs is 2 since only the agglomerated particles are considered in this analysis.

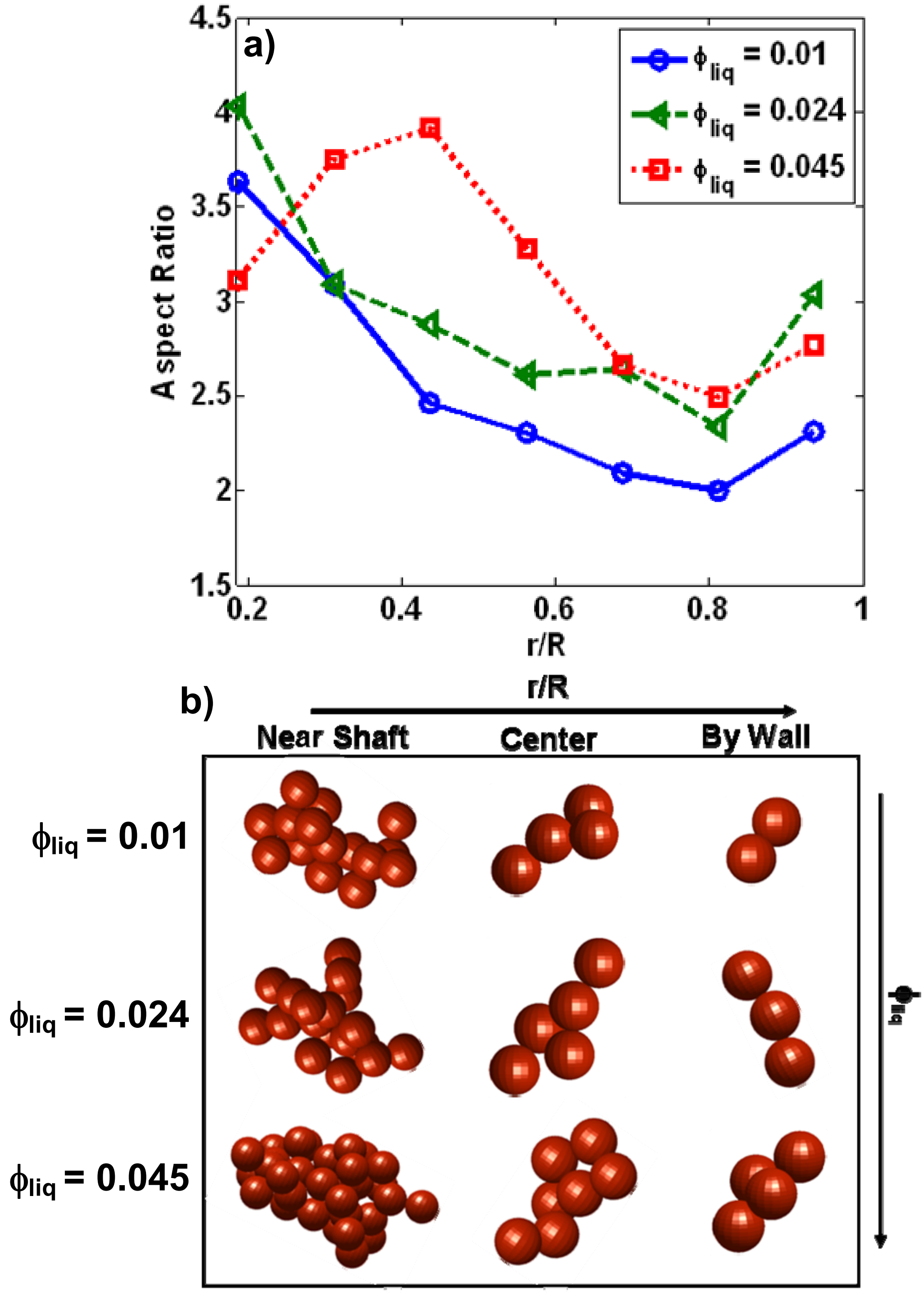

Figure 7.17. Effect of moisture content on agglomerate shape. a) average agglomerate aspect ratio vs. r/R and b) agglomerate morphology at different moisture content.

7.8. Tables for Chapter 8

Variable	Symbol	Value
Liquid surface tension	γ	0.073 N/m
Contact angle	θ	0 °
Liquid density	ρ_{liq}	1.0 g/ml
Liquid volume fraction	ϕ_{liq}	0 - 0.045
Bond number	Bo	5

Table 7.1. Input parameters for capillary liquid bridge model.

ϕ_{liq}	$D_{\theta\theta}$*	D_{rr} *	D_{yy}*	$Pe_{\theta\theta}$	Pe_{rr}	Pe_{yy}
0	6.1×10^{-4}	3.2×10^{-4}	2.0×10^{-3}	860	163	35
0.01	8.1×10^{-4}	4.7×10^{-4}	5.2×10^{-3}	535	131	19
0.024	8.3×10^{-4}	4.8×10^{-4}	5.4×10^{-3}	523	129	18
0.045	3.5×10^{-4}	2.3×10^{-4}	3.6×10^{-3}	1277	189	18

Table 7.2. Effect of moisture content on normalized particle diffusivities and Peclet number. Particle diffusivities were computed with a Δt of ¼ of a revolution.

μ_s	$D_{\theta\theta}$*	D_{rr} *	D_{yy}*	$Pe_{\theta\theta}$	Pe_{rr}	Pe_{yy}
0.1	5.2×10^{-5}	2.5×10^{-5}	8.8×10^{-5}	12334	650	183
0.3	2.0×10^{-4}	1.3×10^{-4}	1.5×10^{-3}	2490	250	29
0.5	3.5×10^{-4}	2.3×10^{-4}	3.6×10^{-3}	1277	189	18

Table 7.3. Effect of microscopic friction on normalized particle diffusivities and Peclet number. Particle diffusivities were computed with a Δt of ¼ of a revolution. Results obtained for ϕ_{liq} = 0.045 moisture content.

Chapter 8. Conclusions and Future Work

The behavior of particulate systems in an industrially relevant geometry was investigated using computational and experimental techniques. The geometry consisted of a vertical, cylindrical mixer mechanically agitated by an impeller with four blades pitched at a 45° angle. The effect of particle properties, mixer properties and operating conditions on the development of flow in bladed mixers was studied. In general, granular flows in bladed mixers were found to be periodic with complex flow patterns developing throughout the particle bed. Particles in bladed mixers were found to move mainly in the tangential direction. However, the formation of secondary flow structures was found to significantly affect mixing and segregation rates. It was observed that particle transport occurs mostly due to convection, although a diffusive mechanism becomes important as system scale and system roughness are increased. Additionally, we demonstrated that the behavior of granular materials in bladed mixer is in many ways analogous to the behavior of visco-plastic or Bingham fluids. The work presented here will contribute to the development of rigorous multi-scale models which can assist in the design and scale-up of bladed mixer operations and on the identification of critical processes parameters. An ultimate goal of research in this area is to enable better control of particle processing technologies by elucidating the underlying physics of particulate flows.

Initially, the flow behavior of monodisperse, cohesionless particles at low blade rotational speeds was investigated via numerical simulations. The numerical tool used here was the discrete element method. Our simulation results were consistent with bladed mixer experimental and computational results found in the literature. Velocity, density and stress profiles within the mixer displayed a periodic behavior with a fluctuation frequency equal to that of the blade rotation. Blade orientation was found to affect flow patterns and mixing kinetics. For an obtuse blade pitch orientation, a 3-dimensional recirculation zone develops in front of the blade due to formation of heaps where the blades are present. This flow pattern promotes vertical and radial mixing. No recirculation zone was observed when the blade orientation was changed to an acute blade pitch. The microscopic frictional characteristics of the system were shown to strongly influence the granular behavior within the mixer. At low friction coefficients the 3-D recirculation in front of the obtuse blade is not present reducing convective mixing. Higher friction coefficients lead to an increase in granular temperature which is associated with an increase in diffusive mixing. Normal and shear stresses were found to vary with mixer height with maximum values near the bottom plate. Additionally, a strong dependence between the magnitude of the shear stresses and the friction coefficient of the particles was found. The stress tensor calculations indicate that the granular flow at low blade rotational speeds occurs in the quasi-static regime. At the same time, the averaged pressure was found to vary linearly with bed height and could be predicted by a simple hydrostatic approximation.

The effect of mixer properties and fill level at low rotational speeds was then studied for monodisperse, cohesionless flows. For fill levels just covering the span of the blades, a 3-dimensional recirculation zone develops in front of the blades which promotes vertical and radial mixing. Increasing fill level reduces the size of the recirculation zone, decreases bed dilation and hinders particle diffusivities. However, above a critical fill level, the behavior of the particles within the span of the blade was found to be invariant of fill level. At low fill levels, the pressure within the particle bed varies linearly with bed height and can be approximated by hydrostatics. At higher fill levels, a constant pressure region develops within the span of the blades due to the angled pitch of the blades. Cylinder wall friction was shown to significantly influence granular behavior in bladed mixers. At low wall friction, the 3-dimensional recirculation zone observed for high wall friction conditions does not develop. High wall friction leads to an increase in convective and diffusive particle mixing. Shear stresses were shown to be a function of wall friction. Blade position along the vertical axis was shown to influence flow patterns, granular temperature and stress. The effect of increasing the mixer diameter at a constant particle diameter was also studied. When the mixer diameter is larger than a critical size such that wall effects are minimized, the observed granular behavior follows simple scaling relations. Particle velocities and diffusivities scale linearly with mixer size and blade speed. Normal and shear stress profiles were found to scale linearly with the total weight of the particle bed.

The kinematics of cohesionless flows was also studied experimentally using Particle Image Velocimetry. The DEM simulation results were then compared to the experimental data. The numerical simulations were able to reproduce the surface velocities, granular temperature profiles and mixing kinetics observed experimentally. Procedures for roughening of glass bead surfaces via coating were developed to study the effect of surface roughness and to test the computational findings regarding the effect of particle friction. Increasing particle surface roughness led to the development of less uniform flows inside the mixer and to increased dilation of the particle bed. Systems composed of rougher particles experienced increased radial and vertical velocities as well as higher particle diffusivities. The computational findings regarding the effect of cylinder wall roughness were also verified via experiments. The laboratory mixer walls were lined with sand paper to create a "rough wall" and these results were compared to the smooth, glass wall behavior. Cylinder wall roughness was shown to significantly influence particle velocities in bladed mixers, a behavior consistent with the simulation results. Rough cylinder walls led to more pronounced particle velocity fluctuations near the top surface and to an increase in granular temperature.

The effect of increasing blade speed was then studied via numerical simulations and experiments for cohesionless flows. Two distinct flow regimes were observed as blade speed was increased. At low rotational speed, the flow occurs in the quasi-static regime where particle surface velocities are linearly proportional to the tip speed of the blades. In this regime, the rotational speed of the blades provides the time scale for momentum transfer and for the mixing process. As expected, average shear stress was found to be independent of blade speed in the quasi-static regime, but shear stress increased with microscopic friction. At higher rotational speeds, the intermediate regime is encountered where particle surface velocities are no longer proportional to the tip speed of the blades. This regime is characterized by enhanced radial and vertical particle velocities as well as faster mixing kinetics. In the intermediate regime, the behavior of the particle bed was demonstrated to be similar to that of Bingham fluids. A yield stress needs to be overcome in order to induce flow and average stresses increase linearly with blade rotational speed. Yield stress and apparent viscosities were shown to be a function of microscopic friction in bladed mixers.

Once the behavior of monodisperse, cohesionless flows was characterized, the behavior of more complex systems was studied. Experiments and DEM simulations were performed to investigate the flow, segregation patterns, mixing kinetics and stresses that develop in cohesionless granular beds containing multiple particle sizes. For a binary system with a 2:1 size ratio, segregation by size occurs due to a sieving mechanism. Segregation in the binary system is fast, with a fully segregated system observed after just 5 revolutions. However, the numerical simulations showed that the extent of segregation in the bladed mixer can be reduced by introducing intermediate particle sizes in between the smallest and the largest particles. Addition of intermediate particle sizes increases convective and diffusive particle motion promoting a mixing mechanism which reduces segregation via the sieving mechanism. Void fraction within the bladed mixer increases as the degree of polydispersity is increased allowing the particles to move more freely throughout the particle bed. Higher void fractions also increase the ability of large particles to penetrate deeper into the particle bed. Normal and shear stresses are also affected by particle size distributions, with lower average values obtained for the system with the largest number of particle species. Differences in the amount of stress generated by each particle species were observed. However, the difference in stresses is reduced as the number of particle species in the system is increased.

Finally, the behavior of wet, monodisperse particles in bladed mixers at low rotational speeds was investigated via experiments and simulations. The presence of water in the system leads to an increase in inter-particle cohesion. The effect of moisture content for wet systems in the pendular state was studied. Experimental and computational results showed that, at low moisture contents, convective and diffusive particle movement is enhanced leading to higher mixing rates when compared to a dry system. However, at higher moisture contents, convective and diffusive particle motion decreases. This in turn leads to lower mixing rates at high moisture contents. Pressure and shear stress profiles were shown to be significantly affected by moisture content. In general, shear stress values increased as moisture content was increased.

The formation of particle agglomerates in wet flows was also studied. A method for determining the extent of agglomeration in the DEM simulations was developed. This analysis showed that the portion of the particle bed which is agglomerated increases as moisture content is increased. The size of these agglomerates is highest near the impeller shaft and towards the top of the particle bed, which corresponds to regions characterized by lower stresses. Agglomerate aspect ratio increased with moisture content indicating the formation of elongated, needle-like agglomerates.

Future work

Most practical granular materials are composed of non-spherical particles. However, few studies are found in the literature that explore the behavior of non-spherical particle assemblies. Particle shape can significantly affect the flowability of granular materials. For example, elongated, needle-like particles have been shown to produce hopper discharge flow rates 30% lower than spherical particles [201]. Non-spherical particles tend to display a high resistance to rolling and are susceptible to particle interlocking. Particle shape also affects the yield strength of a granular assembly as a larger amount of energy is needed to shear non-spherical particles than spherical particles [202]. Various methods have been developed to incorporate the effect of particle shape into DEM simulations for different particle shapes such as ellipses, cylinders, superquadrics and hyperquadrics [202, 203]. These methods include new contact detection algorithms for non-spherical particles along with new explicit force expressions. Particle shape can also be studied via DEM by creating composite, non-spherical particles by “gluing” smaller spherical particles into clusters that act as individual, non-spherical particles [204]. This reduces computational requirements as it simplifies contact detection and enables the use of force models based on contact theory for spheres.

Investigating the effect of particle shape on granular flow is of practical importance to industrial bladed mixer operations as these processes often involve non-spherical particles. Art sand could be used in the laboratory to study the effect of angular shapes and these results could be compared to those obtained with glass beads of an equivalent diameter. Cylinders or L-threonine particles could be use to explore the effect of needle-like shapes. DEM simulations could be used in parallel with the experimental work to measure quantities not easily accessible via current experimental analytical techniques such as localized flow, diffusive particle motion and stress generation. Non-spherical particle morphologies can be modeled by creation of composite particles of rigidly bonded spheres. Code modifications will be required to associate individual particles with particular composites, construct the composites, and follow the composites in time. Initial studies may focus on the behavior of fairly monodisperse, non-spherical particles. Further studies could focus on the effect of system scale.

Two distinct flow regimes were observed in this work, a rate-independent, quasi-static regime and a rate-dependent, intermediate regime. The DEM simulation results showed that impeller torque measurements could be used to determine the parameters leading to flow regime transition. Impeller torque measurements could also provide further insight into the rheology of granular materials. Experimental torque measurements could be used to validate the simulation results and examine the effect of particle properties on granular rheology. The effects of system size, particle shape and size distribution, and fill level on visco-plastic parameters could also be investigated.

The results presented here suggest that while segregation due to sieving occurs in bladed mixers, reduction of segregation rates can be achieve by tailoring the particle size distribution of the system. However, only systems with flat particle size distributions (i.e. equal volume fractions systems) and a maximum size ratio of 2:1 were studied. In industrial scenarios, it is common to find components with Gaussian, lognormal or even bimodal particle size distributions. The width of the particle size distribution in industrial systems can be larger than what was studied here. Particle size distributions of different shapes and width can be produced in the laboratory by mixing particles of different sizes or with the use of sieving trays. These mixtures can then be used to study the effect of these parameters on flow and segregation in bladed mixers. The current DEM code allows for the creation of particles with Gaussian and lognormal particle size distributions at specified widths. It may be interesting to look at the effect of particle size width on void fraction during shearing. While void fraction was observed to increase with polydispersity for systems with a 2:1 size ratio, higher size ratios might lead to a decrease in void fractions [188]. The effect of changing the width of the particle size distribution on bed dilation during flow is also worth investigating.

In polydisperse systems, cohesion forces can act to enhance mixing or to promote segregation [93]. Methods have been developed to assist in the determination of the final state of a cohesive, multi-component granular mixture by examining the strength of the cohesive forces that develop between different particle sizes [92, 93]. The computational and experimental techniques used in this work could also be used to study the effect of water content on the flow and segregation of polydisperse mixtures. Surface characteristics also become important for wet flows, as hydrophobic materials can segregate from hydrophilic materials in the presence of water during flow [93].

The work done on wet particle flows in bladed mixers focused on flows at low blade rotational speeds and at the laboratory scale. The effect of system size on the flow and agglomeration of wetted particles remains unclear. DEM simulations at different D/d ratios could elucidate some of the effects of system scale on wet particle flows. These results could then be compared with the behavior observed for dry, monodisperse particles. The role of blade speed on flow and agglomeration is not well understood. Future experimental and computational work on wet flows could focus on the effect of these parameters.

Analysis of wet flows suggested that liquid distribution within the particle bed can be significantly affected by the liquid's viscosity. Differences in liquid distribution could in turn lead to localized differences in cohesive force magnitude. Additional cohesive forces could also arise due to lubrication effects for liquids with high viscosities [195]. Understanding the effect of liquid viscosity on liquid distribution and on the amount of cohesion in the system is important for bladed mixer processes such as wet granulation and agitated drying. Initial experimental work could investigate the effect of liquid viscosity using mixtures of water and glycerin. The viscosity of these mixtures can be tailored by using different water to glycerin ratios while keeping a surface tension similar to that of water. The current DEM code could be modified to include lubrication forces and to account for localized differences in liquid distribution. A detailed investigation of the effect of liquid viscosity would be invaluable for predicting flow of wet particle beds.

Notations

m_i mass of particle i
R_i radius of particle i
I_i moment of inertial of particle i
v_i velocity of particle i
g acceleration due to gravity
F_{ij}^N normal force resulting from the contact of particle i with particle j
F_{ij}^T tangential force resulting from the contact of particle i with particle j
r_i position vector for particle i
$\widetilde{k}_n$ normal stiffness coefficient
$\widetilde{k}_t$ tangential stiffness coefficient
v_{rel}^t relative tangential velocity of the colliding particles
d particle diameter
E Young's modulus
G Shear modulus
R^* effective radius of the colliding particles
e coefficient of restitution
s tangential decomposition of contact unit vector
F_{ij}^C cohesive force experienced by particle i due to a liquid bridge with particle j
ΔP pressure difference across the air-fluid interface in wet systems
$\widehat{V}$ dimensionless liquid bridge volume
$\widehat{h}$ dimensionless separation distance between surface of particles
$\widehat{h}_c$ critical rupture distance for liquid bridge
Ca Capillary number
U characteristic system velocity
u' fluctuation velocity
T granular temperature
R_C radius of spherical control volume
a distance between center of particle and center of control volume
V_c control volume size
D_{ij} diffusion coefficient in the i direction due to a gradient in the j direction
Δx_i particle displacement in the i direction
$\overline{\Delta x_i}$ mean particle displacement in the i direction
Pe Peclet number
U_i average particle speed
M_{conc} mean particle concentration
M degree of mixing for polydisperse systems
n_k total particle number fraction in cell k

x_i^k	number fraction of species *i* in cell *k*
P	pressure
V_t	tangential velocity
V_r	radial velocity
V_y	vertical velocity
H_{bed}	total height of particle bed
H	bed height prior to blade movement
D	diameter of mixer
V^*	particle velocity normalized by the tip speed
V_{tip}	tip speed of blades
R	radius of mixer
$\langle P \rangle$	temporal averaged pressure
D/d	mixer diameter to particle diameter ratio
D_{ij}^*	normalized diffusion coefficient
P^*	normalized pressure
U_{avg}	average particle speed
P_{adj}	adjusted blade power
C^*_{large}	normalized large particle concentration.
C_{large}	local large particle concentration
$\langle C_{large} \rangle$	average large particle concentration
M_{flux}	mass flux
$\dot{M}_{flux}$	normalized mass flux
t_c	particle-particle contact time
t_{break}^{dry}	characteristic time-of-contact breakage for dry system

Greek Letters

ω_i	angular velocity of particle *i*
τ_{rij}	torque resulting from the contact of particle *i* with particle *j*
δ_n	normal displacement or overlap
δ_t	tangential displacement
$\tilde{\gamma}_n$	normal damping coefficient
$\tilde{\gamma}_t$	tangential damping coefficient
ρ	particle density
σ	Poisson ratio
μ_r	rolling friction coefficient
μ_s	silding friction coefficient

β	half filling angle of a capillary liquid bridge
θ	contact angle of a capillary liquid bridge
γ	surface tension of liquid
η	dynamic viscosity of liquid
ε	void fraction
τ_{ij}	stress on *i* plane in the *j* direction
ρ_{bulk}	total average bulk density
τ_{ij}	stress on *i* plane in the *j* direction
$\left\langle \tau_{ij} \right\rangle$	temporal averaged stress
μ_s^{p-p}	particle-particle sliding friction
μ_s^{p-w}	particle-cylinder wall sliding friction
σ_{conc}	standard deviation of particle concentration
τ_{ij}^*	normalized shear stress
μ	internal friction coefficient from shear cell analysis
$\gamma*$	dimensionless shear rate
$\gamma\circ$	shear rate
τ_y	yield stress of particle bed
κ	apparent viscosity
ρ_{liq}	density of liquid in a capillary liquid bridge
ϕ_{liq}	volume fraction of liquid in wet systems

References

1. Bridgwater, J., *The dynamics of granular materials – towards grasping the fundamentals.* Granular Matter, 2003. **4**: p. 175–181.
2. Poux, M., P. Fayolle, J. Bertrand, D. Bridoux, and J. Bousquet, *Powder mixing: Some practical rules applied to agitated systems.* Powder Technology, 1991. **68**(3): p. 213-234.
3. Prescott, J.K., *Powder Handling*, in *Pharmaceutical Process Scale-up*, M. Levin, Editor. 2001, Marcel Dekker. p. 133-149.
4. Wang, Z.L., W.H. Finlay, M.S. Peppler, and L.G. Sweeney, *Powder formation by atmospheric spray-freeze-drying.* Powder Technology, 2006. **170**(1): p. 45-52.
5. Muzzio, F.J., A. Alexander, C. Goodridge, E. Shen, and T. Shinbrot, *Solids Mixing Part A: Fundamentals of Solids Mixing*, in *Handbook of Industrial Mixing: Science and Practice*, V.A.A.-O. Edward L. Paul, Suzanne M. Kresta, Editor. 2004, John Wiley & Sons, Inc. p. 887-983.
6. Vidales, A.M., I. Ippolito, O.A. Benegas, F. Aguirre, O.C. Nocera, and M.R. Baudino, *Granular components of cement: Influence of mixture composition.* Powder Technology, 2006. **163**(3): p. 196-201.
7. Meier, S.W., R.M. Lueptow, and J.M. Ottino, *A dynamical systems approach to mixing and segregation of granular materials in tumblers.* Advances in Physics, 2007. **56**(5-6): p. 757-827.
8. Geldart, D., *Powder Processing - The Overall View*, in *Principles of Particle Technology*. 1990, John Wiley & Sons Ltd. p. 1-7.
9. Wibowo, C. and K.M. Ng, *Operational issues in solids processing plants: Systems view.* AIChE Journal, 2001. **47**(1): p. 107-125.
10. Goldhirsch, I., *Rapid Granular Flows.* Ann. Rev. Fluid Mech., 2003. **35**: p. 263-297.
11. Campbell, C.S., *Granular material flows - An overview.* Powder Technology, 2006. **162**(3): p. 208-29.
12. Zamankhan, P., A. Mazouchi, and P. Sorkomaa, *Some qualitative features of the Couette flow of monodisperse, smooth, inelastic spherical particles.* Appl. Phys. Lett., 1997. **71**(26): p. 3790-3792.
13. Savage, S.B. and D.J. Jeffrey, *The stress tensor in a granular flow at high shear rates.* J. Fluid Mech., 1981. **110**: p. 255-272.
14. Jenkins, J.T. and F. Mancini, *Kinetic theory for binary mixtures of smooth, nearly elastic spheres.* Phys Fluids A, 1989. **1**(12): p. 2050-2057.
15. Savage, S.B. and R. Dai, *Some aspects of bounded and unbounded shear flows of granular material*, in *Advances in Micromechanics of Granular Materials*, H.H. Shen, et al., Editors. 1992, Elsevier. p. 151-161.
16. Hopkins, M.A. and M.Y. Louge, *Inelastic Microstructure in Rapid Granular Flows of Smooth Disks.* Phys. Fluids A, 1991. **3**(1): p. 47-57.
17. Lun, C.K.K., S.B. Savage, D. Jeffrey, and N. Chepurniy, *Kinetic theories for granular flow: inelastic particles in Couette flow and slightly inelastic particles in a general flowfield.* J. Fluid Mech., 1984. **140**: p. 223-256.

18. Campbell, C.S., *Shear flows of granular materials*, in *Division of Engineering and Applied Science*. 1982, California Institute of Technology: Pasedena, CA. p. 255+.
19. Campbell, C.S., *Granular shear flows at the elastic limit.* J. Fluid Mech., 2002. **465**: p. 261-291.
20. Glasser, B.J. and I. Goldhirsh, *Scale dependence, correlations, and fluctuations of stresses in rapid granular flows.* Phys. Fluids, 2001. **13**(2): p. 407-420.
21. Hopkins, M.A., J.T. Jenkins, and M.Y. Louge, *On the structure of 3D shear flows*, in *Advances in Micromechanics of Granular Materials*, H.H.S.e. al, Editor. 1992, Elsevier Science Publishers. p. 271-279.
22. Conway, S.L. and B.J. Glasser, *Density waves and coherent structures in granular Couette flows.* Phys. Fluids, 2004. **16**(3): p. 509-529.
23. Liu, X., M. Metzger, and B.J. Glasser, *Couette flow with a bidisperse particle mixture.* Physics of Fluids, 2007. **19**(7): p. 073301.
24. Lun, C.K.K., *Granular dynamics of inelastic spheres in Couette flow.* Phys. Fluids, 1996. **8**(11): p. 2868-2883.
25. Sasvári, M., J. Kertész, and D.E. Wolf, *Instability of symmetric Couette flow in a granular gas: Hydrodynamic field profiles and transport.* Physical Review E, 2000. **62**(3): p. 3817-3825.
26. Tardos, G.I., M.I. Khan, and D.G. Schaeffer, *Forces on a slowly rotating, rough cylinder in a Couette device containing a dry, frictional powder.* Physics of Fluids, 1998. **10**(2): p. 335-41.
27. Conway, S.L., D.J. Goldfarb, T. Shinbrot, and B.J. Glasser, *Free surface waves in wall-bounded granular flows.* Physical Review Letters, 2003. **90**(7): p. 074301-1.
28. Forterre, Y. and O. Pouliquen, *Longitudinal vortices in granular flows.* Physical Review Letters, 2001. **86**(26): p. 5886-9.
29. Forterre, Y. and O. Pouliquen, *Stability analysis of rapid granular chute flows: Formation of longitudinal vortices.* Journal of Fluid Mechanics, 2002. **467**: p. 361-387.
30. LaMarche, K., S. Conway, B. Glasser, and T. Shinbrot, *Cellular automata model of gravity-driven granular flows.* Granular Matter, 2007. **9**(3): p. 219-229.
31. Ding, Y.L., R.N. Forster, J.P.K. Seville, and D.J. Parker, *Scaling relationships for rotating drums.* Chemical Engineering Science, 2001. **56**(12): p. 3737-3750.
32. Ottino, J.M. and D.V. Khakhar, *Scaling of granular flow processes: From surface flows to design rules.* AIChE Journal, 2002. **48**(10): p. 2157-2166.
33. Felix, G., V. Falk, and U. D'Ortona, *Granular flows in a rotating drum: the scaling law between velocity and thickness of the flow.* European Physical Journal E, 2007. **22**(1): p. 25-31.
34. Muzzio, F.J., T. Shinbrot, and B.J. Glasser, *Powder technology in the pharmaceutical industry: the need to catch up fast.* Powder Technology, 2002. **124**(1-2): p. 1-7.
35. Laurent, B.F.C., *Scaling factors in granular flow-analysis of experimental and simulations results.* Chemical Engineering Science, 2006. **61**(13): p. 4138-46.
36. Sinnott, M. and P. Cleary. *3D DEM simulations of a high shear mixer*. 2006. Melbourne, Vic., Australia: CSIRO Materials.

37. Lekhal, A., K.P. Girard, M.A. Brown, S. Kiang, B.J. Glasser, and J.G. Khinast, *Impact of agitated drying on crystal morphology: KCl-water system.* Powder Technology, 2003. **132**(2-3): p. 119-130.
38. Lee, T. and J. Lee, *Particle attrition by particle-surface friction in dryers.* Pharmaceutical Technology, 2003. **27**(5): p. 64-72.
39. Lekhal, A., K.P. Girard, M.A. Brown, S. Kiang, J.G. Khinast, and B.J. Glasser, *The effect of agitated drying on the morphology of -threonine (needle-like) crystals.* International Journal of Pharmaceutics, 2004. **270**(1-2): p. 263-277.
40. Campbell, C.S., *Rapid Granular Flows.* Ann. Rev. Fluid Mech., 1990. **22**: p. 57-92.
41. Jackson, R., *Some features of the flow of granular materials and aerated granular materials.* Journal of Rheology, 1985. **30**(5): p. 907-930.
42. Campbell, C.S. and C.E. Brennen, *Computer simulation of granular shear flows.* J. Fluid Mech., 1985. **151**: p. 167-188.
43. Tardos, G.I., S. McNamara, and I. Talu, *Slow and intermediate flow of a frictional bulk powder in the Couette geometry.* Powder Technology, 2003. **131**(1): p. 23-39.
44. Srinivasa Mohan, L., K. Kesava Rao, and P.R. Nott, *A frictional Cosserat model for the slow shearing of granular materials.* Journal of Fluid Mechanics, 2002. **457**: p. 377-409.
45. Remy, B., J.G. Khinast, and B.J. Glasser, *Discrete element simulation of free flowing grains in a four-bladed mixer.* AIChE Journal, 2009. **55**(8): p. 2035-2048.
46. Drucker, D.C. and P. W., *Soil mechanics and plastic analysis of limit design.* Q. Appl. Math., 1952. **10**: p. 157-165.
47. Jackson, R., *The Dynamics of Fluidized Particles.* 1st ed. New York, N. Y. 2000: Cambridge University Press. 368.
48. Tuzun, U., J. Baxter, and D.M. Heyes, *Analysis of the evolution of granular stress-strain and voidage states based on DEM simulations.* Philosophical Transactions of the Royal Society London, Series A (Mathematical, Physical and Engineering Sciences), 2004. **362**(1822): p. 1931-51.
49. Dahl, S.R. and C.M. Hrenya, *Size segregation in gas-solid fluidized beds with continuous size distributions.* Chemical Engineering Science, 2005. **60**(23): p. 6658-6673.
50. Dahl, S.R., R. Clelland, and C.M. Hrenya, *The effects of continuous size distributions on the rapid flow of inelastic particles.* Physics of Fluids, 2002. **14**(6): p. 1972-84.
51. Zamankhan, P., *Kinetic theory of multicomponent dense mixtures of slightly inelastic spherical particles.* Phys Rev. E, 1995. **52**(5): p. 4877-4891.
52. Jaeger, H.M. and S.R. Nagel, *Physics of the granular state.* Science, 1992. **255**(5051): p. 1523.
53. Jop, P., Y. Forterre, and O. Pouliquen, *A constitutive law for dense granular flows.* Nature, 2006. **441**(7094): p. 727-30.
54. Karmakar, S. and R.L. Kushwaha, *Development and laboratory evaluation of a rheometer for soil visco-plastic parameters.* Journal of Terramechanics, 2007. **44**(2): p. 197-204.

55. Savage, S.B., *Analyses of slow high-concentration flows of granular materials.* Journal of Fluid Mechanics, 1998. **377**: p. 1-26.
56. Porion, P., N. Sommier, A.-M. Faugere, and P. Evesque, *Dynamics of size segregation and mixing of granular materials in a 3D-blender by NMR imaging investigation.* Powder Technology, 2004. **141**(1-2): p. 55-68.
57. Alexander, A., F.J. Muzzio, and T. Shinbrot, *Effects of scale and inertia on granular banding segregation.* Granular Matter, 2004. **5**(4): p. 171-175.
58. Hill, K.M., A. Caprihan, and J. Kakalios, *Axial segregation of granular media rotated in a drum mixer: Pattern evolution.* Physical Review E, 1997. **56**(4): p. 4386.
59. Hill, K.M., G. Gioia, D. Amaravadi, and C. Winter, *Moon patterns, sun patterns, and wave breaking in rotating granular mixtures.* Complexity, 2005. **10**(4): p. 79-86.
60. Ennis, B.J., J. Green, and R. Davies, *The Legacy of Neglect in the US.* Chemical Engineering Progress, 1994. **90**: p. 32-43.
61. McCarthy, J.J., *Perspectives: Turning the Corner in Segregation.* Powder Technology, 2009. **192**(2): p. 137-142.
62. Tang, P. and V.M. Puri, *Methods for minimizing segregation: A review.* Particulate Science and Technology, 2004. **22**(4): p. 321-337.
63. Liss, E.D., S.L. Conway, J.A. Zega, and B.J. Glasser, *Segregation of Powders during Gravity Flow through Vertical Pipes.* Pharmaceutical Technology, 2004. **28**(2): p. 78-96.
64. Rosato, A., K.J. Strandburg, F. Prinz, and R.H. Swendsen, *Why the Brazil nuts are on top: size segregation of particulate matter by shaking.* Physical Review Letters, 1987. **58**(10): p. 1038-40.
65. Rosato, A.D., D.L. Blackmore, N. Zhang, and Y. Lan, *A perspective on vibration-induced size segregation of granular materials.* Chemical Engineering Science, 2002. **57**(2): p. 265-275.
66. Rosato, A.D., Y. Lan, and D.T. Wang, *Vibratory particle size sorting in multi-component systems.* Powder Technology, 1991. **66**(2): p. 149-160.
67. Bielenberg, J.R., G.M. Gladysz, and A.L. Graham, *A parametric study of axial segregation in granular systems.* Chemical Engineering Science, 2007. **62**(16): p. 4177-81.
68. Olsen, J.L. and E.G. Rippie, *Segregation Kinetics of Particulate Solids Systems I.* Journal of Pharmaceutical Sciences, 1964. **53**(2): p. 147-150.
69. Wu, S.Y. and J. Baeyens, *Segregation by size difference in gas fluidized beds.* Powder Technology, 1998. **98**(2): p. 139-150.
70. Ottino, J.M. and D.V. Khakhar, *Mixing and segregation of granular materials.* Annual Review of Fluid Mechanics, 2000. **32**: p. 55-91.
71. Shi, D., A.A. Abatan, W.L. Vargas, and J.J. McCarthy, *Eliminating segregation in free-surface flows of particles.* Physical Review Letters, 2007. **99**(14): p. 148001.
72. Williams, J.C., *The segregation of particulate materials. A review.* Powder Technology, 1976. **15**(2): p. 245-251.
73. Kudrolli, A., *Size separation in vibrated granular matter.* Reports on Progress in Physics, 2004. **67**(3): p. 209-47.

74. Conway, S.L., X. Liu, and B.J. Glasser, *Instability-induced clustering and segregation in high-shear Couette flows of model granular materials.* Chemical Engineering Science, 2006. **61**(19): p. 6404-6423.
75. Knight, J.B., H.M. Jaeger, and S.R. Nagel, *Vibration-induced size separation in granular media. The convection connection.* Physical Review Letters, 1993. **70**(24): p. 3728.
76. Schroter, M., S. Ulrich, J. Kreft, J.B. Swift, and H.L. Swinney, *Mechanisms in the size segregation of a binary granular mixture.* Physical Review E (Statistical, Nonlinear, and Soft Matter Physics), 2006. **74**(1): p. 11307-1.
77. Dahl, S.R. and C.M. Hrenya, *Size segregation in rapid, granular flows with continuous size distributions.* Physics of Fluids, 2004. **16**(1): p. 1-13.
78. Pierrat, P. and H.S. Caram, *Tensile strength of wet granular materials.* Powder Technology, 1997. **91**(2): p. 83-93.
79. Schulz, M., B.M. Schulz, and S. Herminghaus, *Shear-induced solid-fluid transition in a wet granular medium.* Physical Review E (Statistical, Nonlinear, and Soft Matter Physics), 2003. **67**(5): p. 52301-1.
80. Herminghaus, S., *Dynamics of wet granular matter.* Advances in Physics, 2005. **54**(3): p. 221-6.
81. Alexander, A.W., B. Chaudhuri, A. Faqih, F.J. Muzzio, C. Davies, and M.S. Tomassone, *Avalanching flow of cohesive powders.* Powder Technology, 2006. **164**(1): p. 13-21.
82. Faqih, A., B. Chaudhuri, F.J. Muzzio, M.S. Tomassone, A. Alexander, and S. Hammond, *Flow - Induced dilation of cohesive granular materials.* AIChE Journal, 2006. **52**(12): p. 4124-4132.
83. Rognon, P.G., J.N. Roux, M. Naaim, and F. Chevoir, *Dense flows of cohesive granular materials.* Journal of Fluid Mechanics, 2008. **596**: p. 21-47.
84. Tomas, J., *Fundamentals of cohesive powder consolidation and flow.* Granular Matter, 2004. **6**(2-3): p. 75-86.
85. Begat, P., D.A.V. Morton, J.N. Staniforth, and R. Price, *The Cohesive-Adhesive Balances in Dry Powder Inhaler Formulations I: Direct Quantification by Atomic Force Microscopy.* Pharmaceutical Research, 2004. **21**(9): p. 1591-1597.
86. Zhu, H.P., Z.Y. Zhou, R.Y. Yang, and A.B. Yu, *Discrete particle simulation of particulate systems: Theoretical developments.* Chemical Engineering Science, 2007. **62**(13): p. 3378-96.
87. Yao, J., Y. Zhang, C.-H. Wang, and Y.C. Liang, *On the electrostatic equilibrium of granular flow in pneumatic conveying systems.* AIChE Journal, 2006. **52**(11): p. 3775-3793.
88. Watano, S., S. Saito, and T. Suzuki, *Numerical simulation of electrostatic charge in powder pneumatic conveying process.* Powder Technology, 2003. **135-136**: p. 112-117.
89. Willett, C.D., M.J. Adams, S.A. Johnson, and J.P.K. Seville, *Capillary bridges between two spherical bodies.* Langmuir, 2000. **16**(24): p. 9396-405.
90. Papadakis, S.E. and R.E. Bahu, *Sticky issues of drying.* Drying Technology, 1992. **10**(4): p. 817-837.

91. Muguruma, Y., T. Tanaka, and Y. Tsuji, *Numerical simulation of particulate flow with liquid bridge between particles (simulation of centrifugal tumbling granulator).* Powder Technology, 2000. **109**(1): p. 49-57.
92. Li, H. and J.J. McCarthy, *Cohesive particle mixing and segregation under shear.* Powder Technology, 2006. **164**(1): p. 58-64.
93. Li, H. and J.J. McCarthy, *Controlling cohesive particle mixing and segregation.* Physical Review Letters, 2003. **90**(18): p. 184301-1.
94. McCarthy, J.J., *Micro-modeling of cohesive mixing processes.* Powder Technology, 2003. **138**(1): p. 63-67.
95. Malhotra, K., A.S. Mujumdar, H. Imakoma, and M. Okazaki, *Fundamental particle mixing studies in an agitated bed of granular materials in a cylindrical vessel.* Powder Technology, 1988. **55**(2): p. 107-114.
96. Malhotra, K. and A.S. Mujumdar, *Particle mixing and solids flowability in granular beds stirred by paddle-type blades.* Powder Technology, 1990. **61**(2): p. 155-164.
97. Malhotra, K., A.S. Mujumdar, and M. Okazaki, *Particle flow patterns in a mechanically stirred two-dimensional cylindrical vessel.* Powder Technology, 1990. **60**(2): p. 179-189.
98. Laurent, B.F.C., J. Bridgwater, and D.J. Parker, *Motion in a particle bed agitated by a single blade.* AIChE Journal, 2000. **46**(9): p. 1723-1734.
99. Laurent, B.F.C. and J. Bridgwater, *Dispersive granular flow in a horizontal drum stirred by a single blade.* AIChE Journal, 2002. **48**(1): p. 50-58.
100. Jones, J.R., D.J. Parker, and J. Bridgwater, *Axial mixing in a ploughshare mixer.* Powder Technology, 2007. **178**(2): p. 73-86.
101. Bridgwater, J., C.J. Broadbent, and D.J. Parker, *Study of the influence of blade speed on the performance of a powder mixer using positron emission particle tracking.* Chemical Engineering Research & Design, Part A: Transactions of the Institute of Chemical Engineers, 1993. **71**(A6): p. 675-681.
102. Bagster, D.F. and J. Bridgwater, *The measurement of the force needed to move blades through a bed of cohesionless granules.* Powder Technology, 1967. **1**(4): p. 189-198.
103. Bagster, D.F. and J. Bridgwater, *The flow of granular material over a moving blade.* Powder Technology, 1970. **3**(1): p. 323-338.
104. Knight, P.C., J.P.K. Seville, A.B. Wellm, and T. Instone, *Prediction of impeller torque in high shear powder mixers.* Chemical Engineering Science, 2001. **56**(15): p. 4457-4471.
105. Stewart, R.L., J. Bridgwater, and D.J. Parker, *Granular flow over a flat-bladed stirrer.* Chemical Engineering Science, 2001. **56**(14): p. 4257-4271.
106. Conway, S.L., A. Lekhal, J.G. Khinast, and B.J. Glasser, *Granular flow and segregation in a four-bladed mixer.* Chemical Engineering Science, 2005. **60**(24): p. 7091-7107.
107. Lekhal, A., S.L. Conway, B.J. Glasser, and J.G. Khinast, *Characterization of granular flow of wet solids in a bladed mixer.* AIChE Journal, 2006. **52**(8): p. 2757-2766.

108. Stewart, R.L., J. Bridgwater, Y.C. Zhou, and A.B. Yu, *Simulated and measured flow of granules in a bladed mixer--a detailed comparison.* Chemical Engineering Science, 2001. **56**(19): p. 5457-5471.
109. Zhou, Y.C., A.B. Yu, and J. Bridgwater, *Segregation of binary mixture of particles in a bladed mixer.* Journal of Chemical Technology and Biotechnology, 2003. **78**(2-3): p. 187-193.
110. Zhou, Y.C., A.B. Yu, R.L. Stewart, and J. Bridgwater, *Microdynamic analysis of the particle flow in a cylindrical bladed mixer.* Chemical Engineering Science, 2004. **59**(6): p. 1343-1364.
111. Sato, Y., H. Nakamura, and S. Watano, *Numerical analysis of agitation torque and particle motion in a high shear mixer.* Powder Technology, 2008. **186**(2): p. 130-136.
112. Faure, A., P. York, and R.C. Rowe, *Process Control and Scale-up of Pharmaceutical Wet Granulation Processes: A Review.* European Journal of Pharmaceutics and Biopharmaceutics, 2001. **52**(3): p. 269-277.
113. Litster, J.D., *Scaleup of wet granulation processes: Science not art.* Powder Technology, 2003. **130**(1-3): p. 35-40.
114. Gotoh, K., H. Masuda, and K. Higashitani, *Powder Technology Handbook*. Journal of Thermal Spray Technology. Vol. 10. 2001: ASM International. 10.
115. Rahmanian, N., M. Ghadiri, and Y. Ding, *Effect of scale of operation on granule strength in high shear granulators.* Chemical Engineering Science, 2008. **63**(4): p. 915-923.
116. Holm, P., T. Schaefer, and H.G. Kristensen, *Granulation in High-Speed Mixers. Part V. Power Consumption and Temperature Changes during Granulation* Powder Technology, 1985. **43**(3): p. 213-223.
117. Holm, P., T. Schaefer, and H.G. Kristensen, *Granulation in High-Shear Mixers. Part VI. Effects of Process Conditions on Power Consumption and Granule Growth.* Powder Technology, 1985. **43**(3): p. 225-233.
118. Knight, P.C., *Investigation of the kinetics of granulation using a high shear mixer.* Powder Technology, 1993. **77**(2): p. 159-169.
119. Sirois, P. and G. Craig, *Scaleup of a High-Shear Granulation Process Using a Normalized Impeller Work Parameter.* Pharmaceutical Development & Technology, 2000. **5**(3): p. 365.
120. Sato, Y., T. Okamoto, and S. Watano, *Scale-Up of High Shear Granulation Based on Agitation Power.* Chem. Pharm. Bull., 2005. **53**(12): p. 1547-1550.
121. Litster, J.D., K.P. Hapgood, J.N. Michaels, A. Sims, M. Roberts, and S.K. Kameneni, *Scale-up of mixer granulators for effective liquid distribution.* Powder Technology, 2002. **124**(3): p. 272-280.
122. Watano, S., T. Okamoto, Y. Sato, and Y. Osako, *Scale-up of High Shear Granulation Based on the Internal Stress Measurement.* Chem. Pharm. Bull., 2005. **53**(4): p. 351-354.
123. Tardos, G.I., K.P. Hapgood, O.O. Ipadeola, and J.N. Michaels, *Stress measurements in high-shear granulators using calibrated "test" particles: application to scale-up.* Powder Technology, 2004. **140**(3): p. 217-227.

124. Darelius, A., A. Rasmuson, I.N. Björn, and S. Folestad, *High shear wet granulation modelling--a mechanistic approach using population balances.* Powder Technology, 2005. **160**(3): p. 209-218.
125. Liu, L.X. and J.D. Litster, *Population balance modelling of granulation with a physically based coalescence kernel.* Chemical Engineering Science, 2002. **57**(12): p. 2183-2191.
126. Realpe, A. and C. Velazquez, *Growth kinetics and mechanism of wet granulation in a laboratory-scale high shear mixer: effect of initial polydispersity of particle size.* Chemical Engineering Science, 2008. **63**(6): p. 1602-11.
127. Gantt, J.A., I.T. Cameron, J.D. Litster, and E.P. Gatzke, *Determination of coalescence kernels for high-shear granulation using DEM simulations.* Powder Technology, 2006. **170**(2): p. 53-63.
128. Hassanpour, A., S.J. Antony, and M. Ghadiri, *Modeling of agglomerate behavior under shear deformation: effect of velocity field of a high shear mixer granulator on the structure of agglomerates.* Advanced Powder Technology, 2007. **18**(6): p. 803-11.
129. Hoekstra, L., P. Vonk, and L.A. Hulshof, *Modeling the scale-up of contact drying processes.* Organic Process Research & Development, 2006. **10**(3): p. 409-416.
130. Metzger, T., M. Kwapinska, M. Peglow, G. Saage, and E. Tsotsas, *Modern modelling methods in drying.* Transport in Porous Media, 2007. **66**(1-2): p. 103-120.
131. Tsuji, Y., T. Tanaka, and T. Ishida, *Lagrangian numerical simulation of plug flow of cohesionless particles in a horizontal pipe.* Powder Technology, 1992. **71**(3): p. 239-250.
132. Stevens, A.B. and C.M. Hrenya, *Comparison of soft-sphere models to measurements of collision properties during normal impacts.* Powder Technology, 2005. **154**(2-3): p. 99-109.
133. Kruggel-Emden, H., E. Simsek, S. Rickelt, S. Wirtz, and V. Scherer, *Review and extension of normal force models for the Discrete Element Method.* Powder Technology, 2007. **171**(3): p. 157-173.
134. Liss, E.D., S.L. Conway, and B.J. Glasser, *Density waves in gravity-driven granular flow through a channel.* Physics of Fluids, 2002. **14**(9): p. 3309-26.
135. Schaefer, J., S. Dippel, and D.E. Wolf, *Force schemes in simulations of granular materials.* Journal de Physique I (General Physics, Statistical Physics, Condensed Matter, Cross-Disciplinary Physics), 1996. **6**(1): p. 5-20.
136. Di Maio, F.P. and A. Di Renzo, *Modelling particle contacts in distinct element simulations - linear and non-linear approach.* Chemical Engineering Research and Design, 2005. **83**(A11): p. 1287-97.
137. Di Renzo, A. and F.P. Di Maio, *Comparison of contact-force models for the simulation of collisions in DEM-based granular flow codes.* Chemical Engineering Science, 2004. **59**(3): p. 525-541.
138. Poschel, T. and T. Schwager, *Computational Granular Dynamics - Models and Algorithms*. Vol. 1. 2005: Springer. 322.
139. Gyenis, J., Z. Ulbert, J. Szépvölgyi, and Y. Tsuji, *Discrete particle simulation of flow regimes in bulk solids mixing and conveying.* Powder Technology, 1999. **104**(3): p. 248-257.

140. Limtrakul, S., A. Boonsrirat, and T. Vatanatham, *DEM modeling and simulation of a catalytic gas-solid fluidized bed reactor: a spouted bed as a case study.* Chemical Engineering Science, 2004. **59**(22-23): p. 5225-5231.
141. Limtrakul, S., A. Chalermwattanatai, K. Unggurawirote, Y. Tsuji, T. Kawaguchi, and W. Tanthapanichakoon, *Discrete particle simulation of solids motion in a gas-solid fluidized bed.* Chemical Engineering Science, 2003. **58**(3-6): p. 915-921.
142. Kruggel-Emden, H., S. Wirtz, and V. Scherer, *A study on tangential force laws applicable to the discrete element method (DEM) for materials with viscoelastic or plastic behavior.* Chemical Engineering Science, 2008. **63**(6): p. 1523-1541.
143. Mindlin, R.D., *Compliance of Elastic Bodies in Contact.* Journal of Applied Mechanics, 1949. **16**: p. 259-268.
144. Mikami, T., H. Kamiya, and M. Horio, *Numerical simulation of cohesive powder behavior in a fluidized bed.* Chemical Engineering Science, 1998. **53**(10): p. 1927-1940.
145. Silverstein, D.L. and T. Fort, *Studies in air-water interfacial area for wet unsaturated particulate porous media systems.* Langmuir, 1997. **13**(17): p. 4758-4761.
146. William, J.L. *Pore-Scale Model for Water Retention in Unsaturated Sand*. in *Powders and Grains 2009*. 2009: AIP.
147. Denoth, A., *Structural phase changes of the liquid water component in Alpine snow.* Cold Regions Science and Technology, 2003. **37**(3): p. 227-232.
148. Grof, Z., C.J. Lawrence, and F. Tepanek, *Computer simulation of evolving capillary bridges in granular media.* Granular Matter, 2008. **10**(2): p. 93-103.
149. Scheel, M., R. Seemann, M. Brinkmann, M. Di Michiel, A. Sheppard, and S. Herminghaus, *Liquid distribution and cohesion in wet granular assemblies beyond the capillary bridge regime.* Journal of Physics: Condensed Matter, 2008. **20**(49): p. 494236 (7 pp.).
150. Lian, G., C. Thornton, and M.J. Adams, *A Theoretical Study of the Liquid Bridge Forces between Two Rigid Spherical Bodies.* Journal of Colloid and Interface Science, 1993. **161**(1): p. 138-147.
151. Richefeu, V., M.S.E. Youssoufi, and F. Radjai, *Shear strength properties of wet granular materials.* Physical Review E (Statistical, Nonlinear, and Soft Matter Physics), 2006. **73**(5): p. 51304-1.
152. Megias-Alguacil, D. and L.J. Gauckler, *Capillary Forces Between Two Solid Spheres Linked by a Concave Liquid Bridge: Regions of Existence and Forces Mapping.* AIChE Journal, 2009. **55**(5): p. 1103-1109.
153. Freireich, B., J. Litster, and C. Wassgren, *Using the discrete element method to predict collision-scale behavior: A sensitivity analysis.* Chemical Engineering Science, 2009. **64**(15): p. 3407-3416.
154. Chung, Y.C. and J.Y. Ooi, *Influence of discrete element model parameters on bulk behavior of a granular solid under confined compression.* Particulate Science and Technology, 2008. **26**(1): p. 83-96.
155. Campbell, C.S., *Self-diffusion in granular shear flows.* J. Fluid Mech., 1997. **348**: p. 85-101.
156. Arntz, M.M.H.D., W.K. Den Otter, W.J. Briels, P.J.T. Bussmann, H.H. Beeltink, and R.M. Boom, *Granular mixing and segregation in a horizontal rotating drum:*

A simulation study on the impact of rotational speed and fill level. AIChE Journal, 2008. **54**(12): p. 3133-3146.
157. Glasser, B.J. and I. Goldhirsch, *Scale dependence, correlations, and fluctuations of stresses in rapid granular flows.* Physics of Fluids, 2001. **13**(2): p. 407-20.
158. *FlowManager Particle ImageVelocimetry Instrumentation Installation and User's Guide*. 1998, Dantec Measurement Technology.
159. Jesuthasan, N., B.R. Baliga, and S.B. Savage, *Use of Particle Tracking Velocimetry for Measurements of Granular Flows: Review and Application.* KONA, 2006. **24**: p. 15-26.
160. Jaworski, Z., K.N. Dyster, and A.W. Nienow, *The Effect of Size, Location and Pumping Direction of Pitched Blade Turbine Impellers on Flow Patterns: LDA Measurements and CFD Predictions.* Chemical Engineering Research and Design, 2001. **79**(8): p. 887-894.
161. Campbell, C.S., *Self-diffusion in granular shear flows.* Journal of Fluid Mechanics, 1997. **348**: p. 85-101.
162. Sperl, M., *Experiments on corn pressure in silo cells - Translation and comment of Janssen's paper from 1895.* Granular Matter, 2006. **8**(2): p. 59-65.
163. Masson, S. and J. Martinez, *Effect of particle mechanical properties on silo flow and stresses from distinct element simulations.* Powder Technology, 2000. **109**(1): p. 164-178.
164. Potapov, A.V. and C.S. Campbell, *Computer simulation of hopper flow.* Physics of Fluids, 1996. **8**(11): p. 2884-94.
165. Ford, K.J., *Experimental Investigation of Phase Behavior and the Dynamics of Vertically Vibrated Deep Granular Beds*, in *Chemical Engineering*. 2008, Lehigh University. p. 177.
166. Duran, J., *The static properties of a granular pile*, in *Sands, Powders and Grains*, L. Lam and D. Langevin, Editors. 1999, Springer: New York. p. 54-75.
167. Bertho, Y., F. Giorgiutti-Dauphine, and J.P. Hulin, *Dynamical Janssen effect on granular packing with moving walls.* Physical Review Letters, 2003. **90**(14): p. 144301-1.
168. Taberlet, N., P. Richard, and R. Delannay, *The effect of sidewall friction on dense granular flows.* Computers and Mathematics with Applications, 2008. **55**(2): p. 230-4.
169. Jaehyuk, C., A. Kudrolli, R.R. Rosales, and M.Z. Bazant, *Diffusion and mixing in gravity-driven dense granular flows.* Physical Review Letters, 2004. **92**(17): p. 174301-1.
170. Mair, K., K.M. Frye, and C. Marone, *Influence of grain characteristics on the friction of granular shear zones.* Journal of Geophysical Research, 2002. **107**(B10): p. 4-1.
171. Frye, K.M. and C. Marone, *The effect of particle dimensionality on granular friction in laboratory shear zones.* Geophysical Research Letters, 2002. **29**(19): p. 22-1.
172. Nilpawar, A.M., G.K. Reynolds, A.D. Salman, and M.J. Hounslow, *Surface velocity measurement in a high shear mixer.* Chemical Engineering Science, 2006. **61**(13): p. 4172-4178.

173. Schwedes, J., *Review on testers for measuring flow properties of bulk solids.* Granular Matter, 2003. **5**(1): p. 1-43.
174. Kadau, D., D. Schwesig, J. Theuerkauf, and D.E. Wolf, *Influence of particle elasticity in shear testers.* Granular Matter, 2006. **8**(1): p. 35-40.
175. Thornton, C. and L. Zhang. *A DEM comparison of different shear testing devices*. in *Powders and Grains 2001*. 2001. Sendai, Japan: A.A. Balkema.
176. Zhang, L. and C. Thornton, *A numerical examination of the direct shear test.* Geotechnique, 2007. **57**(4): p. 343-54.
177. Baran, O., A. DeGennaro, E. Rame, and A. Wilkinson. *DEM Simulation of a Schulze Ring Shear Tester*. 2009: AIP.
178. Theuerkauf, J., S. Dhodapkar, K. Manjunath, K. Jacob, and T. Steinmetz, *Applying the discrete element method in process engineering.* Chemical Engineering & Technology, 2003. **26**(2): p. 157-162.
179. Langroudi, M.K., G.I. Tardos, J.N. Michaels, and P. Mort. *Effect of Material Properties, Boundary Conditions and Flow Fields on the Rheology of Dense Granular Matter*. in *POWDERS AND GRAINS 2009: PROCEEDINGS OF THE 6TH INTERNATIONAL CONFERENCE ON MICROMECHANICS OF GRANULAR MEDIA*. 2009. Golden (Colorado): AIP.
180. Khakhar, D.V., J.J. McCarthy, and J.M. Ottino, *Mixing and segregation of granular materials in chute flows.* Chaos, 1999. **9**(3): p. 594-610.
181. Metzger, M., B. Remy, and B.J. Glasser, *Why all the Brazil nuts are not on top: Vibration induced granular size segregation of binary, ternary and multi-sized mixtures.* Submitted to Powder Technology, 2010.
182. Gauthier, D., S. Zerguerras, and G. Flamant, *Influence of the particle size distribution of powders on the velocities of minimum and complete fluidization.* Chemical Engineering Journal, 1999. **74**(3): p. 181-196.
183. Remy, B., J.G. Khinast, and B.J. Glasser, *The effect of mixer properties and fill level on granular flow in a bladed mixer.* AIChE Journal, 2010. **56**(2): p. 336-353.
184. Visscher, W.M. and M. Bolsterli, *Random packing of equal and unequal spheres in two and three dimensions.* Nature, 1972. **239**(5374): p. 504-7.
185. Yu, A.B. and N. Standish, *Estimation of the porosity of particle mixtures by a linear-mixture packing model.* Industrial and Engineering Chemistry Research, 1991. **30**(6): p. 1372-1385.
186. Suzuki, M. and T. Oshima, *Verification of a model for estimating the void fraction in a three-component randomly packed bed.* Powder Technology, 1985. **43**(2): p. 147-153.
187. Standish, N. and D.E. Borger, *The porosity of particulate mixtures.* Powder Technology, 1979. **22**(1): p. 121-125.
188. Yu, A.B. and N. Standish, *Porosity calculations of multi-component mixtures of spherical partciles.* Powder Technology, 1987. **52**(3): p. 233-241.
189. Sakaie, K., D. Fenistein, T.J. Carroll, M. van Hecke, and P. Umbanhowar, *MR imaging of Reynolds dilatancy in the bulk of smooth granular flows.* Europhysics Letters, 2008. **84**(3): p. 38001 (5 pp.).
190. Dolgunin, V.N., A.N. Kudy, and A.A. Ukolov, *Development of the model of segregation of particles undergoing granular flow down an inclined chute.* Powder Technology, 1998. **96**(3): p. 211-218.

191. Muthuswamy, M. and A. Tordesillas, *How do interparticle contact friction, packing density and degree of polydispersity affect force propagation in particulate assemblies?* Journal of Statistical Mechanics: Theory and Experiment, 2006. **2006**(09): p. 23 pp.
192. Yang, R.Y., R.P. Zou, and A.B. Yu, *Numerical study of the packing of wet coarse uniform spheres.* AIChE Journal, 2003. **49**(7): p. 1656-1666.
193. Anand, A., J.S. Curtis, C.R. Wassgren, B.C. Hancock, and W.R. Ketterhagen, *Segregation of cohesive granular materials during discharge from a rectangular hopper.* Granular Matter, 2010. **in press**.
194. Deliang, S. and J.J. McCarthy, *Numerical simulation of liquid transfer between particles.* Powder Technology, 2008. **184**(1): p. 64-75.
195. Donahue, C.M., C.M. Hrenya, R.H. Davis, K.J. Nakagawa, A.P. Zelinskaya, and G.G. Joseph, *Stokes' Cradle: Normal Three-Body Collisions between Wetted Particles.* J. Fluid Mech., 2010. **in press**.
196. Radl, S., E. Kalvoda, B.J. Glasser, and J.G. Khinast, *Mixing characteristics of wet granular matter in a bladed mixer.* Powder Technology, 2010. **In Press, Accepted Manuscript**.
197. Chaudhuri, B., A. Mehrotra, F.J. Muzzio, and M.S. Tomassone, *Cohesive effects in powder mixing in a tumbling blender.* Powder Technology, 2006. **165**(2): p. 105-114.
198. Pierrat, P., D.K. Agrawal, and H.S. Caram, *Effect of moisture on the yield locus of granular materials: theory of shift.* Powder Technology, 1998. **99**(3): p. 220-227.
199. Kantak, A.A., C.M. Hrenya, and R.H. Davis, *Initial rates of aggregation for dilute, granular flows of wet particles.* Physics of Fluids, 2009. **21**(2): p. 023301-13.
200. Khan, M.I. and G.I. Tardos, *Stability of wet agglomerates in granular shear flows.* Journal of Fluid Mechanics, 1997. **347**: p. 347-368.
201. Cleary, P.W. and M.L. Sawley, *DEM modelling of industrial granular flows: 3D case studies and the effect of particle shape on hopper discharge.* Applied Mathematical Modelling, 2002. **26**(2): p. 89-111.
202. Cleary, P.W., *The effect of particle shape on simple shear flows.* Powder Technology, 2008. **179**(3): p. 144-163.
203. Poeschel, T. and V. Buchholtz, *Molecular dynamics of arbitrarily shaped granular particles.* Journal de Physique I (General Physics, Statistical Physics, Condensed Matter, Cross-Disciplinary Physics), 1995. **5**(11): p. 1431-55.
204. Jensen, R.P., P.J. Bosscher, M.E. Plesha, and T.B. Edil, *DEM simulation of granular media-structure interface: Effects of surface roughness and particle shape.* International Journal for Numerical and Analytical Methods in Geomechanics, 1999. **23**(6): p. 531-547.

Curriculum Vitae

BRENDA REMY

1996-2000 B.S. (Cum Laude) in Chemical Engineering, Rensselaer Polytechnic Institute, *Troy, NY*

2000-2004 Shift Supervisor/Process Engineer, Merck Manufacturing Division, Merck & Co., Inc., *Rahway, NJ*

2004-2007 Research Scientist, Process Research & Development, Bristol-Myers Squibb Co., *New Brunswick, NJ*

2005-2010 Ph.D. in Chemical and Biochemical Engineering, Rutgers, The State University of New Jersey, *Piscataway, NJ*

Publications

Remy, B., Khinast, J.G. and Glasser, B.J., "Wet Granular Flows in a Bladed Mixer: Experiments and Simulations of Monodisperse Spheres", *in preparation*, 2010.

Remy, B., Khinast, J.G. and Glasser, B.J., "Polydisperse Granular Flows in a Bladed Mixer: Experiments and Simulations of Cohesionless Spheres", *in preparation*, 2010.

Metzger, M.J., Remy, B., and Glasser, B.J., "Why all Brazil Nuts are Not on Top: Vibration Induced Granular Size Segregation of Binary, Ternary and Multi-sized Mixtures", *submitted to Powder Tech.*, 2010.

Remy, B., Canty, T.M., Khinast, J.G. and Glasser, B.J., "Experiments and Simulations of Cohesionless Particles with Varying Roughness in a Bladed Mixer", *accepted to Chem. Eng. Sci.*, 2010.

Remy, B., Khinast, J.G. and Glasser, B.J., "The Effect of Mixer Properties and Fill Level on Granular Flow in a Four-Bladed Mixer", *AIChE J.*, **56**, 336-353, 2010.

Remy, B., Khinast, J.G. and Glasser, B.J., "Discrete Element Simulation of Free Flowing Grains in a Four-Bladed Mixer", *AIChE J.*, **55**, 2035-2048, 2009.

Remy, B., Brueggemeier, S., Marchut, A., Lyngberg, O., Lin, D. and Hobson, L., "Modeling-Based Approach towards On-Scale Implementation of a Methanethiol-Emitting Reaction", *Org. Process Res. Dev.*, **12**, 381-391, 2008.